

## ABSTRACT

ZHU, YUWEI. Analysis of Neutron Thermalization in Liquid FLiBe. (Under the direction of Prof. Ayman I. Hawari).

FLiBe, a liquid formed by fusing crystalline LiF and BeF<sub>2</sub> salts at temperatures exceeding 732 K, has the chemical formula Li<sub>2</sub>BeF<sub>4</sub>. FLiBe demonstrates outstanding properties such as chemical stability at high temperatures, high moderating ratio, and high heat capacity. It has therefore been proposed as a coolant, moderator, and heat storage medium in thermal neutron driven nuclear reactors. In proposed reactor designs such as the thorium molten salt reactor (TMSR), and the small modular advanced high-temperature reactor (SmAHTR), liquid FLiBe can compose up to 70% volume of the fuel blanket. Neutronic simulations for the design of such thermal reactors require high fidelity thermal neutron scattering data for FLiBe. However, there is currently no available thermal neutron scattering law for liquid FLiBe. To date, proposed thermal neutron scattering cross sections for FLiBe are based on a crystalline solid model that fundamentally exhibits different thermal neutron scattering behavior from liquid FLiBe.

In this work, the thermal neutron scattering law (i.e.  $S(\alpha, \beta)$ ) for liquid FLiBe is calculated. The process used a liquid FLiBe molecular dynamics (MD) model based on the Born-Mayer pair potential. Predicted physical properties from the MD model such as density, viscosity, heat capacity, and diffusion coefficient showed good agreement with experimental measurements. Velocity autocorrelation functions (VACF) as well as particle trajectories were generated from the model. With these data, two different methods were implemented to calculate the FLiBe thermal scattering law (TSL). The first method is used to evaluate the TSL

of this molten salt liquid by separating the excitation DOS into the bound vibrational mode and the diffusional mode. The partial TSLs of the bound vibrational mode and the diffusional mode were evaluated separately, each using its respective partial DOS. The total TSL of FLiBe was calculated by convolving the partial TSLs. The differential and the total thermal scattering cross sections of FLiBe were subsequently evaluated.

In the second method, MD trajectories were used to evaluate the TSL. This required introducing a quantum correction to the classical width function that appears in the intermediate scattering function. Subsequently, the classical width functions for each element in FLiBe were evaluated and quantum corrected. With the quantum width function, the corresponding TSLs for each element in FLiBe were evaluated at the representative reactor core temperatures of 873K, 923K, and 973K. Generally, good agreement was found between the quantum corrected self scattering law and the DOS evaluated self scattering law.

However, in the MD based analysis, the distinct scattering law is included in the evaluation by enforcing the same quantum correction ratio as for the self scattering law. The inclusion of distinct scattering law, which is validated by thermal neutron scattering measurements using liquid lithium, relaxes the Gaussian and the incoherent approximations and allows capturing the angular aspects of the scattering cross section. Based on that, the total thermal scattering law for each element in FLiBe was generated at the temperatures listed above and all corresponding thermal scattering cross sections were evaluated in a form appropriate for addition to the Evaluated Nuclear Data File (ENDF) and for use in reactor design analysis.

© Copyright 2018 by Yuwei Zhu

All Rights Reserved

Analysis of Neutron Thermalization in Liquid FLiBe

by  
Yuwei Zhu

A dissertation submitted to the Graduate Faculty of  
North Carolina State University  
in partial fulfillment of the  
requirements for the degree of  
Doctor of Philosophy

Nuclear Engineering

Raleigh, North Carolina

2018

APPROVED BY:

---

Nam Dinh

---

Paul Huffman

---

Bernard Wehring

---

Michael Zerkle

---

Ayman I. Hawari  
Committee Chair

## **DEDICATION**

This thesis is dedicated to the development of mankind's knowledge.

## BIOGRAPHY

Yuwei was born in a small town in southwest China. He spent his childhood in a neighborhood under significant planned economy. He became curious about how the universe governs itself since his childhood. In pursuit of science, he went to the University of Science and Technology of China (USTC) and graduated with Bachelor in Nuclear Engineering in 2012. He subsequently came to North Carolina State University (NCSU) for his graduate study. Yuwei began working with Dr. Ayman Hawari and got introduced into the field of thermal neutron scattering. He accomplished Master of Science in 2014 with the work on the thermal neutron scattering cross section of 3C-SiC. After that, he continued his effort in this field. Besides this thesis work, he has implemented the first version of the *FLASH* code. He also published numerous thermal scattering law libraries in the ENDF/B-VIII.0 release.

There is an old Chinese classic named 《生于忧患死于安乐》. It would be quoted here to summarize this biography:

生于忧患，死于安乐。

One thrives and survives under suffering and hardships, and withers if left overly-protected and contented with current situation.

故天将降大任于斯人也，

When the universe is about to confer a great responsibility on man,

必先苦其心志，劳其筋骨，饿其体肤，

it will first fill his heart with suffering, toil his sinews and bones, exposes his body to hunger,

空乏其身，行拂乱其所为，所以动心忍性，

subjects him to extreme poverty, confounds his journey with setbacks and troubles, so as to stimulate his alertness, toughen his nature,

曾益其所不能。

eventually bridging his incompetence gap and prepare him for the task.

## **ACKNOWLEDGMENTS**

I would like to give my wholehearted gratitude to Dr. Ayman Hawari for guiding me in this project. Without his patients and guidance, this project would be impossible. Dr. Hawari's professional outlook and abundant knowledge always shed light on our discussion.

I would also like to thank Jonathan Wormald from my research group. His ample knowledge in nuclear engineering and physics always gives me insight of problems in discussion. Many thanks to Cole Manring, Drew Antony, and Nina Colby Sorrell. They helped me proofread my thesis and gave me a lot of advices.

Last but not least, my roommate Jun Fang and my friend Jinyong Feng gave me a lot of support during my study here. I would also like to thank my family and other friends. Their supports always encourage me to overcome obstacles in my life.

## TABLE OF CONTENTS

LIST OF TABLES .....	viii
LIST OF FIGURES .....	ix
Chapter 1 Introduction .....	1
1.1 Advanced Nuclear Reactors.....	1
1.2 Research and Development of Molten Salt .....	5
1.3 Chemistry of FLiBe .....	8
1.4 Status of FLiBe Thermal Scattering Law Libraries .....	14
Chapter 2 Thermal Neutron Scattering Physics.....	18
2.1 General Theory of Thermal Neutron Scattering .....	18
2.1.1 Background of Thermal Neutron Scattering Theory .....	18
2.1.2 The Dynamic Structure Factor $S(\mathbf{k}, \omega)$ And the Thermal Scattering Law $S(\alpha, \beta)$ .....	22
2.1.3 The $G(\mathbf{r}, t)$ Function and the $I(\mathbf{k}, t)$ Function .....	25
2.1.4 The Self and Distinct Thermal Scattering Laws .....	27
2.1.5 Thermal Neutron Scattering and the Incoherent Approximation .....	29
2.2 The Gaussian Approximation and the Width Function .....	30
2.2.1 The Gaussian Approximation and the Width Function for Solid and Gas Materials ...	30
2.2.2 The Gaussian Approximation and the Width Function for Liquid Materials .....	32
2.3 The Separation of the Diffusive Thermal Scattering Law and the Bound Thermal Scattering Law .....	36
2.4 Thermal Neutron Scattering Models for Liquid Materials .....	38
2.5 The Quantum Thermal Scattering Law and the Classical Thermal Scattering Law.....	44
2.5.1 From the Quantum Thermal Scattering Law to the Classical Thermal Scattering Law – the Classical Approximation .....	44
2.5.2 From the Classical Thermal Scattering Law to the Quantum Thermal Scattering Law – the Quantum Correction .....	46
2.5.3 The Semiclassical Quantum Correction.....	47
2.5.4 The Quantum Correction on Distinct Thermal Scattering Law .....	50
2.6 Computational Techniques .....	51
Chapter 3 The Molecular Dynamics Technique .....	57
3.1 Overview of Molecular Dynamics.....	57
3.2 MD Model of Molten Salt Liquid FLiBe.....	59



3.2.1 Pair Potentials of General Molten Salt.....	59
3.2.2 Pair Potential of Molten Salt Liquid FLiBe .....	60
3.2.3 Equilibration of the MD model of FLiBe .....	63
3.3 Correlation Functions in MD .....	66
3.4 MD Predicted Properties of FLiBe .....	69
3.4.1 Liquid Density .....	69
3.4.2 Liquid Viscosity.....	70
3.4.3 Diffusion Coefficient .....	72
3.4.4 Heat Capacity .....	76
3.4.5 Thermal Conductivity .....	77
3.4.6 Velocity Autocorrelation Function .....	77
3.5 Evaluation of the Dynamic Structure Factor from MD .....	78
Chapter 4 The Quantum Correction of Classical Thermal Scattering Law .....	82
4.1 The MD Model of Liquid Lithium.....	83
4.2 The Classical Thermal Scattering Law and Experimental Measurements .....	84
4.3 Validation of the Gaussian Approximation .....	89
4.4 Deviation from the First Principle .....	91
4.5 The Quantum Correction on the Self Thermal Scattering Law .....	95
4.6 The Quantum Correction Including the Distinct Thermal Scattering Law.....	101
4.7 The Cross Section of Liquid Lithium .....	104
Chapter 5 Thermal Scattering Law of Molten Salt FLiBe.....	108
5.1 The Classical Scattering Law of FLiBe .....	108
5.2 The Quantum Correction of FLiBe.....	112
5.2.1 The Width Function of FLiBe.....	112
5.2.2 The Self Intermediate Scattering Function of FLiBe.....	118
5.2.3 The Self Thermal Scattering Law of FLiBe .....	122
5.2.4 The Thermal Scattering Law of FLiBe Including Distinct Effects.....	126
5.3 The Thermal Scattering Cross Section of FLiBe Using the MD TSL .....	130
5.3.1 The Double Differential Thermal Scattering Cross Section of FLiBe .....	131
5.3.2 The Differential Thermal Scattering Cross Section of FLiBe .....	136
5.3.3 The Integrated Thermal Scattering Cross Section of FLiBe.....	142

5.4 Comparison to the DOS method .....	142
5.4.1 The Density of States of FLiBe .....	143
5.4.2 The Thermal Scattering Law of FLiBe from the DOS method .....	145
5.4.3 The Double Differential Thermal Scattering Cross Section of FLiBe .....	150
5.4.4 The Differential Thermal Scattering Cross Section of FLiBe .....	151
5.4.5 The Integrated Thermal Scattering Cross Section of FLiBe.....	155
Chapter 6 Conclusion and Future Work .....	158
Future work.....	160
Implementation into the <i>FLASSH</i> Code System.....	160
Producing ENDF TSL Evaluation .....	161
Experiments in Support of Liquid FLiBe TSL Evaluation.....	161
REFERENCES .....	163
APPENDICES .....	173
Appendix A. Thermal Neutron Scattering for Solid Materials.....	174
A.1 The Gaussian and Cubic Approximation.....	174
A.2 The Phonon Expansion .....	176
Appendix B. Derivation of the Width Function of the Self Thermal Scattering Law for Liquid Materials .....	179
B.1 The Derivation of the Quantum Width Function .....	179
B.2 Application of the Quantum Width Function Algorithm.....	181
Appendix C. Numerical Issues in the NJOY Code.....	182
Appendix D. Comparison to the Existing FLiBe thermal scattering law analysis .....	185

## LIST OF TABLES

Table 1-1. Molten Salt Reactor Series and key features.....	6
Table 1-2. Physical properties of molten salt coolant candidates compared to those of water. ....	7
Table 3-1. Parameters for FLiBe defining the Born-Mayer potential. ....	61
Table 3-2. Interatomic parameters of FLiBe defining the Born-Mayer potential.....	62
Table 3-3. Generalized Einstein and Green Kubo formulas for transport coefficients .....	68
Table 5-1. Coefficients $d$ , $c$ and DOS weight $w_t$ used for modeling FLiBe diffusive behavior. ....	145
Table 6-1. Comparison of FLiBe cross section calculation using the Schofield model .....	186

## LIST OF FIGURES

Figure 1-1.	3400MWth AHTR concept design [15], which is a graphite-matrix fuel, high temperature, low pressure, molten salt cooled thermal reactor design equipped with advanced gas turbines. ....	3
Figure 1-2.	125MWth SmAHTR concept design [12], which is a graphite moderated, molten salt cooled, pebble bed, high temperature, compact, vehicles transportable thermal reactor. ....	4
Figure 1-3.	10MWth TMSR concept design [18], which is a graphite moderated, pebble bed, molten salt cooled, test thermal reactor for a 100MWth prototype TMSR reactor. ....	4
Figure 1-4.	Molten FLiBe with dissolved UF <sub>4</sub> flowing; the green tint is from dissolved fuel. ....	6
Figure 1-5.	The unit cell of solid FLiBe crystal ( <sup>7</sup> Li <sub>2</sub> BeF <sub>4</sub> ) [38,39], with green atoms for <sup>7</sup> Li, rose atoms for Be and silver atoms for F. ....	8
Figure 1-6.	Space group of FLiBe crystal ( <sup>7</sup> Li <sub>2</sub> BeF <sub>4</sub> ) [38,39]. ....	9
Figure 1-7.	Phase diagram of FLiBe at different mole fractions [60]. ....	10
Figure 1-8.	Compiled FLiBe densities from experimental measurements [32,44-46,49-52]. ....	11
Figure 1-9.	Compiled FLiBe viscosities from experimental measurements [9,43-48]. ....	11
Figure 1-10.	Experimental thermal conductivity [53]. ....	12
Figure 1-11.	Compiled FLiBe diffusion coefficients from experimental measurements [42,55] versus different temperatures. ....	13
Figure 1-12.	The unit cell of LiF crystal, with green atoms for Li, silver atoms for F. ....	15
Figure 1-13.	The unit cell of $\alpha$ -BeF <sub>2</sub> crystal, with rose atoms for Be, silver atoms for F. ....	15
Figure 1-14.	The DOS used in Mei et al. [72] and Li et al. [73-75] is from crystal BeF <sub>2</sub> and crystal LiF; the F in FLiBe DOS is a summation of F in LiF DOS and F in BeF <sub>2</sub> DOS. ....	16
Figure 2-1.	Diagram of the $I(k, t)$ space; the top left corner where $t \gg 1$ and $k \ll 1$ is the case where long-time, long-range diffusion behavior dominants; the bottom right corner where $t \ll 1$ and $k \gg 1$ is the situation where short-time short-range free particle like behavior dominants. ....	33
Figure 2-2.	Scheme of thermal neutron scattering cross section calculation. ....	52
Figure 2-3.	Hierarchy of scientific modes of investigation ....	54

Figure 2-4. Hierarchy of thermal neutron scattering research .....	55
Figure 3-1. The pair potential of FLiBe for different ion pairs, shown from 1 Å to 10 Å.....	62
Figure 3-2. Equilibration of the FLiBe ensemble at representative reactor core temperatures of 873 K.....	64
Figure 3-3. FLiBe MD system, with black as $\text{Be}^{2+}$ ions, red as $\text{F}^-$ ions, and white as $\text{Li}^+$ ions. The $\text{BeF}_4^{2-}$ clusters are showing as tetrahedral structure.....	65
Figure 3-4. The MD calculated density of FLiBe in comparison to the experimental data range. ....	70
Figure 3-5. The MD calculated viscosity of FLiBe in comparison to the experimental data range. ....	71
Figure 3-6. The Diffusion coefficient of Li (upper) and F (lower) in FLiBe in comparison to the experimental data range. ....	73
Figure 3-7. The multiplication of the diffusion coefficient and the viscosity for Li in FLiBe varies linearly with temperature, which is consistent with the Stokes-Einstein relation. ....	74
Figure 3-8. The multiplication of the diffusion coefficient and the viscosity for F in FLiBe varies exponentially with temperature, which is inconsistent with the Stokes-Einstein. ....	75
Figure 3-9. The enthalpy of molten salt liquid FLiBe from MD simulation. Red line fits the calculated enthalpy to evaluate the slope, which is the heat capacity. ....	76
Figure 3-10. Velocity autocorrelation function of each component in FLiBe.....	78
Figure 3-11. The procedure of $I^{cl}(k, t)$ evaluation .....	80
Figure 4-1. The NPA pair potential for liquid lithium.....	83
Figure 4-2. The NPT thermal equilibration of liquid lithium MD model.....	84
Figure 4-3. $I^{cl}(k, t)$ of liquid lithium at different time, i.e. $t = 0, 50, 100, 200 \text{ fs}$ . ....	85
Figure 4-4. $I_s^{cl}(k, t)$ of liquid lithium at different time $t = 0, 50, 100, 200 \text{ fs}$ . ....	86
Figure 4-5. $S^{cl}(k, \omega)$ and $S_s^{cl}(k, \omega)$ of liquid lithium at frequency $\omega = 0, 10, 20, 50 \text{ ps}^{-1}$ . ....	87
Figure 4-6. The $\omega \cdot S_{tot}^{cl}(k, \omega)$ of liquid lithium at different $k$ compared to experiments [121]. ....	88

Figure 4-7. Procedure of validating the Gaussian approximation .....	90
Figure 4-8. Comparison of MSD against width function .....	90
Figure 4-9. Quantum vs. classical $S(\alpha, -\beta)/S(\alpha, \beta)$ of liquid lithium at 484 K, the y-axis is in logarithmic scale. ....	92
Figure 4-10. The first moment of quantum vs. classical $S(\alpha, \beta)$ of liquid lithium at 484 K. ....	93
Figure 4-11. Quantum vs. classical $S_{sym}(\alpha, \beta)$ of liquid lithium at 484 K. ....	94
Figure 4-12. The integrated cross section for liquid lithium at 484 K. The first order Schofield correction applied $S^{cl}(\alpha, \beta)$ vs. $S^{qt}(\alpha, \beta)$ proposed in this work. ....	94
Figure 4-13. The flow diagram of quantum correction process (Eq. (2.5.3) to Eq. (2.5.6)).....	95
Figure 4-14. MSD of liquid lithium used in the quantum correction. ....	97
Figure 4-15. The quantum width function $\gamma(t)$ .....	98
Figure 4-16. The quantum intermediate scattering function $I_s(k, t)$ .....	98
Figure 4-17. The quantum corrected self thermal scattering law at $\alpha = 0.1646$ .....	99
Figure 4-18. Check of the principle of detailed balance. Black line is evaluated from the division of quantum corrected thermal scattering law. Red dashed line is the factor of the principle of detailed balance. ....	100
Figure 4-19. The 0 <sup>th</sup> moment and 1 <sup>st</sup> moment of the quantum corrected $S_s(\alpha, \beta)$ . ....	100
Figure 4-20. Flow chart of quantum correction including distinct effects (Eq. (2.5.15)).....	102
Figure 4-21. The collective structural function $\Gamma(\alpha)$ for liquid lithium .....	102
Figure 4-22. The quantum thermal scattering law: black is $S^{qt}(\alpha, \beta)$ , red dashed is $S_s^{qt}(\alpha, \beta)$ . ....	103
Figure 4-23. The thermal scattering law of liquid lithium from quantum correction including distinct effects (solid black) vs the Egelstaff & Schofield model (dashed blue) at 484 K. Scatter data are from neutron scattering experiment [121].....	104
Figure 4-24. The calculated double differential cross section of liquid lithium at 484 K compared to experiments at different scattering angles.....	105

Figure 4-25. The integrated cross section of liquid lithium. The cross section from quantum correction including distinct effects (solid black) is compared to the Doppler broadened free atom cross section (dashed red).....	106
Figure 5-1. The classical scattering law of Be in FLiBe.....	109
Figure 5-2. The classical scattering law of F in FLiBe.....	110
Figure 5-3. The classical scattering law of Li in FLiBe. ....	110
Figure 5-4. Deviation of the classical scattering law from the quantum scattering law.....	111
Figure 5-5. The deviation of integrated cross section of each species in FLiBe from their free atom cross section (black dashed line) at relative ( $> 0.1$ eV) high incident energies.....	111
Figure 5-6. The MSD of Be, F, Li in FLiBe at 873 K. ....	113
Figure 5-7. Temperature dependence of MSD of FLiBe at representative reactor core temperatures of 873 K, 923 K and 973 K.....	114
Figure 5-8. The quantum width function $\gamma(t)$ of: (a) Be, (b) F, (c) Li in FLiBe. The real part and imaginary part are shown as black dashed line and blue solid line for all species.....	115
Figure 5-9. The real part of the quantum width function at different temperatures for Li in FLiBe. ....	116
Figure 5-10. The imaginary part of the quantum width function at different temperatures for Li in FLiBe. ....	116
Figure 5-11. The quantum corrected width function and classical width function from MD simulation of Be in FLiBe. ....	117
Figure 5-12. The quantum corrected width function and classical width function from MD simulation of F in FLiBe.....	117
Figure 5-13. The quantum corrected width function and classical width function from MD simulation of Li in FLiBe. ....	118
Figure 5-14. The self intermediate scattering function, $I_s(k, t)$ , of each species in FLiBe at small $k$ ( $0.2 \text{ \AA}^{-1}$ ), mid-range $k$ ( $33.8 \text{ \AA}^{-1}$ ), and large $k$ ( $60 \text{ \AA}^{-1}$ ).....	119
Figure 5-15. The real part of intermediate scattering function of Li in FLiBe at different temperatures. ....	120
Figure 5-16. The imaginary part of intermediate scattering function of Li in FLiBe at different temperatures. ....	121

Figure 5-17. The asymmetric $S_s(\alpha, \beta)$ for Be in FLiBe against $\beta$ at different $\alpha$ at 873 K. ....	123
Figure 5-18. The asymmetric $S_s(\alpha, \beta)$ for F in FLiBe against $\beta$ at different $\alpha$ at 873 K. ....	123
Figure 5-19. The asymmetric $S_s(\alpha, \beta)$ for Li in FLiBe against $\beta$ at different $\alpha$ at 873 K. ....	123
Figure 5-20. The asymmetric $S_s(k, \omega)$ for FLiBe at different representative reactor core temperatures. ....	124
Figure 5-21. Moments of Be in FLiBe at 873K. ....	125
Figure 5-22. Moments of F in FLiBe at 873K. ....	125
Figure 5-23. Moments of Li in FLiBe at 873K. ....	126
Figure 5-24. Detailed balance behavior of Be in FLiBe at $\alpha = 2.052$ . ....	126
Figure 5-25. The classical thermal scattering law of FLiBe at $\omega = 1.819 THz$ . The red solid line is $S^{cl}(k, \omega)$ including distinct effects, the black dashed line is $S_s^{cl}(k, \omega)$ with no distinct effects. ....	127
Figure 5-26. The collective structural function of FLiBe. ....	129
Figure 5-27. The total and the self thermal scattering law for Li in FLiBe at $\beta = 0.1$ . ....	129
Figure 5-28. The total and the self thermal scattering law for Be in FLiBe at $\beta = 0.1$ . ....	130
Figure 5-29. The total and the self thermal scattering law for F in FLiBe at $\beta = 0.1$ . ....	130
Figure 5-30. Double differential cross section of Be in FLiBe at $\theta = 30^\circ, 60^\circ,$ $90^\circ, 120^\circ, 150^\circ, 180^\circ$ . The plot is evaluated at 873 K and $E_{in} = 0.075 eV$ . ....	132
Figure 5-31. Double differential cross section of F in FLiBe at $\theta = 30^\circ, 60^\circ,$ $90^\circ, 120^\circ, 150^\circ, 180^\circ$ . The plot is evaluated at 873 K and $E_{in} = 0.075 eV$ . ....	133
Figure 5-32. Double differential cross section of Li in FLiBe at $\theta = 30^\circ, 60^\circ,$ $90^\circ, 120^\circ, 150^\circ, 180^\circ$ . The plot is evaluated at 873 K and $E_{in} = 0.075 eV$ . ....	134
Figure 5-33. Double differential cross section of FLiBe at different representative reactor core temperatures. ....	135
Figure 5-34. The angular differential cross section of Be in FLiBe at representative reactor core temperatures. ....	137
Figure 5-35. The angular differential cross section of Li in FLiBe at representative reactor core temperatures. ....	137
Figure 5-36. The angular differential cross section of F in FLiBe at representative reactor core temperatures. ....	138



Figure 5-37. The differential cross section of Be in FLiBe at different incident energies at 873K. ....	139
Figure 5-38. The differential cross section of F in FLiBe at different incident energies at 873K. ....	140
Figure 5-39. The differential cross section of Li in FLiBe at different incident energies at 873K. ....	140
Figure 5-40. The differential cross section of FLiBe at $E_{in} = 1 \times 10 - 3eV$ at representative reactor core temperatures of 873 K, 923K, and 973 K. The bottom right plot is zoomed in around incident energy, showing details at small energy transfer. ....	141
Figure 5-41. The integrated cross section (a) Be, (b) F, (c) Li, (d) total of FLiBe. The blue solid line is 873K. The black dashed line is 923 K. The red dash-dotted line is 973 K. ....	142
Figure 5-42. The density of states of FLiBe. ....	144
Figure 5-43. The density of states of FLiBe for each species divided into the bound vibrational mode (blue) and the diffusional mode (red). (d) is the density of states of Maxwell-Boltzmann distribution. ....	144
Figure 5-44. The thermal scattering law of Be in FLiBe at 873 K from the DOS method (black) using the Egelstaff & Schofield model and phonon model. The red curve is the corresponding quantum corrected self thermal scattering law in Chapter 5. ....	146
Figure 5-45. The $S_s(\alpha, \beta)$ diffusional quasi-elastic peak of Li in FLiBe from different models. The linear diffusion model (blue dashed line) uses the diffusion coefficient $D$ predicted from MD as input. The Egelstaff & Schofield model (red open dots) uses the separated DOS as input. The quantum correction method (black solid line) uses the width function as input. ....	148
Figure 5-46. The thermal scattering law of Be in FLiBe at 873 K, DOS method (black) compared to the coherent and quantum correction (red). Distinct effects are missing in the DOS method. ....	149
Figure 5-47. Double differential cross sections of Be in FLiBe at 873 K from the DOS method (dashed black) comparing to those from the quantum correction method including distinct effects (solid red). The incident neutron energy is chosen at $E_{in} = 0.075 eV$ . ....	150
Figure 5-48. Secondary energy differential cross section of (a) Be, (b) F, (c) Li in FLiBe from different incident energies at 873 K. The dashed lines are quantum corrected cross section with	

distinct effects. The dotted lines are from the DOS method using the Schofield model.....	152
Figure 5-49. Differential cross section against scattering angle of (a) Be, (b) F, (c) Li in FLiBe at 873 K and at $E_{in} = 0.075 \text{ eV}$ . The solid black line is from the quantum correction method including the distinct effects. The red dashed line is from the DOS method (NJOY). Notice that the y-axis is broken, the peak is $\delta$ -function like. ....	153
Figure 5-50. Differential cross section against scattering angle of (a) Be, (b) F, (c) Li in FLiBe at 923 K and at $E_{in} = 0.080 \text{ eV}$ . ....	154
Figure 5-51. Differential cross section against scattering angle of (a) Be, (b) F, (c) Li in FLiBe at 973 K and at $E_{in} = 0.084 \text{ eV}$ . ....	155
Figure 5-52. Integrated cross section of Be in FLiBe at 873 K at $E_{in} = 0.075 \text{ eV}$ . Black line is the DOS method using the Schofield model. Red line is the quantum corrected cross section including distinct effects. ....	156
Figure 5-53. Integrated cross section of F in FLiBe at 873 K at $E_{in} = 0.075 \text{ eV}$ . ....	156
Figure 5-54. Integrated cross section of Li in FLiBe at 873 K at $E_{in} = 0.075 \text{ eV}$ . ....	157
Figure 6-1. $S(\alpha, \beta)$ showing cut off at $\alpha = 3.1 \times 10^{-9}$ . ....	183
Figure 6-2. $S(\alpha, \beta)$ showing cut off at $\alpha = 2.8 \times 10^{-8}$ . ....	183
Figure 6-3. $S(\alpha, \beta)$ showing cut off at $\alpha = 1.1 \times 10^{-7}$ . ....	184
Figure 6-4. Different shape of diffusional peak at very small scattering angle. ....	184
Figure 6-5. The bound DOS of F in FLiBe used in this work compared to Mei et al [72]. ....	187
Figure 6-6. The integrated cross section of FLiBe in this work compared to Mei et al. [72]. The dotted blue and dashed red lines adapted different $w_d$ values. ....	188

## **Chapter 1 Introduction**

### **1.1 Advanced Nuclear Reactors**

The Paris Agreement, a new global climate treaty, came into force November 4, 2016. It aims to reduce greenhouse gas emissions every five years to stabilize global temperatures. Nuclear power, as a zero greenhouse gas production technology, has significant potential to address the climate change challenge. As of 2017, there are 447 operational nuclear power reactors and 60 under construction across the world. They contributed 11% of the global energy supply [1].

Nuclear reactors are conventionally categorized by generation (e.g. Generation (Gen) I, II, III, and IV). Gen I refers to the prototypes and power reactors that launched civilian nuclear power in the 1950s and 1960s. The last Gen I reactor, Wylfa Nuclear Power Station, was decommissioned on December 30, 2015. Gen II categorizes a class of commercial reactors that were designed to be more economical and reliable. They consist of the majority of the world's current 447 nuclear power reactors. The first Gen II reactor began operation in the early 1960s. Gen III reactors are Gen II reactors with evolutionary, state of the art improvements. The first of these units went on the grid in Japan in 1996. Gen III will continue to be the mainstream units built over the next decade .

The proposed Gen IV reactors are designed with better sustainability, economics, safety, proliferation control, and physical protection. The Generation IV International Forum (GIF) [2] was established to explore areas of mutual interest between different countries. GIF makes recommendations regarding both R&D areas and processes by which collaboration could be conducted. In the current GIF technology roadmap, six design concepts are proposed as Gen IV reactors: very-high-temperature reactors (VHTR), sodium-cooled fast reactors (SFR),

supercritical-water-cooled reactors (SCWR), gas-cooled fast reactors (GFR), lead-cooled fast reactors (LFR), and molten salt reactors (MSR). According to the GIF roadmap, the Gen IV systems are expected to deploy in the 2030s [3].

Among the Gen IV designs, the VHTR design is dedicated to cogeneration of both electricity and hydrogen. The conversion of high temperature nuclear heat (above 550°C) to electricity with increased thermal efficiency was enabled by new advancements in Brayton power cycles [4,5]. Moreover, the temperature requirements for thermochemical hydrogen production are in the 700-850°C range, demanding higher outlet temperatures from reactor designs [6]. Compared to other systems in the Gen IV designs, the MSR design enjoys passive safety and low pressure from its liquid molten salt coolants. Another advantage of the molten salt is its high boiling point of generally above 1200 °C.

From 2004 to 2017, a new reactor concept, i.e., Fluoride-Salt-Cooled High-Temperature Reactors (FHR), has emerged [7-18]. FHR combined the VHTR and MSR technology with their established advantages including: high temperature that can produce electricity and hydrogen, increased thermal efficiency, liquid molten salt coolant, passive safety, and low pressure. The FHR designs include, but are not limited to, the thorium molten salt reactor (TMSR) [18], the advanced high-temperature reactor (AHTR), which is also called the liquid salt cooled high temperature reactor (LS-VHTR) [7-11,13-15], and the small modular advanced high-temperature reactor (SmAHTR) [11,12,15]. The latest research on the FHR project covers comprehensive areas, such as neutronic [19,20], thermal hydraulics [21,22], experiments [23,24], molten salt chemistry [25], and demonstration reactor design [16,17] etc. The proposed reactor concept designs for TMSR, AHTR, and SmAHTR are demonstrated in Figure 1-1 to Figure 1-3.

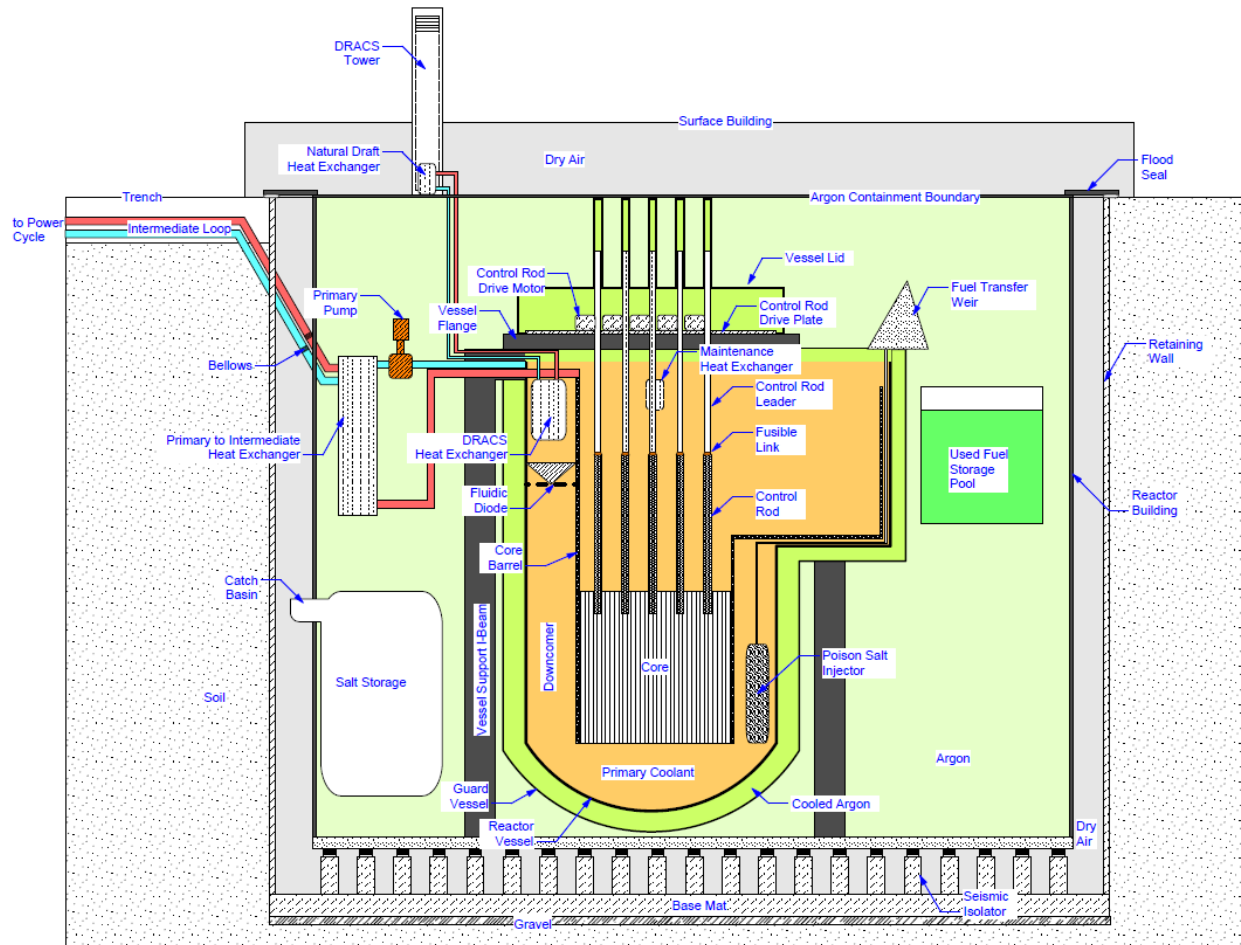


Figure 1-1. 3400MWth AHTR concept design [15], which is a graphite-matrix fuel, high temperature, low pressure, molten salt cooled thermal reactor design equipped with advanced gas turbines.

In the three examples from Figure 1-1 to Figure 1-3, the reactor thermal power scales from 10 MWth to 3400 MWth. The scalability and flexibility of these reactor designs [7-18] stems from the use of TRISO pebble fuels and liquid FLiBe coolant. In all FHR designs, FLiBe ( ${}^7\text{Li}_2\text{BeF}_4$ ) salt, a baseline salt that has been used in previous nuclear applications [26], is proposed as the primary loop coolant. The FLiBe cooled reactor designs share the benefits of stable molten salt. The decay heat removal performance is sufficient to save the reactor during a loss of force circulation (LOFC) event. Significant natural convection occurs, resulting in uniform fuel

temperature distribution, and the high boiling point of FLiBe salt (1430 °C) allows the reactor to safely operate at low pressures with large temperature safety margins.

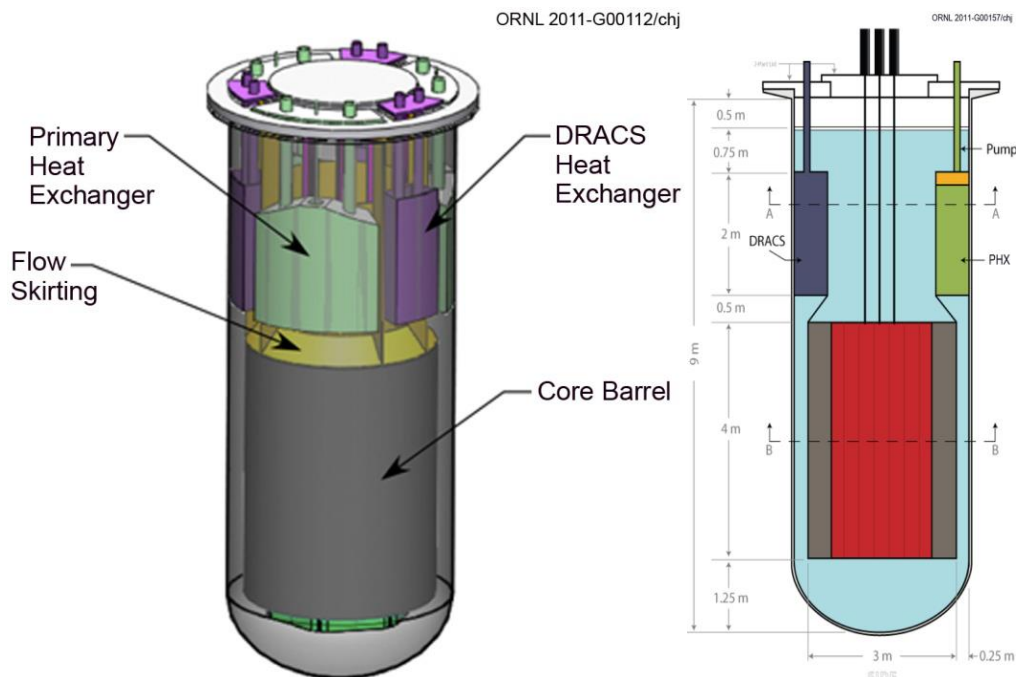


Figure 1-2. 125MWth SmAHTR concept design [12], which is a graphite moderated, molten salt cooled, pebble bed, high temperature, compact, vehicles transportable thermal reactor.

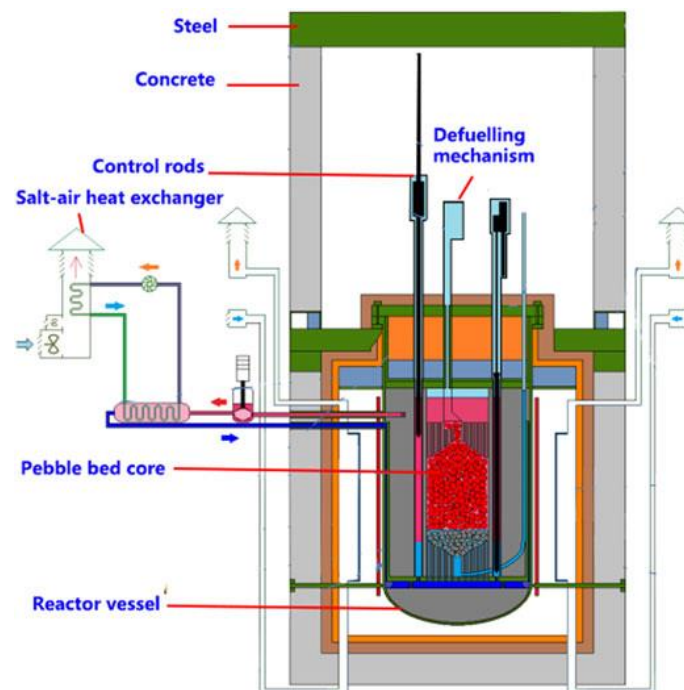


Figure 1-3. 10MWth TMSR concept design [18], which is a graphite moderated, pebble bed, molten salt cooled, test thermal reactor for a 100MWth prototype TMSR reactor.

The FHRs are thermal reactors. The design of such reactors is affected by on its thermal neutrons spectrum. Because the moderating ratio of FLiBe is close to water (see Table 1-2), the molten salt would also serve as a moderator in the reactor core. In FHR reactor blanket, the TRISO fuel's packing factor is 30% to 40% [17]. The coolant salt would make up 60% to 70% of the core volume around the fuel. Consequently, the coolant has a significant contribution to the neutron slowing down behavior in the reactor core. Therefore, a through understanding of the neutronic behaviors of the coolant salt is a requirement of the reactor design.

## **1.2 Research and Development of Molten Salt**

In 1954, the first prototype molten salt reactor that was built was the Aircraft Reactor Experiment (ARE) [27]. It was a 2.5 MWt thermal reactor to be used as high power density engine. Since then the concept has been carried from military applications over to civil power generation. The Molten Salt Reactor Experiment (MSRE) series of tests were conducted through the 1960s [28]. In the experiments, FLiBe ( ${}^7\text{Li}_2\text{BeF}_4$ ) salt (as shown in Figure 1-4) was extensively used as the coolant in the secondary loop. A deeper understanding of the physical, chemical, and neutronic behaviors of molten salts was recorded in more than 1000 reports. The past major MSR programs are summarized in Table 1-1 [29].

A review paper [30] published in 2017 summarized the density, heat capacity, thermal conductivity and viscosity of FLiBe and two other salts. Recently, three internal reference papers [9,29,31] were also compiled to review the historical efforts made in molten salt technology under Gen IV reactor design requirements. In 1988, Janz compiled a general database for molten salts in energy applications. The collected results were published in a 300-page report [32]. These reviews offer important compilations and guidelines for existing literature and experimental measurements.

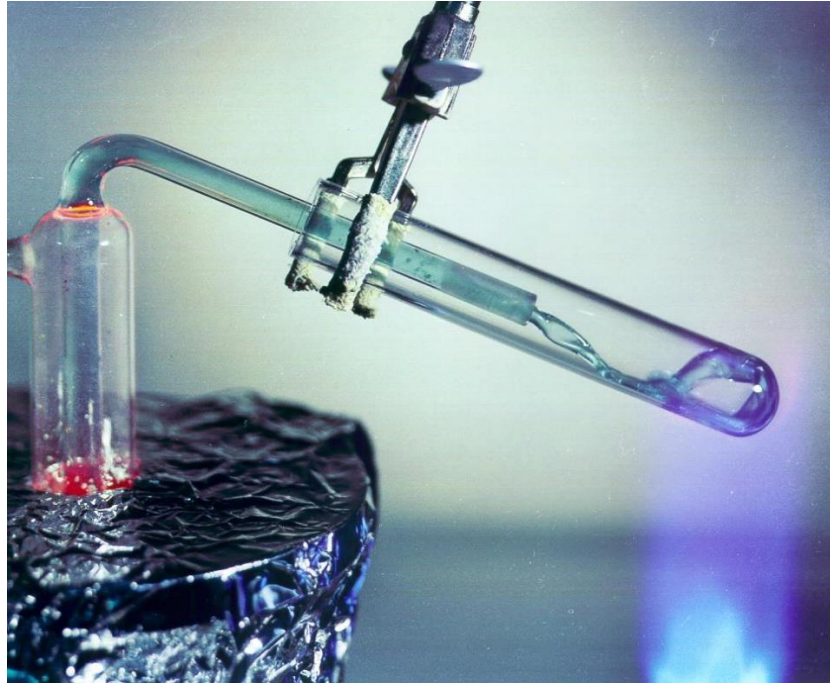


Figure 1-4. Molten FLiBe with dissolved UF<sub>4</sub> flowing; the green tint is from dissolved fuel.

Table 1-1. Molten Salt Reactor Series and key features.

Key Features	ARE	MSRE	MSBR (Design)
Name and Dates	Aircraft Reactor Experiment 1954	Molten Salt Reactor Experiment 1965-1970	Molten Salt Breeder Reactor (Design) 1970-1976
Peak Power Output (MWt)	~2.5	~8	n/a
Peak Temperature (°C)	860	650	705
Solid Moderator	BeO	Graphite	Graphite
Fuel-Salt Composition (% mol)	NaF-ZrF <sub>4</sub> -UF <sub>4</sub> (53-41-6)	<sup>7</sup> LiF-BeF <sub>2</sub> -ZrF <sub>4</sub> -UF <sub>4</sub> (65-30-5-0.1)	<sup>7</sup> LiF-BeF <sub>2</sub> -ThF <sub>4</sub> -UF <sub>4</sub> (72-16-12-0.4)
Secondary Coolant	Na metal	<sup>7</sup> LiF-BeF <sub>2</sub>	NaF-NaBF <sub>4</sub>

FLiBe was not only proposed as the solvent of liquid fuel in MSRs but also as a pure coolant salt in the secondary coolant loop. In addition to FLiBe, earlier reports also covered additional salt compounds such as NaF-ZrF<sub>4</sub> (Nafzirf), and LiF-NaF-KF (Flinak) [9] as thermal reactor coolant



candidates. The properties of these three thermal reactor coolant candidates are summarized and compared to water in Table 1-2. Recent study has also shown FLiBe to be a qualified fusion coolant candidate [33]. NaF-NaBF<sub>4</sub>, <sup>7</sup>LiF-NaF-KF, LiCl-NaCl-MgCl<sub>2</sub>, and NaNO<sub>3</sub>-KNO<sub>3</sub> were additionally proposed as fast reactor coolant salts [34-36].

Table 1-2. Physical properties of molten salt coolant candidates compared to those of water.

<b>Materials</b> <b>Properties*</b>	<b>FLiBe</b>	<b>Nafzirf</b>	<b>Flinak</b>	<b>Water</b>
Moderating ratio ( $\xi\Sigma_s/\Sigma_a$ )	63	6.7	1.7	71
Melting Point (°C)	459	500	462	0
Boiling Point (°C)	1430	1350	1570	100
Density $d$ (kg/m <sup>3</sup> )	1840	2784	1847	988
Dynamic Viscosity $\eta$ ( $\times 10^{-3}$ Pa · s)	1.40	2.27	1.39	0.53
Volumetric Heat Capacity $C$ ( $\times 10^6$ J/m <sup>3</sup> · K)	4.390	3.262	3.480	4.017
Thermal Conductivity $\kappa$ (W/m · K)	1.1	0.49	1.02	0.64
Heat Transfer per Unit Pump Power $\times 10^{15}C^3/d$	45.98	12.47	22.82	65.61

\* The physical properties are at 900°C for molten salts, 50°C for water, dynamic viscosity predicted from Figure 1-9.

As can be seen from Table 1-2, FLiBe has the highest volumetric heat capacity and the highest thermal conductivity compared to all the coolant candidates and water. Density of FLiBe is the lowest of all the molten salts. The moderating ratio is also the highest for FLiBe [37]. These thermal hydraulic friendly properties make FLiBe a good heat storage medium which is also easier to pump through the reactor.

Molten salts, especially FLiBe, have many excellent features, such as a low neutron absorption cross-section (if <sup>6</sup>Li is removed), no radiation damage, large heat capacity, low vapor pressure,

single-phase liquid, appropriate melting temperature, high boiling temperature, chemical inertness, good compatibility with structural material, compatibility with graphite, high solubility for U, Pu, and Th fluorides and fission products, no solubility for gaseous fission products such as Xe and Kr, and very limited radioactivity release in accidents. Therefore, in recent research [7-18], FLiBe is proposed as a primary coolant for the FHR and its numerous variants. The rest of this chapter will focus on the discussion of FLiBe.

### 1.3 Chemistry of FLiBe

FLiBe is a melted eutectic compound of  ${}^7\text{LiF}$  and  $\text{BeF}_2$  with a mole ratio of 2:1 at high temperature. When cooled below the melting temperature, the salt can form a crystal lattice [38,39] as shown in Figure 1-5.

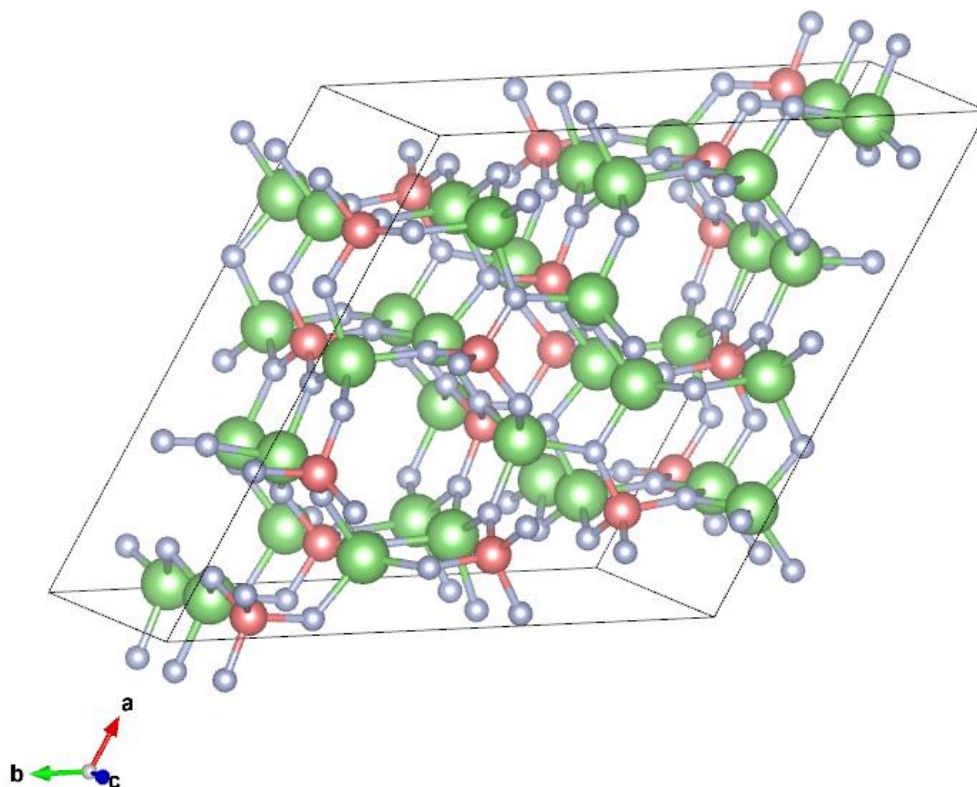


Figure 1-5. The unit cell of solid FLiBe crystal ( ${}^7\text{Li}_2\text{BeF}_4$ ) [38,39], with green atoms for  ${}^7\text{Li}$ , rose atoms for Be and silver atoms for F.

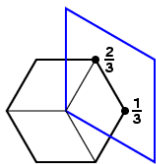


Figure 1-6. Space group of FLiBe crystal ( ${}^7\text{Li}_2\text{BeF}_4$ ) [38,39].

A review of these reports was compiled by Grimes [60], which contains measured density, heat capacity, and viscosity data together with the phase diagrams. An example phase diagram is given for FLiBe in Figure 1-7.

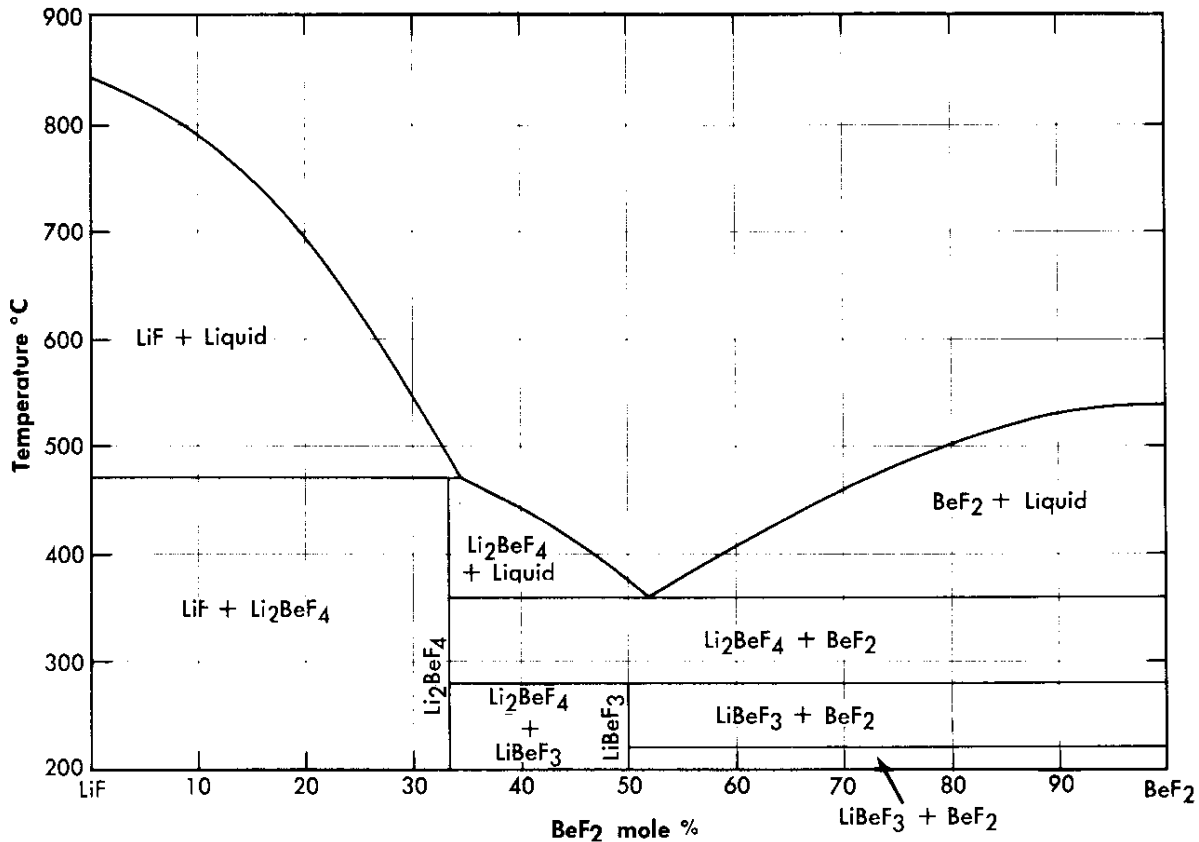


Figure 1-7. Phase diagram of FLiBe at different mole fractions [60].

After these initial efforts, great progress in experimental measurements of molten salts was made in the 1960s. Blanke [44] measured FLiBe's viscosity and density. Cantor [45,46,49] studied the FLiBe density and viscosity as a function of temperature and different melt compositions. Some other experimental studies on the density of FLiBe [32,50-52] report data that vary around  $\pm 10\%$ . The reported experimental density measurements are compiled and graphed in Figure 1-8. The viscosity values of FLiBe are reported from seven different sources, i.e., by William [9], Abe [43], Blanke [44], Cantor [45,46], Cohen [47], and Desyatnik [48]. They are compiled and shown in Figure 1-9.

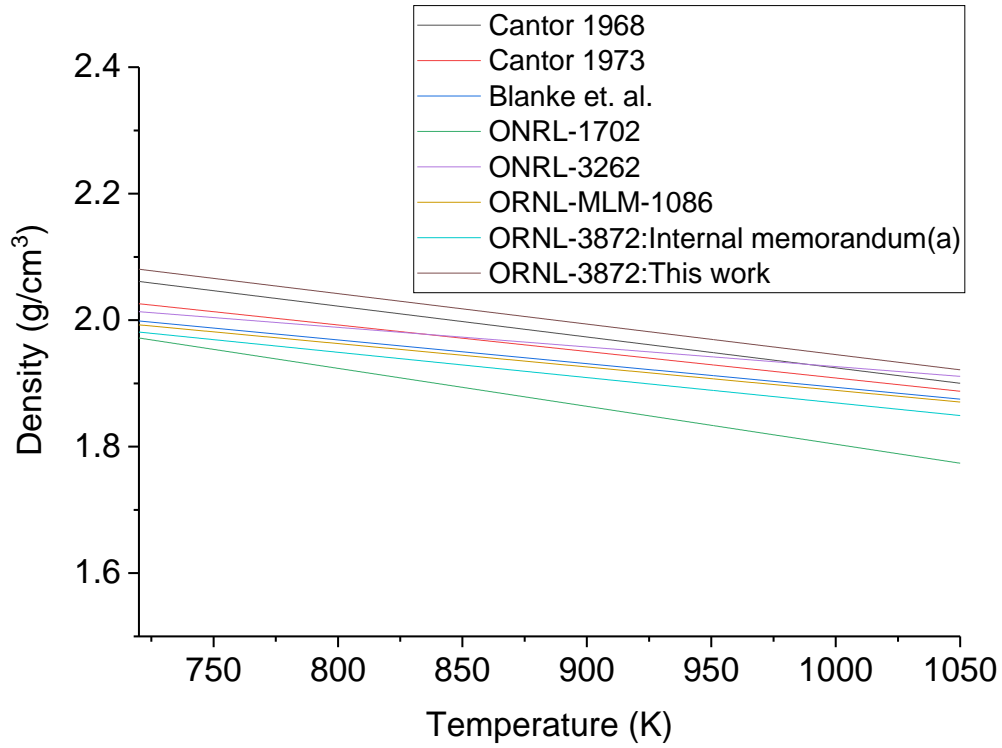


Figure 1-8. Compiled FLiBe densities from experimental measurements [32,44-46,49-52].

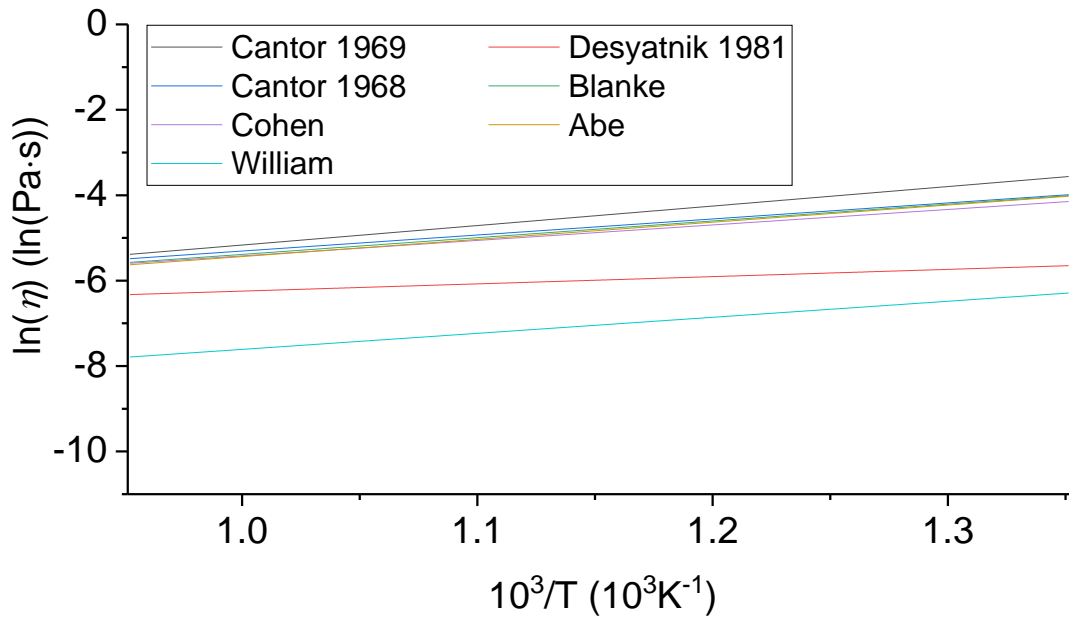


Figure 1-9. Compiled FLiBe viscosities from experimental measurements [9,43-48].

Although many experiments have cited the thermal conductivity of FLiBe being 1.0 to 1.1  $W/m \cdot K$ , the only legitimate reference for a real experimental measurement is by Cooke and

Hoffman from Rosenthal's report [41,53], which reports preliminary results for thermal conductivity using a "be validated variable-gap apparatus technique". Therefore, the thermal conductivity data for FLiBe should only be referenced as a guideline rather than a benchmark. The reported thermal conductivity is shown in Figure 1-10.

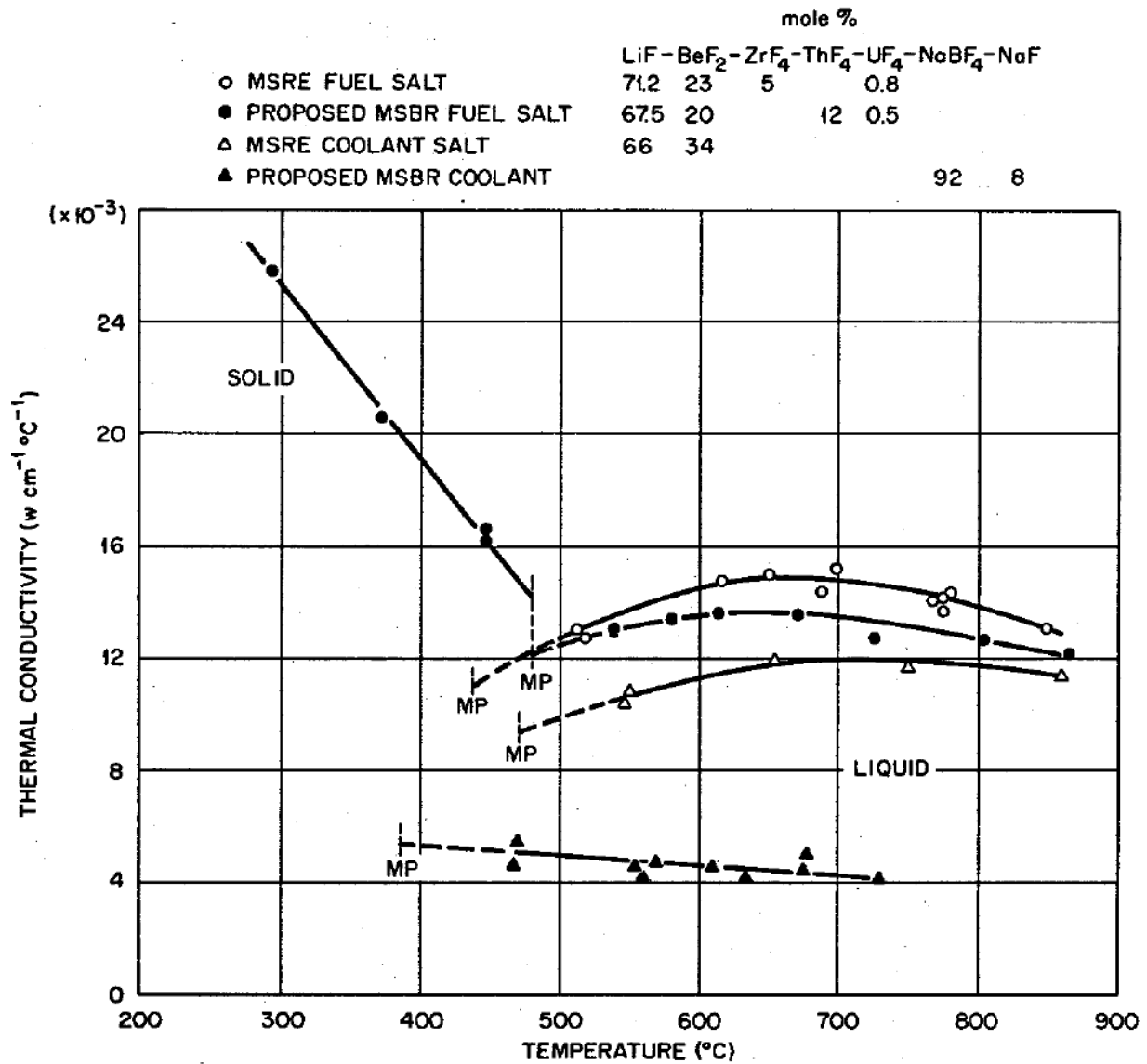


Figure 1-10. Experimental thermal conductivity [53].

There are three heat capacity experiments for FLiBe [41,45,61]. Cantor [45] measured the heat capacity of 0.57 cal/g. Douglas and Payne [61] measured the heat capacity of 0.56 cal/g. Cooke et al. reported measurements of heat capacity at 0.577 cal/g in Rosenthal's ORNL report

[41]. Unlike the measurement for thermal conductivity, the reported heat capacity uncertainty in experiments is small. This is due to the simplicity and maturity of heat capacity experiments.

Two studies [42,55] were performed to investigate the diffusion coefficient of Li and F in FLiBe using the capillary reservoir technique. The experimentally measured diffusion coefficients are shown in Figure 1-11. In Ohmichi et al.'s research [42], the measured diffusion coefficient of F in FLiBe [42] is abnormally high with rising temperature. Ohmichi et al. noticed this “extraordinarily large” diffusion coefficient compared to other salts but could not make a sound justification. This high diffusion coefficient was later found to be untrue based on the Einstein-Stokes relation.

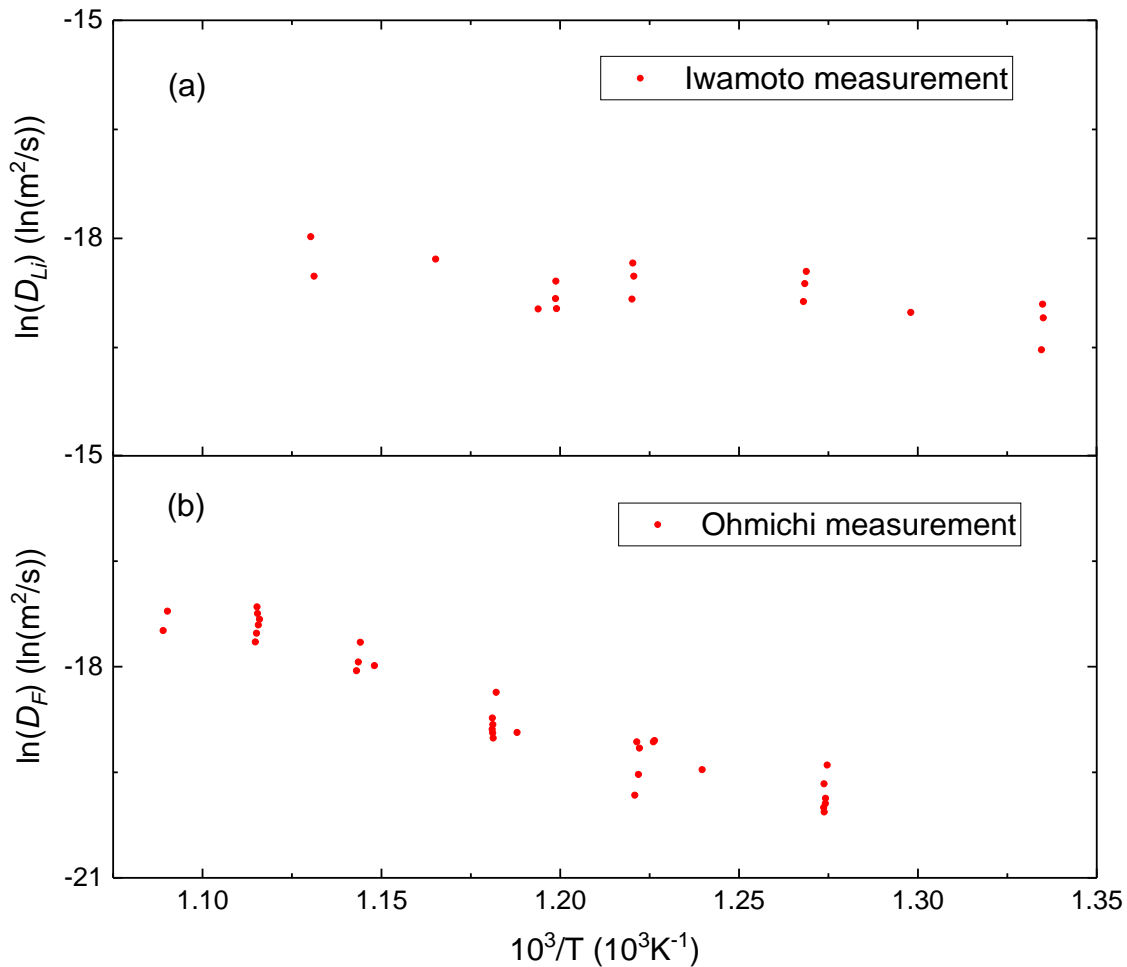


Figure 1-11. Compiled FLiBe diffusion coefficients from experimental measurements [42,55] versus different temperatures.

#### 1.4 Status of FLiBe Thermal Scattering Law Libraries

Due to the rising interest in molten salt driven reactor systems in recent years, two recent studies have been done on the thermal neutron scattering cross section of crystal  $^7\text{LiF}$  and  $\text{BeF}_2$  [62,63]. These works evaluated the thermal motion energy density of states of the  $^7\text{LiF}$  and  $\text{BeF}_2$  crystals using DFT and lattice dynamics theory. The DFT results analyzed the Hellmann Feynman forces in the crystal, which were used as input to the lattice dynamics to evaluate the density of states from phonon theory. This methodology is proven to work well for analyzing a crystalline material's vibrational density of states [64-67]. The coherent elastic cross section and inelastic cross section under the incoherent approximation for both  $^7\text{LiF}$  and  $\text{BeF}_2$  crystals were reported in the research. The research from Wang et al. [62] reported improved cross section calculations for  $^7\text{LiF}$  crystal compared to the calculation from Mei et al. [63]. These results are helpful in understanding the solid state thermal scattering for  $^7\text{LiF}$  and  $\text{BeF}_2$  crystals, such as shown in Figure 1-12 and Figure 1-13. However, the solid state FLiBe ( $^7\text{Li}_2\text{BeF}_4$ ) has a very different crystalline structure [39] and bonding symmetry [38] compared to stand-alone  $\text{BeF}_2$  crystals [68,69] and  $^7\text{LiF}$  crystals [70,71]. As can be seen in Figure 1-5, the tetragonal binding between Be and F, Li and F is unique in FLiBe crystals. The interaction between Be-Li ions is also distinctive in FLiBe crystals. Therefore, the calculation of thermal scattering cross sections for stand-alone  $^7\text{LiF}$  and  $\text{BeF}_2$  crystals cannot represent the interactions in FLiBe crystals.

There are two recent studies [72-75] evaluating the liquid FLiBe thermal neutron scattering cross section. The cross section by Li et al. [73-75] is a re-evaluation of the cross section by Mei et al. [72]. As a consequence, the two thermal scattering law evaluations are the same. Mei et al. [72] applied the DOS method with the Schofield diffusion model in the evaluation of the inelastic scattering cross section.



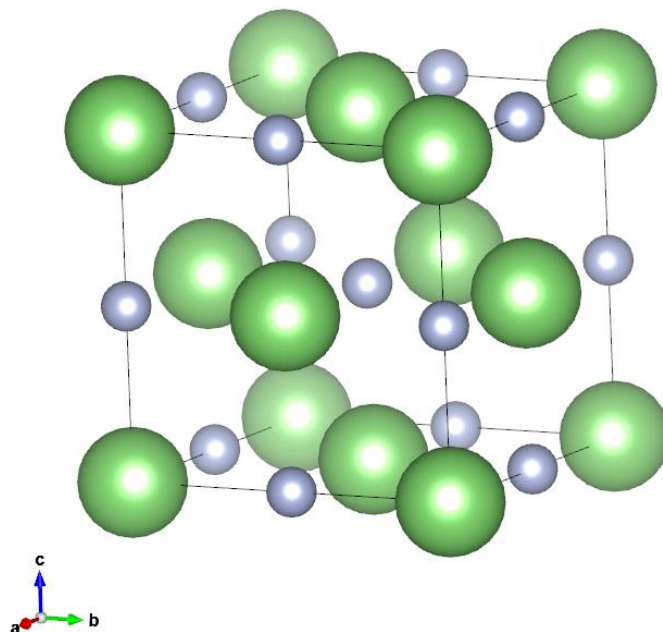


Figure 1-12. The unit cell of LiF crystal, with green atoms for Li, silver atoms for F.

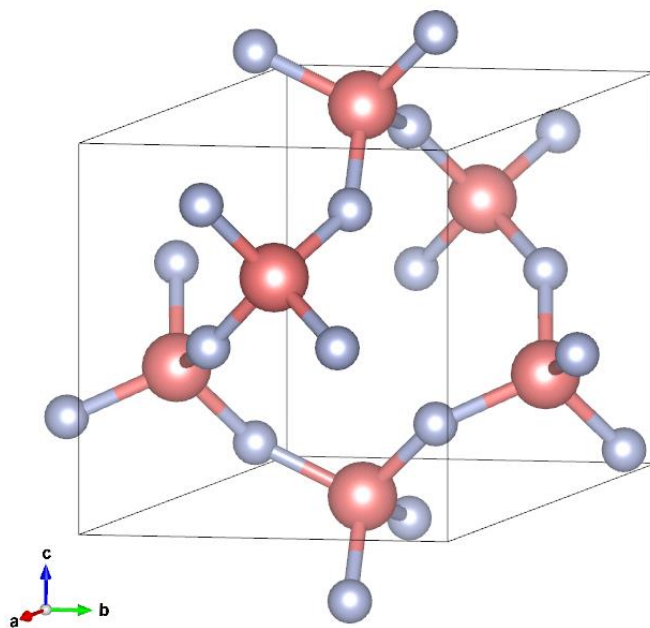


Figure 1-13. The unit cell of  $\alpha$ -BeF<sub>2</sub> crystal, with rose atoms for Be, silver atoms for F.

However, inconsistencies were found between the evaluation and theories. First and foremost, as shown in Figure 1-14, the bound vibrational part of the DOS was obtained from a DFT calculations for the solid crystalline material. The liquid materials and solid materials are known

to exhibit different motion characteristics. Therefore, the DOS of solid state systems cannot replace that of a liquid system.

Second, the vibrational DOS of FLiBe was calculated separately as  $^7\text{Li}$  in a  $^7\text{LiF}$  solid crystalline system and Be in a  $\text{BeF}_2$  solid crystalline system. The F in FLiBe was calculated by simply summing the DOS of F in  $^7\text{LiF}$  solid crystalline system and F in  $\text{BeF}_2$  solid crystalline system (as shown in Figure 1-14). As discussed above, the FLiBe system is different from  $^7\text{LiF}$  crystalline and  $\text{BeF}_2$  crystalline. A simple summation and replacement of DOS is wrong and not theoretically supported.

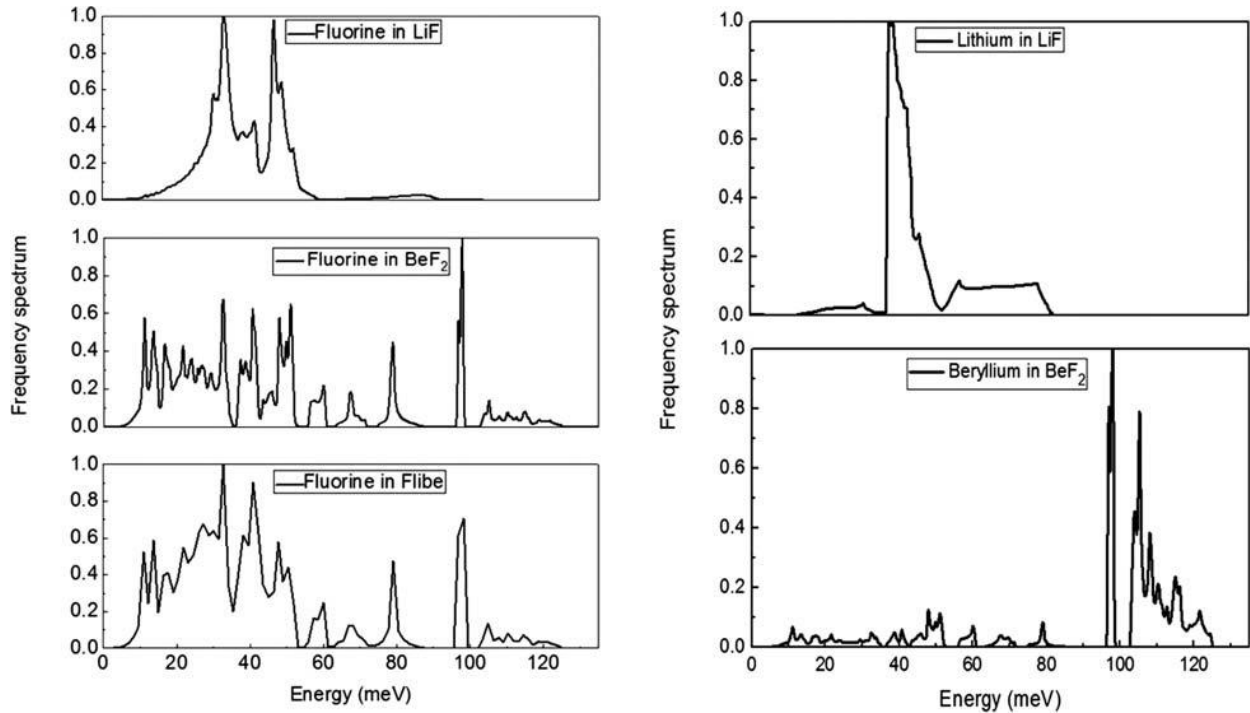


Figure 1-14. The DOS used in Mei et al. [72] and Li et al. [73-75] is from crystal  $\text{BeF}_2$  and crystal  $\text{LiF}$ ; the F in FLiBe DOS is a summation of F in  $\text{LiF}$  DOS and F in  $\text{BeF}_2$  DOS.

Third, the diffusional Egelstaff & Schofield model used by Mei et al. [72] and Li et al. [73-75] based its input coefficients on incorrect physics. In their work, the coefficient  $c$  from Egelstaff & Schofield model is used as an unitless diffusion coefficient; and the weight of the DOS is evaluated from effective mass  $w_d = 1/M^*$ . The effective mass  $M^*$  is a variable quantifying how

much a motion state is hindered relative to the total motion of the system. In Schofield's model, however, the coefficient  $c$  is unitless relaxation time. Whereas the unitless diffusion coefficient is the coefficient  $d$ , which can be connected to real diffusion coefficient by  $D = d\hbar/M^*$ . Furthermore, the relation between the DOS weight  $w_d$  and  $M^*$  is  $w_d = M/M^*$  instead of  $w_d = 1/M^*$ , where  $M$  is the real mass of the particle.

Fourth, the cited diffusion coefficient is obtained from an MD model [76] which shows clear deviation from experimental measurements. This is because the cited MD simulation [76] used the pair potential targeting to reproduce the crystal structure and lattice energy for solid state crystal FLiBe [40]. This solid state FLiBe MD pair potential is not suited to simulating liquid FLiBe.

For the above reasons, the thermal neutron scattering cross section evaluation for FLiBe should be reexamined. This work will present an evaluation for liquid FLiBe. It will compare to previous work to demonstrate the differences resulting from the rigorous treatment of FLiBe as a liquid. Details of the comparison could be found in Appendix D.

## Chapter 2 Thermal Neutron Scattering Physics

In this chapter, concepts that underlie thermal neutron scattering physics are discussed. In Section 2.1, the general thermal neutron scattering theory and its development history are outlined. The application of the Gaussian approximation and the width function to liquid, solid, and gas phases is discussed in Section 2.2. Subsequently, Section 2.3 outlines the theory that separates the diffusive thermal scattering law and the bound thermal scattering law from the total thermal scattering law. This separation is fundamental to evaluating the total thermal scattering law by combining various ideal models. Section 2.4 details analytical models regarding ideal diffusional systems that could be applied in the proposed thermal scattering law separation-combination strategy. In Section 2.5, the relation between the quantum formula and the classical formula is investigated, and a quantum correction method is proposed. Section 2.6 discusses the evaluation technique of the thermal scattering law from MD simulations.

### 2.1 General Theory of Thermal Neutron Scattering

#### 2.1.1 Background of Thermal Neutron Scattering Theory

The concept of the dynamic structure factor  $S(\mathbf{k}, \omega)$  was introduced together with the Van Hove space-time correlation function  $G(\mathbf{r}, t)$  by Van Hove in 1954 [77]. The dynamic structure factor  $S(\mathbf{k}, \omega)$  is a two-fold Fourier transform of  $G(\mathbf{r}, t)$ . The thermal neutron double differential scattering cross section formula proposed by Van Hove is

$$\frac{d^2\sigma}{d\Omega dE'} = \frac{a^2 N}{2\pi\hbar} \frac{k}{k_0} \iint \exp[i(\mathbf{k} \cdot \mathbf{r} - \omega t)] \cdot G(\mathbf{r}, t) d\mathbf{r} dt \quad (2.1.1)$$

where  $a$  is the scattering length,  $N$  is the number of particles in the system,  $\mathbf{k}$  is a reciprocal space vector that represents the periodic repeating structure of the system,  $\omega$  is a frequency that represents the energy states of system's motion. With  $\mathbf{k}$  space and  $\omega$  space combined, the two-fold Fourier transform of  $G(\mathbf{r}, t)$  reveals the system dynamics and system response to a perturbation in the system. It is an inherent property of the scattering system, independent of the incident particle type. This quantity is termed the dynamic structure factor, i.e. the thermal scattering law and is given by

$$S(\mathbf{k}, \omega) = \int \int \exp[i(\mathbf{k} \cdot \mathbf{r} - \omega t)] \cdot G(\mathbf{r}, t) d\mathbf{r} dt \quad (2.1.2)$$

The dynamic structure factor also consistently describes the scattering system dynamics regardless of its phase. The general scattering theory should be the same mathematical functional of the interatomic potential, independent of phase types.

Van Hove breaks down the  $G(\mathbf{r}, t)$  function further into the self-part  $G_s(\mathbf{r}, t)$  and distinct part  $G_d(\mathbf{r}, t)$ , quantifying the probability of finding the atom itself or any other distinct atoms at a distance  $\mathbf{r}$  and time  $t$ . The corresponding  $S_s(k, \omega)$  and  $S_d(k, \omega)$  quantifies the contribution to the system dynamics from the atom itself and the interference between different atoms, respectively.

The response of a system of interacting particles to an external perturbation can be represented by the dynamical properties of the system, namely the dynamic structure factor  $S(\mathbf{k}, \omega)$ . It is a general property of the system in the sense that: (1) This description of the dynamical properties of the system is independent of the incoming particle/source type that creates the perturbation in the system, and (2) The methodology used to evaluate  $S(\mathbf{k}, \omega)$  is consistent among different system phases - whether it is a solid, liquid, or gas. To prove that the scattering system response is independent of the incident beam type, a thought experiment can be performed. Imagine that a neutron or a proton is injected into a sample material. One can also assume that technology allows

the same amount of energy and the same direction of momentum to be injected into the system. Under this experiment, the perturbation created in the system would be the same. The system response to the scattering event should be solely dependent on the displaced atom itself. Because the atom is displaced by the same magnitude and direction, the response of the system itself must be the same, i.e. independent of incoming particle type. Therefore, regardless of the scattering source, the dynamics of the perturbed system should be the same. In this work, thermal neutron scattering will be the focus. From this point, the discussion will be limited to thermal neutrons as incident particles.

The  $S(\mathbf{k}, \omega)$  was not written out in explicit analytical form until Vineyard's highly cited 1958 paper [78]. In Vineyard's discussion, the analytical form of the  $S(\mathbf{k}, \omega)$  function is proposed for ideal liquid and gaseous diffusion models. Vineyard also proposed the Gaussian approximation for the self-part of the space-time correlation function  $G_s(\mathbf{r}, t)$ , as shown in Eq. (2.1.3). This approximation assumes that the probability of finding an atom around its initial position at time  $t$  is a Gaussian function of the distance from its initial position. The half width at half maximum (HWHM) of the Gaussian  $G_s(\mathbf{r}, t)$  is a function of  $t$ , and  $w(t)$ . The  $w(t)$  function is named the width function.

$$G_s(\mathbf{r}, t) \rightarrow \text{Gaussian of } \mathbf{r}, \text{ HWHM} \rightarrow w(t) \quad (2.1.3)$$

Another important approximation that Vineyard made is the convolution approximation, as shown in Eq. (2.1.4), resulting in

$$G(r, t) = G_s(r, t) + \int G(r', 0) \cdot G_s(r - r', t) dr' \quad (2.1.4)$$

The strength of this approximation is that it separates the distinct contribution from the self contribution in the system dynamics. The convolution approximation can be written for the dynamic structure factor by Fourier transforming Eq. (2.1.4).

$$S_d(k, \omega) = S_s(k, \omega) \cdot \Gamma(k) \quad (2.1.5)$$

where the  $\Gamma(\alpha)$  is called the collective structural function. Demonstrated even more explicitly in Eq. (2.1.5), it separates the distinct structural contribution from the self contribution in  $S(k, \omega)$ . These models and approximations will be discussed in detail in Chapter 2.

Following Van Hove's effort, in parallel with Vineyard's research in liquids, Sjolander investigated the analytical dynamic structure factor model in crystalline materials [79]. This 1958 paper is the fundamental of the phonon expansion algorithm used in traditional thermal neutron scattering processing codes such as GASKET, LEAP, and later the LEAPR module of the NJOY system. In this research, Sjolander demonstrated the cubic approximation for the first time. The Debye-Waller matrix, i.e. the  $\mathcal{M}_{kk'}^l$  tensor in the paper [79], contributes to both the distinct and self dynamic structure factor. By assuming the cubic approximation, the directional weighting of the reciprocal space is removed. Only by doing this can the phonons be sampled uniformly throughout the reciprocal space. On the other hand, the phonon density of states, i.e. the frequency spectrum of the velocity autocorrelation function, is the uniform sampling of the reciprocal space frequencies. Therefore, if and only if the cubic approximation is assumed, the phonon density of states can then appear in the cross section evaluation with the phonon expansion. In coherent elastic scattering, the cubic approximation also enables the usage of a single uniform density of states throughout reciprocal space. The cubic approximation proposed in this paper later became the fundamental assumption for conventional thermal neutron scattering algorithms. For liquid materials, the atom's arrangement may be viewed as amorphous. Therefore, an isotropic "cubic" approximation works well. Detail discussion of the cubic approximation in liquids will be presented in Appendix A.

In Sjolander's paper [79], a generalized formula (Eq. I.10 and I.28 in the original paper) for the width function of crystalline materials was proposed. However, this formula is deduced under the cubic approximation and the Gaussian approximation for solid crystalline materials using phonon oscillators. Three years later, in 1961, Rahman, Singwi, and Sjolander co-authored a highly cited paper [80]. In this work, they deduced the width function for liquid materials. Notably, due to the applicability of the assumptions to liquids, the deduced width function for liquids is the same as that for solid crystals using phonon oscillators.

With this fundamental research in place, researchers in 1960s reported great progress in estimating the dynamic structure factor. Because Sjolander and Rahman's proposal required system trajectory data which was impossible to obtain at that time, the models proposed in 1960s [81] aimed to overcome the difficulty of data preparation. Reviews of these endeavors in 1970s and 1980s are available from Copley and Lovesey [82] and Hess and Klein [83]. In the 1990s, with the development of modern computers, large scale molecular dynamics (MD) simulations were made possible for the first time. Generated particle trajectories of hundreds of atoms enabled the analysis of the dynamic structure factor directly from MD data without resorting to approximated models. This methodology re-opened the investigation into direct MD simulated classical dynamic structure factors and the quantum correction scheme [84,85].

### **2.1.2 The Dynamic Structure Factor $S(k, \omega)$ And the Thermal Scattering Law $S(\alpha, \beta)$**

The scattering of a neutron with a nucleus is characterized by two important features: the strength of the interaction between the neutron and the nucleus, and the extremely short interaction distance compared to the separation distance between atoms in the system. Fermi pointed out that the scattering potential between a neutron and a nucleus can adopt a  $\delta$ -function form



$$V(x) = \frac{2\pi\hbar^2}{m_n} b \cdot \delta(x) \quad (2.1.6)$$

The  $b$  in Eq. (2.1.6) is the scattering length between the neutron and the nucleus. It represents the strength of the nuclear potential. By applying Fermi's potential in Schrodinger's equation with the Born approximation [67], which is essentially taking the first order Born expansion of the wave function, the double differential cross section of a neutron can be deduced as [86]

$$\frac{d^2\sigma}{d\Omega dE'} = \sqrt{\frac{E'}{E}} \frac{1}{2\pi\hbar} \sum_{jj'} b_j b_{j'} \int_{-\infty}^{+\infty} e^{-i\omega t} \left\langle e^{-ik \cdot \mathbf{R}_{j'}(0)} \cdot e^{ik \cdot \mathbf{R}_j(t)} \right\rangle dt . \quad (2.1.7)$$

The subscript  $j$  and  $j'$  denote different atoms  $j$  and  $j'$ . The angle bracket  $\langle \rangle$  is the thermal average of the system over all the possible thermal states, i.e.,  $\langle A \rangle = \sum p_\lambda A_\lambda$ ,  $p_\lambda$  denotes the probability that the system is in the  $\lambda$  state. Equation (2.1.7) implies two contributions of thermal neutron scattering. One is the way a neutron interacts with the atoms in the system, another is the property of the dynamical interactions in the scattering system itself.

It should be noted that this representation of double differential cross section is in the Heisenberg Picture. The time dependent position operator  $\mathbf{R}_j(t)$  is a function of the position of atom  $j$  at time  $t$  and the Hamiltonian  $H$  of the system

$$\mathbf{R}_j(t) = e^{iHt/\hbar} \cdot \mathbf{R}_j \cdot e^{-iHt/\hbar} \quad (2.1.8)$$

As stated above, the first contribution to thermal neutron scattering is the neutron dependent properties, i.e., the incoming and scattered neutron energy  $E$  and  $E'$ , and the scattering length  $b_j$ . These properties measure the initial and final state of the neutron, and the probability of interaction between a neutron and a single nucleus. The second contribution to thermal neutron scattering is the Fourier transform of the thermal average  $\langle e^{-ik \cdot \mathbf{R}_{j'}(0)} e^{ik \cdot \mathbf{R}_j(t)} \rangle$ . As can be seen in Eq. (2.1.8), this Fourier transform depends on the quantum operator  $\mathbf{R}_j(t)$ , which further depends on how the

system's Hamiltonian  $H$  and atom position  $\mathbf{R}_j$  evolve with time. It does not involve any neutron properties. Therefore, this quantity is a dynamical and structural property that is solely dependent on the scattering system. Due to the involvement of the Heisenberg Picture with  $\mathbf{R}_j(t)$ , it is necessary to apply quantum mechanics to evaluate this property.

In the evaluation of the thermal neutron scattering cross section, the incoming and outgoing neutron energies are predefined; the bound scattering length is known from experiment; hence the evaluation becomes the sole task of evaluating the scattering kernel in the Fourier transform using quantum mechanics. It is necessary to define the scattering kernel in the Fourier transform. The dynamic structure factor,  $S(\mathbf{k}, \omega)$ , is defined as the Fourier transform in Eq. (2.1.9)

$$S(\mathbf{k}, \omega) = \frac{1}{2\pi\hbar} \int_{-\infty}^{+\infty} \frac{1}{N} \sum_{jj'} \left\langle e^{-i\mathbf{k} \cdot \mathbf{R}_{j'}(0)} \cdot e^{i\mathbf{k} \cdot \mathbf{R}_j(t)} \right\rangle e^{-i\omega t} dt \quad (2.1.9)$$

which has a unit of inverse energy  $1/J$ . The dynamic structure factor is also known as the thermal scattering law, as it is the kernel of thermal neutron scattering evaluation. The dynamic structure factor  $S(\mathbf{k}, \omega)$  in general depends on the dynamical and structural properties of the scattering system. Since the energy Hamiltonian  $H$  and the structural reciprocal space vector  $\mathbf{k}$  are cross correlated with  $e^{i\mathbf{k} \cdot \mathbf{R}_j(t)}$ , the  $\omega$  dimension of  $S(\mathbf{k}, \omega)$  stores the energy states information; the  $\mathbf{k}$  dimension of  $S(\mathbf{k}, \omega)$  stores the structural information. The classical approximation ignoring the correlation between the Hamiltonian  $H$  in  $\mathbf{R}_j(t)$  and  $\mathbf{R}_{j'}(t)$  will unavoidably mismatch quantum behavior in  $S(\mathbf{k}, \omega)$ .

In the context of neutron scattering data library related applications,  $S(\mathbf{k}, \omega)$  is conventionally written as unitless  $S(\alpha, \beta)$ , namely the thermal scattering law (TSL).  $\alpha$  is a unitless momentum transfer variable corresponding to  $\mathbf{k}$ ,  $\beta$  is a unitless energy transfer variable corresponding to  $\omega$

$$\alpha = \frac{E' + E - 2\mu\sqrt{E'E}}{Mk_B T} = \frac{\hbar(k_0^2 + k'^2 - 2\mu k'k_0)}{2Mk_B T} = \frac{\hbar^2 k^2}{2Mk_B T} \quad (2.1.10)$$

$$\beta = \frac{E' - E}{k_B T} = -\frac{\hbar\omega}{k_B T} \quad (2.1.11)$$

where  $\mathbf{k}$  is the wave vector of momentum transfer:  $\mathbf{k} = \mathbf{k}_0 - \mathbf{k}'$ . The following relation holds between the dynamic structure factor  $S(\mathbf{k}, \omega)$  and the thermal scattering law  $S(\alpha, \beta)$

$$S(\alpha, \beta) = k_B T \cdot S(\mathbf{k}, \omega) \quad (2.1.12)$$

The spin directions of the scattering system are assumed to be homogenously and isotropically distributed in Eq. (2.1.25). In this way, the neutron does not have a preferred azimuth scattering angle  $\varphi$ . Eq. (2.1.25) could be integrated over all the azimuth scattering angle  $\varphi$  from 0 to  $2\pi$ . The double differential cross section will be against the scattering angle  $\mu = \cos \theta$  instead of the solid angle  $\Omega$ . The thermal scattering law  $S(\alpha, \beta)$  becomes direction independent, solely dependent on the magnitude of momentum transfer. By multiplying  $S(\mathbf{k}, \omega)$  with  $k_B T$ , the unit  $1/J$  in  $S(\mathbf{k}, \omega)$  is removed. Thus, the thermal scattering law  $S(\alpha, \beta)$  is unitless.

In short, the dynamic structure factor  $S(\mathbf{k}, \omega)$  is direction dependent and has units of inverse energy while the thermal scattering law  $S(\alpha, \beta)$  is direction independent and unitless. In the future, all the discussion in this work will distinguish between the usage of dynamic structure factor  $S(\mathbf{k}, \omega)$  and the thermal scattering law  $S(\alpha, \beta)$  as discussed above.

### 2.1.3 The $G(\mathbf{r}, t)$ Function and the $I(\mathbf{k}, t)$ Function

The previous section focused on the dynamic structure factor  $S(\mathbf{k}, \omega)$  and the thermal scattering law  $S(\alpha, \beta)$  in the context of thermal neutron scattering. It is worth recalling that the dynamic structure factor  $S(\mathbf{k}, \omega)$  is a property that solely depends on the atomic motions in a

scattering system without any reference to a neutron scattering event.  $S(\mathbf{k}, \omega)$  shows advantages in analyzing the structural and energy states of the system. It is also necessary to investigate the behavior in time space  $t$  and spatial space  $\mathbf{r}$  as well.

The basic idea given by van Hove [77] proposed that the dynamics of a system can be written as the van Hove correlation function  $G(\mathbf{r}, t)$ :

$$G(\mathbf{r}, t) = \frac{1}{N} \sum_{jj'} \int \left\langle \delta[\mathbf{r}' - \mathbf{R}_{j'}(0)] \delta[\mathbf{r}' + \mathbf{r} - \mathbf{R}_j(t)] \right\rangle d\mathbf{r}' \quad (2.1.13)$$

This equation is in quantum operator notation – the  $\mathbf{R}_j(0)$  and  $\mathbf{R}_j(t)$  operators are in the Heisenberg Picture and contain the Hamiltonian  $H$  of the system. Therefore, the two  $\delta$ -functions do not commute. This function measures the time-dependent generalization of the evolution of spatial correlations in the system. It is particularly useful in interpreting the system dynamics in spatial and time domains. Besides  $\mathbf{R}_j(t)$  being a quantum operator and not commuting with other  $\mathbf{R}_j(t)$  terms, the quantum mechanics behavior of  $G(\mathbf{r}, t)$  stems from the uncertainty of the  $\mathbf{R}_j(t)$  itself. Particles in a thermal system travels as a quantum thermal cloud, which is a probability density distribution clouding the most probable position. The thermal cloud depends on the  $\mathbf{R}_j(t)$  operator. This behavior of position uncertainty fundamentally stems from the wave-particle duality of any particle.

In a disordered system, e.g. liquid, gas, randomly oriented crystalline solids, the material is said to be isotropic (i.e., its properties are unchanged along all directions of  $\mathbf{r}$ ). Hence,  $G(\mathbf{r}, t)$  does not contain any new information in different directions of  $\mathbf{r}$ . Thus the  $G(\mathbf{r}, t)$  function can be simplified to  $G(r, t)$ .

We consider the summation of atom  $j$  and atom  $j'$  in Eq. (2.1.9) and Eq. (2.1.13) to represent the analysis of the coherent correlation effect between the atom itself ( $j = j'$ ) plus all other distinct

atoms ( $j \neq j'$ ); therefore, the definitions of  $S(\mathbf{k}, \omega)$  and  $G(\mathbf{r}, t)$  in Eq. (2.1.9) and Eq. (2.1.13) are also named coherent  $S_{coh}(\mathbf{k}, \omega)$  and  $G_{coh}(\mathbf{r}, t)$  [64,87]. From this point on, the *coh* subscript will be implicitly applied when written correlation functions without subscript, e.g.  $S(\mathbf{k}, \omega)$  would implicitly mean  $S_{coh}(\mathbf{k}, \omega)$ .

To connect the space-time correlation function  $G(\mathbf{r}, t)$  with the dynamic structure factor, van Hove [77] introduced the intermediate scattering function  $I(\mathbf{k}, t)$ . The intermediate scattering function  $I(\mathbf{k}, t)$  is Fourier transform of  $G(\mathbf{r}, t)$  to the reciprocal space

$$I(\mathbf{k}, t) = \int e^{i\mathbf{k} \cdot \mathbf{r}} G(\mathbf{r}, t) d\mathbf{r} \quad (2.1.14)$$

$$G(\mathbf{r}, t) = \frac{1}{(2\pi)^3} \int e^{-i\mathbf{k} \cdot \mathbf{r}} I(\mathbf{k}, t) d\mathbf{k} \quad (2.1.15)$$

The dynamic structure factor  $S(\mathbf{k}, \omega)$  is then the Fourier transform of  $I(\mathbf{k}, t)$  to the frequency space

$$S(\mathbf{k}, \omega) = \frac{1}{2\pi\hbar} \int e^{-i\omega t} I(\mathbf{k}, t) dt \quad (2.1.16)$$

$$I(\mathbf{k}, t) = \hbar \int e^{i\omega t} S(\mathbf{k}, \omega) d\omega \quad (2.1.17)$$

By comparing Eq. (2.1.16) with Eq. (2.1.9) it is easy to define  $I(\mathbf{k}, t)$  with quantum operator  $\mathbf{R}_j(t)$

$$I(\mathbf{k}, t) = \frac{1}{N} \sum_{jj'} \left\langle e^{-i\mathbf{k} \cdot \mathbf{R}_{j'}(0)} \cdot e^{i\mathbf{k} \cdot \mathbf{R}_j(t)} \right\rangle \quad (2.1.18)$$

There are two advantages in directly accessing  $I(\mathbf{k}, t)$  in a calculation compared to  $S(\mathbf{k}, \omega)$  and  $G(\mathbf{r}, t)$ . Firstly, unlike  $S(\mathbf{k}, \omega)$  in Eq. (2.1.9) and  $G(\mathbf{r}, t)$  in Eq. (2.1.13), the calculation is considerably simplified by working with  $I(\mathbf{k}, t)$ . Secondly, in the case of self  $I_s(\mathbf{k}, t)$ , the important Gaussian approximation can be connected to mean square displacement (MSD) on a sound physical basis, enabling the power of predictive analysis.

#### 2.1.4 The Self and Distinct Thermal Scattering Laws

The discussion in this work would extensively use the self ( $j = j'$ ) and distinct ( $j \neq j'$ ) definition of the thermal scattering law, intermediate scattering function, and van Hove correlation function. Compared to the coherent definitions, the self, or incoherent, definitions of these dynamic quantities are the summation of the same atom, when  $j = j'$ :

$$S_s(\mathbf{k}, \omega) = \frac{1}{2\pi\hbar} \int_{-\infty}^{+\infty} \frac{1}{N} \sum_j \left\langle e^{-i\mathbf{k} \cdot \mathbf{R}_j(0)} \cdot e^{i\mathbf{k} \cdot \mathbf{R}_j(t)} \right\rangle e^{-i\omega t} dt \quad (2.1.19)$$

$$I_s(\mathbf{k}, t) = \frac{1}{N} \sum_j \left\langle e^{-i\mathbf{k} \cdot \mathbf{R}_j(0)} \cdot e^{i\mathbf{k} \cdot \mathbf{R}_j(t)} \right\rangle \quad (2.1.20)$$

As discussed in the previous section, the self term is a summation over the atoms when  $j = j'$ , the distinct term is a summation over the atoms when  $j \neq j'$  [64,87]. It is obvious that

$$\begin{aligned} G(\mathbf{r}, t) &= G_d(\mathbf{r}, t) + G_s(\mathbf{r}, t) \\ I(\mathbf{k}, t) &= I_d(\mathbf{k}, t) + I_s(\mathbf{k}, t) \\ S(\mathbf{k}, \omega) &= S_d(\mathbf{k}, \omega) + S_s(\mathbf{k}, \omega) \end{aligned} \quad (2.1.21)$$

The  $I_s(\mathbf{k}, t)$ ,  $S_s(\mathbf{k}, \omega)$ ,  $G_s(\mathbf{r}, t)$ ,  $I_d(\mathbf{k}, t)$ ,  $S_d(\mathbf{k}, \omega)$ , and  $G_d(\mathbf{r}, t)$  still follow the same Fourier transform relation as the coherent quantities discussed above. The thermal scattering law  $S(\alpha, \beta)$  has some general properties which are independent of the structure and dynamics of the scattering system. There are three properties which are widely used to demonstrate the quantum behavior of scattering system.

The first of such property is the principle of detailed balance [86]

$$\begin{aligned} S_s(\alpha, \beta) &= e^{-\beta} S_s(\alpha, -\beta) \\ S_d(\alpha, \beta) &= e^{-\beta} S_d(\alpha, -\beta) \end{aligned} \quad (2.1.22)$$

In the perspective of neutron scattering, the detailed balance indicates that the probability of the neutron gaining energy in scattering is  $e^{-\beta}$  orders of magnitude lower than the probability of it losing the same amount of energy. From the perspective of the scattering system, it is the opposite.

That is, the probability of the system losing energy in scattering is  $e^{-\beta}$  orders of magnitude lower than the probability of gaining the same amount of energy. The second such property is the 0<sup>th</sup> moment of  $S_s(\alpha, \beta)$ , also called the 0<sup>th</sup> order sum rule, of the self thermal scattering law

$$\int_{-\infty}^{\infty} S_s(\alpha, \beta) d\beta = 1 \quad (2.1.23)$$

The third property is the 1<sup>st</sup> moment, or the  $I^{st}$  order sum rule, of the self thermal scattering law

$$\int_{-\infty}^{\infty} \beta \cdot S_s(\alpha, \beta) d\beta = \alpha \quad (2.1.24)$$

The rules from Eq. (2.1.22)-(2.1.24) can serve as consistency checks on the quantum mechanical behavior of the thermal scattering law.

### 2.1.5 Thermal Neutron Scattering and the Incoherent Approximation

One of the applications of  $S(\mathbf{k}, \omega)$  is the evaluation of the thermal neutron scattering cross section. The double differential cross section in Eq. (2.1.7) can be written using the dynamic structure factor  $S(\mathbf{k}, \omega)$  or the thermal scattering law  $S(\alpha, \beta)$

$$\frac{d^2\sigma}{d\Omega dE'} = \frac{\sigma_b}{4\pi} \sqrt{\frac{E'}{E}} S_{tot}(\mathbf{k}, \omega) \quad (2.1.25)$$

$$\frac{d^2\sigma}{d\mu dE'} = \frac{\sigma_b}{2k_B T} \sqrt{\frac{E'}{E}} S_{tot}(\alpha, \beta) \quad (2.1.26)$$

where the  $S_{tot}(\alpha, \beta)$  is the weighted total scattering law. The total thermal scattering law, defined in Eq. (2.1.26), is a mixture of the self and distinct thermal scattering law weighted by the corresponding bound cross section.

$$S_{tot}(\alpha, \beta) = \frac{\sigma_{coh} S_d(\alpha, \beta) + (\sigma_{coh} + \sigma_{inc}) S_s(\alpha, \beta)}{\sigma_{coh} + \sigma_{inc}} \quad (2.1.27)$$

Eq. (2.1.26) and relation  $\sigma_b = \sigma_{coh} + \sigma_{inc}$  give the following equation

$$\frac{d^2\sigma}{d\mu dE'} = \frac{1}{2k_B T} \sqrt{\frac{E'}{E}} (\sigma_{coh} S_d(\alpha, \beta) + \sigma_b S_s(\alpha, \beta)) \quad (2.1.28)$$

A widely-used approximation is the incoherent approximation, which assumes that  $S_d(\alpha, \beta) = 0$ . Under this approximation, Eq. (2.1.28) would be written as

$$\left. \frac{d^2\sigma}{d\mu dE'} \right|_{\text{inc appr}} = \frac{\sigma_b}{2k_B T} \sqrt{\frac{E'}{E}} S_s(\alpha, \beta) \quad (2.1.29)$$

By substituting  $S_{tot}$  with  $S_s$ , the approximation effectively removes the distinct contribution. Because distinct effects cannot be well predicted from theory, this approximation is widely used in evaluating the thermal neutron scattering cross section across all phases of materials.

## 2.2 The Gaussian Approximation and the Width Function

### 2.2.1 The Gaussian Approximation and the Width Function for Solid and Gas Materials

As stated in Eq. (2.1.3), the Gaussian approximation states that  $G_s^{cl}(r, t)$  is a Gaussian function of  $r$ . Though the Gaussian approximation was first proposed for liquid materials by Vineyard [78], it has also been found to be especially useful for solid materials [79]. Regarding gas materials, the Gaussian approximation is exactly true. In this section, the Gaussian approximation for both solid and gas materials will be discussed.

For an ideal gas, the classical self thermal scattering law can be deduced exactly. Assume an atom is at origin when  $t = 0$ , the classical probability of it being between  $r$  and  $r + dr$  at time  $t$  is  $P(r, t) = 4\pi r^2 G_s^{cl}(r, t) dr$ , because the classical van Hove correlation function is a probability density function  $G_s^{cl}(r, t)$ . The same probability can be written with the Maxwellian probability distribution using velocity  $v$ . If the atom has a velocity between  $v$  and  $v + dv$ , where  $v = r/t$ , the Maxwellian probability density function should be



$$P(v, t) = h_1 v^2 e^{-\frac{Mv^2}{2k_B T}},$$

where  $h_1$  is a normalization constant. Therefore, with  $P(r, t) = P(v, t)$ :

$$4\pi r^2 G_s^{cl}(r, t) dr = h_1 v^2 e^{-\frac{Mv^2}{2k_B T}} dv,$$

so that

$$G_s^{cl}(r, t) = \frac{1}{\sqrt{2\pi w(t)}} e^{-r^2/2w(t)}, \text{ where } w(t) = k_B T t^2 / M \quad (2.2.1)$$

The classical self van Hove correlation function for free gas is therefore a Gaussian function of  $r$ .

The Half Width at Half Maximum (HWHM) of the Gaussian depends on a function, the width function  $w(t)$ . Note that the above derivation is based on classical notation  $r$  and  $t$ . The quantum self van Hove correlation function can be obtained by simply substituting  $t$  with  $t + i\hbar/2k_B T$  [88,89] in the classical van Hove correlation function for an ideal gas. This will give the quantum self van Hove correlation function

$$G_s(r, t) = \frac{1}{\sqrt{2\pi w(t)}} e^{-r^2/2w(t)}, \text{ where } w(t) = (k_B T t^2 - i\hbar t) / M \quad (2.2.2)$$

To conclude, the self van Hove correlation function is a Gaussian function for the ideal gas. The HWHM of the Gaussian is a width function  $w(t)$  depending on time  $t$ . For solid materials, the rigorous theory of thermal neutron scattering was developed by Sjolander [79]. A computationally applicable algorithm for evaluating the thermal scattering law was formulated for the first time in history in this paper. As the first step, Sjolander applied the cubic approximation to all the crystalline structures. The cubic approximation assumes that the interatomic forces are isotropic along all directions. The cubic approximation is accurate for crystalline materials where interatomic forces belong to the same kind (i.e., covalent, ionic, metallic, etc.). However, for materials such as graphite, the forces along different directions differentiate by orders of

magnitude (e.g., Van der Waals forces between carbon atoms in separate layers and covalent forces between carbon atoms in the same 2D layer). The cubic approximation should be examined cautiously for these types of complex materials. Assuming a cubic approximation, a Gaussian van Hove correlation function (i.e. Eq. (I.21) in Sjolander [79]) can be obtained with the following width function

$$w(t) = M^0(t) = \frac{\hbar}{2M} \int_0^\infty \frac{f(\omega)}{\omega} \left[ (1 - \cos \omega t) \coth \frac{\hbar \omega}{2k_B T} - i \sin \omega t \right] d\omega \quad (2.2.3)$$

Eq. (2.2.3) along with the cubic approximation is the foundation of phonon expansion, a technique widely applied to evaluate thermal neutron cross section from phonon DOS. It also proves that the Gaussian approximation is valid for solid materials under the cubic approximation. For materials with a highly heterogeneous force field, such as graphite, it is proven that the Gaussian approximation also works well [89].

### 2.2.2 The Gaussian Approximation and the Width Function for Liquid Materials

In this section, the Gaussian approximation for liquid systems will be discussed and an analytical width function model for liquid materials will be proposed. As discussed in the previous section, the  $G_s(r, t)$  function is a Gaussian function of  $r$ . The width function  $w(t)$  is the HWHM function of the  $G_s(r, t)$  function at different  $t$ . Because the intermediate scattering function  $I_s(k, t)$  is the Fourier transform of the  $G_s(r, t)$  function from real space to reciprocal space, it is still a Gaussian function of  $k$ . It is therefore equivalent to discuss the Gaussian approximation for the  $G_s(r, t)$  function in real space or for the  $I_s(k, t)$  function in reciprocal space. In this section, discussion on the Gaussian approximation and the width function will be applied to the intermediate scattering function  $I_s(k, t)$ .

In Figure 2-1, a diagram of  $I(k, t)$  space is shown. The directional dependence of  $\mathbf{k}$  vector is removed because liquid systems are isotropic in all directions of  $\mathbf{k}$ . There are two cases where  $I_s(k, t)$  is analytically solvable. As the first step to introducing the Gaussian approximation, analytical models under two special situations will be discussed.

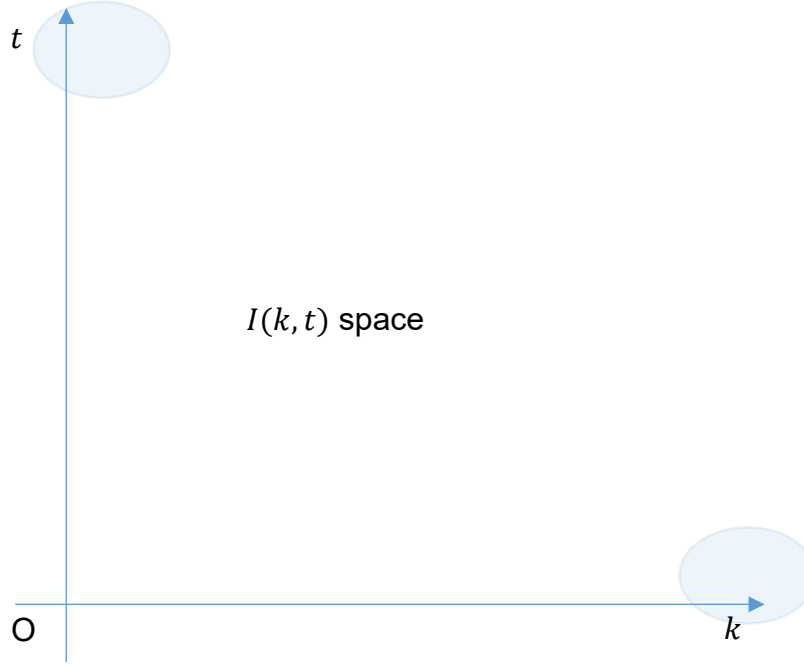


Figure 2-1. Diagram of the  $I(k, t)$  space; the top left corner where  $t \gg 1$  and  $k \ll 1$  is the case where long-time, long-range diffusion behavior dominants; the bottom right corner where  $t \ll 1$  and  $k \gg 1$  is the situation where short-time short-range free particle like behavior dominants.

The top left corner is the case where  $t \gg 1$  and  $k \ll 1$ . This is the region where long-time, long-range diffusion behavior is dominant. Therefore, in the  $t \gg 1$  and  $k \ll 1$  limit, the liquid system can be modeled as purely diffusive. The intermediate scattering function is analytically solvable in this case [78]. It is proven to be

$$I_s(k, t) = e^{-Dr \cdot k^2} \quad (2.2.4)$$

where  $D$  is the diffusion coefficient. The mean square displacement (MSD) is related to the diffusion constant by

$$\delta r^2(t) = 6Dt \quad (2.2.5)$$

The bottom right corner is the situation where  $t \ll 1$  and  $k \gg 1$ . This is the region where short-time short-range free particle like behavior is dominant. In this region, the probing time is small. Hence the probing distance is very limited. The particle's motion is nearly free of collisions with any other neighboring particles. This behavior is close to that of the ideal gas. The intermediate scattering function is well understood for a free gas system [90] and is defined as:

$$I_s(k, t) = e^{-\frac{k_B T t^2}{2m} k^2} \quad (2.2.6)$$

The MSD for the free gas system is known to be [90]

$$\delta r^2(t) = \frac{3k_B T}{m} t^2 \quad (2.2.7)$$

It is found that the intermediate scattering function  $I_s(k, t)$  is a Gaussian function in both the diffusive region ( $t \gg 1$  and  $k \ll 1$ ) and the ideal-gas region ( $t \ll 1$  and  $k \gg 1$ ). This phenomenon suggests further investigation into whether such a simple assumption is valid for intermediate ranges of  $t$  and  $k$ . By comparing Eq. (2.2.4)-(2.2.6), it is easy to deduce that the classical self intermediate scattering function  $I_s^{cl}(k, t)$  should be

$$I_s^{cl}(k, t) = e^{-\frac{1}{6} \delta r^2(t) \cdot k^2} \quad (2.2.8)$$

And the classical width function  $w(t)$  is defined as [91]

$$w(t) = 1/3 \cdot \delta r^2(t) \quad (2.2.9)$$

Following this definition, the classical self intermediate function and the van Hove correlation function with the classical width function  $w(t)$  notation should be

$$I_s^{cl}(k, t) = e^{-\frac{1}{2} w(t) \cdot k^2} \quad (2.2.10)$$

$$G_s^{cl}(r, t) = \frac{1}{\sqrt{2\pi w(t)}} e^{-\frac{r^2}{2w(t)}} \quad (2.2.11)$$

Eq. (2.2.11) implies the fundamental assumption of the Gaussian approximation, that is, the probability of finding a particle around its initial position is a Gaussian function of the displaced distance  $r$ . Meanwhile, the width of the Gaussian function is determined by its MSD at different time. The validity of the Gaussian approximation will be tested using a liquid lithium molecular dynamics model in Chapter 4. The classical width function  $w(t)$  can be connected to the eigen-frequency function  $f(\omega)$  by the following relation [91]

$$w(t) = \frac{2k_B T}{M} \int_0^\infty \frac{f(\omega)}{\omega^2} (1 - \cos \omega t) d\omega \quad (2.2.12)$$

In the situation of a solid material, the eigen-frequency function  $f(\omega)$  is equivalent to the phonon density of states function  $\rho(\omega)$ . However, the  $f(\omega)$  function is not well defined for a liquid system [91]. It is therefore more practical to apply Eq. (2.2.9) rather than Eq. (2.2.12) to evaluate the width function. In a quantum mechanical system, the Gaussian approximation is still valid [91]. With the quantum width function  $\gamma(t)$ , the self intermediate scattering function and the van Hove correlation function are

$$I_s(k, t) = e^{-\gamma(t) \cdot k^2} \quad (2.2.13)$$

$$G_s(r, t) = \frac{1}{\sqrt{4\pi\gamma(t)}} e^{-\frac{r^2}{4\gamma(t)}} \quad (2.2.14)$$

where the  $\gamma(t)$  function is the quantum width function. It is given in Eq. (2.2.15) by Rahman [80].  $\gamma(t)$  is a complex function, even of  $t$  in its real part and odd of  $t$  in its imaginary part. A review of the derivation of the following  $\gamma(t)$  function is provided in Appendix B.

$$\gamma(t) = \frac{\hbar}{2M} \int_0^\infty \frac{f(\omega)}{\omega} \left[ (1 - \cos \omega t) \coth \frac{\hbar \omega}{2k_B T} - i \sin \omega t \right] d\omega \quad (2.2.15)$$

### 2.3 The Separation of the Diffusive Thermal Scattering Law and the Bound Thermal Scattering Law

In the previous section, the Gaussian approximation and the width function model are discussed for solid, liquid and gas materials. It is, however, still difficult to solve the dynamic structure factor analytically. In this section, a reductional technique that facilitates a mathematical solution of the dynamic structure factor will be illustrated. This technique includes the separation of the thermal scattering law by its motion modes (e.g. diffusive, vibrational etc.), the evaluation of each partial thermal scattering law from different analytical models, and the recombination of all partial thermal scattering laws using convolution. The theoretical background of this thermal scattering law separation-combination technique is discussed in this section.

First, it should be noted that this technique is valid only under the Gaussian approximation. In other words, it cannot be used to evaluate the distinct thermal scattering law. The Gaussian approximation for self thermal scattering law is assumed in the following discussion.

The self intermediate scattering function,  $I_s(k, t)$ , is assumed to follow the analytical form in Eq. (2.2.13) and (2.2.15). If one intends to decompose the  $I_s(k, t)$  as a multiplication of different motion component  $I_s^j(k, t)$  functions by different motion states  $j$

$$I_s(k, t) = \prod_j I_s^j(k, t), \quad (2.3.1)$$

the width function,  $\gamma(t)$ , must be written in the form of summation of motion states

$$\gamma(t) = \sum_j \gamma_j(t), \quad (2.3.2)$$

where subscript  $j$  denotes different motion states, e.g. diffusion, vibration, rotation, etc. This separation of the width function results naturally in the separation of the frequency spectrum,  $f(\omega)$ , in Eq. (2.2.3) and (2.2.15) as

$$\frac{f(\omega)}{M} = \sum_j \frac{f_j(\omega)}{M_j} \quad (2.3.3)$$

where the  $M_j$  is the effective mass of motion state  $j$ . The self dynamic structure factor is the Fourier transform of the multiplication in Eq. (2.3.1), which is equivalent to a convolution of different dynamic structure components.

$$S_s^{(J)}(k, \omega) = \int_{-\infty}^{\infty} S_s^j(k, \omega') \cdot S_s^{(J-1)}(k, \omega - \omega') d\omega' \quad (2.3.4)$$

$$S_s^j(k, \omega) = \frac{1}{2\pi} \int_{-\infty}^{\infty} e^{-i\omega t} I_s^j(k, t) dt \quad (2.3.5)$$

This is a convenient form to evaluate the dynamic structure factor if each individual motion component can be easily analyzed. A recursive convolution of all individual components can subsequently give the self dynamic structure factor for all motion modes combined.

As an example, a system with both the diffusive mode and the vibrational mode will be discussed in the following discussion. The methodology can be easily expanded to situations where other types of motion modes exist.

Assume that the motion frequency spectrum  $f(\omega)$  can be separated as Eq. (2.3.3)

$$f(\omega) = \frac{M}{M_{diff}} f_{diff}(\omega) + \frac{M}{M_{bound}} f_{bound}(\omega) \quad (2.3.6)$$

As both partial frequency spectrums  $f_{diff}(\omega)$  and  $f_{bound}(\omega)$  normalize to 1, it is easy to see that the  $M/M_j$  is the weight of the frequency spectrum and that the weight should add to unity.

$$\begin{aligned}
w_{diff} &= M / M_{diff} \\
w_{bound} &= M / M_{bound} \\
w_{diff} + w_{bound} &= 1
\end{aligned}
\tag{2.3.7}$$

The effective mass  $M_j$  is a variable quantifying how much a motion state is hindered relative to the total motion of the system. With this defined, the diffusive dynamic structure factor  $S_{diff}(k, \omega)$  can be predicted using one of the models defined in Section 2.4. The bound vibrational dynamic structure factor  $S_{bound}(k, \omega)$  can be evaluated using the phonon expansion from Eq. (A.14) to (A.17). The zeroth term in the phonon expansion is a  $\delta$ -function of  $\omega$  that represents elastic scattering with zero energy transfer, the convolution of  $S_{diff}(k, \omega)$  and  $S_{bound}(k, \omega)$  can be written as

$$\begin{aligned}
S(k, \omega) &= \int_{-\infty}^{\infty} S_{diff}(k, \omega') \cdot S_{bound}(k, \omega - \omega') d\omega' \\
&= \int_{-\infty}^{\infty} S_{diff}(k, \omega') \cdot \left[ S_{bound}^0(k, \omega - \omega') + S_{bound}^{\geq 1}(k, \omega - \omega') \right] d\omega' \\
&= \int_{-\infty}^{\infty} S_{diff}(k, \omega') \cdot \left[ \delta(\omega - \omega') + S_{bound}^{\geq 1}(k, \omega - \omega') \right] d\omega' \\
&= S_{diff}(k, \omega) + \int_{-\infty}^{\infty} S_{diff}(k, \omega') \cdot S_{bound}^{\geq 1}(k, \omega - \omega') d\omega'
\end{aligned}
\tag{2.3.8}$$

Therefore, the overall dynamic structure factor can be evaluated from the combination of the ideal diffusion model and the phonon model.

## 2.4 Thermal Neutron Scattering Models for Liquid Materials

In this section, four diffusive dynamic structure factor models will be reviewed. These models are all classical models with no quantum behavior. The methodology of evaluating thermal neutron scattering cross sections from ideal diffusional liquids will be discussed. As outlined in Eq. (2.3.8), these analytical diffusive models are usually combined with the phonon expansion (deduced in



Appendix A) to quantify the effects of both vibration and diffusion in the overall dynamic structure factor. This section will review existing classical liquid models for  $I^{cl}(\mathbf{k}, t)$  and  $S^{cl}(\mathbf{k}, \omega)$  and their limitations.

In the 1960s, relevant research attempted to analytically interpret the diffusional behavior of liquids. In these studies, the analytical liquid diffusional model is simplified with different assumptions. There were four representative models, namely the Linear diffusion model [78], the Free gas diffusion model [86], the Egelstaff & Schofield diffusion model [92], and the Langevin diffusion model [81]. The assumption and relation of these models will be reviewed in this section.

The first model is the Linear diffusion model [78]. Following the definition of a diffusion coefficient  $D$ , the MSD can be written as

$$\delta r^2(t) = 6Dt . \quad (2.4.1)$$

The concept of a width function has been proposed in Eq. (2.2.9). In this representation, the width function is a linear function of diffusion time  $t$ ,

$$w(t) = 1/3 \cdot \delta r^2(t) = 2Dt . \quad (2.4.2)$$

Following the Gaussian approximation, the self intermediate scattering function is a Gaussian of  $k$ ,

$$I_s(k, t) = e^{-Dt \cdot k^2} \quad (2.4.3)$$

A Fourier transform of Eq. (2.4.3) gives

$$S_s(k, \omega) = \frac{1}{\pi} \frac{Dk^2}{\omega^2 + (Dk^2)^2} \quad (2.4.4)$$

The underlying assumption of this model is the diffusion assumption, which states that the MSD is linearly proportional to the diffusion time  $t$ . However, this assumption is only valid in the

limit of  $t \gg 1$  and  $k^2Dt \ll 1$ . Therefore, the Linear diffusion model is applicable in the  $t \gg 1$  and  $k \ll 1$  region.

The second model to investigate is the Free gas diffusion model [86]. In this model, the particles are assumed to move freely in the ensemble. The only interaction between the particles is the perfect elastic collision. There is no short range or long range force field in this model. This kind of system is called the free gas or the ideal gas. The MSD of the ideal gas is

$$\delta r^2(t) = \frac{3k_B T \cdot t^2}{m} \quad (2.4.5)$$

By Eq. (2.2.9), the width function is

$$w(t) = \frac{k_B T \cdot t^2}{m} \quad (2.4.6)$$

Therefore, the self intermediate function of an ideal gas is

$$I_s(k, t) = e^{-\frac{k_B T \cdot t^2}{2m} k^2} \quad (2.4.7)$$

Finally, a Fourier transform to the frequency domain yields

$$S_s(k, \omega) = \sqrt{\frac{m}{2\pi k_B T k^2}} e^{-\frac{m\omega^2}{2k_B T k^2}} \quad (2.4.8)$$

As discussed above, this model is only valid when the liquid system can be viewed as free traveling particle. This assumption imposes  $t \ll 1$  limitation in time domain and  $r \ll 1$  limitation in spatial domain, which is equivalent to the requirement of  $k \gg 1$  limitation in reciprocal space domain.

The third model is the Egelstaff & Schofield diffusion model [92]. A simple ad-hoc form of  $w(t)$  is chosen to obtain a convenient analytical form of  $S_s(k, \omega)$

$$w(t) = 2d(\sqrt{t^2 + c^2 + 1/4} - c) \quad (2.4.9)$$

It is obvious that the width function asymptotes to that of the Linear diffusion model as  $t \gg c$ , where the  $c$  is a unitless relaxation time constant. The  $d$  is a unitless diffusion coefficient constant. The time  $t$  in this equation is unitless time, scaled by  $\hbar/k_B T$ . The self intermediate scattering function therefore is

$$I_s(k, t) = e^{-d(\sqrt{t^2 + c^2 + 1/4} - c) \cdot k^2} \quad (2.4.10)$$

The Fourier transform of the time domain is

$$S_s(k, \omega) = \frac{e^{dk^2 c}}{\pi} \frac{dk^2 \sqrt{c^2 + 0.25}}{\sqrt{\omega^2 + (dk^2)^2}} K_1 \left[ \sqrt{(c^2 + 0.25)(\omega^2 + (dk^2)^2)} \right] \quad (2.4.11)$$

There is an analytical form of diffusion density of states associated with Eq. (2.4.9)

$$p_d(\beta) = \frac{2d\beta}{\pi} \sqrt{c^2 + 0.25} \cdot K_1 \left( \beta \sqrt{c^2 + 0.25} \right) \quad (2.4.12)$$

where the  $K_1$  function is the modified Bessel function of the second kind. The two parameters  $c$  and  $d$  in Eq. (2.4.10) have different physical meanings. As stated above, the parameter  $d$  is linearly proportional to diffusion coefficient  $D$ .

$$d = \frac{MD}{\hbar} \quad (2.4.13)$$

It is a measurement of diffusion speed. The parameter  $c$  is proportional to relaxation time. The larger  $c$  is, the longer time a particle spends hovering around its initial position until the diffusional effects dominate the motion. As shown in Eq. (2.4.12), the diffusional behavior dominates low energy states in its DOS. On the contrary, the parameter  $c$  predominantly represents the high energy quasi-free particle motion at small  $t$ . Therefore, the length of the DOS tail in Eq. (2.4.12) is determined by the parameter  $c$ .

From another perspective, the  $K_1(x)$  function asymptotes to  $1/x$  as  $x \rightarrow 0$  and to  $\sqrt{\pi/x}e^{-x}$  as  $x \rightarrow \infty$ . Therefore, when  $dk^2 \rightarrow 0$ , the Linear diffusion model is recovered from the Egelstaff & Schofield model; when  $dk^2 \rightarrow \infty$ , the Free gas model is recovered from the Egelstaff & Schofield model.

As discussed above, the Egelstaff & Schofield diffusion model is an approximation that suits diffusion in simple liquids. Monoatomic, Brownian liquids are well suited to adopt this model. However, this model is known to fail in liquid systems that exhibit complex force fields and midrange order, such as glass liquids, macromolecule liquids, etc.

The fourth model is the Langevin diffusion model [81,93]. In this model,  $\delta r^2(t)$  and  $w(t)$  are obtained by solving the Langevin equation. The Langevin equation of motion is

$$\frac{d^2\mathbf{r}}{dt^2} + \gamma \frac{d\mathbf{r}}{dt} = \frac{1}{M^*} \mathbf{f}(t) \quad (2.4.14)$$

where the  $\mathbf{f}(t)$  is a “stochastic” driving force, with  $\gamma$  being the friction constant

$$\gamma = \frac{1}{\tau_0} = \frac{k_B T}{M^* D} \quad (2.4.15)$$

It measures the force impeding the atomic motion by “friction”.  $M^*$  is the effective mass of particle in the motion, which is always larger than the actual mass of the particle. By applying the Gaussian approximation, the width function can be solved from Eq. (2.4.14). Following the solution given by Springer [93], the width function is given by

$$w(t) = 2D \left[ t - \tau_0 \left( 1 - e^{-t/\tau_0} \right) \right] \quad (2.4.16)$$

Following the solution given by Egelstaff [81], the width function is given by

$$w(t) = 2D \left[ \sqrt{t^2 + 1/\gamma^2} - 1/\gamma \right] \quad (2.4.17)$$

The first order terms in the Taylor series of both solutions are the same. Therefore, Eq. (2.4.16) and (2.4.17) are the same solution in different forms.

As we can see, the friction constant,  $\gamma$ , or relaxation time,  $\tau_0$ , are closely related to the relaxation time parameter  $c$  in the Egelstaff & Schofield diffusion model in Eq. (2.4.9). In short, the friction constant is inversely proportional to the relaxation time. This is easy to comprehend since the “friction force” is a simple measurement of the impedance of motion. The relaxation time, on the other hand, is a measurement of how long the particles can practice quasi-free motion. If we connect the friction constant  $\gamma$  and the relaxation time constant  $c$  with  $\gamma = 1/c = 1/\tau_0$ , then the only difference between the Langevin model and the Egelstaff & Schofield model is the inclusion of the  $1/4$  term. Without the  $1/4$  term, the  $S_s(k, \omega)$  from Langevin model is a delta function at  $k = 0$  and  $\omega = 0$ . This term is introduced in Schofield’s model to avoid singularity points at small  $k$  and small  $\omega$ . With the above width function, the self intermediate scattering function can be put as

$$I_s(k, t) = e^{-D \left[ \sqrt{t^2 + 1/\gamma^2} - 1/\gamma \right] k^2} \quad (2.4.18)$$

After taking the Fourier transform of Eq. (2.4.18), the  $S_s(k, \omega)$  is given by

$$S_s(k, \omega) = \frac{e^{Dk^2/\gamma}}{\pi} \frac{Dk^2 / \gamma}{\sqrt{\omega^2 + (Dk^2)^2}} K_1 \left( \frac{\sqrt{\omega^2 + (Dk^2)^2}}{\gamma} \right) \quad (2.4.19)$$

where the  $K_1$  function is the modified Bessel function of the second kind. The Linear diffusion model is recovered from this model if  $Dk^2 \rightarrow 0$ . The Free gas model is recovered as  $Dk^2 \rightarrow \infty$ .

## 2.5 The Quantum Thermal Scattering Law and the Classical Thermal Scattering Law

### 2.5.1 From the Quantum Thermal Scattering Law to the Classical Thermal Scattering Law – the Classical Approximation

In the quantum mechanics description of a system, the position operator  $\mathbf{R}_j(t)$  does not commute because it depends on the system Hamiltonian  $H$  shown in Eq. (2.1.8). Therefore, the correlation functions  $G(r, t)$  and  $I(k, t)$  are asymmetric in  $t$  space. This asymmetry is carried over to the  $S(k, \omega)$  function through the Fourier transform to  $\omega$  space as the principle of detailed balance. In some situations, the quantum mechanical nature of the thermal scattering law is not easy to capture and interpret. The classical approximation could be introduced to help interpret the mechanics of the system.

In the classical approximation, the quantum nature of  $\mathbf{R}_j(t)$  operator is neglected. The  $\mathbf{R}_j(t)$  is instead merely the position of atom  $j$  at time  $t$ . In this way, the  $\mathbf{R}_j(t)$  commutes in the definition of  $G(r, t)$ ,  $I(k, t)$ , and  $S(k, \omega)$ . There are two merits in doing this. First, the classical approximation enables the evaluation of the thermal scattering law from classical particle trajectories, which will be discussed in detail in Chapter 3. Second, the classical approximation helps to interpret the correlation functions  $G(r, t)$ ,  $I(k, t)$  and  $S(k, \omega)$  more easily. With the classical approximation, the  $G(r, t)$  function can be interpreted as

$$G_s^{cl}(r, t)dr = \begin{cases} \text{Probability that at time } t \text{ an atom is a} \\ \text{distance } r \text{ from an origin } (r=0) \text{ given} \\ \text{that the same atom was at the origin} \\ \text{at the initial time } t=0. \end{cases}$$

$$G_d^{cl}(r,t)dr = \begin{cases} \text{Probability that at time } t \text{ an atom is a} \\ \text{distance } r \text{ from an origin } (r=0) \text{ given} \\ \text{that any other atom was at the origin} \\ \text{at the initial time } t=0. \end{cases}$$

As we can see from the classical picture, the corresponding  $I(k,t)$  function consists of the same position information of the  $G(r,t)$  function in the reciprocal space. The  $S(k,\omega)$  function, correspondingly, consists of the information in reciprocal space and frequency space. In general, reciprocal space reveals the periodic structural information of the system, while frequency space reveals the excitation dynamics of the system.  $S(k,\omega)$  is named the dynamic structure factor for its ability to demonstrate the correlation of the structural information and the excitation dynamics of the system. An analog is the dielectric function  $\epsilon(k,\omega)$ , which demonstrates the correlated dynamics and space structure of dielectric permittivity.

The behavior in  $t$  or  $\omega$  space for the correlation functions is symmetric. The  $I(k,t)$  and  $S(k,\omega)$  are purely real for classical systems. They are also even functions in  $t$  and  $\omega$  space. In a classical system

$$S^{cl}(\alpha, -\beta) = S^{cl}(\alpha, \beta) \quad (2.5.1)$$

And the well-known first moment of  $S^{cl}(\alpha, \beta)$  is 0

$$\int_{-\infty}^{\infty} \beta \cdot S^{cl}(\alpha, \beta) d\beta = 0 \quad (2.5.2)$$

In the quantum description,  $G(r,t)$  and  $I(k,t)$  are non-even and complex, and  $S(k,\omega)$  follows Eq. (2.1.22) and (2.1.23). To eliminate these divergences from the quantum behavior, a quantum correction could be applied.

### 2.5.2 From the Classical Thermal Scattering Law to the Quantum Thermal Scattering Law – the Quantum Correction

As stated in the previous section, the quantum mechanical nature of the thermal scattering law can be neglected in some cases to help with the interpretation. However, it is not always sufficient to substitute the quantum correlation functions with their classical counterpart. This insufficiency is rooted in the quantum uncertainty of the thermal cloud as discussed in Section 2.1.3. The phenomena will be further illustrated in Chapter 4 using liquid lithium as an example. In this section, the discussion will focus on how to effectively apply the quantum correction.

From the discussion in Section 2.2.1, it is shown that both the classical and quantum  $I_s(k, t)$  can be evaluated from the width function using the Gaussian Approximation. Since the classical width function  $w(t)$  is based on trajectory  $\mathbf{R}_j(t)$  instead of the quantum operator, the direct evaluation methodology of  $w(t)$  is well developed [91]. One straight forward method is to use  $\delta r^2(t)$  to evaluate  $w(t)$  as shown in Eq. (2.2.9).

It is therefore necessary to understand how to apply quantum correction to the evaluated classical width function  $w(t)$  to obtain the quantum width function  $\gamma(t)$ . Equation (2.2.12) and (2.2.15) show that the  $w(t)$  and  $\gamma(t)$  width functions are associated by the characteristic function  $f(\omega)$ . The quantum correction effectively corrects the characteristic function  $f^{cl}(\omega)$  in  $w(t)$  to the quantum  $f^{qt}(\omega)$  to obtain the quantum width function  $\gamma(t)$ .

A review of the derivation of the quantum correction will be shown in the Appendix B. Only application methodology will be discussed here.

The first step is to rescale  $\delta r^2(t)$  with unit  $\hbar/k_B T$  to time  $t'$ . The advantage of using  $t'$  is that the Fourier transform of  $t'$  will result in unitless energy  $\beta$ . Based on Eq. (2.2.12), the classical



characteristic function  $f^{cl}(\beta)$  can be evaluated from the Fourier transform of  $\delta r^2(t')$  with unit  $\hbar/k_B T$  for time  $t'$

$$\frac{f^{cl}(\beta)}{\beta^2} = \frac{Mk_B T}{3\hbar^2} \int_{-\infty}^{\infty} e^{i\beta t'} \delta r^2(t') dt' \quad (2.5.3)$$

The second step is to correct the classical characteristic function  $f^{cl}(\beta)$  to the quantum characteristic function  $f^{qt}(\beta)$  based on Eq. (2.2.15). Note that the  $f^{qt}(\beta)$  function is a complex function with its real and imaginary part given by

$$\begin{aligned} \text{Re}[f^{qt}(\beta)] &= \frac{\beta e^{\beta/2}}{2 \sinh(\beta/2)} \cdot \frac{f^{cl}(\beta)}{\beta^2} \\ \text{Im}[f^{qt}(\beta)] &= -\frac{\beta}{2} \cdot \frac{f^{cl}(\beta)}{\beta^2} \end{aligned} \quad (2.5.4)$$

The third step is to restore the quantum width function from the quantum characteristic function  $f^{qt}(\beta)$  using the inverse Fourier transform

$$\begin{aligned} \text{Re}(\gamma(t')) &= \text{Re}\left(\int_{-\infty}^{\infty} e^{-i\beta t'} \text{Re}(f^{qt}(\beta)) d\beta\right) \\ \text{Im}(\gamma(t')) &= \text{Im}\left(\int_{-\infty}^{\infty} e^{-i\beta t'} \text{Im}(f^{qt}(\beta)) d\beta\right) \end{aligned} \quad (2.5.5)$$

The last step is to apply the Gaussian approximation to evaluate the quantum intermediate scattering function and the quantum thermal scattering law

$$\begin{aligned} I_s^{qt}(\alpha, t') &= e^{-\alpha \cdot \gamma(t')} \\ &\downarrow \\ S_s^{qt}(\alpha, \beta) &= \int_{-\infty}^{\infty} e^{i\beta t'} I_s^{qt}(\alpha, t') dt' \end{aligned} \quad (2.5.6)$$

### 2.5.3 The Semiclassical Quantum Correction

In past research, extensive effort has been made to approximate quantum time correlation functions. Focusing especially on the form of:

$$Q(k, \omega) = \frac{S(k, \omega)}{S^{cl}(k, \omega)} \quad (2.5.7)$$

While a universal analytical solution of  $Q(k, \omega)$  seems highly unlikely, various approximation schemes have been proposed in the past 50 years. Many of them have been discussed in Brian Hehr's PhD thesis [89] and in a recent literature [84]. For most corrections, the semiclassical correction factor  $Q(k, \omega)$  only depends upon the material's energy structure. Thus the  $Q(k, \omega)$  is often written as  $Q(\omega)$ . In this section, the merits and disadvantages of such methodologies will be discussed.

The most significant advantage of such semiclassical corrections is that they all follow the principle of detailed balance to different extents. Accordingly, they approach the classical limit  $S^{cl}(k, \omega) = S^{cl}(k, -\omega)$  as  $\omega \rightarrow 0$ . Furthermore, in the classical limit as  $\omega \rightarrow 0$ , the  $Q(k, \omega)$  approaches 1.

The simplest correction was proposed by Schofield [94]. It uses the classical  $S^{cl}(k, \omega)$  as symmetric  $S_{sym}(k, \omega)$  and applies half of the detailed balance condition to both the positive and the negative  $\omega$  side. This is directly equivalent to having  $Q(\omega)$  as

$$Q_{sc}(\omega) = \exp\left[\frac{\hbar\omega}{2k_B T}\right] \quad (2.5.8)$$

An improved prescription to Schofield's semiclassical correction is proposed by Aamodt et al. [95] to include the recoil effects, giving  $Q(\omega)$  as

$$Q_{sc2}(\omega) = \exp\left[\frac{\hbar\omega}{2k_B T}\right] \exp\left[-\frac{p^2}{8k_B T M}\right] \quad (2.5.9)$$

where  $p$  is the momentum and has the order of  $\hbar$ . This can be treated as the second order Schofield semiclassical correction. This correction effectively includes recoil effects that the average energy loss is  $p^2/2M$  rather than the set value 0. The third order correction is introduced by Rosenbaum

et al. [96] to include leading asymptotic expansion terms to  $\hbar^3$ . This extension cannot be written with  $Q(\omega)$ , but shares a basic form similar to Eq. (2.5.9)

$$S(k, \omega) = \exp\left[\frac{\hbar\omega}{2k_B T}\right] \exp\left[-\frac{p^2}{8k_B TM}\right] \left\{ S^{cl}(k, \omega) + \frac{1}{6k_B Tp} \sqrt{\frac{M}{2\pi k_B T}} (F - F_c) \left(1 - \frac{\hbar^2 \omega^2 M}{k_B T p^2} + \frac{p^2}{8k_B TM}\right) \exp\left[-\frac{\hbar^2 \omega^2 M}{2k_B T p^2}\right] \right\} \quad (2.5.10)$$

where the  $F$  and  $F_c$  are the impulse force for momentum exchange with/without quantum operator

$$F = \frac{1}{2} p \cdot \delta(t).$$

The series of corrections based on Schofield's prescription all fulfill the principle of detailed balance exactly. However, the behavior of the corrected  $S(k, \omega)$  generally does not for higher  $\omega$ . The exponential with  $\exp(\hbar\omega/2k_B T)$  rises the scattering law too fast at high  $\omega$ . As a result, the integrated total cross section rises to unrealistically high value at high energies ( $> 1$  eV). Physically, the integrated total cross section should always asymptote to the bound cross section at high energies ( $> 1$  eV). An example of this phenomenon will be shown in Chapter 4.

The second form of  $Q(\omega)$  is the harmonic correction proposed by Bader and Berne [97].

$$Q_h(\omega) = \frac{\hbar\omega / k_B T}{1 - \exp(-\hbar\omega / k_B T)} \quad (2.5.11)$$

The third form of  $Q(\omega)$  is the standard correction, associated with the name Litovitz [98], Berne [99], and Oxtoby [100].

$$Q_{st}(\omega) = \frac{2}{1 + \exp(-\hbar\omega / k_B T)} \quad (2.5.12)$$

These two approximations are known for mitigating the rising exponential at high  $\omega$  in the Schofield approximation. However, the integrated cross section evaluated from these two

approximations still does not converge to the bound cross section at relative high energy ( $> 1 \text{ eV}$ ). For further details on the discussion of the harmonic correction and the standard correction, readers are referred to Brian Hehr's PhD thesis [89].

The fourth correction is proposed by Abe and Tasaki [85]. It chooses the dynamic structure factors pair in Eq. (2.5.7) from Rahman [80]. There are two points that need to be clarified with this  $Q(k, \omega)$  strategy. The first is that the approximation in the form of Eq. (2.5.7) requires prior knowledge of the corrected quantum  $S(k, \omega)$ , whereas the  $S(k, \omega)$  is unknown and should be the final product to be evaluated. The form of  $S(k, \omega)$  is more like *a posteriori* thermal scattering law evaluation from prior experience rather than quantum correction.

The second reason is that the approximation applies the same frequency spectrum  $f^{vacf}(\omega)$  from the VACF in both the classical and the quantum  $S(k, \omega)$ . As stated by Parks, Nelkin, et al. [91], replacing the  $f(\omega)$  with  $f^{vacf}(\omega)$  is not a consistent substitution for liquids. Though the substitution is precisely correct for solid materials, it is difficult to know how much deviation it will cause to replace  $f(\omega)$  with  $f^{vacf}(\omega)$  for liquids. The origin of the velocity operator in  $f(\omega)$  is certainly quantum mechanical and related to Hamiltonian of the system. The reduction from  $f(\omega)$  to  $f^{vacf}(\omega)$  has an implicit impact on the evaluated shape of  $S(k, \omega)$ .

## 2.5.4 The Quantum Correction on Distinct Thermal Scattering Law

There are two parts for the thermal scattering law, i.e.  $S_d(k, \omega)$  and  $S_s(k, \omega)$ . To quantum correct  $S_d(k, \omega)$ , a quantum self  $S_s(k, \omega)$  needs to be obtained first. With  $S_s(k, \omega)$ , the  $Q(k, \omega)$  for the self thermal scattering law can be evaluated. By assuming that the quantum picture and the classical picture of  $S_s(k, \omega)$  and  $S_d(k, \omega)$  follow the same quantum correction relation, the correction factor is given by

$$Q(k, \omega) = \frac{S_s^{qt}(k, \omega)}{S_s^{cl}(k, \omega)} = \frac{S_d^{qt}(k, \omega)}{S_d^{cl}(k, \omega)} \quad (2.5.13)$$

This correction scheme is essentially the same as the convolution approximation [78], which assumes that the van Hove space-time correlation function  $G(r, t)$  can be related to the self part by

$$G(r, t) = G_s(r, t) + \int G(r', 0) \cdot G_s(r - r', t) dr' \quad (2.5.14)$$

A two-fold Fourier transform in the reciprocal and frequency space would give a multiplication relation between the distinct part and the self thermal scattering law

$$S_d(k, \omega) = \Gamma(k) \cdot S_s(k, \omega) \quad (2.5.15)$$

where  $\Gamma(k)$  is called the collective structural function. It indicates that the distinct attribution is a spatial physical property, which depends on the spatial particle distribution correlation  $G(r', 0)$ , independent of time. The time dependence of the coherent van Hove correlation function stems from the self-motion only, i.e.  $G_s(r - r', t)$ . In short, the distinct correlation provides the spatial structural information, while the self correlation provides the time space evolution information.

Eq. (2.5.13) and (2.5.15) are the same in that they both assume the same ratio between the distinct part and the self part. Either Eq. (2.5.7) or (2.5.15) would generate the same result for the quantum correction on the distinct thermal scattering law.

## 2.6 Computational Techniques

In order to evaluate the thermal neutron scattering cross section, two simulation techniques are conventionally used as fundamental input to the theory: density functional theory (DFT) simulation and MD simulation. These two techniques can also be adapted in two ways – the density

of states (DOS) methodology and the direct trajectory to thermal scattering law methodology.

Figure 2-2 demonstrates the application of DFT and MD techniques.

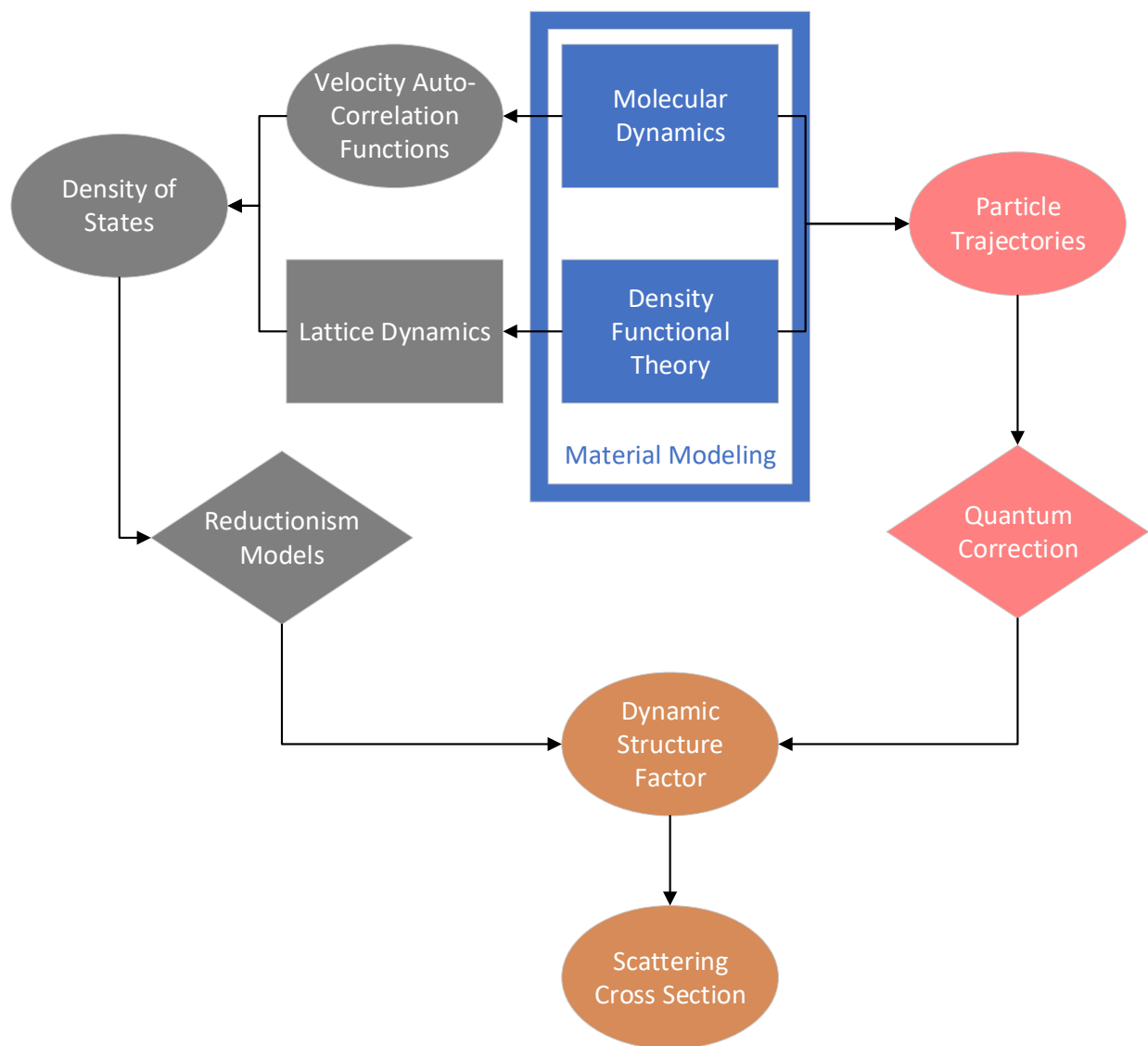


Figure 2-2. Scheme of thermal neutron scattering cross section calculation.

The DFT technique is more accurate in evaluating the interaction forces because it solves the Kohn-Sham equations from first principles for the electronic density distribution. Subsequently, particle-particle interacting forces are determined from the electronic density distribution. Compared to most MD inter-particle pair potentials, DFT's pseudopotential is more fundamental. However, this benefit means solving a more complex system and a much longer CPU time to

execute the algorithm. It is most practical to apply the DFT methodology to highly symmetrical crystalline systems. In these situations, the symmetry of the system can unfold the electric density distribution, resulting in a smaller highly symmetric space to solve the Kohn-Sham equations. In complex amorphous systems such as large organic molecules and liquids, the DFT methodology usually takes much larger computational resources than symmetric systems.

Compared to the DFT technique, the MD technique has the advantages of a simpler algorithm, larger simulation system size, longer simulation time length, capability to handle amorphous materials better, etc. These features are critical because they enable the analysis of long-time trajectories of a large system directly to obtain the thermal scattering law. The above advantages come with limitations as well. The MD method is extremely fast with the sacrifice of fundamental potentials. The technique is limited especially for multi-body systems.

In light of Figure 2-2, there is a fundamental difference between the DOS approach and the direct trajectory to thermal scattering law approach. To better illustrate the difference, a diagram (Figure 2-3) is adapted from Haile [101]. As can be seen in Figure 2-3, to explain nature or a phenomenon, two tools can be applied, i.e. theory and experiment. The simulation, on the high level, could be used to adapt and explore the theory. On the other side, reductionism can be applied, where multiple mathematical models would be assumed. These mathematical models combined could restore the original theory with an acceptable degree of accuracy when assumed criteria are met. These models are, in most cases, simpler and easier to analyze than the top level original theory. However, these models fall short in predicting consistent physical behavior when their presumed criteria are not met. In these situations, the high level simulation restores realities better than the reduced approach.

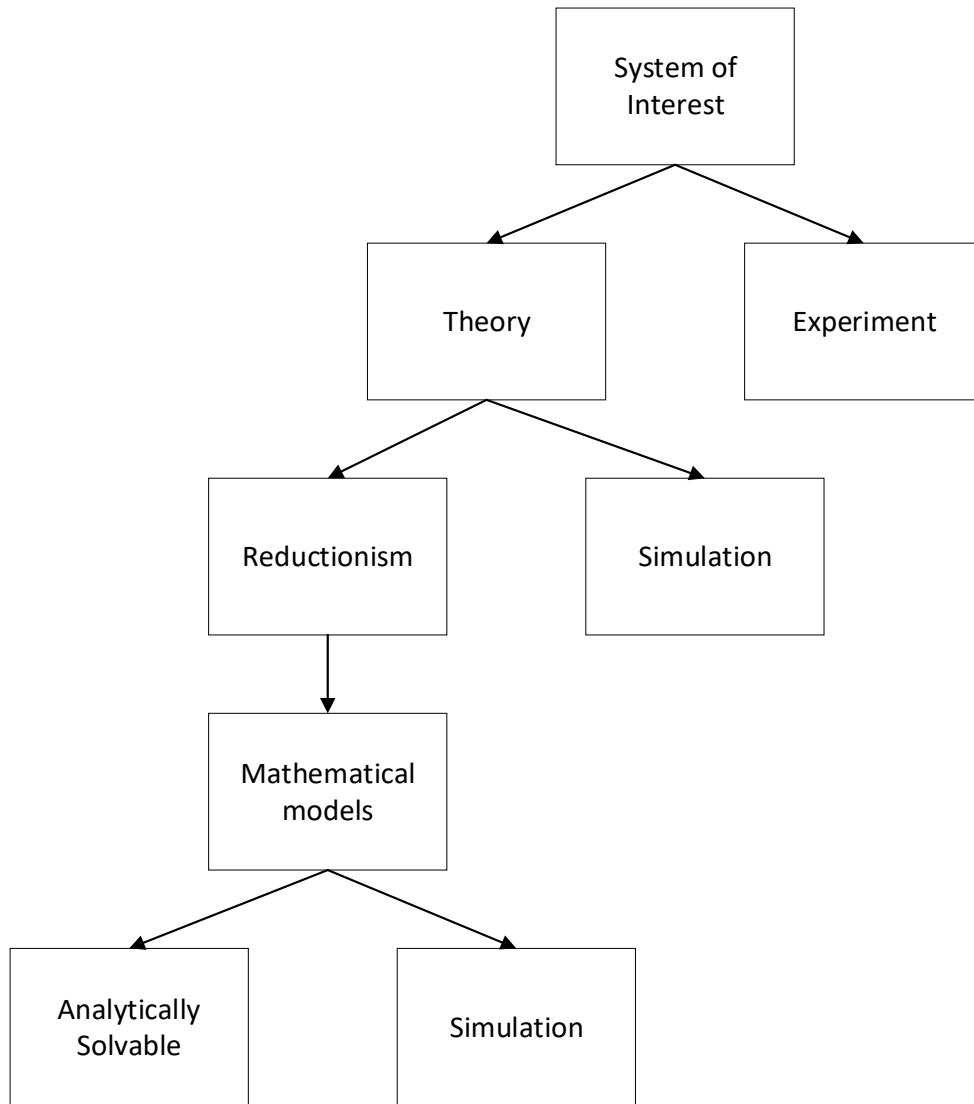


Figure 2-3. Hierarchy of scientific modes of investigation

In the case of understanding thermal neutron scattering and evaluating the dynamic structure factor, the same diagram is replotted in Figure 2-4. To understand thermal neutron scattering phenomena, experiments such as neutron spallation experiments can be deployed to measure it. Thermal neutron scattering theory, under the 1<sup>st</sup> Born approximation combined with the Fermi's pseudo-potential [67,86], can also be developed with the dynamic scattering factor, i.e. the thermal scattering law. The dynamic scattering factor under the general theory is computationally expensive to evaluate directly from particle trajectories. However, with the help of reductionism,



the general theory can be decomposed into several sub-models under different assumptions. For example, the phonon model for the vibrational motion, the ideal diffusional model for diffusive-only motion, and the free gas model for the Brownian motion can be combined and convoluted to describe a system with these motion characteristics. These models are most often simple, ideal and analytical. Simulation on the same low level could be applied to provide input information for these models, for example, the density of states.

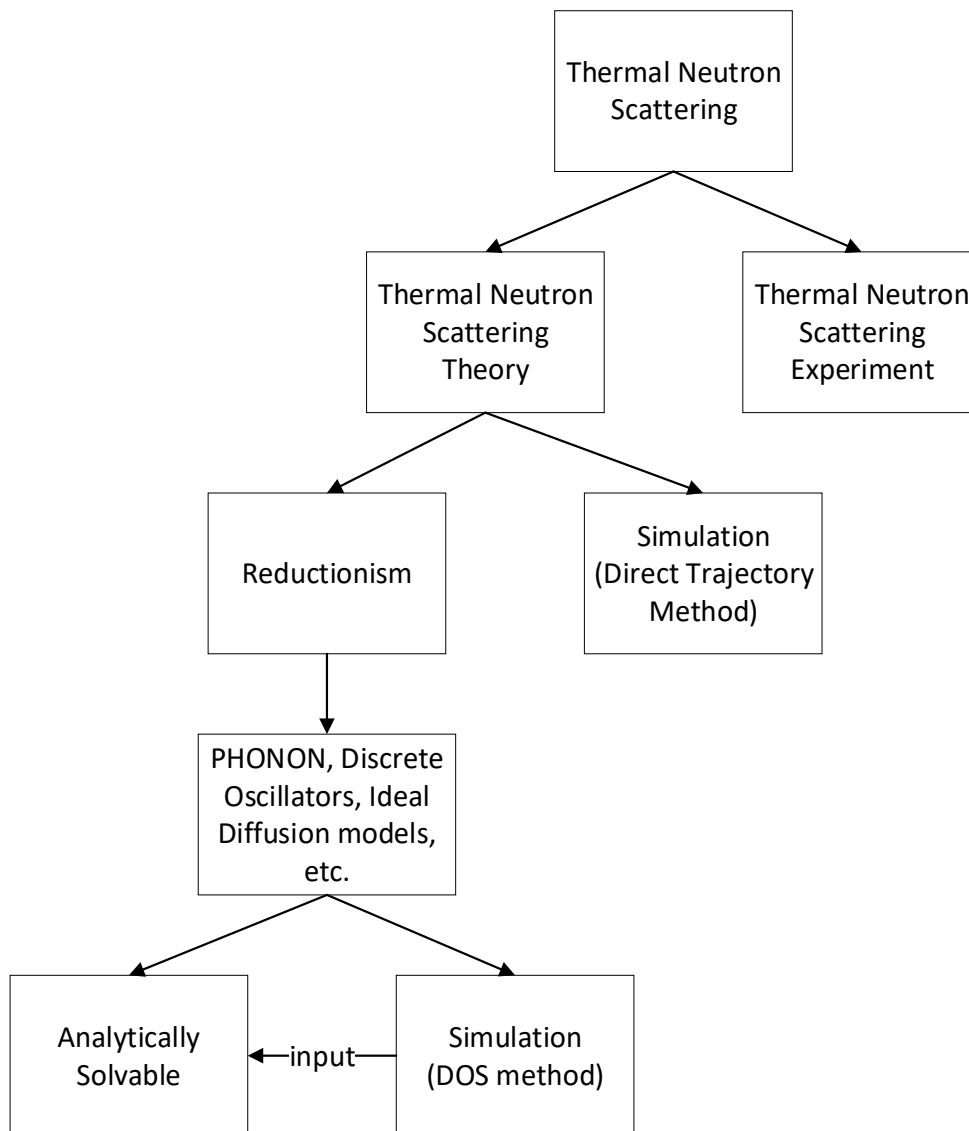


Figure 2-4. Hierarchy of thermal neutron scattering research

The simulation applied at high hierarchy level to directly calculate the dynamic structure factor only require low-level data, i.e. the particles' trajectories. On the contrary, simulations at low hierarchy level must have high level input data provided for the simplified models, i.e. the density of states. This difference stems from the level of reductionism and the level of assumptions in the theoretical models.

To study the thermal neutron scattering law, input for either the DOS method or the trajectory method would be needed. It is worth mention that both the particle trajectories and the DOS can be obtained from MD simulations. In this work, MD is chosen to simulate liquid FLiBe. In the next chapter, the discussion will focus on building an MD model for FLiBe and the validation of the model.

## Chapter 3 The Molecular Dynamics Technique

The primary goal of this chapter is to introduce molecular dynamics (MD) simulations and present frequently used analysis techniques that provide atomic- and molecular-scale details of the system. The mechanics of MD are reviewed. The direct use of MD trajectories to evaluate the dynamic structure factor is discussed. Various applications of MD, which are applied in this work, are also demonstrated [102]. These MD techniques are especially useful in the thermal neutron scattering field.

### 3.1 Overview of Molecular Dynamics

Classical MD simulations are based on Newton's equation of motion for a system of interacting particles:

$$\mathbf{F} = m \cdot \mathbf{a},$$

where the force,  $\mathbf{F}$ , acting on each particle is defined as the first derivative of the potential energy function,  $U$ , with respect to distance,  $r$ :

$$\mathbf{F} = \frac{\partial U}{\partial r}$$

From the above equations, it is clear that the particle trajectories and resulting properties of the material system is highly dependent on the interatomic potential energy function. The combination of the long-established Newton's law of equation with the modern computation power give birth to molecular dynamics. Molecular dynamics (MD) is a combination of these well-established classical equations along with modern computational power gives rise to large-scale classical MD. Well-developed MD computer codes generally implement the following steps:

1. Initialize the position and momentum of every particle in the system. Build the neighbor list of each particle based on the position.
2. Calculate the forces on each atom from the neighbor list based on the interatomic potential. Update particle positions, momenta, and forces toward the minimum energy state using some time-integration algorithm, e.g., the velocity-Verlet algorithm).
3. Repeat step 2 until the system reaches its minimum energy state, i.e., thermal equilibrium.

The equilibrated system can then be used to study steady state system properties. Dynamic system properties can also be studied using non-equilibrium MD, which is based on the equilibrated MD model. Several kinds of raw data can be collected from MD simulations including trajectories, momenta, energies, etc. Properties such as density, viscosity, diffusion coefficient, thermal conductivity, and radial distribution functions can be calculated by post processing the raw data.

As alluded to earlier, the interatomic potential is of paramount importance in MD simulations. The MD system's equilibration run and data production run are deterministic procedures that solely depend on the interatomic potential. In classical MD, it is usually assumed that the electron distribution around each atom does not change with environment (i.e., fixed atomic charges). Consequently, the potential, which generates the force field due to different bonding environments is always assumed to be unchanged. In an N-atom system, the potential can be written as

$$U = \sum_{i < j} U_{i,j}^2 + \sum_{i < j < k} U_{i,j,k}^3 + \cdots,$$

where the terms are potentials for two-body, three-body and higher order interactions. The increasing summation order in the above equation stands for summation over all distinct pairs, triplets, quadruplets and so forth.

In classical MD, the most commonly applied potential is the two-body pair potential. Pair potentials are the simplest form of a potential that consider only two atom interactions and neglects all others. The pair potential is commonly applied in liquids, gas, and solids. However, in solids, the bonding of atoms is usually stronger and more complex. Such a complex bonding environment has spurred the development of even more robust interatomic potentials, oftentimes designed for specific materials systems. For example, the embedded atom method (EAM) potential [103,104] is designed to include many-body effects which account for the unique de-localization of electrons observed in bulk metallic systems. Covalently bonded solid systems deviate even further from the pairwise interaction potential because they are bonded more strongly with highly directional forces. The Tersoff potential which depends on the geometric distribution of the neighboring atoms was introduced in order to capture these directionality-dependent bonding environments [105]. This potential is commonly applied to covalently bonded systems such as diamond, Si, SiC, graphite, etc. With the development of MD techniques in recent years, various potential forms have been proposed. Some of them are highly optimized for just one substance, e.g., TIP4P for water [106], while other potentials focus on one specific type of application, such as organic molecules.

### **3.2 MD Model of Molten Salt Liquid FLiBe**

#### **3.2.1 Pair Potentials of General Molten Salt**

At room temperature and standard pressure, molten salts are solid materials formed by ionic bonding. When temperature rises above their melting point, ionic liquids are formed by breaking of ionic bonding due to intense thermal motion.

Ever since Born, Mayer, and Huggins [107,108] published their theoretical analysis of the pair potential between the ionic crystal, research on alkali halide pair potentials has been focused on the Born-Mayer formula. The pair potential of alkali halides has been developed for all elements in the periodic table. Significant progress [40,109-113] in the alkali halides pair potential was made in 1960s and 1970s when molten salt technology development was most active. Fumi and Tosi developed a Born-Mayer pair potential table for a number of ions [109,110]. Abrahamson extended the pair potential table for neutral ground-state atoms for  $2 \leq Z \leq 105$  [111]. Furthermore, Gaydaenko and Nikulin optimized the pair potential for atoms for  $2 \leq Z \leq 36$  [112]. Busing optimized and applied the alkali halide pair potential on crystalline FLiBe to predict its lattice constant [40]. The efforts of applying the alkali halides pair potential to molten salt liquids was reviewed and summarized by Sangster [113]. These efforts, along with increasing computational capabilities of modern computers, provide powerful tools to simulate molten salt liquid FLiBe.

### **3.2.2 Pair Potential of Molten Salt Liquid FLiBe**

Busing successfully predicted the lattice constant and lattice energy for crystalline FLiBe [40] using Born-Mayer potential; however, the potential has difficulties in predicting liquid state FLiBe properties [76]. Liquid phase molten salts are different from their corresponding solid crystalline counterparts with regard to separation distances between atoms and the organization pattern of atoms. Consequently, the predicted properties from Jabes [76] using Busing's potential [40] do not match the experimental measurements. It is therefore necessary to develop an optimized pair potential for molten salt liquid FLiBe. In this work, the pair potential of molten salt liquid FLiBe is chosen to be the Born-Mayer pair potential. The coefficients of the pair potential were optimized to predict the experimentally measured properties. The interaction Born-Mayer potential between ions is given by:

$$U_{i,j}(r_{i,j}) = U_1 + U_2 + U_3 + U_4, \quad (3.2.1)$$

where

$$U_1 = \frac{Z_i Z_j e^2}{r_{i,j}}, U_2 = -\frac{c_i c_j}{r_{i,j}^6}, U_3 = \frac{D}{r_{i,j}^8}, U_4 = b_{i,j} \left( 1 + \frac{Z_i}{N_i} + \frac{Z_j}{N_j} \right) \exp \left( \frac{r_i + r_j - r_{i,j}}{\rho} \right). \quad (3.2.2)$$

$U_1$  is the Coulomb potential, which is the major contributor to cohesive forces in FLiBe. In the above equation,  $r_{i,j}$  is the distance between ions of type  $i$  and  $j$  in the system,  $r_i$  is the radius of type  $i$  ion,  $Z_i$  is the effective charge of the ion, and  $N_i$  is the number of electrons in the outermost shell of the ion. These parameters are given in Table 3-1.

Table 3-1. Parameters for FLiBe defining the Born-Mayer potential.

	$Z_i$	$N_i$	$r_i (\text{\AA})$
Be	+1.5	2	0.472
F	-0.75	8	0.952
Li	+0.75	2	0.720

$U_2$  and  $U_3$  are the dipole-dipole interaction term and its cutoff term, respectively, which are the attractive force contributors at small separation distances. In Eq. (3.2.2),  $c_i c_j$  describes the contribution of electric dipole-dipole attractive interactions. This potential is infinitely negative as  $r \rightarrow 0$  due to the  $r^6$  term. This large attractive force will cause the atomic system to collapse at small  $r$ . The  $r^8$  term is therefore introduced in Born-Mayer potential to mitigate the unstable attractive behavior when  $r$  approaches 0. The coefficient  $D$  is chosen to be 3 in this work to properly mitigate the attractive force.

$U_4$  is the Born-Mayer repulsive term, which is a major contributor of the repulsive forces in the potential. In Eq. (3.2.2),  $b_{i,j}$  is the repulsion coefficient between ions of type  $i$  and  $j$ ,  $b_{i,j}$  and  $c_i c_j$  are both given in Table 3-2. The denominator of the exponential is  $\rho$  which is the softness parameter given in angstroms ( $\text{\AA}$ ). It determines how close two particles can approach each other relative to their radius  $r_i$ . In this work,  $\rho$  is set to  $0.232 \text{ \AA}$ .

Table 3-2. Interatomic parameters of FLiBe defining the Born-Mayer potential.

	$b_{i,j}$ (Kcal/mol)	$c_i c_j$ ( $\text{\AA}^6 \cdot \text{Kcal/mol}$ )
Be-Be	22	16
Be-F	22	20
Be-Li	31	16
F-F	12	25
F-Li	9	20
Li-Li	22	16

Figure 3-1 shows the plot of pairwise potential interactions for  $\text{F}^-\text{F}^-$ ,  $\text{Li}^+\text{Li}^+$ ,  $\text{Be}^{2+}\text{Be}^{2+}$ ,  $\text{Li}^+\text{F}^-$ ,  $\text{Be}^{2+}\text{F}^-$ , and  $\text{Be}^{2+}\text{Li}^+$  pairs. The  $\text{Be}^{2+}\text{F}^-$  ion pair shows a much larger attractive force than the  $\text{Li}^+\text{F}^-$  pair, which is why the liquid FLiBe prefers forming a  $\text{BeF}_4^{2-}$  tetragonal bonding structure. The repulsive force of the  $\text{Be}^{2+}\text{Be}^{2+}$  ion pair is the strongest due to ionic charges that are twice as large as  $\text{Li}^+$  and  $\text{F}^-$ .

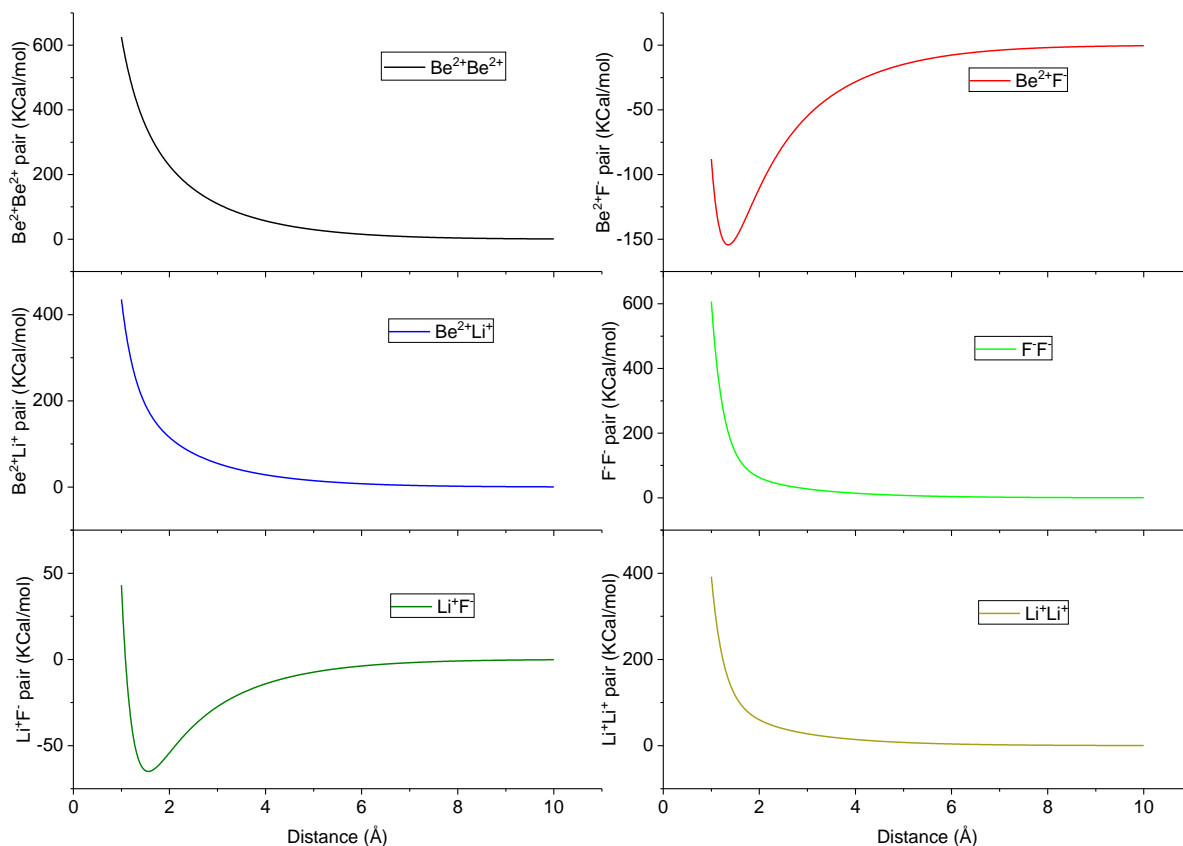


Figure 3-1. The pair potential of FLiBe for different ion pairs, shown from 1 Å to 10 Å.



Compared to Busing's potential [40], it was found that a softer behavior of the liquid FLiBe potential is necessary to better predict physical properties at higher temperatures. The coefficients were adjusted accordingly to achieve a stable potential that reproduces FLiBe physical properties at liquid state.

### 3.2.3 Equilibration of the MD model of FLiBe

In this work, all MD simulations are executed using the classical MD LAMMPS (Large-scale Atomic/Molecular Massively Parallel Simulator) software [114]. LAMMPS integrates a wide variety of forcefields (including the Born-Mayer potential used in this dissertation) and various conditions that allow for simulations of materials in unique, and sometimes extreme, environments. The code also runs parallelly using different message-passing techniques on a spatial-decomposition of the simulation domain. The Born Mayer potential in LAMMPS runs on GPU as well. The charge assignment and force interpolation portions of PPPM can also be accelerated through the GPU.

The MD simulations presented here are from an initial configuration of a 7000 atom FLiBe crystal supercell. The system consists of 2000  $\text{Li}^+$ , 1000  $\text{Be}^{2+}$ , and 4000  $\text{F}^-$  ions. The simulation uses 1 *fs* timestep. An orthorhombic simulation box ( $43.7 \text{ \AA} \times 43.7 \text{ \AA} \times 43.7 \text{ \AA}$ ) is used to accelerate the particle-particle particle-mesh (PPPM) interpretation of forces in the reciprocal space. The crystalline FLiBe structure was simulated at temperatures above its melting point 732 K.

A typical equilibration process is shown in Figure 3-2. To reach equilibrium faster, the temperature was set to a constant 873 K during the simulation. The total energy of the system, which is a summation of the kinetic energy and the internal energy, was monitored until it

converged. During this process, the system moves in its phase space and find its minimum energy states. The thermodynamic properties, such as the temperature, internal energy, and pressure should fluctuate around stable average values, such as shown in Figure 3-2. This state of the system is called thermal equilibrium.

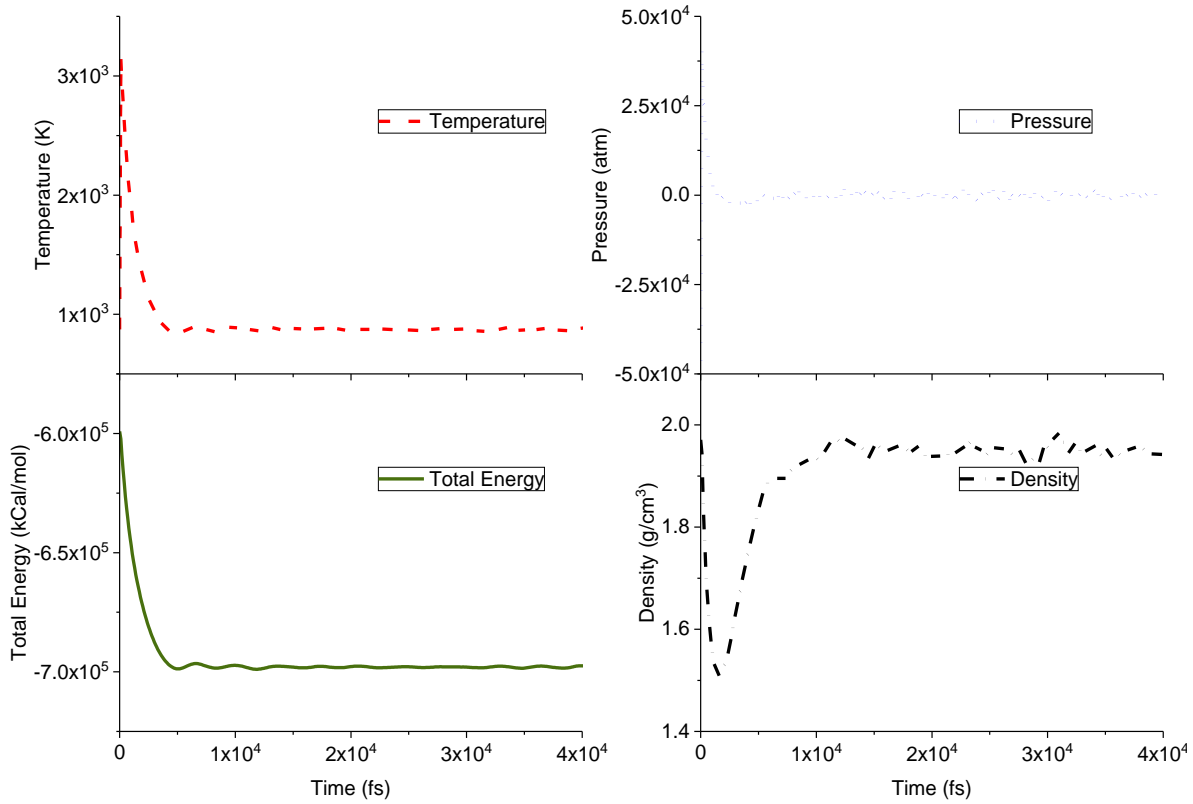


Figure 3-2. Equilibration of the FLiBe ensemble at representative reactor core temperatures of 873K.

The system with 7000 ions was first equilibrated for 40 *ps* using conditions in which the number of atoms (N), pressure (P), and temperature (T) were held constant (i.e., NPT conditions) at multiple temperatures and zero pressure in different runs. As shown in Figure 3-2, the pressure after equilibration was relaxed to 0 *atm* and the total energy was minimized to around  $-7 \times 10^5$  *kCal/mol* , indicating that the system has found its equilibrated state. After equilibration, the average density becomes 19.4 *g/cm*<sup>3</sup> and the temperature fluctuates around

873 K. The production phase consists of two runs. A 200 *ps* equilibration run was first conducted to determine the system properties such as density, viscosity and diffusion coefficient for the corresponding temperature. A trajectory run, which persists for 10 *ps*, writes the trajectories for each element in FLiBe to a text file for further analysis.

A snapshot of a sample of the system is shown in Figure 3-3. As can be seen, the  $\text{Be}^{2+}$  and  $\text{F}^-$  ions form a tetrahedral binding structure  $\text{BeF}_4^{2-}$ . The  $\text{Li}^+$  ions interact with the surrounding  $\text{BeF}_4^{2-}$  clusters. By analyzing atomistic motion from the animation of atom trajectories within short time frames ( $< 100$  fs), the Be atoms are observed to vibrate in the  $\text{BeF}_4^{2-}$  structure. Meanwhile, the  $\text{F}^-$  ions vibrate and collide with surrounding  $\text{BeF}_4^{2-}$  clusters. It is suggested in later analysis of the density of states (DOS) that the ionic liquid exhibits weak bonding in which the bonds can be broken easily in comparison to the bonds in molecular liquids. Therefore, the exchange of  $\text{F}^-$  ions between  $\text{BeF}_4^{2-}$  clusters associated with the breaking and reforming of  $\text{BeF}_4^{2-}$  clusters during collisions is highly possible.

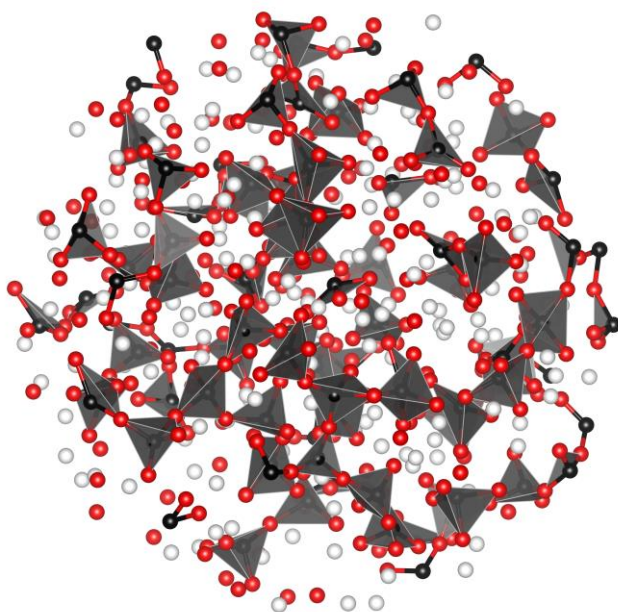


Figure 3-3. FLiBe MD system, with black as  $\text{Be}^{2+}$  ions, red as  $\text{F}^-$  ions, and white as  $\text{Li}^+$  ions. The  $\text{BeF}_4^{2-}$  clusters are showing as tetrahedral structure.

Because the melting/boiling point of FLiBe is 732/1703 K [115], coolant operating temperature of molten salt reactors is generally between 850 K and 1000 K [12,18,116,117]. In this work, five different temperatures ranging from 828 K to 1000 K are used for equilibration and physical property investigation in the molecular dynamics simulations. Three representative core temperatures, i.e., 873 K, 923 K, and 973 K, are used for scattering law and cross section demonstration purposes.

### 3.3 Correlation Functions in MD

To evaluate thermal transport coefficients, such as viscosity, diffusion coefficient, and thermal conductivity, from equilibrated system, the corresponding correlation function is used. The evaluation can be done by invoking either Green-Kubo formulas or Einstein relations. Both methods involve the calculation of correlation functions. To understand how the transport coefficients are computed, it is necessary to understand the mechanism of correlation functions.

Time correlation functions illustrate how a dynamic entity  $A(t)$  is related to some other entity  $B(t)$ . For example, the velocity autocorrelation function measures how the velocity of an atom at time  $t$  influences the velocity at a later time,  $t + \Delta t$ . The time correlation function  $C(t)$  of two time-independent entities  $A(t)$  and  $B(t)$  is defined as

$$C(t) = \lim_{\tau \rightarrow \infty} \frac{1}{\tau} \int_0^\tau A(t_0)B(t_0 + t)dt_0, \quad (3.3.1)$$

with the shorthand notation

$$C(t) = \langle A(t_0)B(t_0 + t) \rangle. \quad (3.3.2)$$

$C(t)$  measures the correlation between  $A(t)$  and  $B(t)$ . If  $A(t)$  and  $B(t)$  are unrelated,  $C(t)$  reduces to the product of two independent time average

$$C(t) = \langle A(t) \rangle \langle B(t) \rangle. \quad (3.3.3)$$

When  $A(t)$  and  $B(t)$  are different entities,  $C(t)$  is named the cross-correlation function. When  $A(t)$  and  $B(t)$  are the same entity,  $C(t)$  is named the auto-correlation function. In the example given in the above paragraph, the correlation function of velocity measures how the velocity of an atom relates with itself. Therefore, it is called the velocity autocorrelation function.

The use of the time-correlation function to evaluate transport coefficients involves another important theory, the Green-Kubo relation [118,119]. Consider  $A(t)$  and its time derivative  $\dot{A}(t)$ , the mean square of the dynamic quantity  $A(t)$  can be written as

$$\begin{aligned} msd &= \langle [A(t) - A(0)]^2 \rangle \\ &= \int_0^t dt'' \int_0^{t''} dt' \langle \dot{A}(t') \dot{A}(t'') \rangle = 2 \int_0^t dt'' \int_0^{t''} dt' \langle \dot{A}(t') \dot{A}(t'') \rangle \\ &= 2 \int_0^t dt'' \int_0^{t''} d\tau \langle \dot{A}(\tau) \dot{A}(0) \rangle = 2 \int_0^t d\tau \langle \dot{A}(\tau) \dot{A}(0) \rangle \int_\tau^t dt'', \text{ or} \\ &= 2t \int_0^t d\tau \langle \dot{A}(\tau) \dot{A}(0) \rangle (1 - \tau/t) \\ \frac{\langle [A(t) - A(0)]^2 \rangle}{2t} &= \int_0^t d\tau \langle \dot{A}(\tau) \dot{A}(0) \rangle (1 - \tau/t). \end{aligned}$$

In the long-time limit, it gives the Green-Kubo relation

$$\lim_{t \rightarrow \infty} \frac{\langle [A(t) - A(0)]^2 \rangle}{2t} = \int_0^\infty \langle \dot{A}(\tau) \dot{A}(0) \rangle d\tau. \quad (3.3.4)$$

This relation establishes the connection between the time integral of a correlation function and the corresponding long-time slope of the mean square of the dynamic property. The Green-Kubo relation is extremely useful if one needs to evaluate a transport coefficient that measures the proportionality on the change rate of a field. For example, the thermal conductivity measures proportionality of the heat flux to the change rate of the temperature

$$\mathbf{J} = -\kappa \nabla T.$$

With the Green-Kubo relation, the thermal conductivity is the average of the auto-correlation of the heat flux  $\mathbf{J}$

$$\kappa = \frac{V}{3k_B T^2} \int_0^\infty \langle \mathbf{J}(0) \cdot \mathbf{J}(t) \rangle dt. \quad (3.3.5)$$

The relation between the mean square of the dynamic property and the transport coefficient is named the generalized Einstein relation, i.e. the left hand side of Eq. (3.3.4):

$$K = \lim_{t \rightarrow \infty} \frac{\langle [A(t) - A(0)]^2 \rangle}{2t}. \quad (3.3.6)$$

This equation was obtained by Einstein from the fluctuation-dissipation theory. The same analog can be applied to viscosity, and diffusion coefficient. These relations are summarized in Table 3-3.

Table 3-3. Generalized Einstein and Green Kubo formulas for transport coefficients

$$K = \lim_{t \rightarrow \infty} \langle [A(t) - A(0)]^2 \rangle / 2t = \int_0^\infty \langle \dot{A}(\tau) \dot{A}(0) \rangle d\tau,$$

$K$	Einstein relation	Green Kubo relation
Self-diffusion coefficient $D$	$\frac{1}{N} \lim_{t \rightarrow \infty} \frac{1}{2t} \langle \sum_i [\mathbf{r}_i(t) - \mathbf{r}_i(0)]^2 \rangle$	$\frac{1}{3N} \int_0^\infty \langle \mathbf{v}(0) \cdot \mathbf{v}(t) \rangle dt$
Shear viscosity $\eta$	$\frac{1}{Vk_B T} \lim_{t \rightarrow \infty} \frac{1}{2t} \langle (\sum_i p_\mu^i(t) r_\nu^i(t) - p_\mu^i(0) r_\nu^i(0))^2 \rangle$	$\frac{1}{3Vk_B T} \int_0^\infty \langle S_{\mu\nu}(t) S_{\mu\nu}(0) \rangle dt$
Thermal conductivity $\kappa$	$\frac{1}{Vk_B T^2} \lim_{t \rightarrow \infty} \frac{1}{2t} \langle [\mathbf{Q}(t) - \mathbf{Q}(0)]^2 \rangle$	$\frac{1}{3Vk_B T^2} \int_0^\infty \langle \mathbf{J}(0) \cdot \mathbf{J}(t) \rangle dt$

where  $\mathbf{r}$ ,  $\mathbf{v}$  are the position and velocity vector,  $p_\mu^i$  is the momentum for the  $i^{th}$  atom at  $\mu^{th}$  direction,  $S_{\mu\nu}$  is the shear stress at the  $\mu\nu$  plane,  $\mu \neq \nu$  is required for the shear viscosity relation. The  $\mathbf{J}$  is the heat current,  $\mathbf{Q}$  is the integral of the heat current. The Green Kubo relation for diffusion coefficient is the integral of the velocity autocorrelation function, which is an indication

of the connection between the diffusion coefficient  $D$  and the setoff at the origin of VACF's spectrum – the density of states.

### **3.4 MD Predicted Properties of FLiBe**

Despite the fact that many experiments are conducted on Be-F-Li mixed molten salt with different mole fraction and fuel mixed FLiBe molten salt, limited data can be used to validate a proposed force field for pure  $\text{Li}_2\text{BeF}_4$  at different temperatures. Available data include density, viscosity and diffusion coefficient. They were chosen to benchmark both static and dynamic properties of the proposed pair potential (Born-Mayer parameters given in Table 3-1 and Table 3-2) of FLiBe. In all the available experiments, noticeable spread of measured properties is observed. In this work, the experimental data spreads are used to establish lower/upper limits for the properties that stem from the spread in the measurements. The experimental limits and simulated properties are compared to benchmark the MD model.

#### **3.4.1 Liquid Density**

One of the measured properties of FLiBe at different temperatures is its liquid density. As can be seen in Figure 1-8, in most of these reports, measured raw data points are not available; thus, the experimental data range was established by choosing the highest and lowest bound of the reported density curve. MD predicted densities are recorded as an average value for 5000 timesteps with  $dt = 1fs$  after equilibration, such as seen in Figure 3-2. The MD predicted density and the experimentally determined range are plotted in Figure 3-4. The calculated density of FLiBe (shown in Figure 3-4) is within the experimental range. It is noted that, in our simulations, the density is not sensitive to the dipole-dipole interaction term for all the ion types.

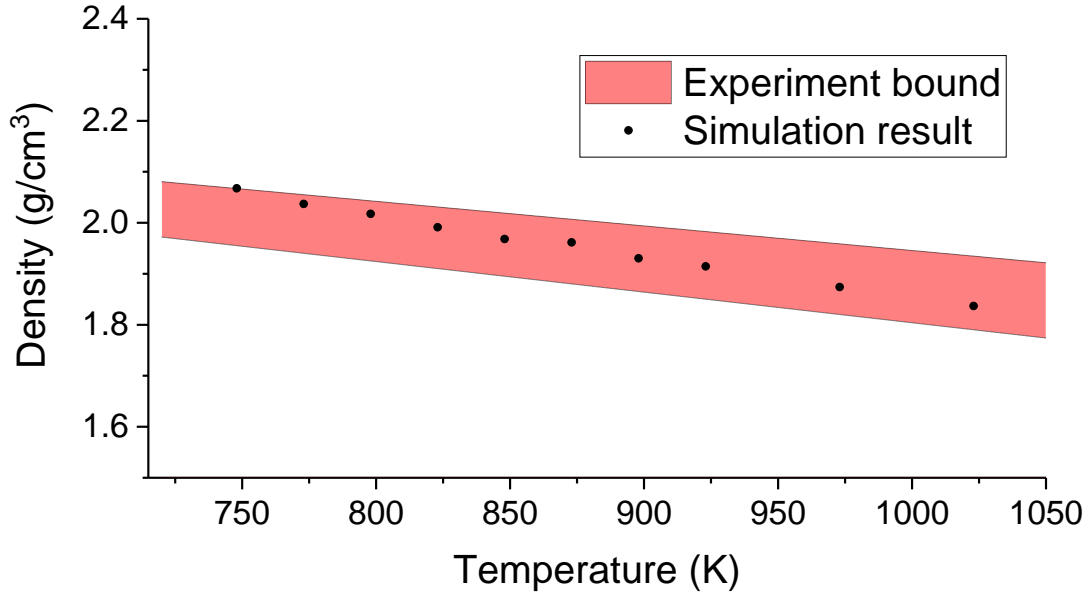


Figure 3-4. The MD calculated density of FLiBe in comparison to the experimental data range.

### 3.4.2 Liquid Viscosity

In Newton's law of viscosity,  $\eta$  is a coefficient describing the proportionality of the shear stress  $S_{xy}$  to the strain rate. Consequently, as shown in Table 3-3, viscosity can be calculated from the equilibrated system using Green-Kubo formalism

$$\eta = \frac{V}{3k_B T} \int_0^\infty \left\langle \sum_{x < y} S_{xy}(t) S_{xy}(0) \right\rangle dt, \quad (3.4.1)$$

where  $S_{xy}$  is the shear stress in  $xy$  direction,  $V$  is the volume of the ensemble,  $k_B$  is the Boltzmann constant times and  $T$  is the temperature. The summation in Eq. (3.4.1) is over  $xy$ ,  $xz$ , and  $yz$  direction. The shear stresses are system properties, which originate from the Born-Mayer potential, averaged over all the atoms in the ensemble. To examine the potential of FLiBe, the shear stress in the system is analyzed and used in Eq. (3.4.1) to calculate  $\eta$ . Molten salt viscosity is expected to follow Arrhenius behavior. The viscosity can be expressed as

$$\eta = A \exp\left(\frac{E_\eta}{RT}\right), \quad (3.4.2)$$



where  $E_\eta$  is the activation energy for viscous flow,  $R$  is the gas constant,  $A$  is a coefficient with unit of viscosity  $cP$ . Both  $A$  and  $E_\eta$  are independent of the temperature.

Because the measured raw viscosity data are not available in all the cited reports, the spread of experimentally predicted viscosity data is determined by using the lowest and the highest reported viscosity curves as bounds, such as shown in Figure 1-9. In Figure 3-5, the calculated viscosity  $\ln(\eta)$  shows the predicted linear behavior versus  $10^3/T$  and is within the experimental data range. It is found that the viscosity is affected by the softness factor  $\rho$  and the dipole-dipole interaction in the potential.

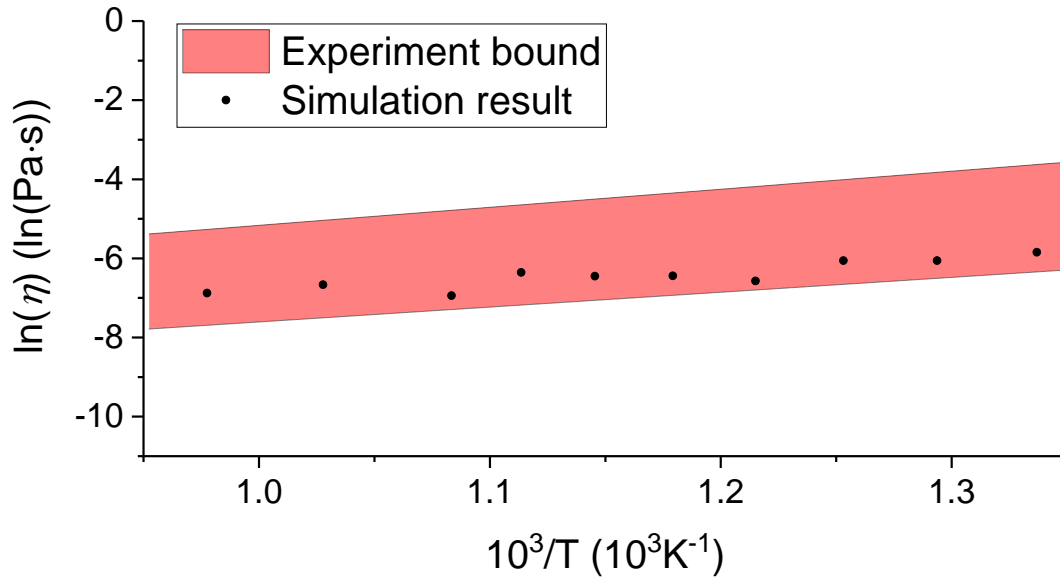


Figure 3-5. The MD calculated viscosity of FLiBe in comparison to the experimental data range.

The viscosity is closely related to the relaxation time in the liquid. Viscosity directly quantifies the friction mechanism in liquids. The time an atom spends to relax to the diffusional behavior is inversely proportional to the friction force inside the system. In other words, the stronger the friction force, the shorter time an atom will spend to relax to the diffusional behavior. This relation can be referred to Eq. (2.4.15). The famous Stokes-Einstein equation also points out this inverse proportionality between the viscosity and diffusion coefficient

$$D = \frac{k_B T}{Br} \cdot \frac{1}{\eta}, \quad (3.4.3)$$

where  $D$  is the diffusion coefficient,  $r$  is the radius of the moving particle,  $B$  is a material dependent numerical coefficient.

### 3.4.3 Diffusion Coefficient

A way to characterize the particle dynamics in a dense fluid is through the self-diffusion behavior. The corresponding 90% confidence interval for non-simultaneous experimental limits was calculated in this work from experiment data [120]. The measured experimental points as well as constructed experimental bounds are shown in Figure 3-6. An obvious difference in the change of diffusion coefficient as a function of temperature can be observed between Li and F in FLiBe. However, this phenomenon is not predicted from the Stokes Einstein relation (i.e. Eq. (3.4.3)). This indicates a possible bias in the experimental treatment of the cited diffusion coefficient experiments [42,55].

In a homogeneous liquid, the MSD exhibits the same linear behavior in all directions (i.e. the liquid self-diffusion coefficient is isotropic). The self-diffusion coefficient,  $D$ , can be obtained using the Einstein equation by estimating the slope of MSD

$$D = \frac{1}{6} \lim_{t \rightarrow \infty} \frac{d \langle (\mathbf{r}(t) - \mathbf{r}(0))^2 \rangle}{dt}, \quad (3.4.4)$$

where the MSD is averaged over all the atoms of the same type. In this work, the MD model was run for 20 *ps* using a time step of 10 *fs* and the self-diffusion coefficient was obtained by linear fitting of the MSD. As shown in Figure 3-6, the calculated diffusion coefficient fits well within the experimental data range.

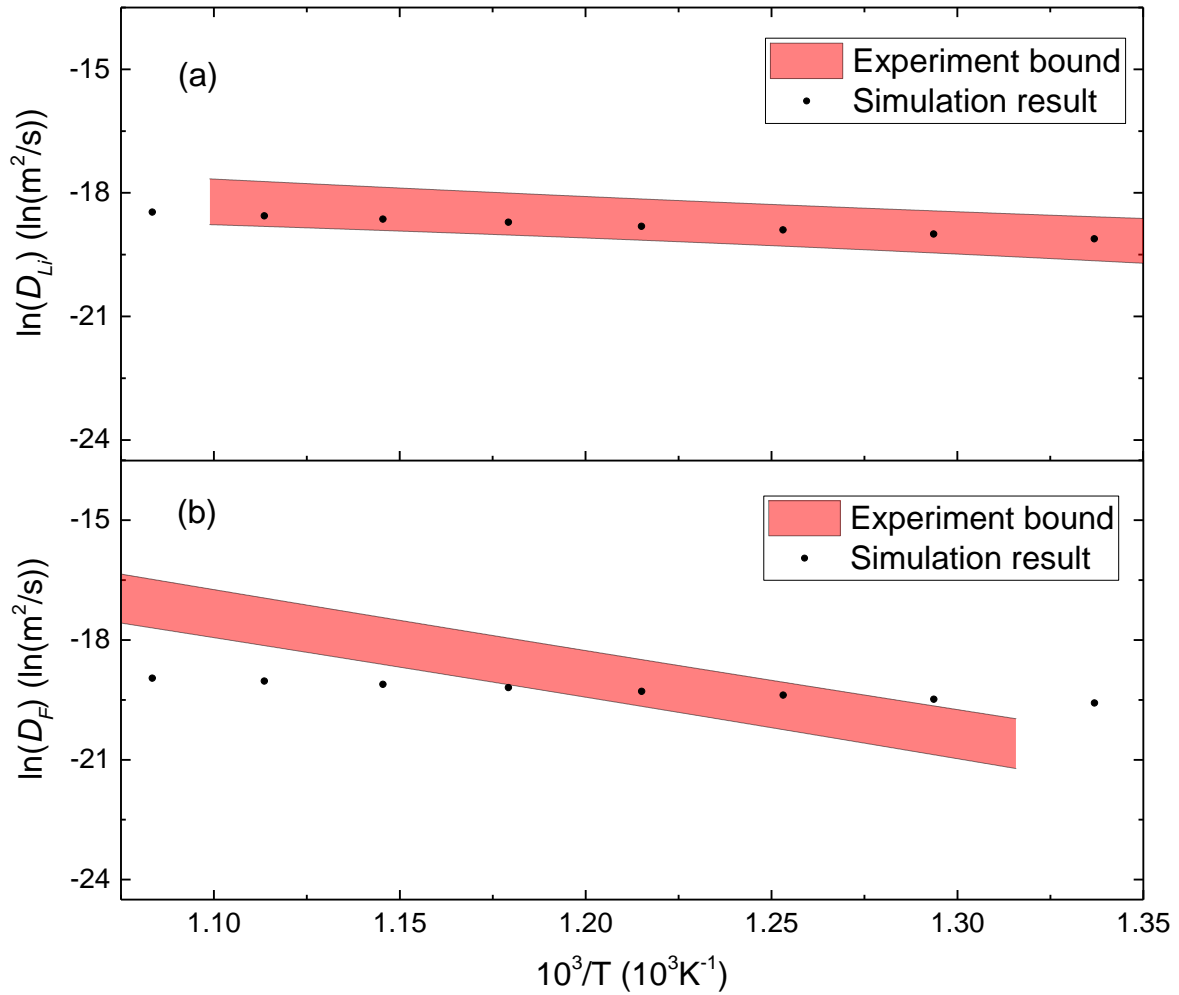


Figure 3-6. The Diffusion coefficient of Li (upper) and F (lower) in FLiBe in comparison to the experimental data range.

However, a divergence in the slope of the measured  $D_F$  and  $D_{Li}$  is also noticeable. In Ohmichi's measurement [42], he noted that the measured diffusion coefficient is too large compared to those of other molten salt systems. However, he did not give a valid explanation of the reason. In the conclusion of this paper, Ohmichi remarks, "Our results for fluorine diffusion are considerably difficult to explain by a simple model because of the unusual combination of a relatively large diffusion coefficient and a high activation energy." It is later found that the measured diffusion coefficient of F in FLiBe [42] is orders of magnitude larger than that of Li in FLiBe [55].

Despite these divergences of measured diffusion coefficient of F in FLiBe from experiments. It is also found that the F in FLiBe diffusion coefficient diverges severely from the Stokes-Einstein relation. As predicted by Eq. (3.4.3), the multiplication of diffusion coefficient and the viscosity should be proportional to the temperature in  $K$ :

$$D\eta = \frac{k_B T}{Br}. \quad (3.4.5)$$

This relation could be used to examine the experimental data from Iwamoto and Ohmichi [42,55]. In Eq. (3.4.5), the viscosity of FLiBe is taken directly from Cantor's experimental measurements [45]. Diffusion coefficients for Li [55] and F [42] in FLiBe are multiplied with the viscosity data. As shown in Figure 3-7,  $D\eta$  for Li in FLiBe is close to the linear relation predicted by Stokes-Einstein relation.

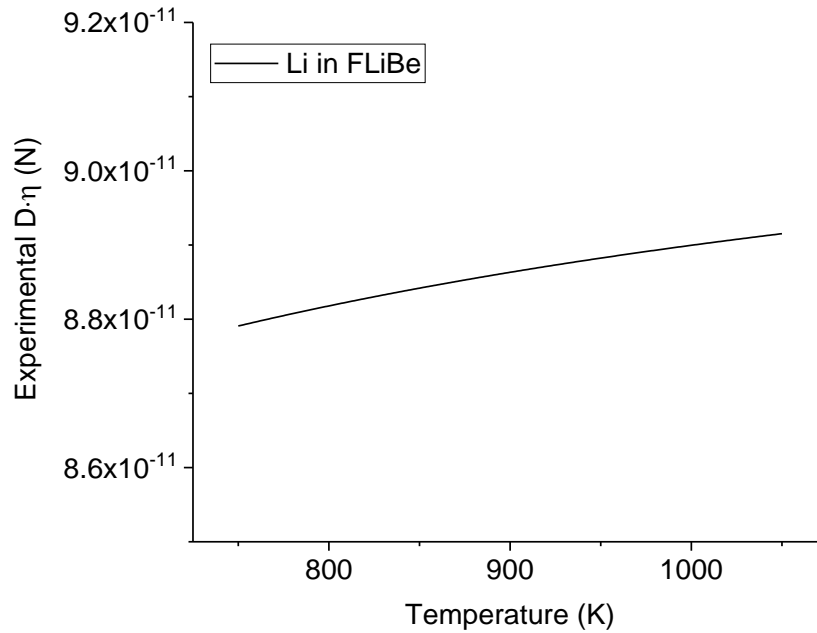


Figure 3-7. The multiplication of the diffusion coefficient and the viscosity for Li in FLiBe varies linearly with temperature, which is consistent with the Stokes-Einstein relation.

In comparison, Figure 3-8 shows  $D\eta$  for F in FLiBe. As can be seen, the multiplication increases exponentially with temperature and fails to follow the linear relation predicted by the

Stokes-Einstein relation. This is an obvious indication that the measured diffusion coefficient of F in FLiBe is inconsistent with the physics. A tremendously increasing rate of the diffusion coefficient of F in FLiBe might be contributed by some systematic deviations in Ohmichi's experiment [42]. In the simulated molten salt FLiBe fluid, the change rate of diffusion coefficient against increasing temperature of  $F^-$  is the same as that of  $Li^+$ . This suggests that the mechanisms of diffusion of  $F^-$  is the same as that for  $Li^+$ . This behavior is consistent with the Stokes-Einstein relation and the experimental measurement of the diffusion coefficient of Li in FLiBe [55].

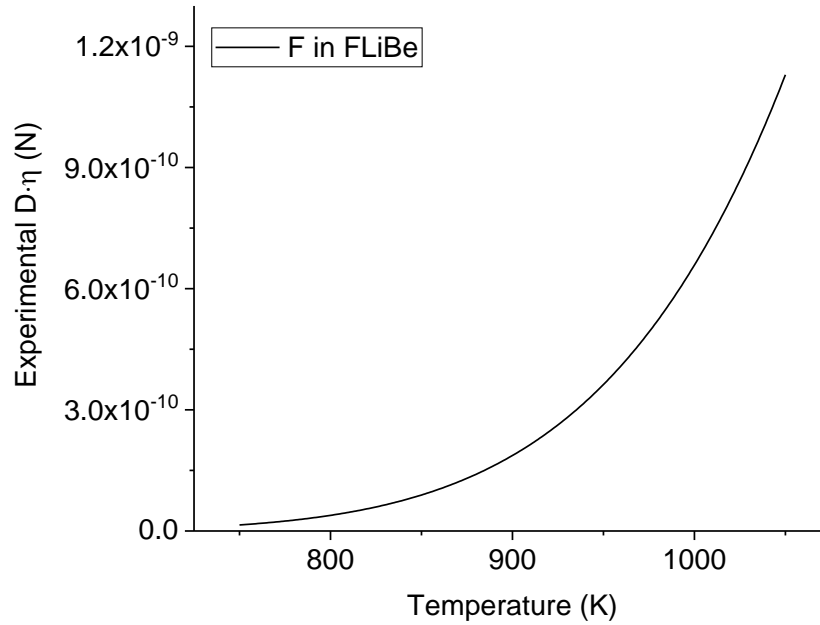


Figure 3-8. The multiplication of the diffusion coefficient and the viscosity for F in FLiBe varies exponentially with temperature, which is inconsistent with the Stokes-Einstein.

To conclude, the MD predicted diffusion coefficient of Li in FLiBe shows excellent agreement with the experimental measurement. However, the experimentally measured diffusion coefficient for F in FLiBe does not exhibit correct order of magnitude and fails to follow the prediction of liquid physics. We therefore judge that the diffusion coefficient experiment of F in FLiBe contains systematic errors. However, the evaluated diffusion coefficients of all three species from MD show behavior consistent with the Stokes-Einstein relation.

### 3.4.4 Heat Capacity

Currently, there are two heat capacity experiments on FLiBe [41,45]. The measured heat capacity is  $0.577 \text{ Cal/g} \cdot \text{K}$ . The heat capacity of a system is defined as the change rate of the enthalpy against temperature

$$C_p = \left( \frac{\partial H}{\partial T} \right)_{p,N} . \quad (3.4.6)$$

To evaluate the enthalpy, the FLiBe system was equilibrated under NPT (isothermal-isobaric) conditions for 20000 timesteps with 1 fs time interval intervals. Then the enthalpy of the system was calculated for another 20000 timesteps. The same procedure was repeated for different temperatures at NPT condition, such as shown in Figure 3-9.

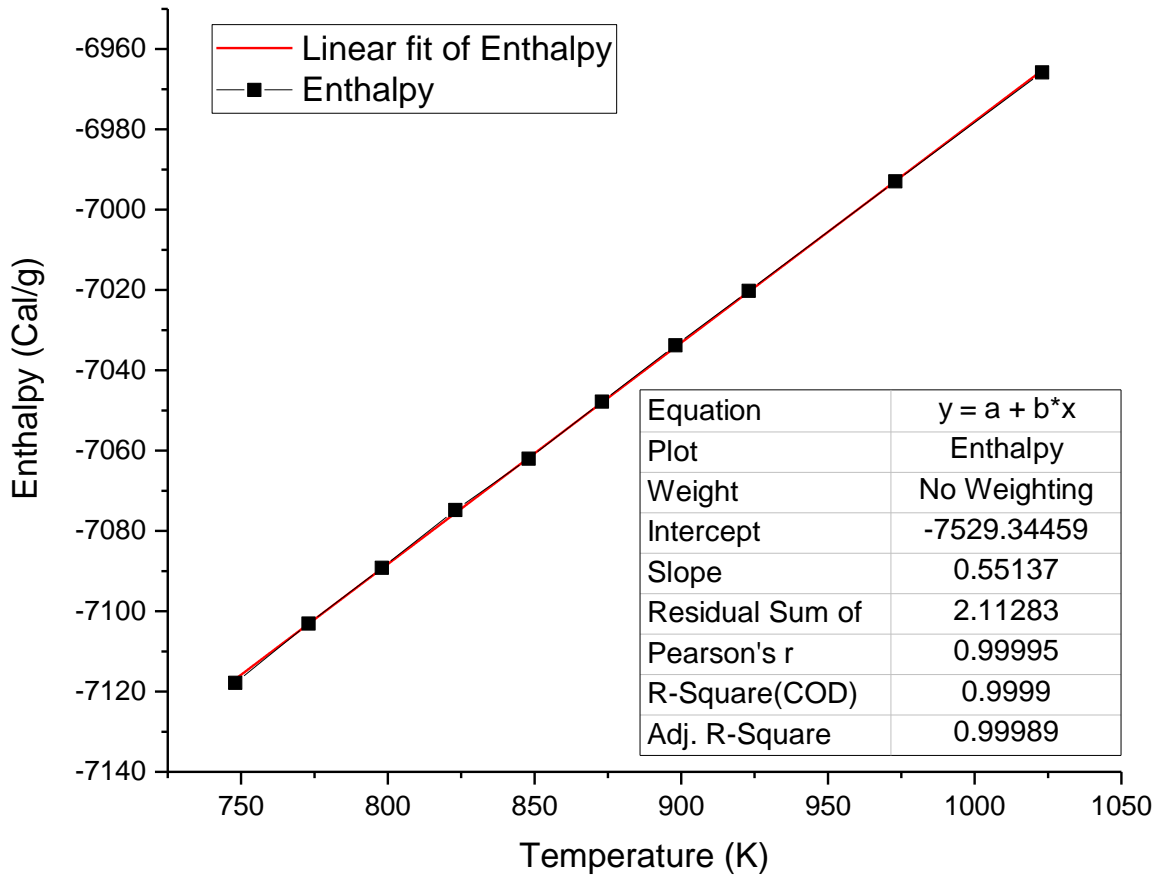


Figure 3-9. The enthalpy of molten salt liquid FLiBe from MD simulation. Red line fits the calculated enthalpy to evaluate the slope, which is the heat capacity.

A first order polynomial fit is applied to the calculated enthalpy data. As indicated by Eq. (3.4.6), the slope of the fit is the heat capacity  $C_p$ , which is evaluated to be  $0.551 \text{ Cal/g} \cdot K$ . This is in good agreement with the experimental measured heat capacity  $0.577 \pm 0.008 \text{ Cal/g} \cdot K$ .

To conclude, the heat capacity calculated from MD ( $0.551 \text{ Cal/g} \cdot K$ ) is in good agreement with the experimental measurement ( $0.577 \pm 0.008 \text{ Cal/g} \cdot K$ ). This heat capacity is relatively large compared to other molten salts (shown in Table 1-1), which makes it a good coolant candidate.

### 3.4.5 Thermal Conductivity

The thermal conductivity is another important thermodynamic property of FLiBe. As indicated by Table 3-3 and Eq. (3.3.5), the thermal conductivity can be evaluated by the Green Kubo relation. In this work, the equilibrium MD model was executed for 20000 timesteps with  $1 \text{ fs}$  interval. The autocorrelation function of the heat flux was evaluated and transformed to thermal conductivity. The evaluated thermal conductivity is around  $1.8 \text{ W/m} \cdot K$ . On the experimental side, however, there is merely one set of measured data by Cooke and Hoffman [41,53]. As discussed in Chapter 1, this data is not reliable because of the method used to measure the thermal conductivity. Therefore, the experimentally measured thermal conductivity should be used as a reference value with caution. With this observation noted, the experimentally measured value is  $1.1 \text{ W/m} \cdot K$ . This is still within 40% of the value calculated from this MD work.

### 3.4.6 Velocity Autocorrelation Function

The velocity autocorrelation function (VACF) is a good probe of microscopic motion of ions in FLiBe. VACF is a measurement of the dynamic motion of atoms in the time domain

$$C(t) = \langle \mathbf{v}(t) \cdot \mathbf{v}(0) \rangle / \langle \mathbf{v}(0) \cdot \mathbf{v}(0) \rangle, \quad (3.4.7)$$

where  $\mathbf{v}(t)$  is the velocity of an atom in the ensemble. In this work, the VACF for a particular group of atoms in the ensemble is averaged over all the atoms in the same group. The VACF of each component of FLiBe is evaluated for 10 ps and is shown in Figure 3-10.

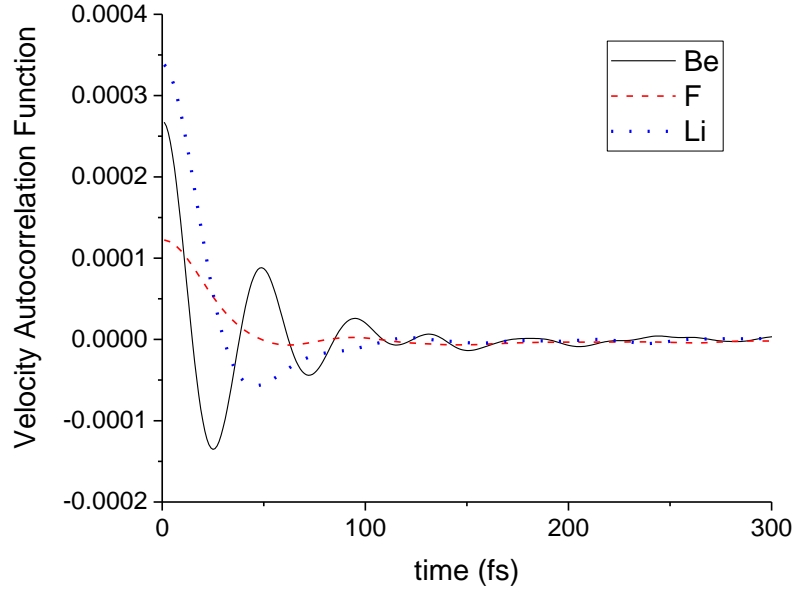


Figure 3-10. Velocity autocorrelation function of each component in FLiBe.

Figure 3-10 presents the VACF for the first 300 *fs* of the simulation after which the correlation weakens and converges to approximately 0.  $\text{Be}^{2+}$  shows a relatively long correlation time up to 150 *fs*, which is attributed to the tetrahedral  $\text{BeF}_4^{2-}$  structure formation in the system.  $\text{F}^-$  is weakly correlated to its previous motion compared to  $\text{Be}^{2+}$  and  $\text{Li}^+$ . This is due to the bond formation and bond breaking between different  $\text{Be}^{2+}$ ,  $\text{Li}^+$  with  $\text{F}^-$ . The frequent exchange of atomic bonds makes the motions steps of  $\text{F}^-$  loosely correlated.

### 3.5 Evaluation of the Dynamic Structure Factor from MD

In Section 2.1, we introduced the van Hove space-time correlation function, the intermediate scattering function and the dynamic structure factor. They are Fourier transforms of each other in



time-frequency and real-reciprocal space. It is useful to summarize these relations again in this section:

$$\begin{aligned} I(\mathbf{k}, t) &= \int e^{i\mathbf{k} \cdot \mathbf{r}} G(\mathbf{r}, t) d\mathbf{r} \\ S(\mathbf{k}, \omega) &= \frac{1}{2\pi\hbar} \int e^{-i\omega t} I(\mathbf{k}, t) dt \end{aligned} \quad (3.5.1)$$

In Section 2.5, the classical approximation was introduced. The classical interpretation enables direct evaluation of  $G^{cl}(\mathbf{r}, t)$ ,  $I^{cl}(\mathbf{k}, t)$  and  $S^{cl}(\mathbf{k}, \omega)$  from MD trajectories. The quantum correction in Section 2.5.2 operates on the classical width function of  $I_s^{cl}(\mathbf{k}, t)$ , which is also evaluated from MD trajectories. The MD trajectories, therefore, can be used to evaluate both the classical and quantum dynamic structure factor. In this section, the methodology of evaluating the  $S^{cl}(\mathbf{k}, \omega)$  from MD trajectories will be shown.

From the MD trajectories, there are two correlation functions that can be directly evaluated from particle trajectories, i.e.  $G^{cl}(\mathbf{r}, t)$  and  $I^{cl}(\mathbf{k}, t)$

$$G^{cl}(\mathbf{r}, t) = \frac{1}{N} \sum_{jj'} \int \left\langle \delta[\mathbf{r}' - \mathbf{R}_{j'}(0)] \delta[\mathbf{r}' + \mathbf{r} - \mathbf{R}_j(t)] \right\rangle d\mathbf{r}' \quad (3.5.2)$$

$$I^{cl}(\mathbf{k}, t) = \frac{1}{N} \sum_{jj'} \left\langle e^{-i\mathbf{k} \cdot \mathbf{R}_{j'}(0)} \cdot e^{i\mathbf{k} \cdot \mathbf{R}_j(t)} \right\rangle \quad (3.5.3)$$

The calculation of  $G^{cl}(\mathbf{r}, t)$  from particle trajectories is a binning process. The  $G^{cl}(\mathbf{r}, t)$  function is a continuous four-dimension function with three space dimensions and a time dimension. In MD simulation, the  $G^{cl}(\mathbf{r}, t)$  function is recorded as particle trajectories, which are the collections of atom positions evolving with time. In other words, the MD trajectories are the discrete version of the  $G^{cl}(\mathbf{r}, t)$  function. The calculation of  $G^{cl}(\mathbf{r}, t)$  is straight forward by binning the distance between atoms  $j$  and  $j'$  with time lag  $t$  from the MD trajectories.

The calculation of  $I^{cl}(k, t)$  from particle trajectories is the process of combining the cross-correlation with the Fourier transform. The evaluation can either happen by: 1) Doing cross-correlation in the three dimensional  $\mathbf{r}$  space and consolidating to the one dimensional  $r$  space to evaluate the  $G^{cl}(r, t)$ . And then Fourier transform to  $I^{cl}(k, t)$ , as shown in Eq. (3.5.2). 2) Or first Fourier transform  $\mathbf{R}_j(t)$  to  $e^{i\mathbf{k}\cdot\mathbf{R}_j(t)}$ , evaluate the cross-correlation function subsequently, and consolidate the information from three dimensional  $\mathbf{k}$  space to one dimensional  $k$  space as the last step, such as shown in Eq. (3.5.3). The first approach is inaccurate because the information in  $G^{cl}(r, t)$  function is compressed. As a result, a Fourier transform from  $G^{cl}(r, t)$  to  $I^{cl}(k, t)$  would introduce significant noises. The method using cross correlation and consolidation of  $e^{i\mathbf{k}\cdot\mathbf{R}_j(t)}$  afterward is preferred because all the information in a raw trajectory file can be utilized before the compression took place.

To calculate  $I^{cl}(k, t)$  in the reciprocal space, three general steps could be followed. The procedure is demonstrated in Figure 3-11.

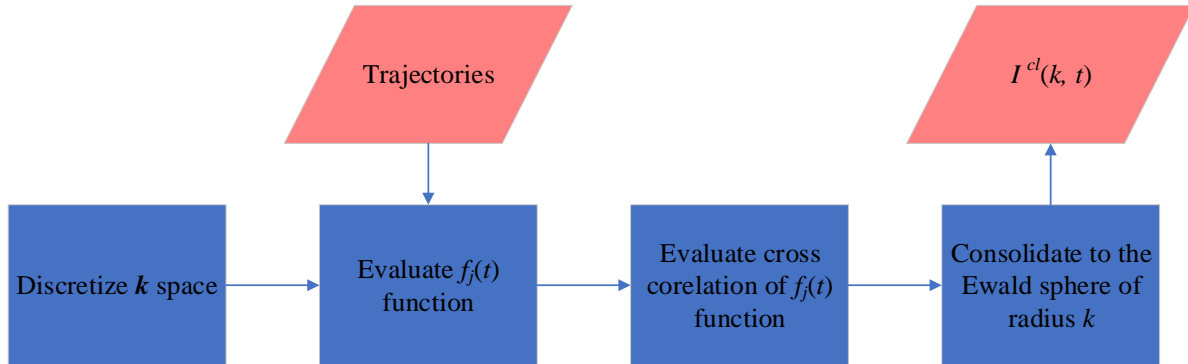


Figure 3-11. The procedure of  $I^{cl}(k, t)$  evaluation

First, a grid of available reciprocal space points  $\mathbf{k}$  should be built. Second,  $I^{cl}(k, t)$  on each reciprocal space point  $\mathbf{k}$  for all the time  $t$  would be calculated. Third, three-dimensional reciprocal space points  $\mathbf{k}$  could be consolidated to the Ewald sphere with radius  $k$ . In the second step, the

calculation of  $I^{cl}(\mathbf{k}, t)$  applies Eq. (3.5.3). Evaluation of the two time dependent exponential functions are based on the MD trajectory  $\mathbf{R}_j(t)$

$$\begin{aligned} f_{j'}(t) &= e^{-i\mathbf{k} \cdot \mathbf{R}_{j'}(t)} \\ f_j(t) &= e^{i\mathbf{k} \cdot \mathbf{R}_j(t)} \end{aligned} \quad (3.5.4)$$

The  $I^{cl}(\mathbf{k}, t)$  function is the average of the above two functions' cross-correlation function over all the atoms. The  $I_s^{cl}(\mathbf{k}, t)$  function is the average of the auto-correlation function of  $f_j(t)$  over all the atoms. Corresponding  $S^{cl}(k, \omega)$  function can be evaluated from the Fourier transform of the  $I^{cl}(k, t)$  function. In terms of the evaluation of the quantum correction proposed in Eq. (2.5.3)-(2.5.6), the MSD, i.e.  $\delta r^2(t')$  in Eq. (2.5.3), also needs to be evaluated from MD trajectories. In this situation, a few thousand samples of MD  $\delta r^2(t')$  will be evaluated and averaged to minimize statistical uncertainty.

In conclusion,  $G^{cl}(r, t)$  is calculated from binning the trajectories into discrete  $r$  bins.  $I^{cl}(k, t)$  is evaluated by cross-correlation of the  $f_j(t)$  function. The quantum correction utilizes the averaged MSD  $\delta r^2(t')$ .  $S(k, \omega)$  can be evaluated from the Fourier transform of  $I(k, t)$ . All these evaluations could use MD trajectory data as basic input. Examples of these evaluations will be demonstrated with liquid lithium in the next chapter. The evaluated results will be further compared to experimental measurements of liquid lithium to examine the proposed methods.

## Chapter 4 The Quantum Correction of Classical Thermal Scattering Law

In this chapter, a molecular dynamics (MD) model of liquid lithium that was built using a validated pair potential will be described. This model is used to test the thermal scattering law  $S(\alpha, \beta)$  evaluation and the quantum correction methodology. The pair potential and the MD model for liquid lithium is discussed. Following a valid MD model, the procedure of calculating the classical scattering law,  $S^{cl}(\alpha, \beta)$ , is illustrated. The Gaussian approximation, which serves as a basic framework for implementing the quantum correction, is validated. To prove the necessity of quantum correction, the deviation of  $S^{cl}(\alpha, \beta)$  from the quantum physics is additionally discussed. Thereafter, the quantum correction on the self thermal scattering law,  $S_s(\alpha, \beta)$ , of liquid lithium is implemented. Moments of the thermal scattering law as well as the principle of detailed balance are examined on the quantum corrected self thermal scattering law. To include the distinct effects, quantum correction on the distinct thermal scattering law of liquid lithium is discussed. After the total thermal scattering law is prepared, the cross section of liquid lithium is evaluated.

Liquid lithium was chosen as the demonstration material for four reasons. 1) Lithium is one of the three species in FLiBe. 2) Liquid lithium and FLiBe are both ionic liquids, and mastering the mechanisms of liquid lithium will improve the understanding of FLiBe. 3) The bound scattering cross section of lithium is a mixture of coherent and incoherent bound cross sections. Therefore, both the  $S_s(\alpha, \beta)$  and the  $S_d(\alpha, \beta)$  can be studied through this material. 4) Also, neutron scattering experimental measurements [121] of liquid lithium  $S(\alpha, \beta)$  have been published.

## 4.1 The MD Model of Liquid Lithium

The most important component for a valid MD model of liquid lithium is a valid pair potential. Liquid lithium has long been a focus in pair potential development [122-134]. In early works, studies applied a methodology that transformed the Ashcroft pseudopotential to an effective pair potential [122,123,126-129]. In recent publications, a more advanced neutral pseudopotential (NPA) method [130-134] was applied to evaluate the liquid lithium pair potential. The NPA potential is shown in Figure 4-1.

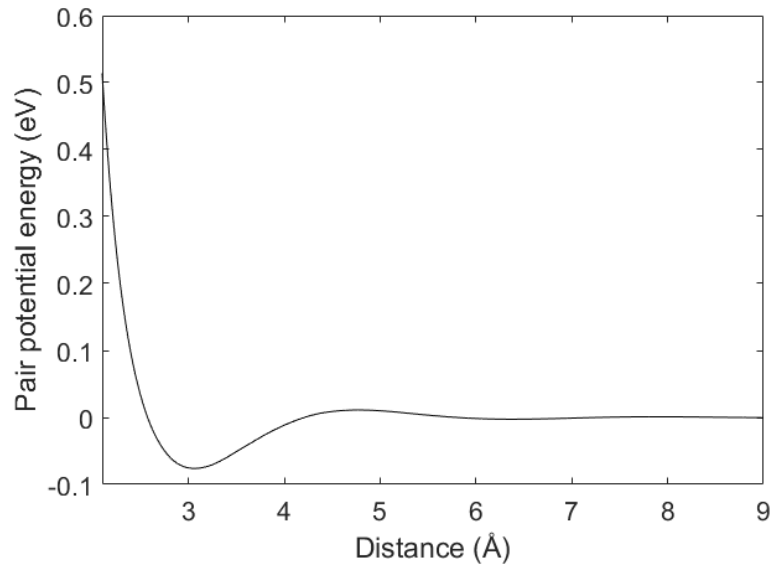


Figure 4-1. The NPA pair potential for liquid lithium.

In this work, the NPA pair potential was adapted to build the liquid lithium MD model. The NPA potential has been proven to be one of the most accurate pair potentials for liquid lithium [132,133,135]. This potential has also been extensively validated in a series of simulations conducted by Gonzalez, et al. comparing against structural and thermodynamic properties for liquid lithium [132,133].

The liquid lithium MD model was built with 1000 atoms in an equally spaced lattice structure. The ensemble was melted at 484 K for  $6 \times 10^4$  fs. Equilibration was achieved using the NPT

(constant number of particles, constant pressure, constant temperature) thermostat in LAMMPS, which is shown in Figure 4-2. After equilibration, the NPT thermostat was changed to the NVE (constant number of particles, constant volume, constant energy) thermostat and equilibrated further for  $1.64 \times 10^5 fs$  at 484 K. The equilibrated model was used to generate trajectories for the 1000 particles, which are subsequently used in the analysis of MSD,  $I(k, t)$ ,  $S(k, \omega)$ , etc.

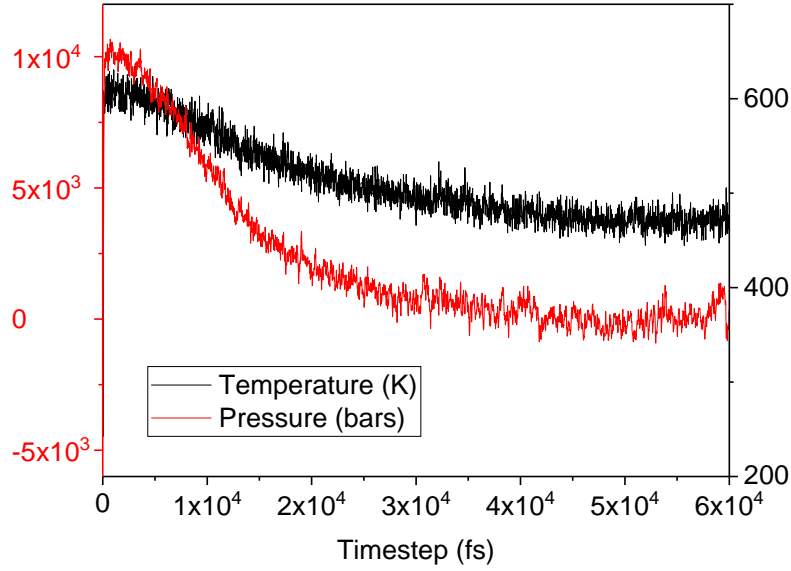


Figure 4-2. The NPT thermal equilibration of liquid lithium MD model.

## 4.2 The Classical Thermal Scattering Law and Experimental Measurements

The classical intermediate scattering function  $I^{cl}(k, t)$  of liquid lithium was evaluated using Eq. (3.5.3). As discussed previously in Section 3.5, this procedure basically applies the Fourier transformation, evaluates the cross-correlation function subsequently, and consolidates the information from three dimensional  $\mathbf{k}$  space to one dimensional  $k$  space.

In the simulation, trajectories of equilibrated liquid lithium were obtained for  $6.55 \times 10^5 fs$ , with a time step of 1 fs. The intermediate scattering functions were evaluated utilizing Eq. (3.5.3) and Eq. (3.5.4). Because of the large volume of trajectory data, a parallel FORTRAN code was

written using Message Passing Interface (MPI) to distribute the calculation to different processors. The Fast Fourier Transform (FFT) and the correlation and convolution algorithm were implemented using the intel MKL library. The evaluated  $I^{cl}(k, t)$  and  $I_s^{cl}(k, t)$  are shown in Figure 4-3 and Figure 4-4 respectively.

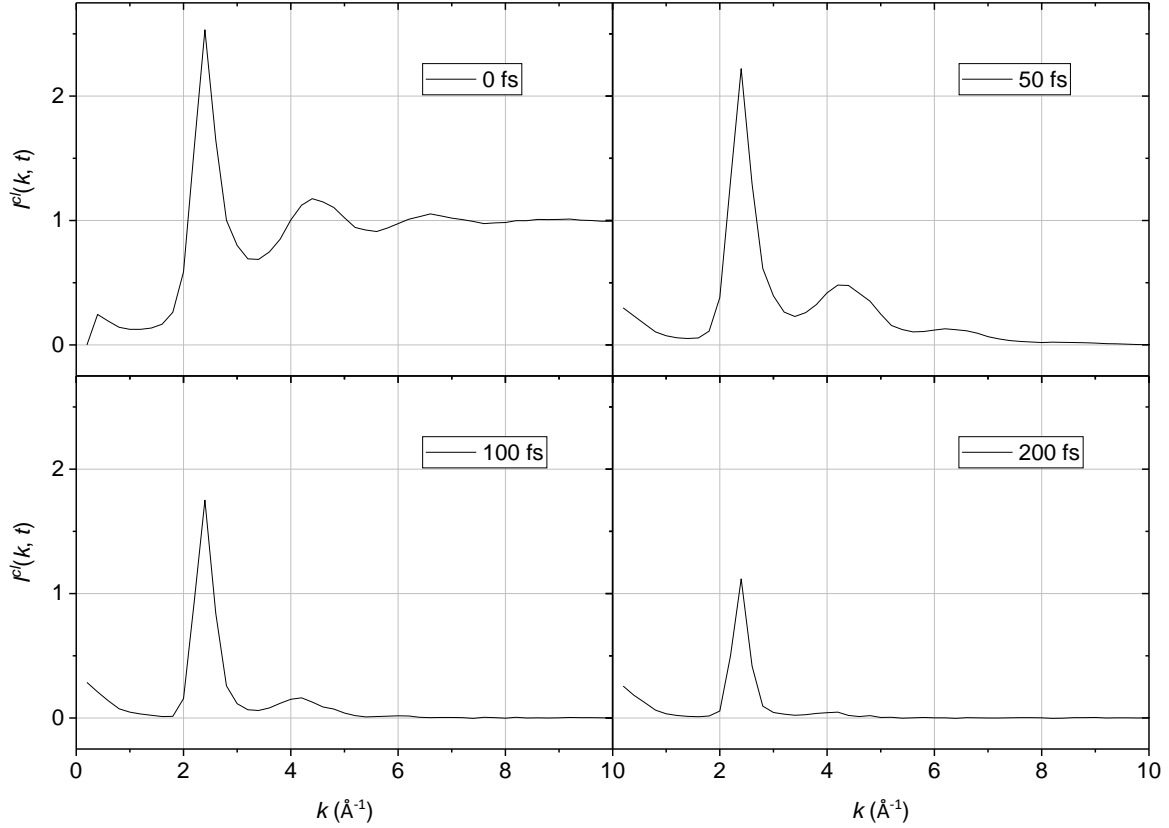


Figure 4-3.  $I^{cl}(k, t)$  of liquid lithium at different time, i.e.  $t = 0, 50, 100, 200$  fs.

$I^{cl}(k, t)$  represents two kinds of properties: the structural property that describes how the atoms are collectively binding to each other in  $k$  space and the dynamical property that describes excitation states of the atom's motion in  $\omega$  space. As shown in Figure 4-3, the structural peaks are observed at  $2.5 \text{ \AA}^{-1}$ ,  $4.4 \text{ \AA}^{-1}$  and  $6.5 \text{ \AA}^{-1}$ . These peaks correspond to the most dominant neighboring atom shells around a lithium atom in the real space. As we can see later, this structural information will be carried over to the dynamic structural factor  $S(k, \omega)$ . As  $I^{cl}(k, t)$  evolves with

time, distinct effects decay to zero. Consequently, at the long time limit, the distinct  $I^{cl}(k, t)$  essentially asymptotes to the self  $I_s^{cl}(k, t)$ .

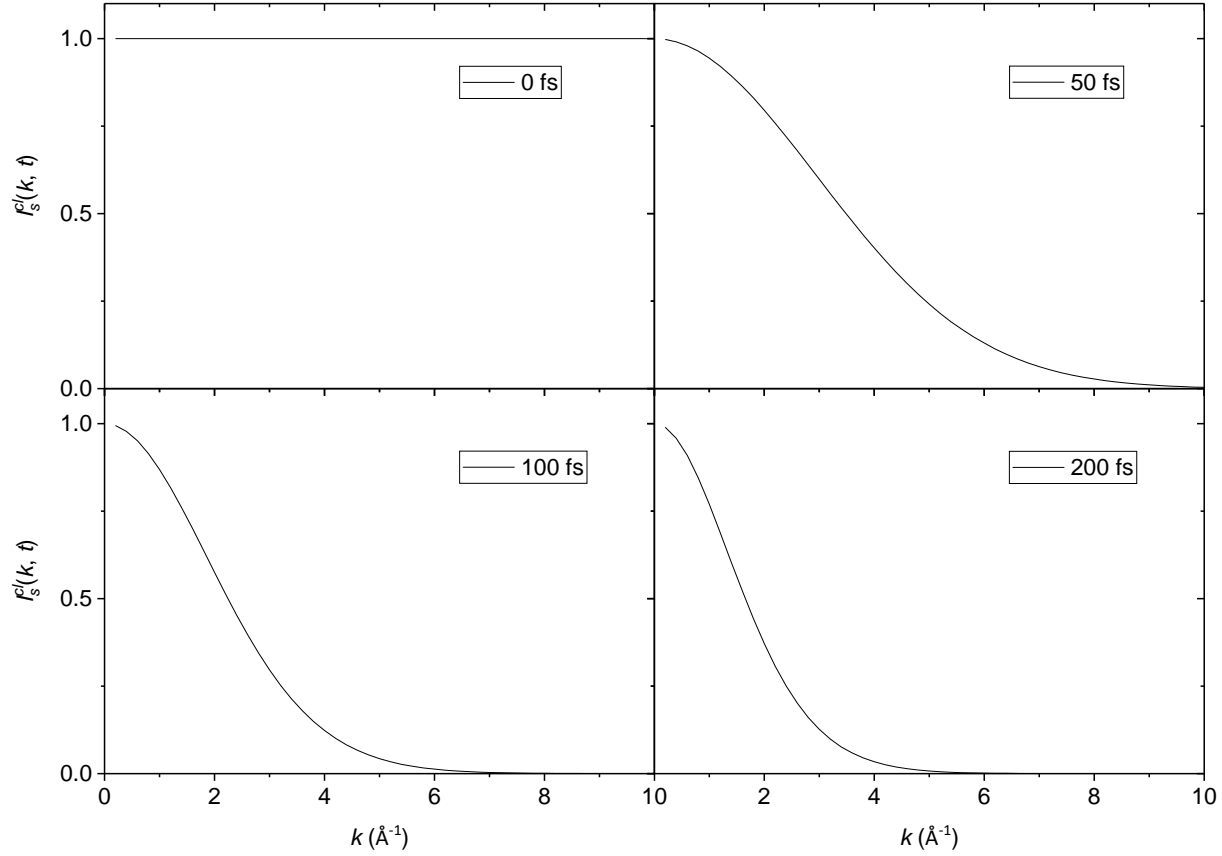


Figure 4-4.  $I_s^{cl}(k, t)$  of liquid lithium at different time  $t = 0, 50, 100, 200$  fs.

The self intermediate scattering function  $I_s^{cl}(k, t)$  consists of an auto-correlation function that measures the extent of correlation of the atom with itself at time differences  $t = \Delta t$ . As shown in Figure 4-4, the correlation of the atom with itself is a constant unity at  $t = 0$ . In other words, the atom is fully correlated with itself throughout the whole reciprocal space when the correlation time  $\Delta t = 0$ . When  $\Delta t$  becomes larger, the correlation of the atom with itself drops rapidly with increasing  $k$ . As the correlation time becomes larger, the atom “forgets” its original position when moving.



The classical dynamic structure factor  $S^{cl}(k, \omega)$  was evaluated from the Fourier transform of the classical intermediate scattering function  $I^{cl}(k, t)$ . The corresponding  $S^{cl}(k, \omega)$  and self  $S_s^{cl}(k, \omega)$  are shown in Figure 4-5.

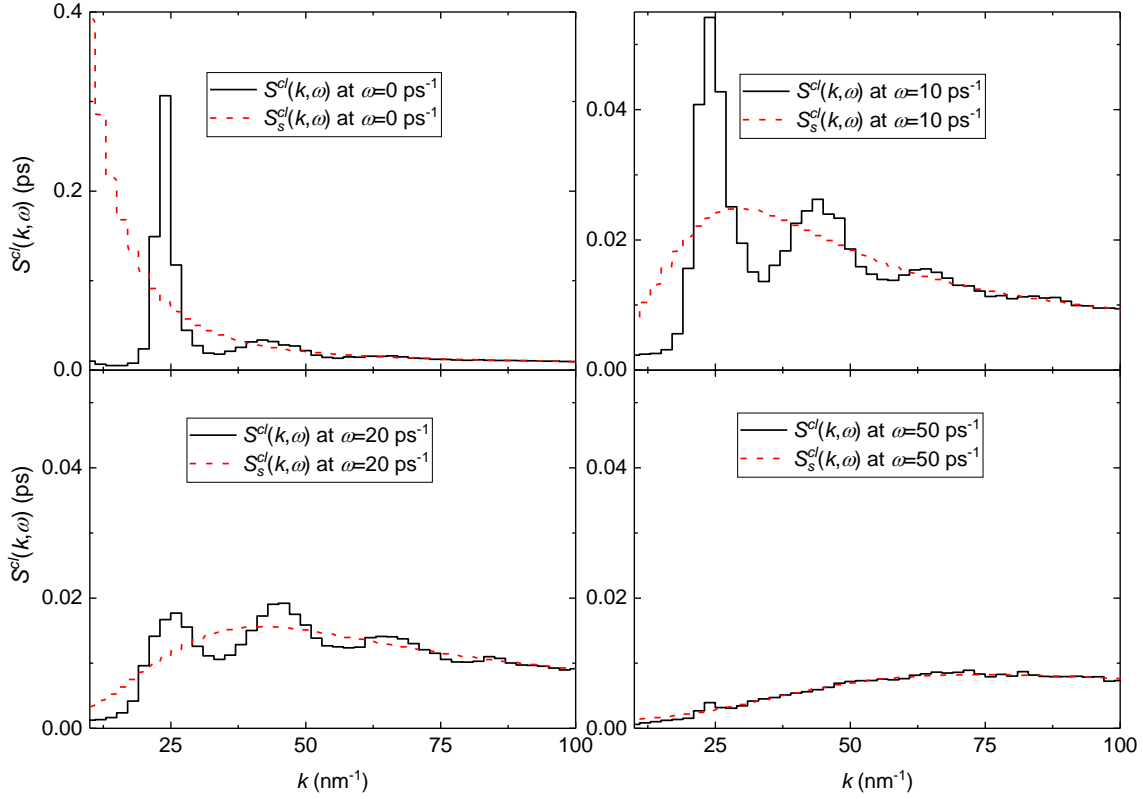


Figure 4-5.  $S^{cl}(k, \omega)$  and  $S_s^{cl}(k, \omega)$  of liquid lithium at frequency  $\omega = 0, 10, 20, 50 \text{ ps}^{-1}$ .

In Figure 4-5, it is shown that  $S^{cl}(k, \omega)$  asymptotes to  $S_s^{cl}(k, \omega)$  at large  $\omega$ . This behavior implies that the structural contribution from  $S^{cl}(k, \omega)$  is only dominant for small energies. Another feature in  $S^{cl}(k, \omega)$  is the positions of structural peaks which are inherited from  $I^{cl}(k, t)$ . The peaks at  $25 \text{ nm}^{-1}$ ,  $44 \text{ nm}^{-1}$  and  $65 \text{ nm}^{-1}$  are located at the same position as in  $I^{cl}(k, t)$ . These peaks are the manifestation of shell-like structures in liquids.

The total thermal scattering law can be evaluated from Eq. (2.1.27). The total thermal scattering law is a weighted sum of  $S_d^{cl}(k, \omega)$  and  $S_s^{cl}(k, \omega)$  using  $\sigma_{coh} = 0.619 b$  and  $\sigma_{inc} = 0.78 b$ . As a comparison to experiments [121], the behavior of  $\omega \cdot S_{tot}^{cl}(k, \omega)$  at different  $k$  against

$\omega$  is examined and plotted in Figure 4-6. As can be seen, the  $\omega \cdot S_{tot}^{cl}(k, \omega)$  also shows good agreement with experimental measurements.

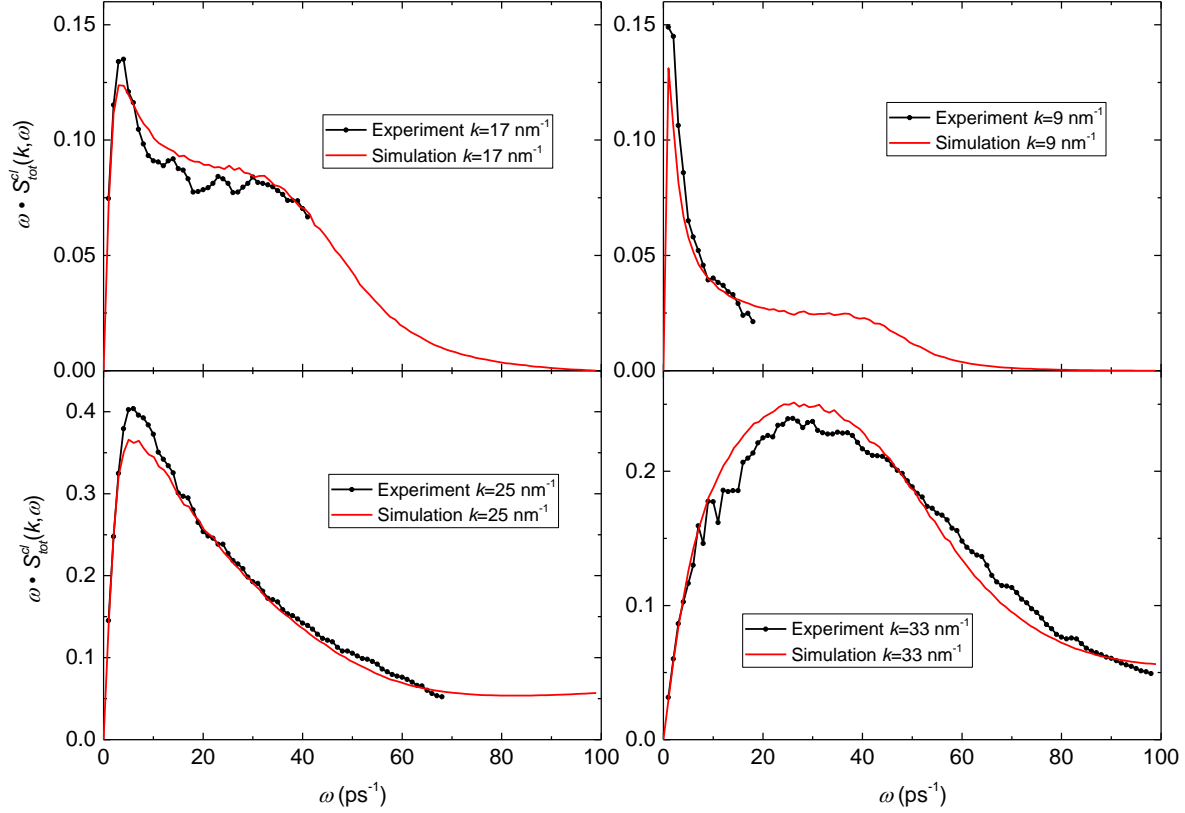


Figure 4-6. The  $\omega \cdot S_{tot}^{cl}(k, \omega)$  of liquid lithium at different  $k$  compared to experiments [121].

The experiments conducted by De Jong [121] used a sample furnace to keep the sample melted at a specific temperature. A pulsed monochromatic neutron beam was produced from a 2 MW reactor using a rotating crystal. The secondary energies were measured by time-of-flight spectrometry. The useful detector range due to shielding was limited to  $\varphi < 63.8^\circ$ . The measured experimental double differential cross sections were provided at four angles:  $9.3^\circ$ ,  $28.7^\circ$ ,  $48.4^\circ$  and  $63.8^\circ$ .

To conclude,  $I^{cl}(k, t)$  of liquid lithium was evaluated from an equilibrated MD model's trajectory data. Corresponding  $S^{cl}(k, \omega)$  was subsequently evaluated using the Fourier

transformation. The  $S_{tot}^{cl}(k, \omega)$ , which is a weighted sum by the bound cross section of  $Li^7$ , was evaluated and showed good agreements to the experimental measurements.

### 4.3 Validation of the Gaussian Approximation

The Gaussian approximation, which is assumed in the quantum correction methodology and the DOS methodology, was discussed in Section 2.2. For free gases,  $I_s(k, t)$  and  $S_s(k, \omega)$  are known to have a Gaussian shape (i.e. Eq. (2.2.2)). For solid materials, Sjolander [79] proposed the Gaussian approximation. In this section, the Gaussian approximation for liquid materials will be examined using liquid lithium as an example material.

Following a brief review of the Gaussian approximation, the validation method will be proposed below. According to Section 2.2, the Gaussian approximation assumes that  $I_s^{cl}(k, t)$  is a Gaussian function of  $k$ :

$$I_s^{cl}(k, t) = e^{-\frac{1}{2}k^2 w(t)} = e^{-\frac{1}{6}k^2 \delta r^2(t)}, \quad (4.3.1)$$

where the  $w(t)$  function is called the width function, and  $\delta r^2(t)$  is the MSD. By this relation, the Gaussian approximation states that the shape of the  $I_s^{cl}(k, t)$  function is a Gaussian in  $k$ . The half width at half maximum (HWHM) of  $I_s^{cl}(k, t)$  is proportional to the MSD at  $t$ . The HWHM of  $I_s^{cl}(k, t)$  is also a function that depends on  $t$ ,

$$w(t) = \frac{1}{3} \delta r^2(t). \quad (4.3.2)$$

The procedure of validating the Gaussian approximation is illustrated in Figure 4-7. The first step is to evaluate  $I_s^{cl}(k, t)$  from MD trajectories at different  $t$ . The second step involves evaluating the half width at half maximum of the calculated  $I_s^{cl}(k, t)$  using Eq. (4.3.1) to obtain a fitted width function  $w(t)$ . The last step is to compare the width function  $w(t)$  with  $\delta r^2(t)/3$  to test if they

follow the relation shown in Eq. (4.3.2). If the above check is satisfied, it could be concluded that the Gaussian approximation is valid for liquid materials.

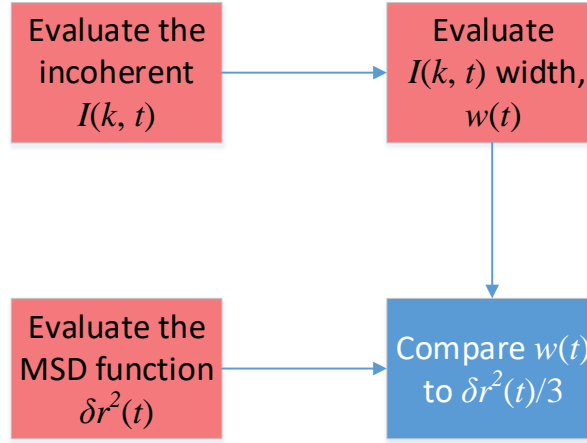


Figure 4-7. Procedure of validating the Gaussian approximation.

Figure 4-8 shows the comparison of  $\delta r^2(t)/3$  and the  $w(t)$  function. As can be seen, they are in good agreement at both the long time diffusive and the short time gaseous-like behavior. Therefore, the Gaussian approximation is valid for liquid materials.  $S_s(k, \omega)$ , which is a Fourier transform of  $I_s(k, t)$ , would remain a Gaussian function of  $k$  after Fourier transformation.

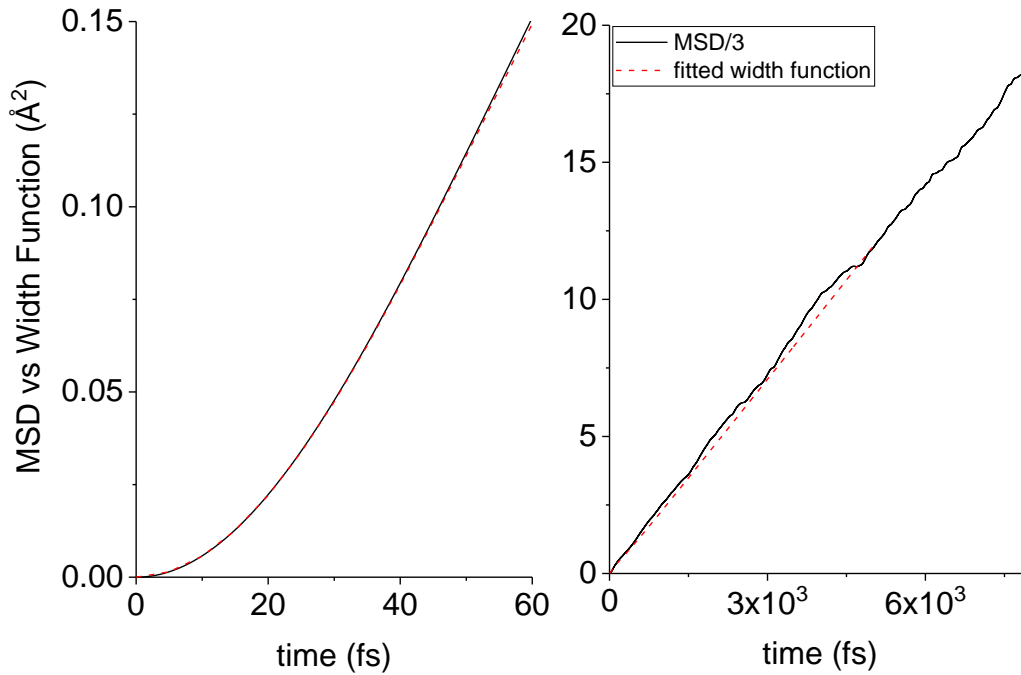


Figure 4-8. Comparison of MSD against width function.

#### 4.4 Deviation from the First Principle

Though  $I^{cl}(k, t)$  and  $S^{cl}(k, \omega)$  demonstrated reasonable structural information in  $k$  space, there are still systematic deviations from their theoretically predicted quantum behavior. As discussed in Section 2.5, due to treating Heisenberg position operators as classical position variables, there will be divergence between quantum and classical behavior in  $t$  space. Because  $\omega$  space is simply the reciprocal space of  $t$ , divergence in  $\omega$  space is also expected. It is therefore equivalent to discuss the deviation from classical approximation in either  $t$  or  $\omega$  space. In this section, liquid lithium will be used as an example to demonstrate three major deviations between the quantum and the classical  $S(k, \omega)$  in  $\omega$  space.

The first deviation from quantum behavior is the violation of the principle of detailed balance. As explained in Section 2.5, the first feature that the  $S^{cl}(k, \omega)$  lacks versus its quantum counterpart is the detailed balance relation,

$$S(k, -\omega) = e^{-\hbar\omega/k_B T} S(k, \omega).$$

The detailed balance relation using the nomenclature of scattering law should be written as

$$S(\alpha, \beta) = e^{-\beta} S(\alpha, -\beta). \quad (4.4.1)$$

In Figure 4-9, the  $S(\alpha, -\beta)/S(\alpha, \beta)$  of liquid lithium is plotted.  $S^{cl}(\alpha, \beta)$  is an even function of  $\beta$ , which results from  $I^{cl}(k, t)$  being a real and even function of  $t$ . The quantum  $S(\alpha, \beta)$  clearly shows detailed balance behavior between  $+\beta$  and  $-\beta$ . This asymmetric behavior arises from the quantum uncertainty of particle motion as a thermal cloud. In terms of  $I(k, t)$ , it is a complex function of  $t$  with an even real part and an odd imaginary part. This asymmetric behavior will be discussed in detail in the next section.

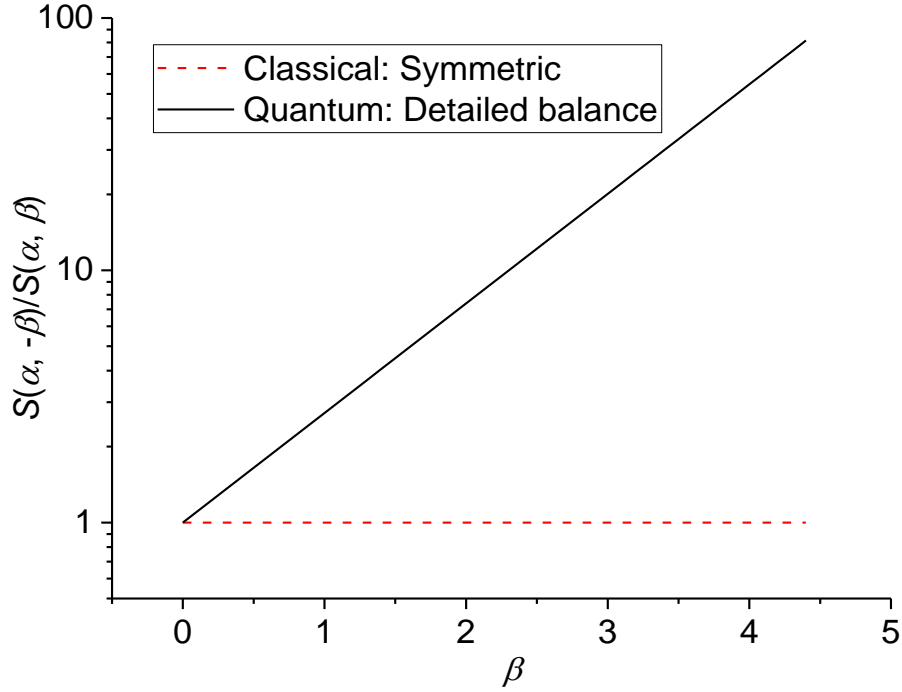


Figure 4-9. Quantum vs. classical  $S(\alpha, -\beta)/S(\alpha, \beta)$  of liquid lithium at 484 K, the y-axis is in logarithmic scale.

The second deviation from the quantum behavior is the theoretical predicted 1<sup>st</sup> moment of the thermal scattering law. As discussed in Section 2.4, the 1<sup>st</sup> moment of the quantum and classical thermal scattering law is

$$\begin{aligned} \int_{-\infty}^{\infty} S(\alpha, \beta) d\beta &= \alpha \\ \int_{-\infty}^{\infty} S^{cl}(\alpha, \beta) d\beta &= 0 \end{aligned} \quad (4.4.2)$$

The 1<sup>st</sup> moment is an  $S(\alpha, \beta)$  weighted average of  $\beta$ , which represents the expected value of energy transfer assuming that all the energy excitation states were available. The quantum first moment suggests that the positive energy transfer is preferred. Furthermore, the average energy transfer  $\beta$  is related to the momentum transfer  $\alpha$ . On the contrary, the first moment of classical thermal scattering law is a constant zero, which shows no preference in the direction of energy transfer. In Figure 4-10, the first moments of both the quantum and the classical thermal scattering law are compared.

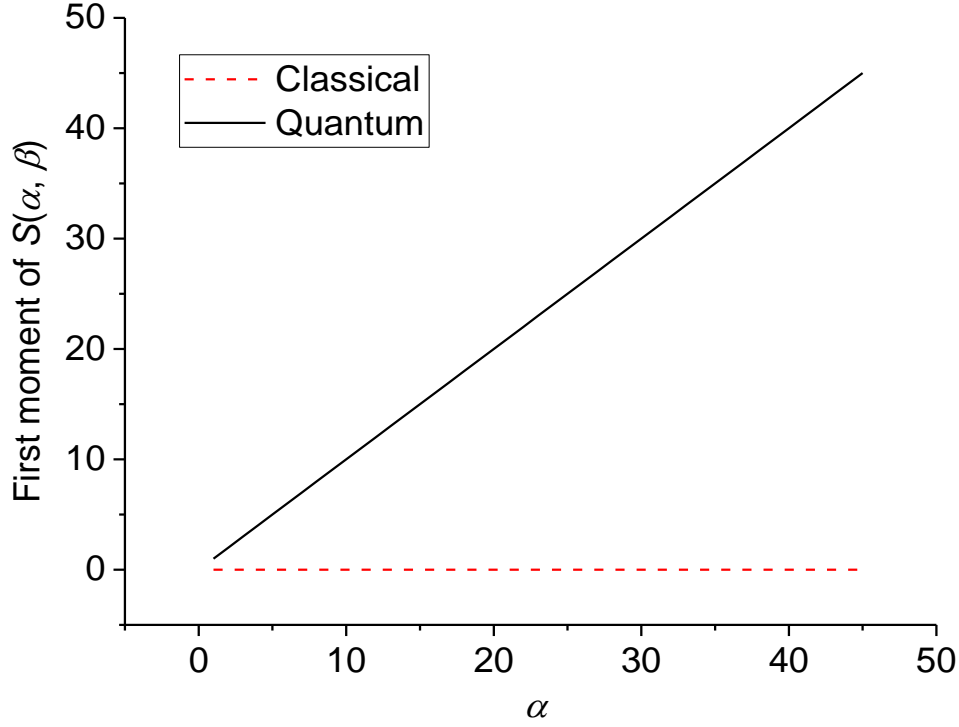


Figure 4-10. The first moment of quantum vs. classical  $S(\alpha, \beta)$  of liquid lithium at 484 K.

The third deviation from the quantum behavior is that the evaluated  $S^{cl}(\alpha, \beta)$  does not converge to 0 with large  $\alpha$ . Figure 4-11 is the symmetric thermal scattering law  $S^{sym}(\alpha, \beta)$  for both the classical and quantum case. As momentum transfer  $\alpha$  increases to a very large value, the scattering probability should drop to zero. In other words

$$\lim_{\alpha \gg 0} S^{sym}(\alpha, \beta) = 0, \quad (4.4.3)$$

which the classical  $S^{sym}(\alpha, \beta)$  clearly violates.

It was suggested by Schofield [94] that the classical  $S^{cl}(\alpha, \beta)$ , an even function of  $\beta$ , can be treated as the symmetric thermal scattering law, i.e.  $S^{sym}(\alpha, \beta)$ . Under this proposition, the asymmetric  $S^{asym}(\alpha, \beta)$  can be recovered from  $S^{cl}(\alpha, \beta)$ , i.e. Eq. (2.5.8). This procedure is widely known as the simplest first order quantum correction that recovers the detailed balance relation. This correction is applied to the liquid lithium  $S^{cl}(\alpha, \beta)$ . The deviation of the evaluated thermal scattering cross section is illustrated in Figure 4-12.

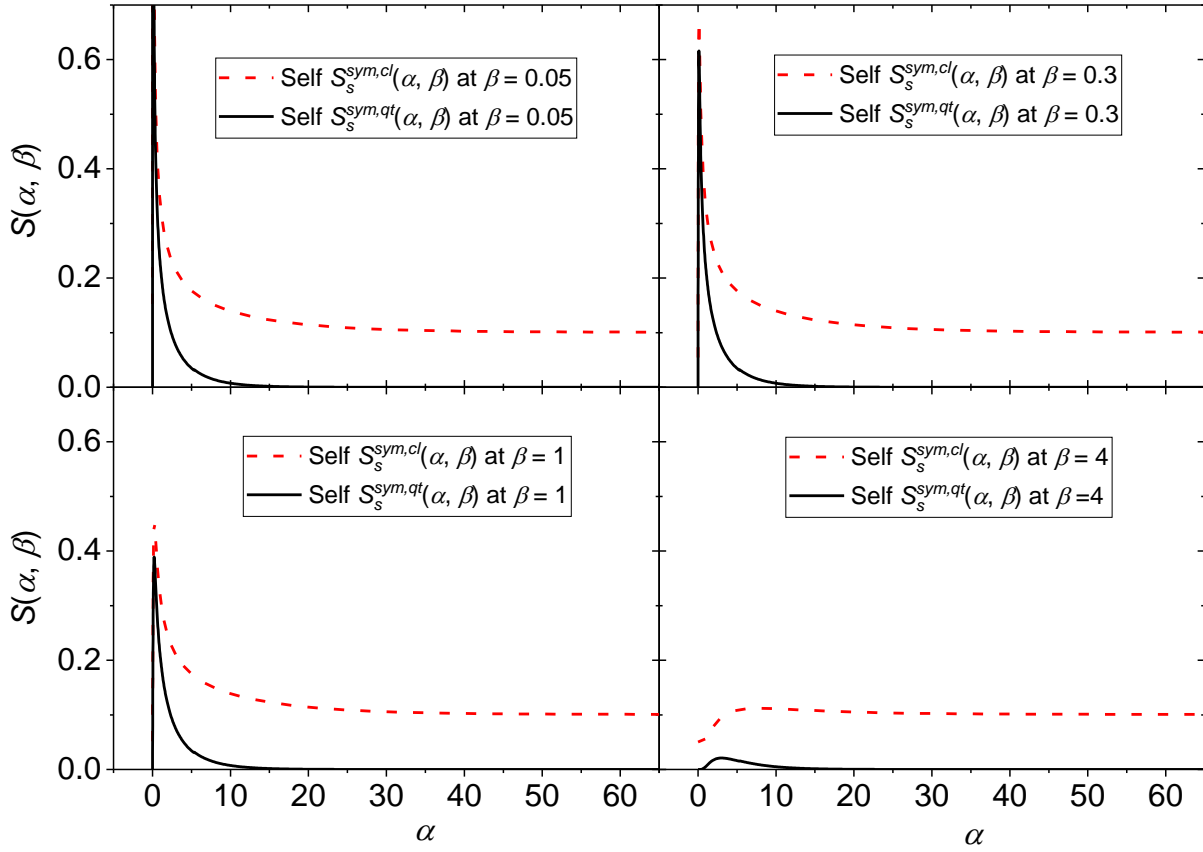


Figure 4-11. Quantum vs. classical  $S^{sym}(\alpha, \beta)$  of liquid lithium at 484 K.

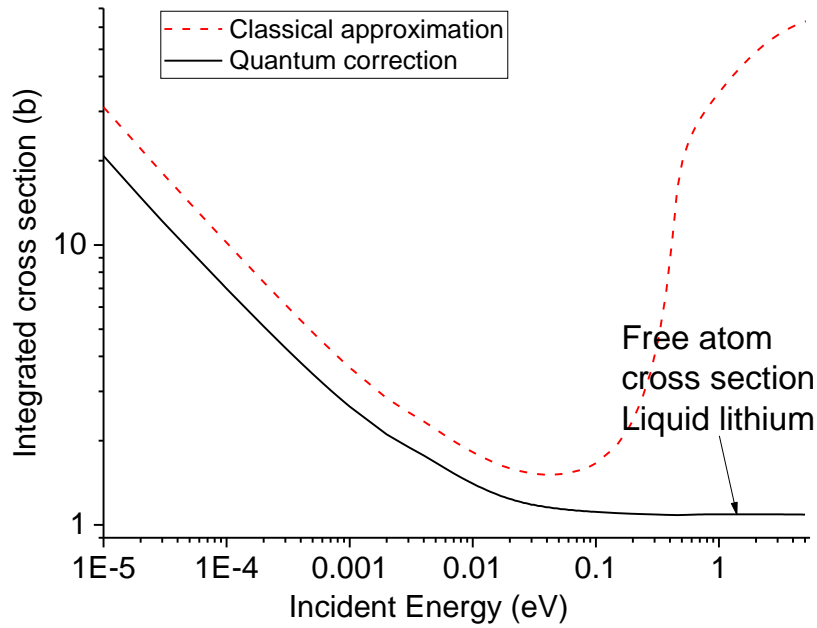


Figure 4-12. The integrated cross section for liquid lithium at 484 K. The first order Schofield correction applied  $S^{cl}(\alpha, \beta)$  vs.  $S^{qt}(\alpha, \beta)$  proposed in this work.



In Figure 4-11, the classical  $S^{sym}(\alpha, \beta)$  exhibits an unrealistically high probability of momentum transfer at high  $\alpha$ . This results in significant overestimation of the scattering probability at large momentum transfer and large energy transfer. As a result, the integrated thermal scattering cross section in Figure 4-12 deviates from the free atom cross section at high energy ( $> 1\text{eV}$ ).

#### 4.5 The Quantum Correction on the Self Thermal Scattering Law

In the previous section, the classical thermal scattering law deviates from its quantum behavior in various checks. Furthermore, the Schofield's correction, i.e. Eq. (2.5.8), cannot produce satisfactory results. For these reasons, the implementation of a general quantum correction is necessary. The quantum correction methodology proposed in Section 2.5.2 will be demonstrated with liquid lithium in this section. It is a predictive methodology that does not depend on *a posteriori* thermal scattering law knowledge, such as that proposed by Abe and Tasaki [85] introduced in Section 2.5.3. The flow diagram of the quantum correction is shown in Figure 4-13.

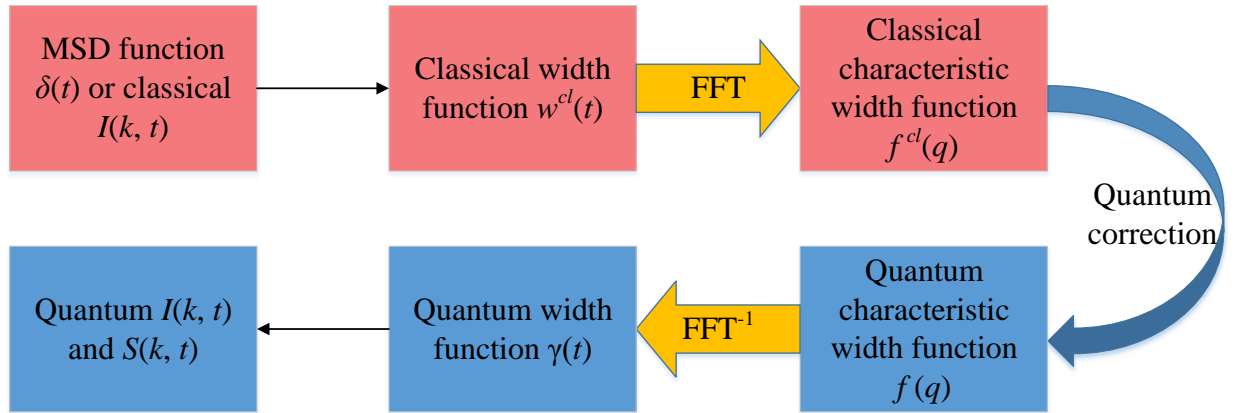


Figure 4-13. The flow diagram of quantum correction process (Eq. (2.5.3) to Eq. (2.5.6)).

The procedures and precautions of the proposed quantum correction methodology from Section 2.5.2 (i.e. Eq. (2.5.3) to Eq. (2.5.6)) are discussed below.

1. As the first step, the classical width function  $w^{cl}(t)$  can be obtained either from  $I_s^{cl}(k, t)$  or from the MSD, i.e.  $\delta r^2(t)$ . It is less computational expensive to calculate the  $\delta r^2(t)$  function than to calculate  $I_s^{cl}(k, t)$  from MD analysis. Therefore, it is recommended to calculate the width function from the MSD.
2. The second step is to apply the Fourier transform to the classical width function  $w^{cl}(t)$  to obtain the classical characteristic function, i.e.  $f^{cl}(\omega)$ , in frequency space. In practice, it is more computationally convenient to apply Eq. (2.5.3). From this equation,  $f^{cl}(\beta)/\beta^2$  is obtained in unitless energy  $\beta$  units. The Fast Fourier Transform (FFT) algorithm produces complex results. Because  $w^{cl}(t)$  is an even function of time,  $f^{cl}(\beta)/\beta^2$  is a real function of frequency. Hence, only the real part of the FFT result should be kept as the  $f^{cl}(\beta)/\beta^2$  function.
3. The third step is to apply the quantum correction in Eq. (2.5.4) to  $f^{cl}(\beta)$  to obtain quantum characteristic function  $f(\beta)$ . The quantum corrected  $f(\beta)$  function is a complex function with an even real part and an odd imaginary part.
4. The fourth step is to apply the reversed FFT algorithm to the quantum characteristic function  $f(\beta)$ . The quantum width function  $\gamma(t')$  obtained from this step is a complex function that is even in its real part and odd in its imaginary part.  $t'$  has a unit of  $\hbar/k_B T$ .
5. The last step is to apply Eq. (2.5.6) to  $\gamma(t')$  to calculate  $I_s(k, t')$  and  $S_s(\alpha, \beta)$ .

There is always a cost-benefit consideration of discretizing  $\delta r^2(t)$  regarding its total time length  $t_{tot}$  and its  $\Delta t$  resolution. The  $I_s^{cl}(k, t)$  function at small  $k$  decays much more slowly to zero compared to large  $k$ . This long decay time is comparable to the diffusion characteristic time. Therefore, the  $\delta r^2(t)$  function with longer time window  $t_{tot}$  and coarser  $\Delta t$  resolution would be best suited to be used to evaluate the  $I_s^{cl}(k, t)$  function at small  $k$ . The behavior of  $I_s^{cl}(k, t)$  at large

$k$  is opposite. In this situation, the  $I_s^{cl}(k, t)$  decays faster with shorter decay time. It often approaches zero before the linear diffusion region. Thus, a  $\delta r^2(t)$  function with finer  $\Delta t$  resolution and a shorter  $t_{tot}$  is necessary to evaluate the  $I_s^{cl}(k, t)$  function at large  $k$ .

Three  $\delta r^2(t)$  functions, i.e. with short  $t_{tot}$ , with middle  $t_{tot}$ , and with long  $t_{tot}$ , would be adequate to cover all the  $k$  range with enough resolution for the quantum correction. The three  $\delta r^2(t)$  used for liquid lithium are shown in Figure 4-14. The  $t_{tot}$  for the three functions are 10 ps, 1 ps, and 0.1 ps. There are 10,000 points in each  $\delta r^2(t)$  function. The  $\Delta t$  resolution for each function is 1 fs, 0.1 fs, and 0.01 fs respectively.

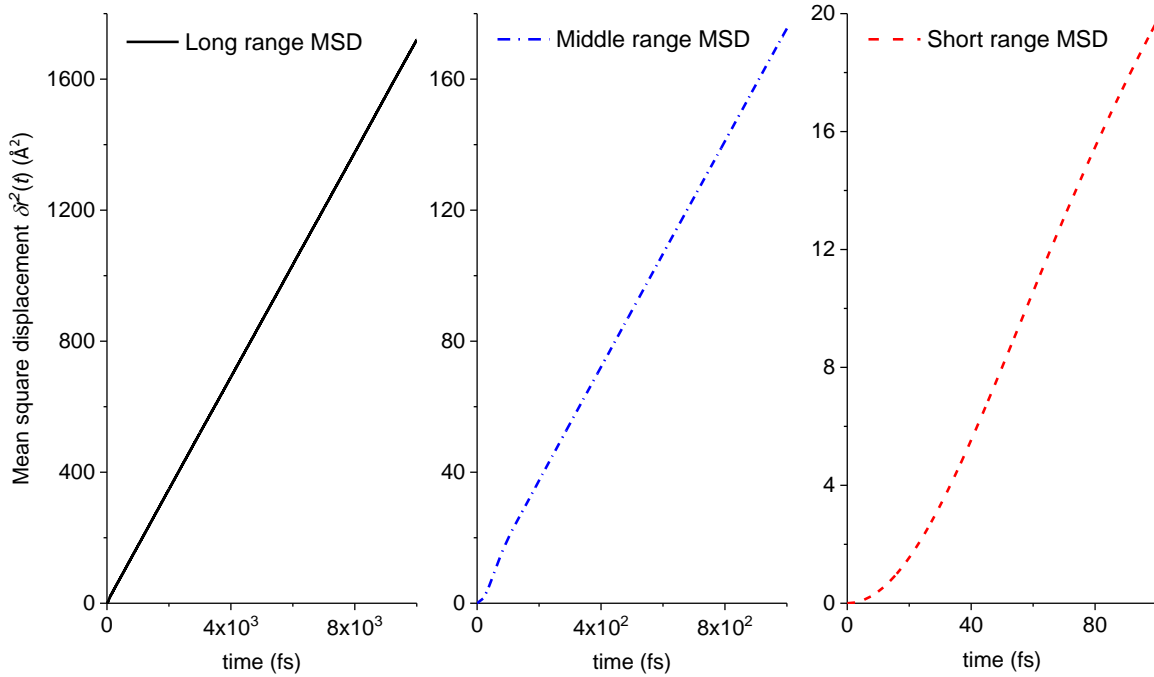


Figure 4-14. MSD of liquid lithium used in the quantum correction.

The implemented quantum correction algorithm will locate  $k$  and switch input files automatically for each combination of  $t_{tot}$  and  $\Delta t$ . The corrected quantum width function is plotted in Figure 4-15. An example of  $I_s(k, t)$  at  $k = 3 \text{ \AA}^{-1}$  against  $t$  is plotted in Figure 4-16. As can be seen, the quantum width function  $\gamma(t)$  and the quantum  $I_s(k, t)$  are even functions of  $t$  for

the real part, and odd functions of  $t$  for the imaginary part. In  $I_s(k, t)$ , the imaginary part is obviously smaller than the real part. The real part contributes to the absolute value of  $I_s(k, t)$ , while the imaginary part contributes to the detailed balance behavior after the Fourier transformation.

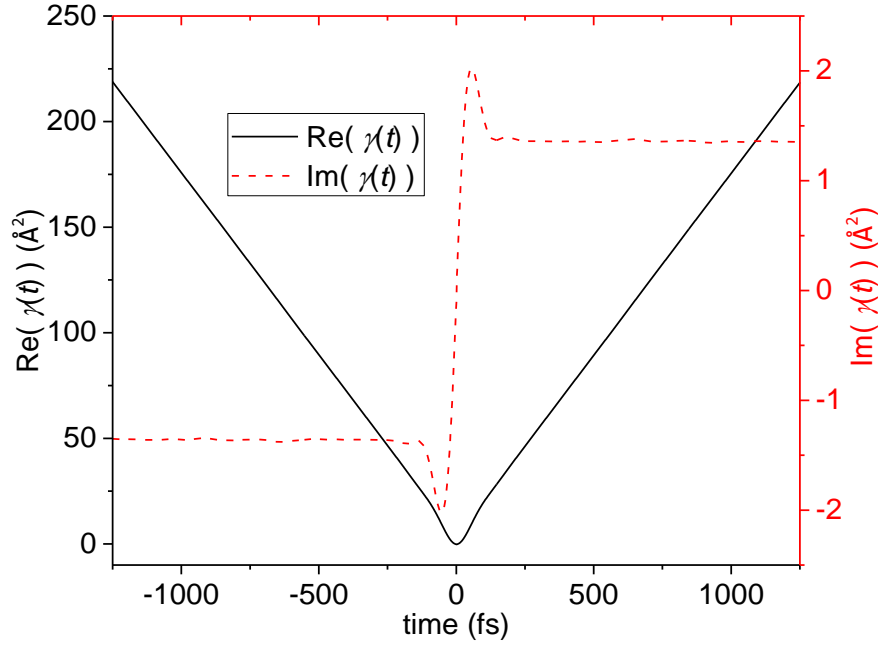


Figure 4-15. The quantum width function  $\gamma(t)$ .

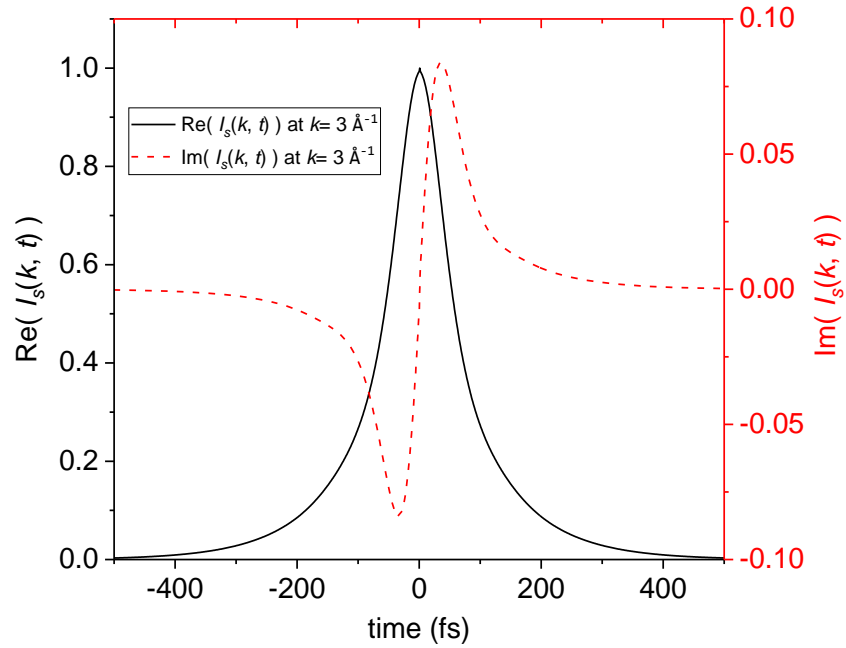


Figure 4-16. The quantum intermediate scattering function  $I_s(k, t)$ .

By applying the Fourier transform, this asymmetric behavior of quantum  $I_s(k, t)$  directly results in detailed balance behavior of  $S_s(\alpha, \beta)$ . As an example,  $S_s(\alpha, \beta)$  at  $\alpha = 0.1646$  is plotted in Figure 4-17. As  $\alpha$  increases, a general trend indicated by the principle of detailed balance is that  $S_s(\alpha, \beta)$  becomes increasingly asymmetric and moves to the negative  $\beta$  side.

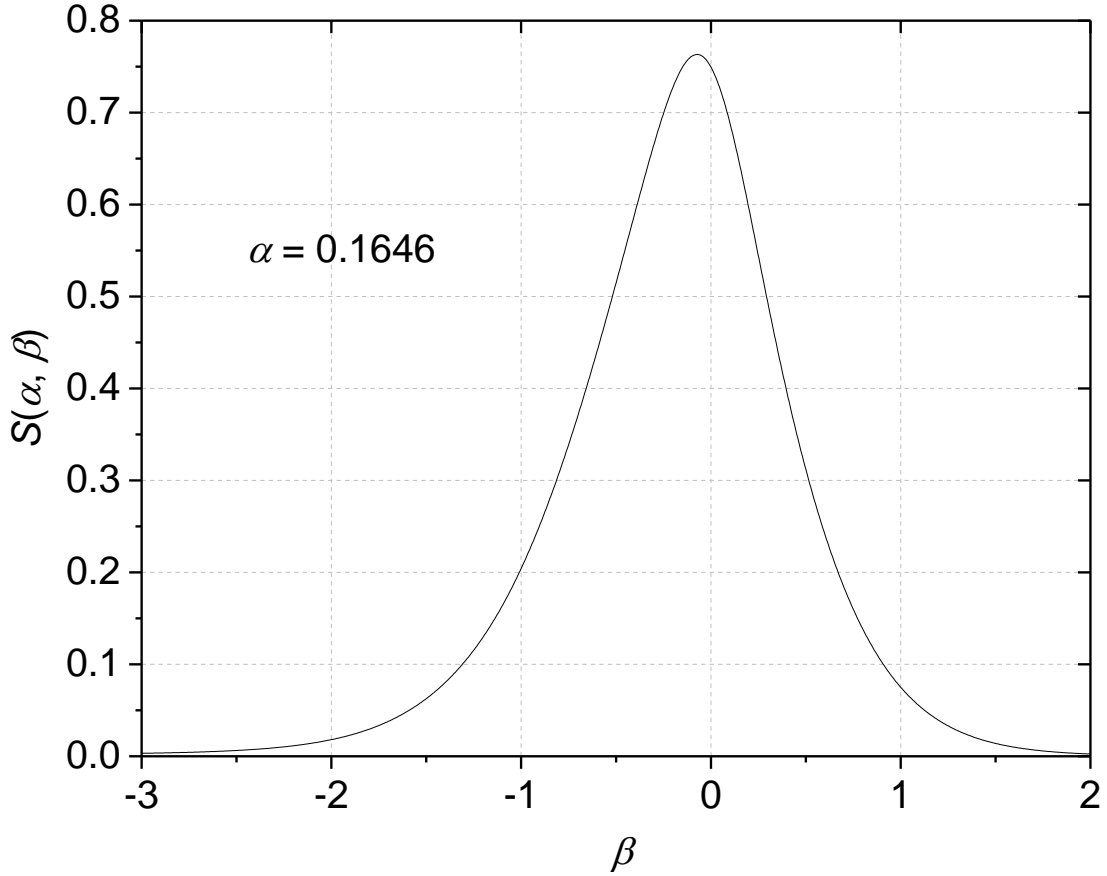


Figure 4-17. The quantum corrected self thermal scattering law at  $\alpha = 0.1646$ .

To check the principle of detailed balance, the magnitude of  $S_s(\alpha, -\beta)/S_s(\alpha, \beta)$  is compared to  $e^\beta$ . As demonstrated by Figure 4-18, the principle of detailed balance is followed by the quantum corrected  $S_s(\alpha, \beta)$ . As shown in Figure 4-19, the 0<sup>th</sup> moment and the 1<sup>st</sup> moment of the corrected thermal scattering law was also checked to validate the quantum behavior. As can be seen,  $S_s(\alpha, \beta)$  normalized to 1. The quantum corrected  $S_s(\alpha, \beta)$  has its 1<sup>st</sup> moment equaling to  $\alpha$ , instead of the zero of its classical counterpart.

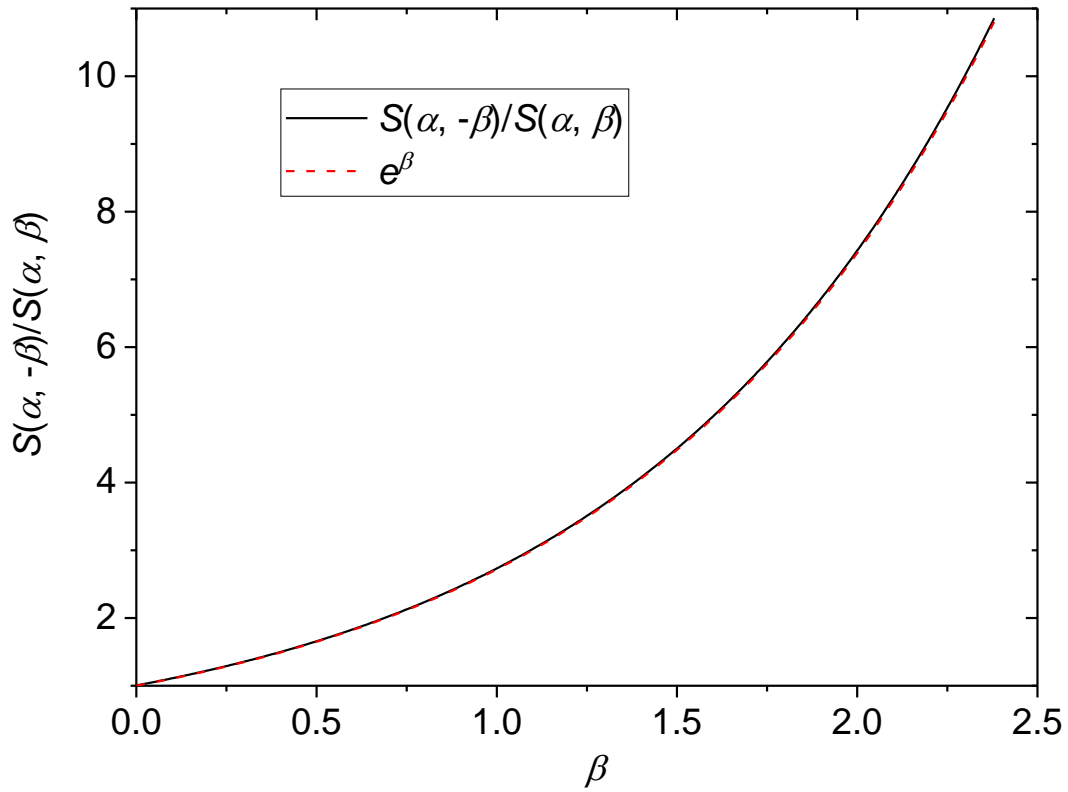


Figure 4-18. Check of the principle of detailed balance. Black line is evaluated from the division of quantum corrected thermal scattering law. Red dashed line is the factor of the principle of detailed balance.

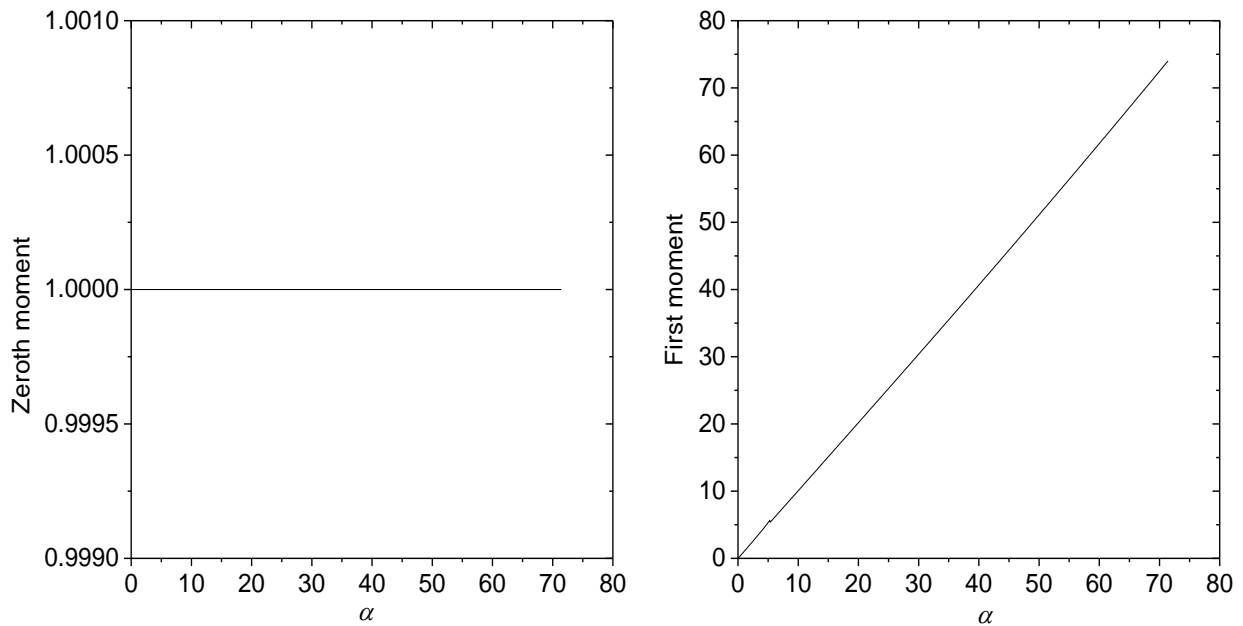


Figure 4-19. The 0<sup>th</sup> moment and 1<sup>st</sup> moment of the quantum corrected  $S_s(\alpha, \beta)$ .

## 4.6 The Quantum Correction Including the Distinct Thermal Scattering Law

From Section 4.3 to Section 4.5, a generalized quantum correction on  $I_s(k, t)$  has been illustrated. According to Figure 4-3 and Figure 4-5, it is obvious that the  $I^{cl}(k, t)$  and  $S^{cl}(\alpha, \beta)$  are not Gaussians. Therefore, the width function model cannot be applied on the distinct correlation functions. However, Eq. (2.5.13) points out that  $S_d^{cl}(\alpha, \beta)$  deviates from  $S_d^{qt}(\alpha, \beta)$  by the same factor  $S_s^{cl}(\alpha, \beta)$  deviates from  $S_s^{qt}(\alpha, \beta)$ .

In Section 2.5.4, it was demonstrated that there are two equivalent ways to apply quantum corrections to the distinct scattering law. Analytically, scaling by either  $Q(k, \omega)$  or  $\Gamma(k)$  will produce equivalent results. In terms of computational algorithm implementation, the  $\Gamma(k)$  approach will produce less noisy evaluations. This is because the Fourier transformation creates sampling noises in the frequency space that can be carried over by  $Q(k, \omega)$ .  $\Gamma(k)$  effectively averages out this noise. Therefore, Eq. (2.5.15) will be applied to evaluate the quantum  $S^{qt}(\alpha, \beta)$  in this section. Distinct effects will be included in this evaluation, consequently relaxing the Gaussian approximation in  $S_s^{qt}(\alpha, \beta)$ . The quantum correction to the distinct thermal scattering law can be achieved by the procedure shown in Figure 4-20. Following the procedure in Figure 4-20, liquid lithium was used as an example to illustrate the evaluation.

The first step is to evaluate  $S^{cl}(\alpha, \beta)$  and  $S_s^{cl}(\alpha, \beta)$ , which was already accomplished in Section 4.2 and shown in Figure 4-3 and Figure 4-5. As shown in these two plots, some detailed structural peaks of liquid lithium appear in  $k$  space when  $k < 80 \text{ nm}^{-1}$ . The classical thermal scattering law  $S^{cl}(\alpha, \beta)$  converges to the classical self thermal scattering law  $S_s^{cl}(\alpha, \beta)$  with increasing  $\alpha$ . The quantum self thermal scattering law  $S_s(\alpha, \beta)$ , however, is constantly lower than its classical counter part  $S_s^{cl}(\alpha, \beta)$ .

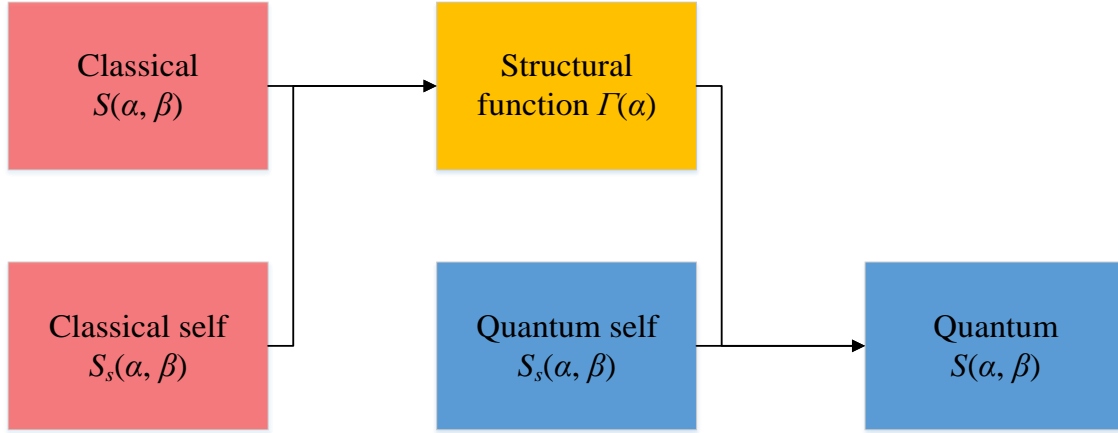


Figure 4-20. Flow chart of quantum correction including distinct effects (Eq. (2.5.15)).

The second step is to evaluate the collective structural function  $\Gamma(\alpha)$ . Using the calculated  $S^{cl}(\alpha, \beta)$  and  $S_s^{cl}(\alpha, \beta)$ , the  $\Gamma(\alpha)$  function for liquid lithium was evaluated by Eq. (2.5.15) and plotted in Figure 4-21.

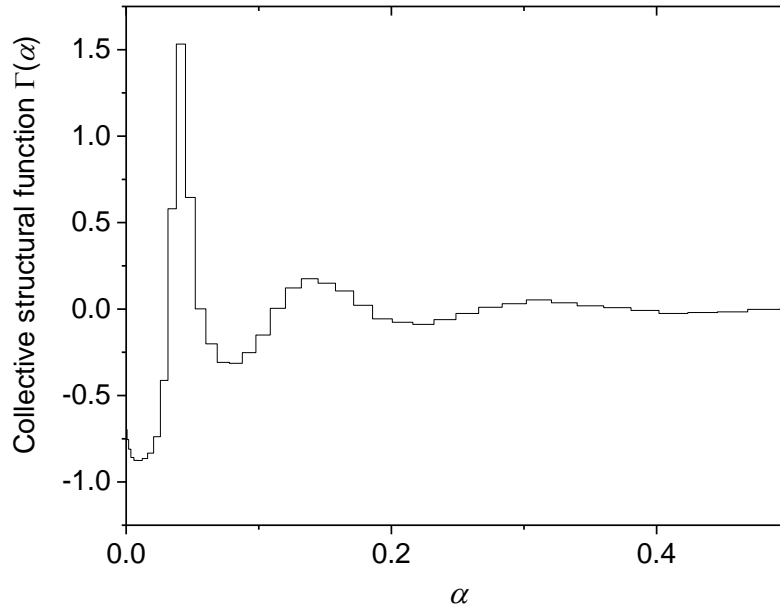


Figure 4-21. The collective structural function  $\Gamma(\alpha)$  for liquid lithium

The collective structural function  $\Gamma(\alpha)$  shows strong coherent peak at  $\alpha = 0.041$ , which corresponds to  $k = 0.24 \text{ nm}^{-1}$  in reciprocal space. This indicates high probability of repeating structure at  $r = 2\pi/k = 26 \text{ nm}$ . In Figure 4-1,  $26 \text{ nm}$  is the breakeven point for attractive forces



and repulsive forces in the pair potential, which is also the most probable bond length for liquid lithium. Other peaks in the collective structural function  $\Gamma(\alpha)$  demonstrate the other possible periodic structure formation in liquid lithium. The  $\Gamma(\alpha)$  function, to a great extent, is the radial distribution function (RDF) in reciprocal space.

The third and the last step is to evaluate  $S^{qt}(\alpha, \beta)$  using  $\Gamma(\alpha)$  to account for the distinct contribution. This is done based on Eq. (2.5.15). As an example, the quantum corrected  $S^{qt}(\alpha, \beta)$  and  $S_s^{qt}(\alpha, \beta)$  at  $\beta = 0.3$  are plotted together in Figure 4-22.

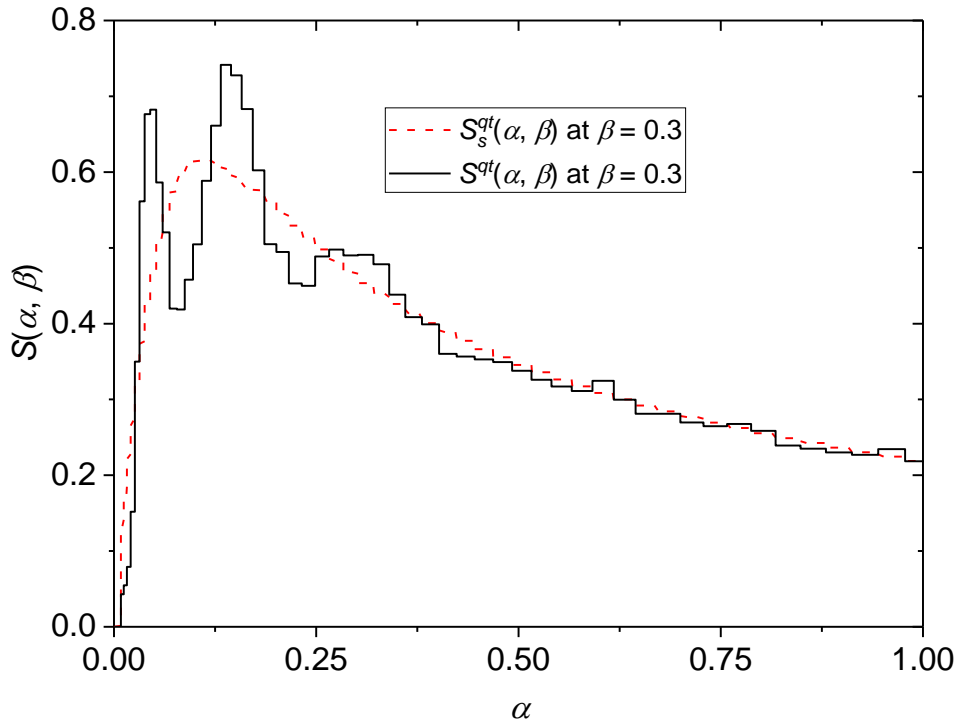


Figure 4-22. The quantum thermal scattering law: black is  $S^{qt}(\alpha, \beta)$ , red dashed is  $S_s^{qt}(\alpha, \beta)$ .

In Figure 4-23, the  $S_{tot}(\alpha, \beta)$ , which weights the  $S^{qt}(\alpha, \beta)$  and  $S_s^{qt}(\alpha, \beta)$  according to the bound cross section, is plotted together with neutron scattering experimental measurements [121]. As can be seen in Figure 4-23, distinct effects are correctly contained in  $S_{tot}(\alpha, \beta)$ . Compared to experimental measurements [121], distinct effects correctly predict the structure of the liquid. Whereas the Egelstaff & Schofield model, which consists of only the self thermal scattering law,

lacks the detail structure from  $\Gamma(\alpha)$ . A complete quantum correction of the self and distinct contribution is necessary to correctly evaluate the total thermal scattering law.

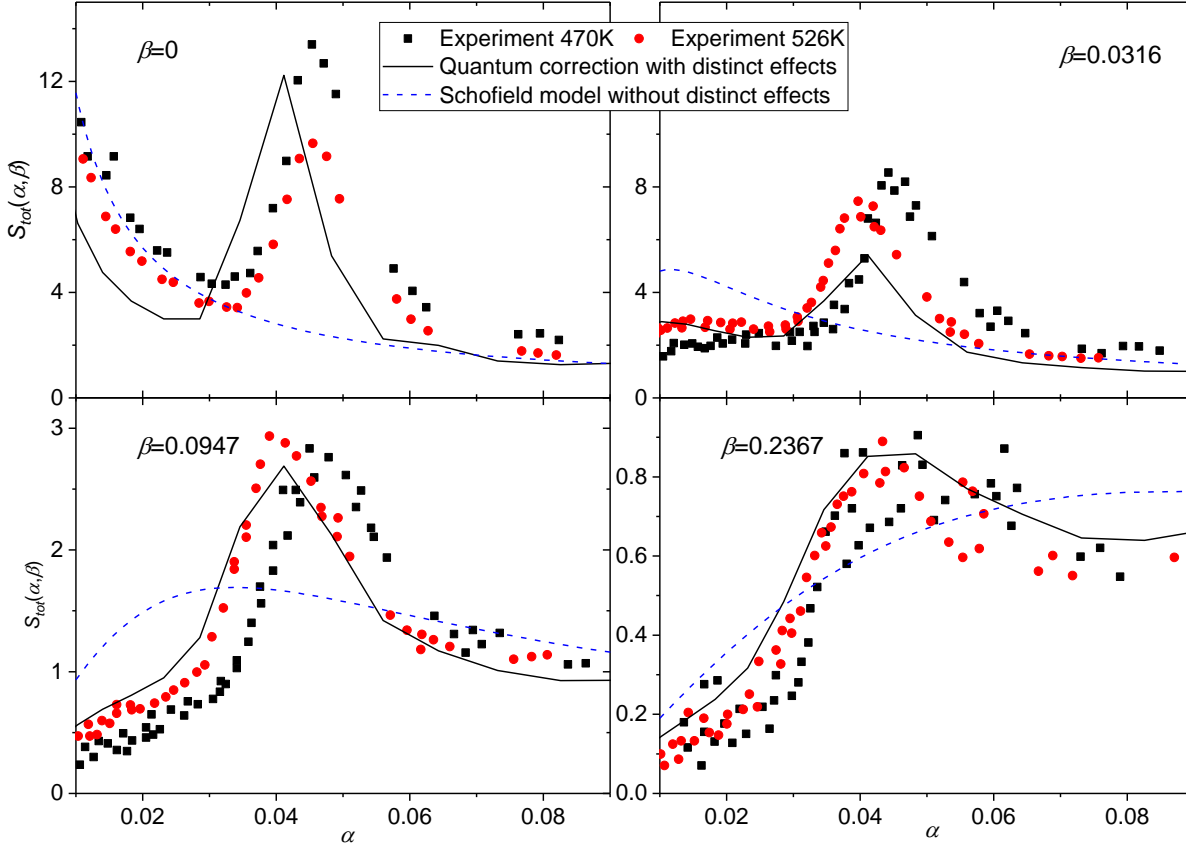


Figure 4-23. The thermal scattering law of liquid lithium from quantum correction including distinct effects (solid black) vs the Egelstaff & Schofield model (dashed blue) at 484 K. Scatter data are from neutron scattering experiment [121].

#### 4.7 The Cross Section of Liquid Lithium

In this section, the double differential cross sections of liquid lithium at 4 different scattering angles are compared to experimental measurements [121]. The double differential cross section was evaluated from the quantum corrected total thermal scattering law  $S_{tot}(\alpha, \beta)$ . De Jong provides the double differential cross section against scattered neutron wavelength. The transformation from a secondary wave length differentiated scattering cross section, i.e. Eq. (2.1.26), to a secondary energy differentiated scattering cross section is

$$\frac{d^2\sigma}{d\Omega dE'} = \frac{M\lambda'^3}{h^2} \cdot \frac{d^2\sigma}{d\Omega d\lambda'} \quad (4.7.1)$$

The scattering cross sections from both the self and total scattering law at 484 K were evaluated and plotted in Figure 4-24. The experimental measured double differential cross section [121] at 470 K and 574 K were also shown in Figure 4-24 for comparison.

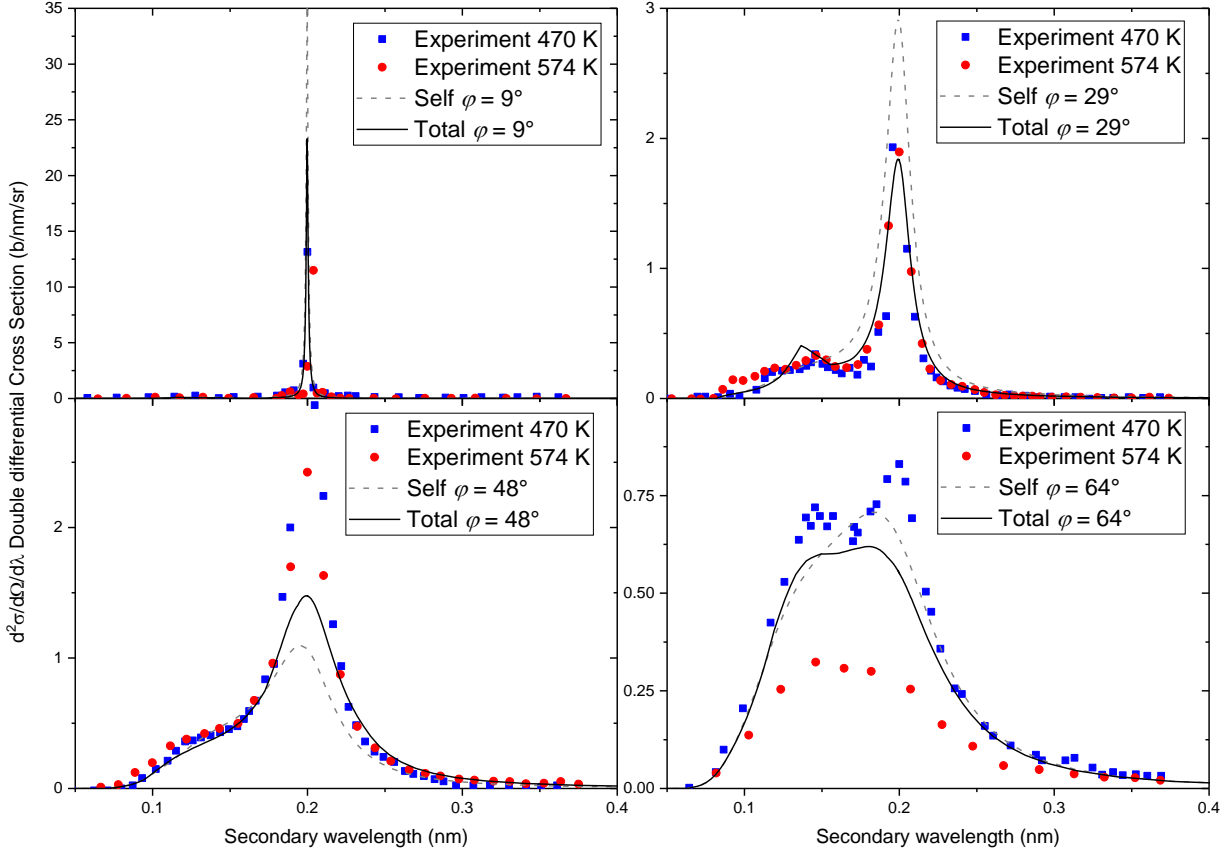


Figure 4-24. The calculated double differential cross section of liquid lithium at 484 K compared to experiments at different scattering angles.

As can be seen, the experimental measurement shows a quasi-elastic peak at the  $\lambda_{out} = \lambda_{in}$  position. The shape and position of the peak structure from the evaluation exhibit good agreement with the experimental measurements. The dashed curve is the  $S_s(\alpha, \beta)$  contribution to the double differential cross section. The solid curve is the  $S_{tot}(\alpha, \beta)$  contribution to the double differential cross section. As can be seen, the included distinct contribution changes how the neutron scatters

for different scattering angles. It lowers the double differential cross section at  $9^\circ$  and  $29^\circ$  while raises the cross section at  $48^\circ$ . The shape of the cross section is also changed at  $64^\circ$ . The distinct effects are consistent with the experimental measurements at  $470\text{ K}$  and  $574\text{ K}$ . It can therefore be concluded that the quantum correction including the distinct effects can reproduce experimental measurements.

In the experimental measurements, with increasing scattering angles, higher quasi-elastic peaks are observed. This is a bias from the normalization calibration used in the experiment. In the experiments, vanadium was used as sample material to benchmark the absolute scattering cross section. The liquid lithium measurements were normalized to the elastically scattered neutron intensity from vanadium. This normalization procedure will produce a bias in the magnitude in the quasi-elastic peak because the distinct scattering effects for liquid lithium are not the same as that for vanadium.

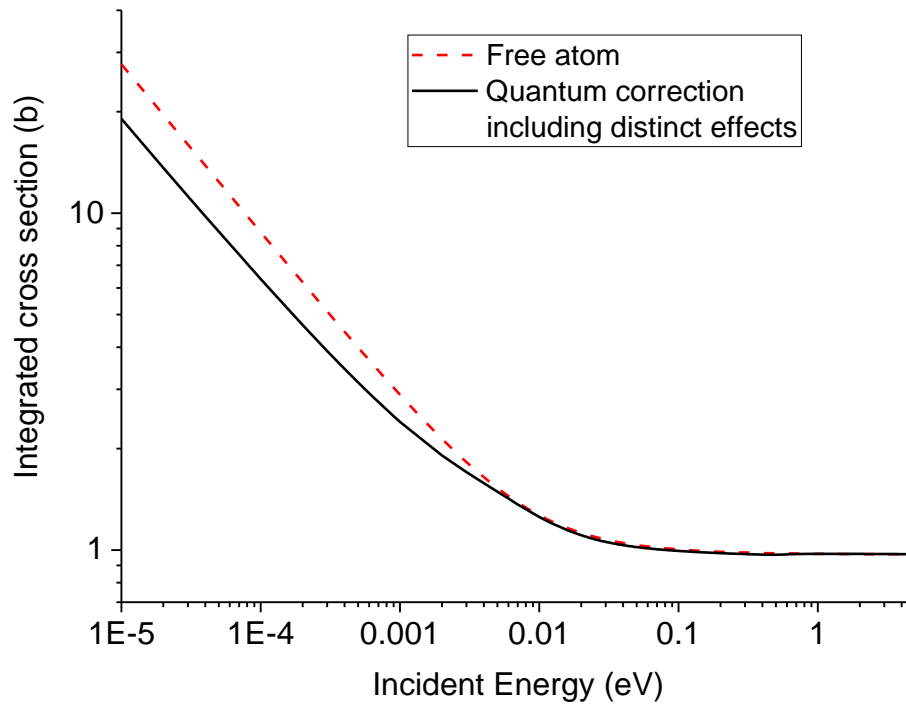


Figure 4-25. The integrated cross section of liquid lithium. The cross section from quantum correction including distinct effects (solid black) is compared to the Doppler broadened free atom cross section (dashed red).

The integrated cross section of liquid lithium is shown in Figure 4-25. The red dashed curve is the Doppler broadened free atom cross section. The black solid curve is the quantum corrected cross section including distinct effects. As can be seen, the solid black line converged to the free atom cross section at high energy. At the cold neutron and ultra-cold neutron energy region, the Doppler broadened cross section is higher than the quantum corrected cross section.

## Chapter 5 Thermal Scattering Law of Molten Salt FLiBe

In this chapter, the thermal neutron scattering cross section of molten salt FLiBe will be evaluated following the verified quantum correction methodology. For the data preparation step, the molecular dynamics model of molten salt FLiBe was presented in Chapter 3. The model was verified against experimental measurements of molten salt FLiBe properties such as density, viscosity, heat capacity, etc. Trajectory data from the proposed model were then used with the quantum correction method that was demonstrated in Chapter 4.

In this chapter, the classical width function,  $w(t)$ , was evaluated from  $\delta r^2(t)$  at different time scales. Subsequently, quantum correction were applied to the classical width function  $w(t)$  to obtain the quantum width function  $\gamma(t)$ . The quantum self intermediate function  $I_s(k, t)$  was evaluated from the obtained quantum width function  $\gamma(t)$ .  $I_s(k, t)$  was Fourier transformed to  $S_s(\alpha, \beta)$ . The distinct effects were added to the quantum corrected thermal scattering law afterwards. In the last step, the evaluated total thermal scattering law,  $S_{tot}(\alpha, \beta)$ , was used to calculate the scattering cross section.

### 5.1 The Classical Scattering Law of FLiBe

The classical scattering law as shown in Section 4.4 deviates from the quantum scattering law in numerous checks. In this section, the same checks will be implemented for Be, Li and F in FLiBe. These deviations will be eliminated after quantum correction is applied in Section 5.2. Because the deviation at all three temperatures behaves in the same way, in this section, only the classical deviation at 873 K will be demonstrated. Without further notation, the evaluation in this section will implicitly assume 873 K.

The classical scattering law of Be, Li and F in FLiBe at different  $\beta$  is illustrated from Figure 5-1 to Figure 5-3. The deviation of the detailed balance and first moment of the classical scattering law is shown in Figure 5-4. As a common trend, the classical scattering law does not converge to zero at large  $\alpha$ . The deviations of integrated cross sections are shown in Figure 5-5. Though the cross section should converge to the free atom cross section (black dashed line) in Figure 5-5, the non-zero tail results in overestimation of integrated cross section at relative large incident neutron energy ( $> 0.1$  eV). These deviations can be corrected using the proposed quantum correction method.

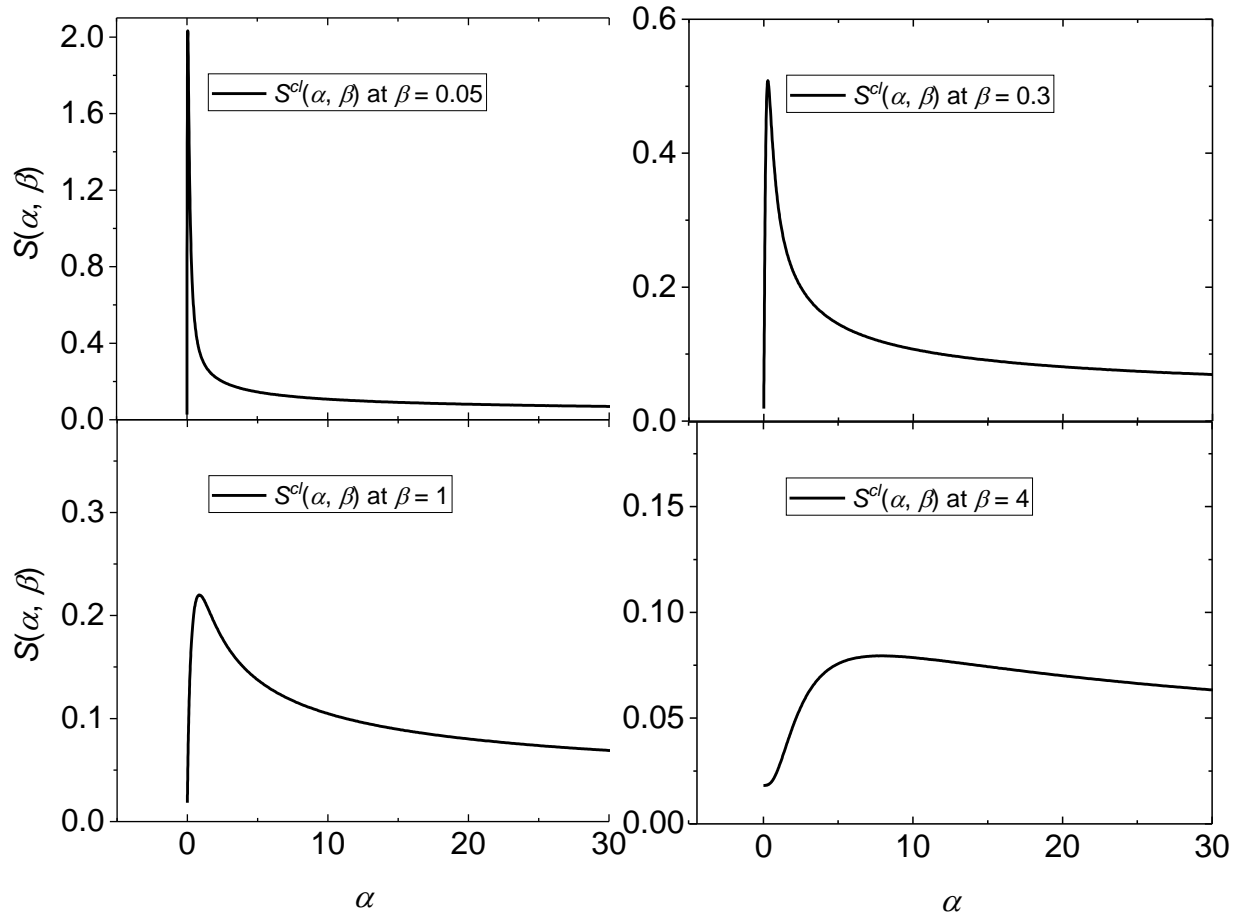


Figure 5-1. The classical scattering law of Be in FLiBe.

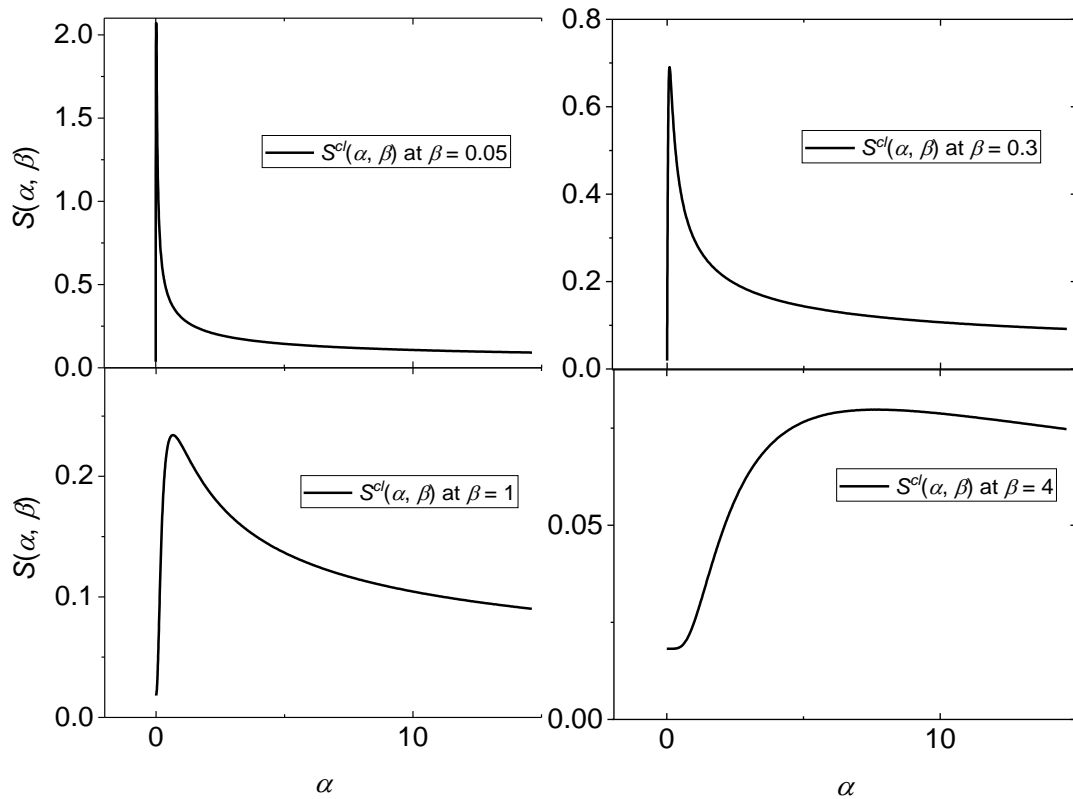


Figure 5-2. The classical scattering law of F in FLiBe

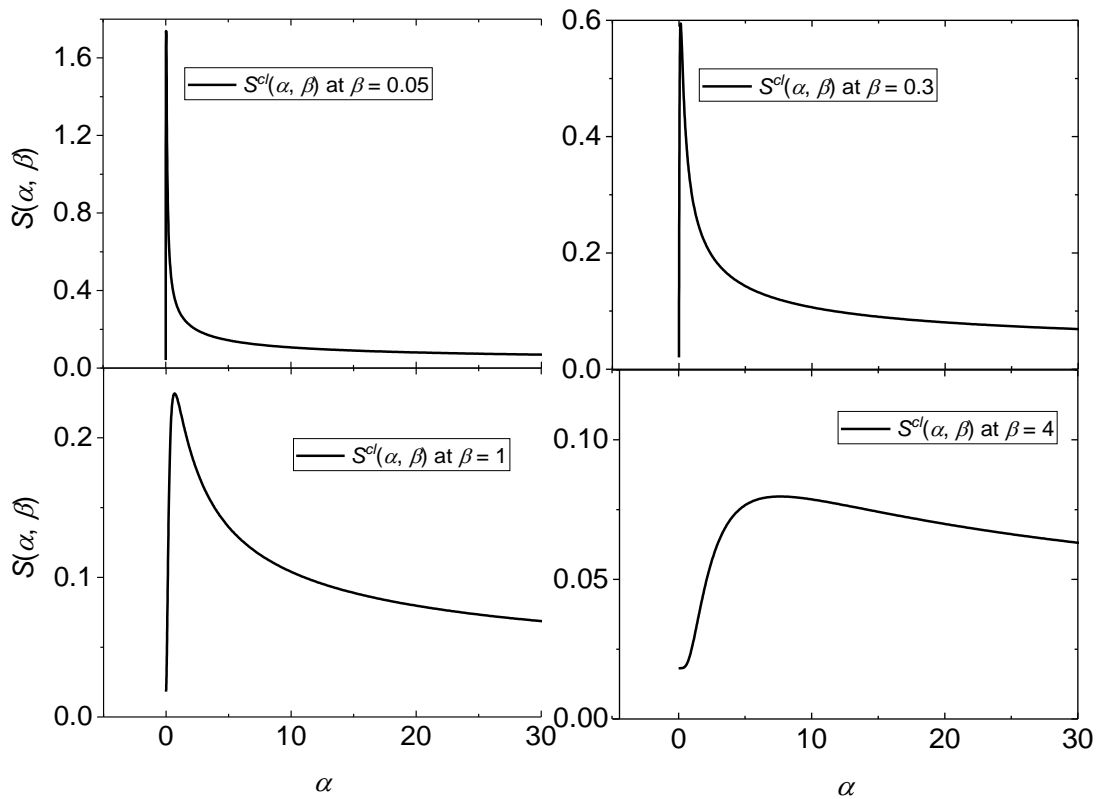


Figure 5-3. The classical scattering law of Li in FLiBe.



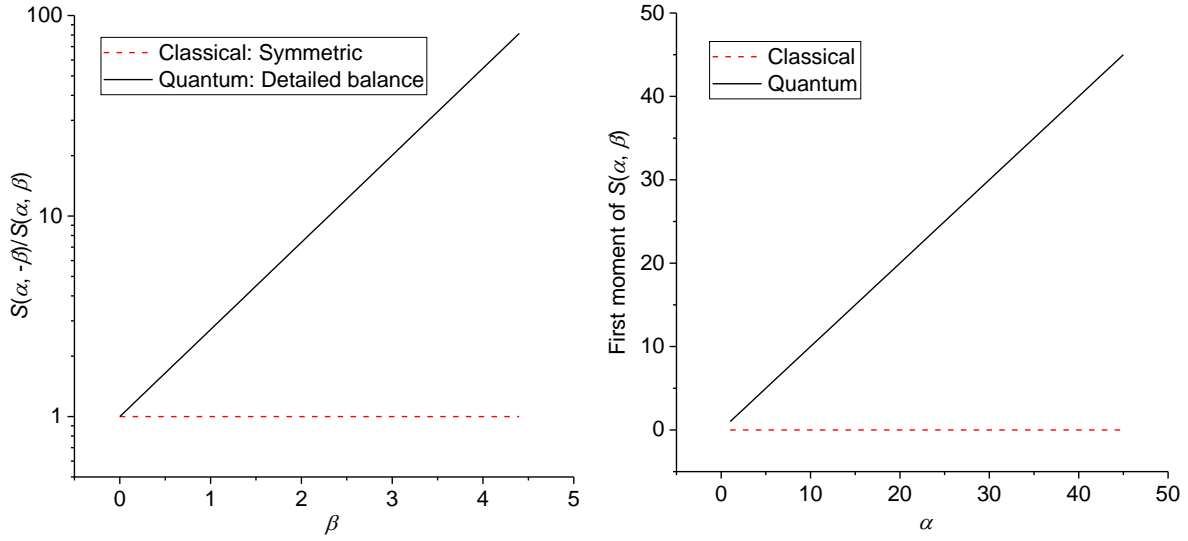


Figure 5-4. Deviation of the classical scattering law from the quantum scattering law.

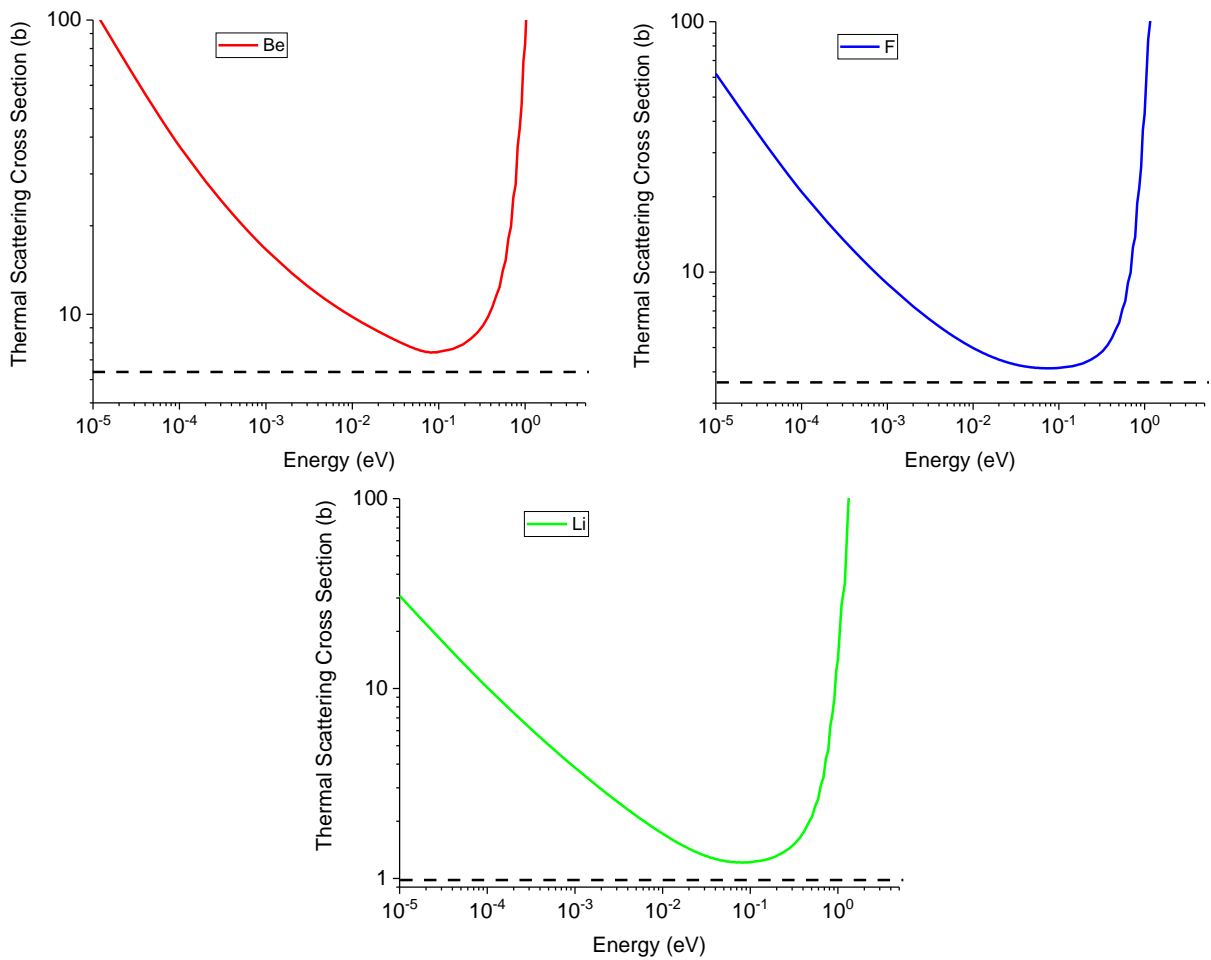


Figure 5-5. The deviation of integrated cross section of each species in FLiBe from their free atom cross section (black dashed line) at relative ( $> 0.1$  eV) high incident energies.

## 5.2 The Quantum Correction of FLiBe

In Section 4.5, the steps for the quantum correction of the self thermal scattering law  $S_s(\alpha, \beta)$  were discussed in details. Three MSDs with different time length and resolution were transformed to the corresponding classical width functions,  $w(t)$ . The  $w(t)$  functions were subsequently corrected to the quantum width function  $\gamma(t)$ . In this section, the same methodology is applied on each species in FLiBe. All evaluations are carried out for three representative reactor core temperatures of 873 K, 923K, and 973 K.

### 5.2.1 The Width Function of FLiBe

In this section, the procedures introduced in Section 4.5 are followed to apply the quantum correction to the classical width function, i.e.  $w(t)$ . The classical width function is obtained from  $\delta r^2(t)$  as demonstrated in Section 4.5. FLiBe at 873K is used as an example to illustrate the above procedures.

The Gaussian approximation indicates that the MSD can be used to obtain the classical width function  $w(t)$ . As discussed in Section 4.5, a proper combination of the resolution and the time length of  $\delta r^2(t)$  is necessary to obtain the characteristic function  $f(\omega)$  in reasonable precision. Regarding the range of time length  $t_{tot}$  that needs to be evaluated, three MSDs are chosen for FLiBe. They are (1) time length  $t_{tot} = 10 \text{ ps}$  with resolution  $\Delta t = 1 \text{ fs}$ , (2) time length  $t_{tot} = 1 \text{ ps}$  with resolution  $\Delta t = 0.1 \text{ fs}$ , and (3) time length  $t_{tot} = 100 \text{ fs}$  with resolution  $\Delta t = 0.01 \text{ fs}$ . The MSD for each species in FLiBe is plotted in Figure 5-6.

The lithium ions develop a fast diffusion process in FLiBe. At 873 K, the evaluated diffusion coefficients for Li, F, and Be in FLiBe are  $7.808 \times 10^{-9} \text{ m}^2/\text{s}$ ,  $4.862 \times 10^{-9} \text{ m}^2/\text{s}$ ,  $3.098 \times 10^{-9} \text{ m}^2/\text{s}$  respectively. At small time scales, the Be ion in general moves faster than the

F ion. However, at around 30 *fs*, the MSD for the Be ion crosses over the MSD for the F ion. This behavior will be explained in the following discussion.

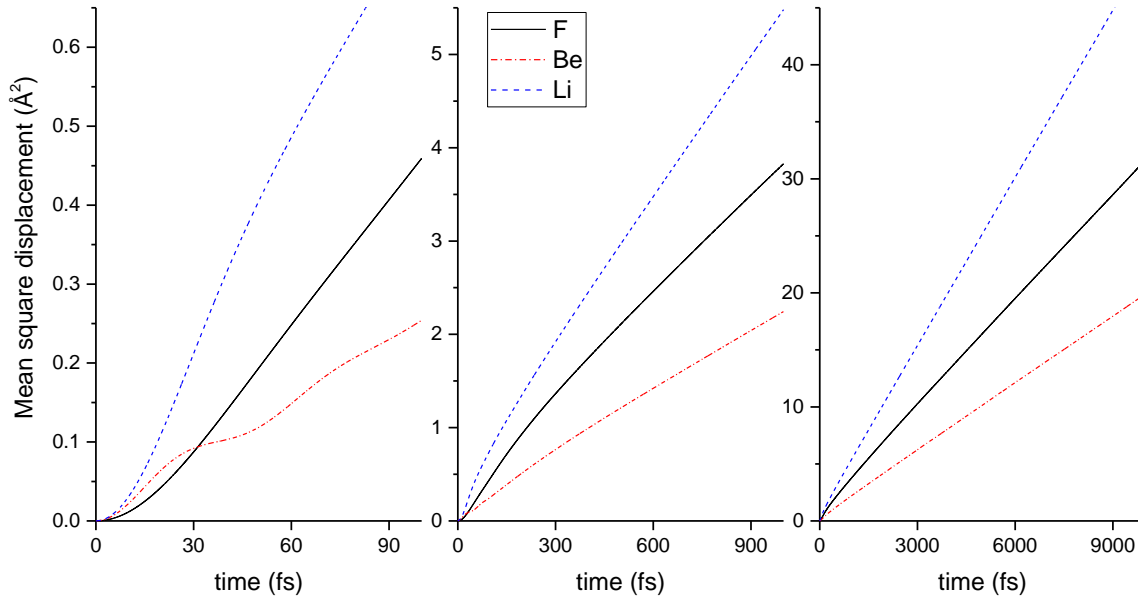


Figure 5-6. The MSD of Be, F, Li in FLiBe at 873 K.

Be ions move noticeably faster than F ions at small time ( $< 20\text{ fs}$ ). Around 30 *fs*, Be ions reach a plateau and then continue on to linear diffusion behavior for  $t > 60\text{ fs}$ . Since when  $t < 30\text{ fs}$ , Be ions demonstrate a free gas behavior; its MSD follows a quadratic shape. At this small time scale, the atom is generally moving freely without interacting too much with neighboring atoms. Therefore when  $t < 30\text{ fs}$ , the particle speed is inversely proportional to the particle mass  $M$  at the same thermal energy. This results in the slopes of MSDs at small time ordered such that  $Li > Be > F$ . In Figure 3-3, it is clearly seen that Be ions and F ions are forming  $BeF_4^{2-}$  ions on a short time scale. Between  $30\text{ fs} < t < 60\text{ fs}$ , Be ions begin to interact with the potential “wall” and oscillating inside of the  $BeF_4^{2-}$  structure. Be ions are contained inside of the tetragonal structure, resulting in a plateau in the MSD. At the end of this time period, while the  $BeF_4^{2-}$  structure is gradually destructed, Be ions start to diffuse by themselves. At  $t > 60\text{ fs}$ , Be ions

break through the tetragonal binding structure and enter the linear diffusion region. In this region, the diffusion coefficient of Be ions is smaller than that of F ions. This is due to the exchange of fluorine ions between neighboring  $BeF_4^{2-}$  and  $LiF$  units, or it is due to fluorine diffusion by means of a neutral ion pair, such as  $LiF$  [42].

The temperature dependence of MSD of FLiBe is shown in Figure 5-7. As the diffusion effects increase with higher temperature, the slopes of MSDs increase with higher temperature. According to Eq. (2.2.9), the classical width function,  $w(t)$ , is directly proportional to  $\delta r^2(t)$ . This equation is applied to evaluate  $w(t)$  for FLiBe. The shape of  $w(t)$  will therefore be the same as Figure 5-6 except for the different units.

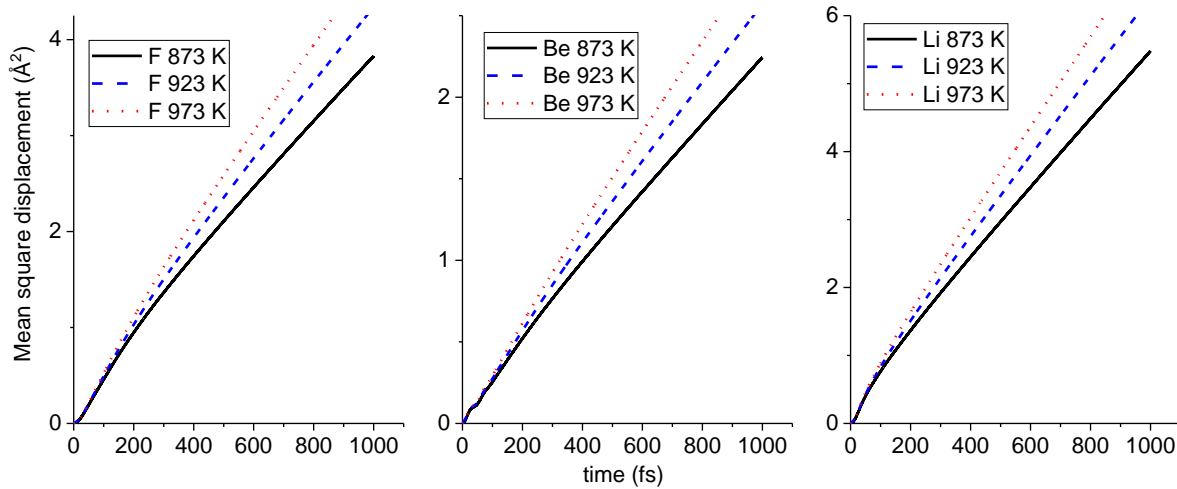


Figure 5-7. Temperature dependence of MSD of FLiBe at representative reactor core temperatures of 873 K, 923 K and 973 K.

By applying Eq. (2.5.3) to (2.5.5), the classical width function can be corrected to the quantum width function. Figure 5-8 graphs the quantum width functions  $\gamma(t)$  for each species of FLiBe at 873 K, with  $t_{tot} = 100$  fs and  $\Delta t = 0.01$  fs as an example. From Figure 5-11 to Figure 5-13, the real part and imaginary part of the quantum corrected width function  $\gamma(t)$  are compared to the classical width function  $w(t)$ . As can be seen in Figure 5-8, the real part of  $\gamma(t)$  is an even function of time  $t$ , while the imaginary part of the function is an odd function of time  $t$ . The imaginary part

is smaller than the real part of  $\gamma(t)$ . Therefore, the magnitude of the width function, which represents the atom motion states, is majorly contributed by its real part.

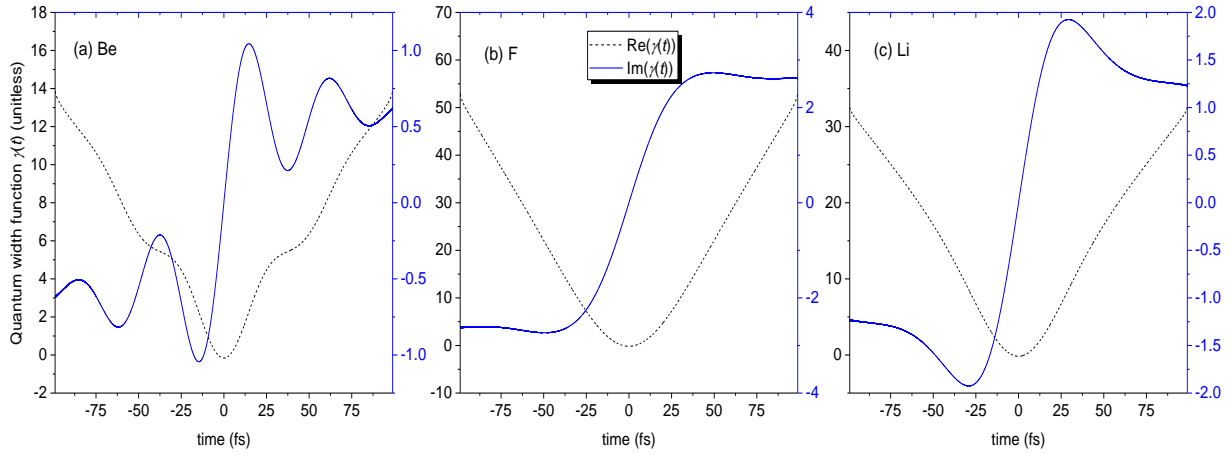


Figure 5-8. The quantum width function  $\gamma(t)$  of: (a) Be, (b) F, (c) Li in FLiBe. The real part and imaginary part are shown as black dashed line and blue solid line for all species.

The temperature dependence of the real part and the imaginary part of the quantum width function is illustrated in Figure 5-9 and Figure 5-10. The quantum width functions for Be and F in FLiBe exhibit the same trend with temperature. As we can see, the real part of the quantum width function tends to increase with higher temperature. At both positive and negative time, the increase in the real part is the same. However, the imaginary part of the quantum width function is asymmetric. At negative time, the width function decreases with higher temperature, and vice versa. This would result in an increasing phase shift in the intermediate scattering function.

As shown from Figure 5-11 to Figure 5-13, the real part of the quantum width function  $\text{Re}[\gamma(t)]$  is close to the classical width function  $w(t)$ . As discussed in Section 2.3, the total width function is a composite of atomic motions, such as vibration, diffusion, and rotation. The nearly identical  $\text{Re}[\gamma(t)]$  and  $w(t)$  function indicates that the motion modes captured in the classical width function are entirely passed on to the quantum width function. This is because the quantum

correction procedure requires no decomposition and recombination of motion models. Thus the effects on the width function is minimum.

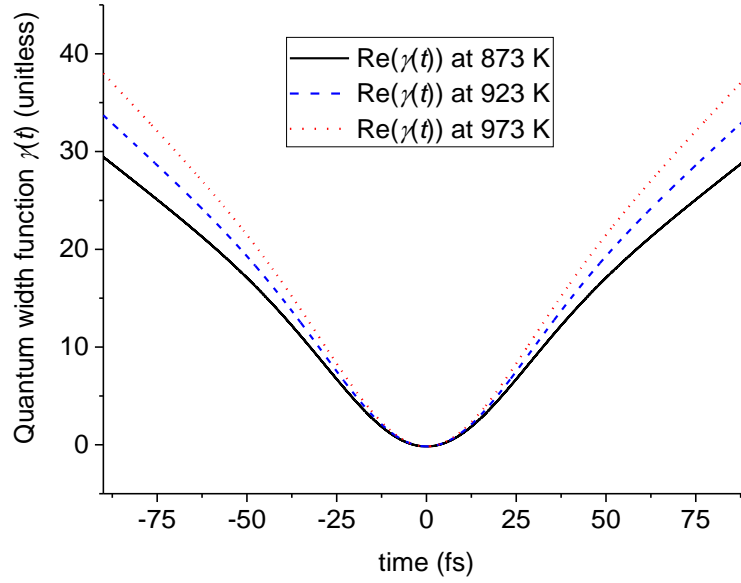


Figure 5-9. The real part of the quantum width function at different temperatures for Li in FLiBe.

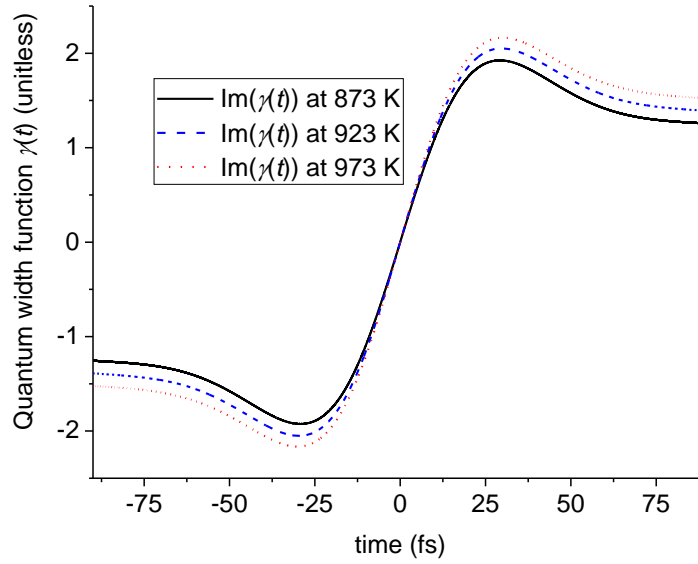


Figure 5-10. The imaginary part of the quantum width function at different temperatures for Li in FLiBe.

The imaginary part of the quantum width function  $\text{Im}[\gamma(t)]$ , on the other hand, stems from the quantum nature of the atoms moving and interacting in the system as a quantum thermal cloud.

The imaginary part represents the phase of the intermediate scattering function  $I(k, t)$ . While the phase does not introduce new information about the motion states of the system, it creates asymmetry of the  $I(k, t)$  function by introducing a phase shift. The phase shift is also predicted by the fluctuation-dissipation theorem [91]. This phenomenon is demonstrated in detail in the following section's discussion.

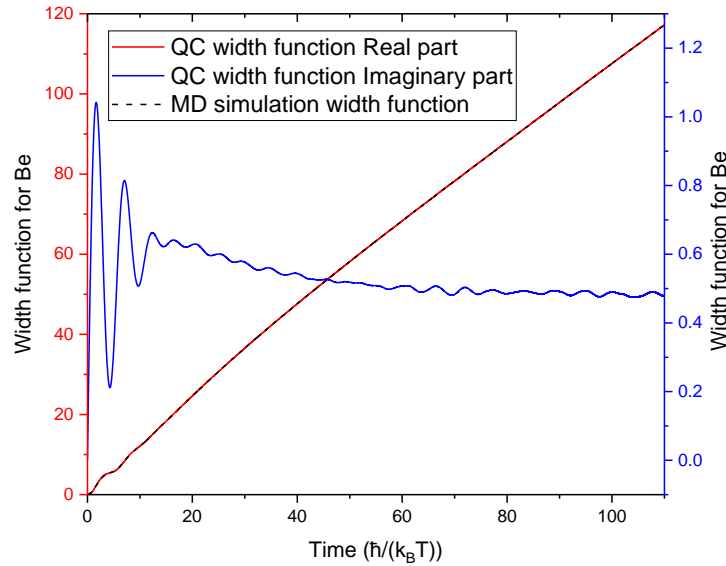


Figure 5-11. The quantum corrected width function and classical width function from MD simulation of Be in FLiBe.

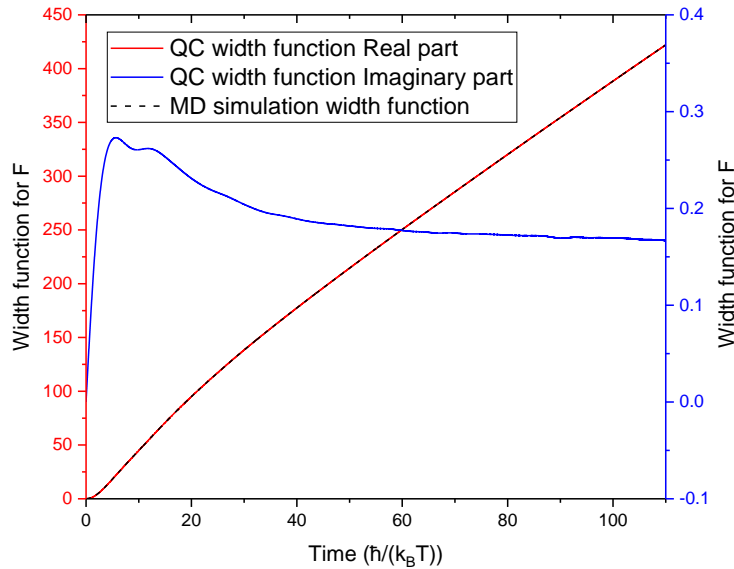


Figure 5-12. The quantum corrected width function and classical width function from MD simulation of F in FLiBe.

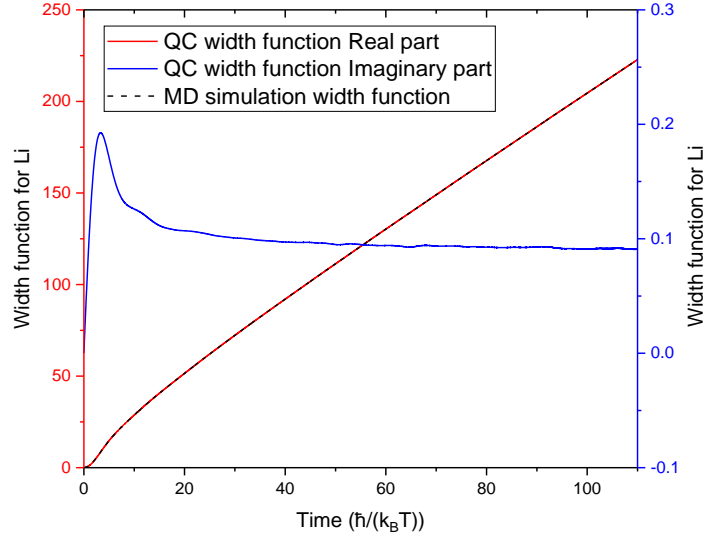


Figure 5-13. The quantum corrected width function and classical width function from MD simulation of Li in FLiBe.

### 5.2.2 The Self Intermediate Scattering Function of FLiBe

As demonstrated in Section 4.5, the same width function with different time scale  $t_{tot}$  and resolution  $\Delta t$  can be applied at different  $k$  ranges to accommodate resolution requirements for  $I_s(k, t)$ . In the previous section, three quantum width functions at different time scale  $t_{tot}$  were evaluated. These quantum width functions evaluated in the previous section can be utilized with Eq. (2.2.13) to calculate the self intermediate scattering function  $I_s(k, t)$ .

In this work, an automatic algorithm was written to determine the time resolution  $\Delta t$  requirement at different  $k$  values for  $I_s(k, t)$ . Five hundred and twenty eight  $k$  values from  $0.001 \text{ \AA}^{-1}$  to  $100 \text{ \AA}^{-1}$  are used to evaluate  $I_s(k, t)$ . Figure 5-14 shows the self intermediate scattering function  $I_s(k, t)$  at small  $k$  ( $0.2 \text{ \AA}^{-1}$ ), mid-range  $k$  ( $33.8 \text{ \AA}^{-1}$ ), and large  $k$  ( $60 \text{ \AA}^{-1}$ ) for each species in FLiBe at 873 K. Note that in this plot, the time range on the x-axis decreases as  $k$  increases from small  $k$  to large  $k$ . In the small  $k$  ( $0.2 \text{ \AA}^{-1}$ ) region,  $I_s(k, t)$  extends to the longest time scale (around 300 ps). This phenomenon can be explained from the material structure



perspective. The  $I_s(k, t)$  at small  $k$  represents structure information at large distance  $r$  in real space. This scale of distance is closely related to the diffusional behavior which happens at long times  $t$ . To contain this behavior,  $I_s(k, t)$  extends to a long time scale at small  $k$ . Therefore, the calculation of  $I_s(k, t)$  at small  $k$  applies the width function with the longest time window  $t_{tot}$  and the largest resolution  $\Delta t = 1$  fs, such as shown in the first row in Figure 5-14.

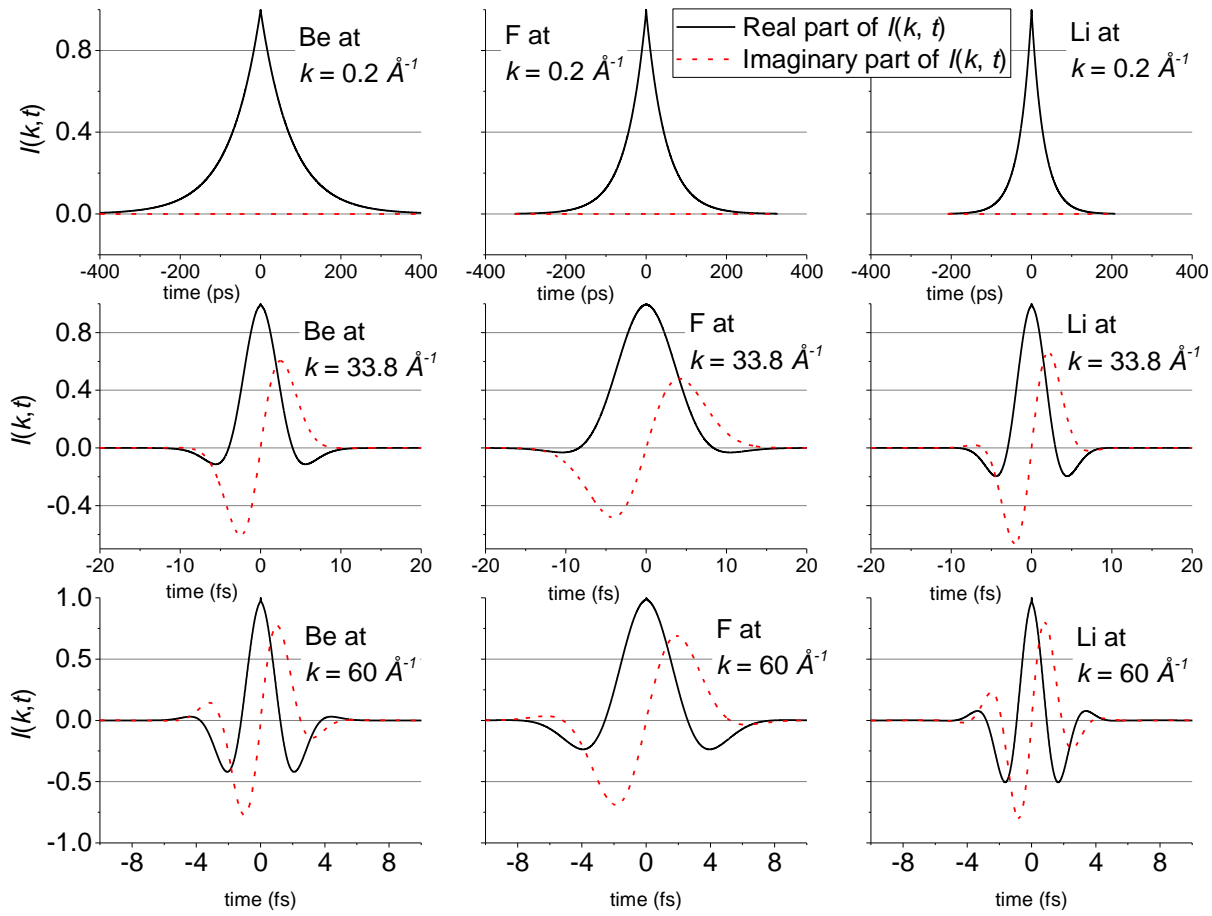


Figure 5-14. The self intermediate scattering function,  $I_s(k, t)$ , of each species in FLiBe at small  $k$  ( $0.2 \text{ \AA}^{-1}$ ), mid-range  $k$  ( $33.8 \text{ \AA}^{-1}$ ), and large  $k$  ( $60 \text{ \AA}^{-1}$ ).

The  $I_s(k, t)$  at large  $k$ , vice versa, represents structural information at small  $r$  and neutron scattering events at large momentum transfers. At small  $r$ , the particles in the system are moving around the equilibrated position without colliding into each other. Therefore, the system behavior

at small  $r$  is close to that of a free gas. This behavior is only maintained at a small characteristic time. From the neutron scattering perspective, neutron scattering for large momentum transfers favors high energy neutron and a small scattering interaction time  $t$ . Therefore, the calculation at the large  $k$  range applies the width function with the smallest time window  $t_{tot}$  and the smallest resolution  $\Delta t = 0.01 \text{ fs}$ .

In the mid-range  $k$ , as  $t$  increases, the atoms start to collide with their neighbor atoms and diffuse through the system. The small  $r$  free gas behavior is no longer valid. As discussed above, the system transitions between the free gas behavior and the diffusional behavior. In the meantime, as the atoms deviate from their original equilibrium positions, they dynamically relocate themselves to find new equilibrium positions. As this process accumulates at long  $t$ , the linear diffusional behavior dominates. The  $I_s(k, t)$  function in the mid-range  $k$  should therefore use mid-range  $t_{tot}$  and a resolution of  $\Delta t = 0.1 \text{ fs}$ .

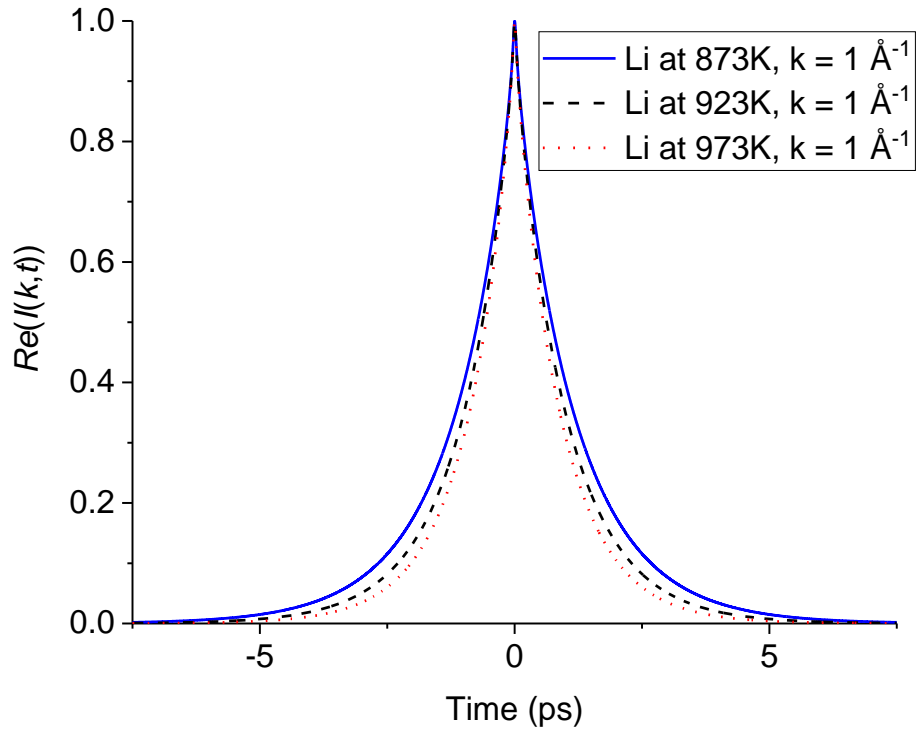


Figure 5-15. The real part of intermediate scattering function of Li in FLiBe at different temperatures.

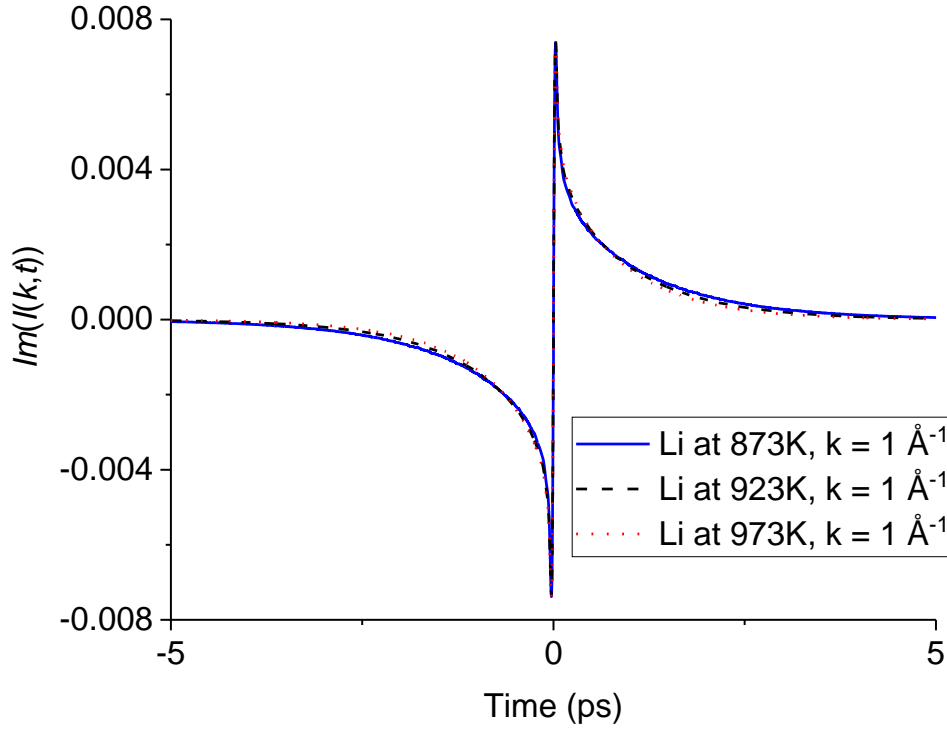


Figure 5-16. The imaginary part of intermediate scattering function of Li in FLiBe at different temperatures.

The evaluated  $I_s(k, t)$  is a complex function with an even real part and odd imaginary part. At small  $k$ , the imaginary part is close to 0. As  $k$  increases, the imaginary part gradually increases to the magnitude of the real part. This increasing imaginary part will create more and more phase shift in Fourier transform. As it will be seen in the next section, this increasing phase shift introduces more obvious detailed balance behavior in  $S_s(\alpha, \beta)$ .

The temperature dependence of  $I(k, t)$  is shown in Figure 5-15 and Figure 5-16. Li in FLiBe is taken as an example. As the real part of the quantum width function of FLiBe increases with increasing temperature (Figure 5-9), the real part of  $I(k, t)$  becomes narrower with increasing temperature. It can be predicted that the decreased-width  $I(k, t)$  would introduce a wider  $S(\alpha, \beta)$  after Fourier transform, which would result in higher scattering cross section at higher temperature.

This phenomenon will be proven in later section. The imaginary part of  $I(k, t)$ , on the contrary, did not show too much difference with increasing temperature. This is because the increase in the imaginary part of the quantum width function (Figure 5-10) is compensated by the increase in the real part. As a result, though the change in the imaginary part of  $I(k, t)$  is relatively small, the decreasing in the real part makes the imaginary part of  $I(k, t)$  more significant, which contributes to higher phase shift of  $I(k, t)$ . In conclusion, with increasing temperature, higher quantum effects are observed.

### 5.2.3 The Self Thermal Scattering Law of FLiBe

The self thermal scattering law  $S_s(k, \omega)$  is known to be the Fourier transform of the  $I_s(k, t)$  function. However, in the thermal neutron scattering field, instead of using the dynamic structure factor  $S_s(k, \omega)$ , the thermal scattering law  $S(\alpha, \beta)$  is more conventionally tabulated to evaluate scattering cross sections.

In this work, instead of rescaling the dynamic structure factor  $S_s(k, \omega)$  to the thermal scattering law,  $I_s(k, t)$  is preprocessed to directly produce  $S_s(\alpha, \beta)$ . If the reciprocal space vector  $k$  in  $I_s(k, t)$  is pre-scaled to unitless momentum transfer  $\alpha$  and time  $t$  pre-scaled to time  $t'$  with unit  $\hbar/k_B T$ , the Fourier transform of the scaled  $I_s(\alpha, t')$  function will directly generate  $S_s(\alpha, \beta)$ . In this work, the Fourier transforms were performed on the pre-scaled  $I_s(\alpha, t')$ . The evaluated  $S_s(\alpha, \beta)$  for each species in FLiBe are plotted in Figure 5-17 to Figure 5-19. As can be seen, at small  $\alpha$ , the  $S_s(\alpha, \beta)$  demonstrates much less asymmetric behavior. As  $\alpha$  increases, the asymmetric character of  $S_s(\alpha, \beta)$  also increases. The  $S_s(\alpha, \beta)$  at high  $\alpha$  is dominated by negative energy transfer ( $\beta < 0$ ). As stated in the previous section, this increase in asymmetric character of

$S_s(\alpha, \beta)$  with increasing  $\alpha$  is caused by the increasing phase shift of  $I_s(k, t)$  in the Fourier transforms.

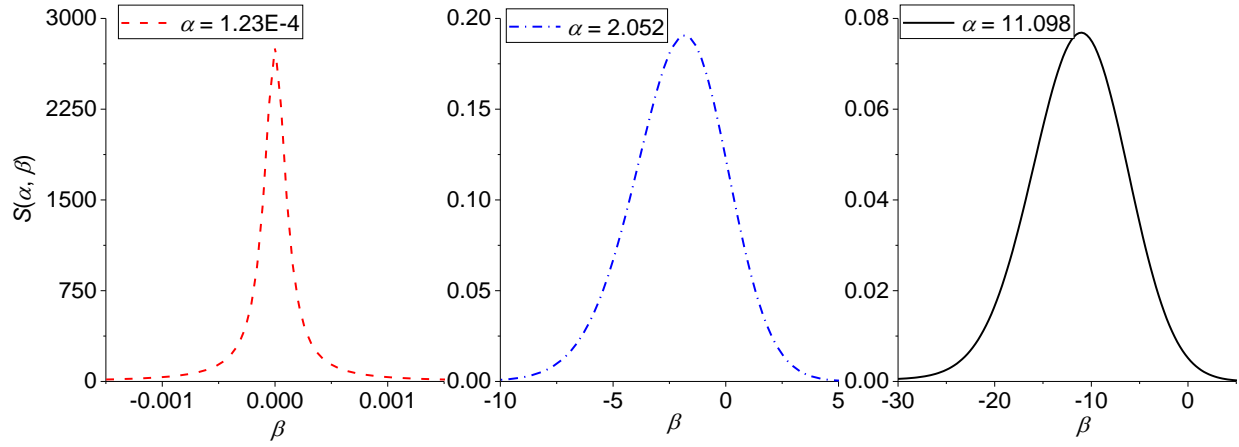


Figure 5-17. The asymmetric  $S_s(\alpha, \beta)$  for Be in FLiBe against  $\beta$  at different  $\alpha$  at 873 K.

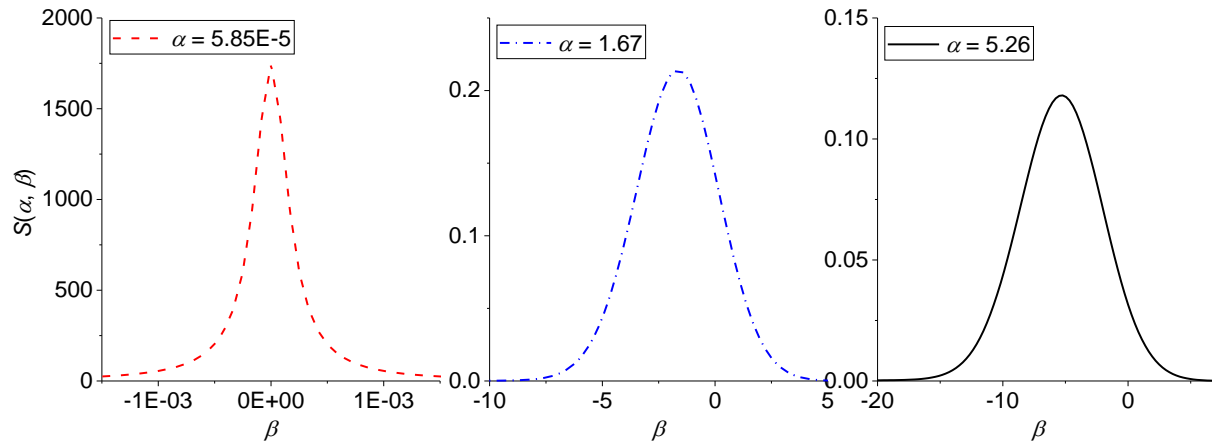


Figure 5-18. The asymmetric  $S_s(\alpha, \beta)$  for F in FLiBe against  $\beta$  at different  $\alpha$  at 873 K.

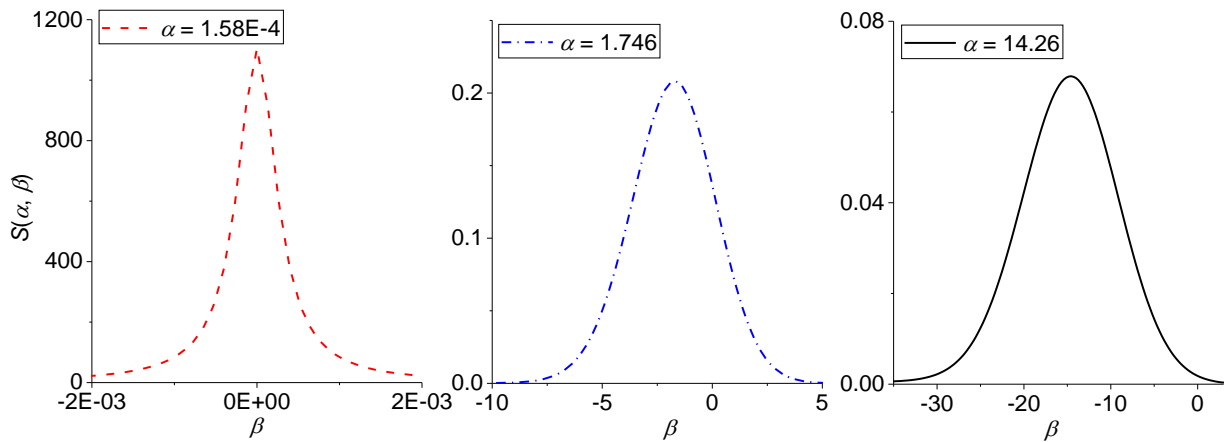


Figure 5-19. The asymmetric  $S_s(\alpha, \beta)$  for Li in FLiBe against  $\beta$  at different  $\alpha$  at 873 K.

The temperature dependence of  $S_s(\alpha, \beta)$  of FLiBe is shown in Figure 5-20. According to Eq. (2.1.10) and (2.1.11),  $\alpha$  and  $\beta$  are scaled differently at different temperatures. Because of this,  $S_s(\alpha, \beta)$  at different temperatures would not be comparable. In Figure 5-20,  $S_s(k, \omega)$ , instead of  $S_s(\alpha, \beta)$ , is compared at different temperatures. The scattering law in Figure 5-20 corresponds to plots using intermediate  $\alpha$  values in Figure 5-17 to Figure 5-19. As can be seen, the scattering law increases with increasing temperature. The width of the scattering law is also increasing due to increasing width function. As discussed in the previous section, the decrease in the width of  $I(k, t)$  will result in the increase in the width in  $S(\alpha, \beta)$ . Figure 5-20 proves this prediction. The peak value of the scattering law, which locates on the positive  $\omega$ , increases more than the tails.

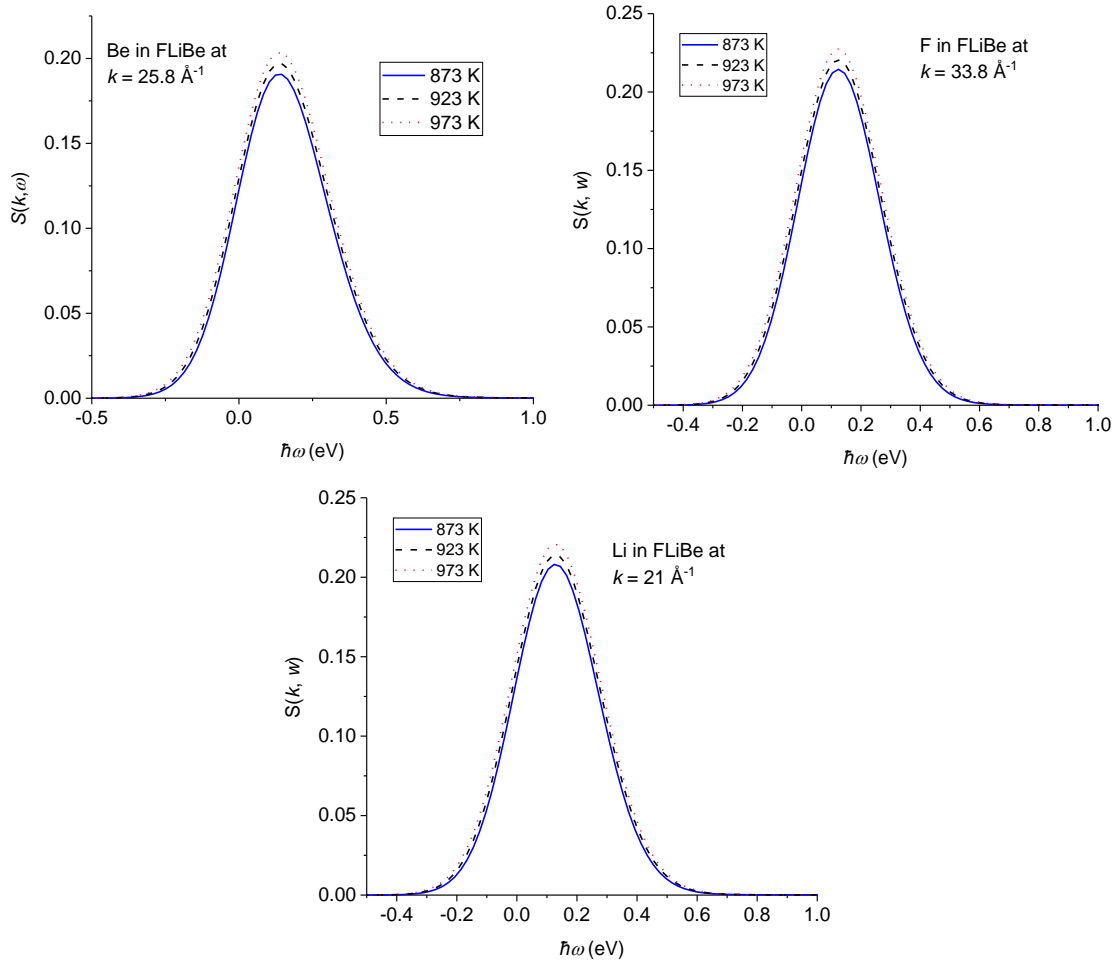


Figure 5-20. The asymmetric  $S_s(k, \omega)$  for FLiBe at different representative reactor core temperatures.

The moments of  $S_s(\alpha, \beta)$  can also be used to validate the quantum characteristic. The  $0^{th}$  moment and  $1^{st}$  moment of  $S_s(\alpha, \beta)$  for each species in FLiBe at 873 K are shown in Figure 5-21 to Figure 5-23. As can be seen, the sum rules are in excellent agreement with their theoretical predictions, i.e. 1 for the  $0^{th}$  moment,  $\alpha$  for the  $1^{st}$  moment. Detailed investigation shows that the evaluated thermal scattering law follows the principle of detailed balance rigorously. As an example, the test of detailed balance behavior for Be in FLiBe at  $\alpha = 2.052$  is plotted in Figure 5-24.

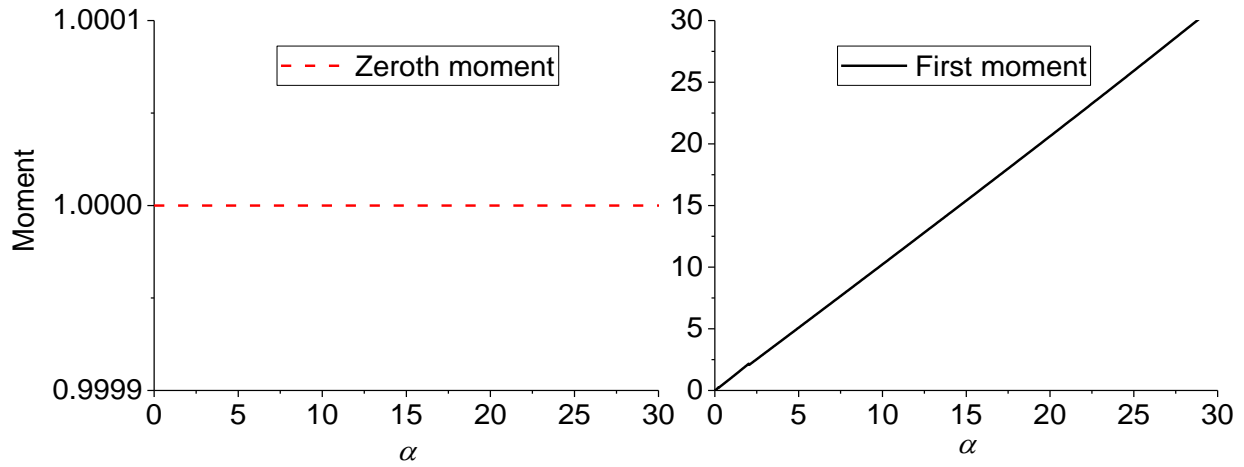


Figure 5-21. Moments of Be in FLiBe at 873K.

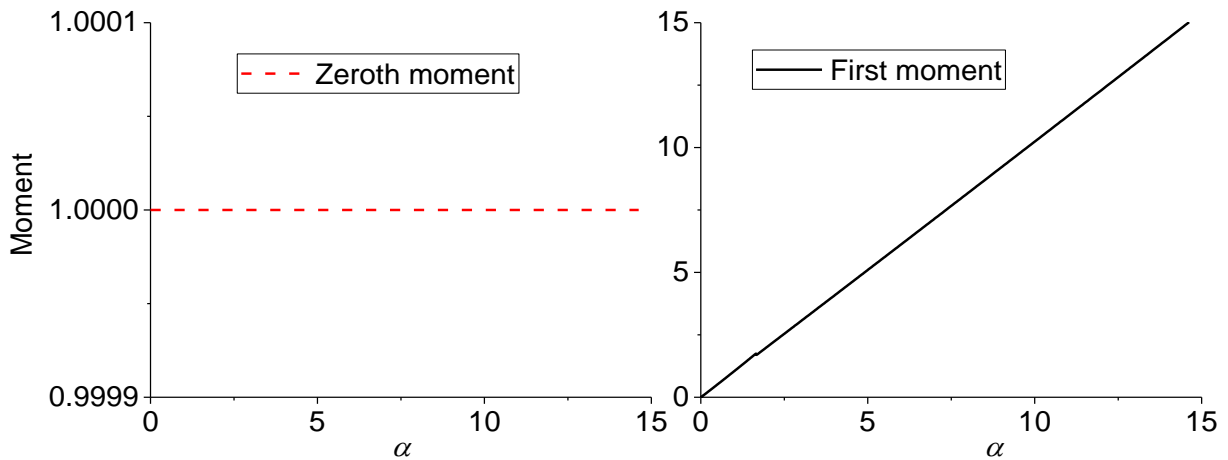


Figure 5-22. Moments of F in FLiBe at 873K.

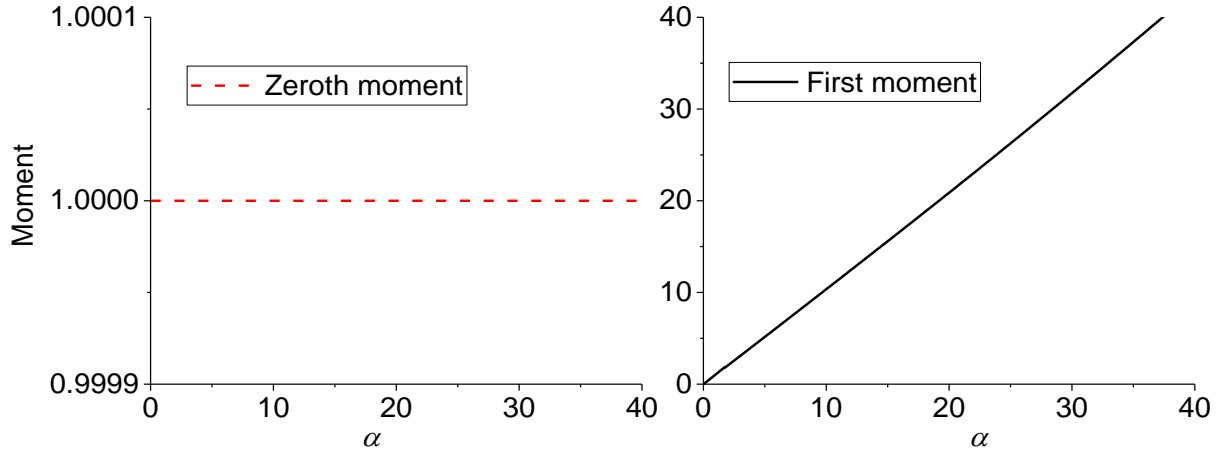


Figure 5-23. Moments of Li in FLiBe at 873K.

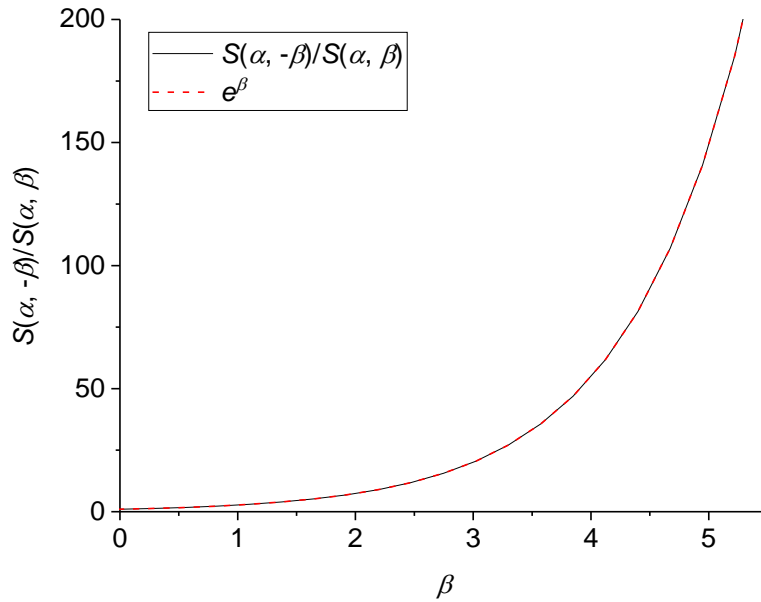


Figure 5-24. Detailed balance behavior of Be in FLiBe at  $\alpha = 2.052$ .

#### 5.2.4 The Thermal Scattering Law of FLiBe Including Distinct Effects

In Section 4.6, the quantum correction including distinct effects was demonstrated for liquid lithium. In this section, instead of using the notation  $\Gamma(\alpha)$ , which uses  $\alpha$  that depends on temperature,  $\Gamma(k)$  is going to be discussed because it removes the temperature dependence. Based on the scattering law evaluated in the previous section, the quantum corrected thermal scattering



law for Be, F, Li in FLiBe including the distinct effects was evaluated. Following the flowchart in Figure 4-20, as the first step, the classical thermal scattering law  $S^{cl}(k, \omega)$  and  $S_s^{cl}(k, \omega)$  was evaluated. Evaluated  $S^{cl}(k, \omega)$  and  $S_s^{cl}(k, \omega)$  at  $\omega = 1.819 \text{ THz}$  or  $\beta = 0.1$  are shown in Figure 5-25 as an example.

In this work,  $I^{cl}(k, t)$  of FLiBe as a compound including distinct effects was evaluated based on Eq. (3.5.2). The correlation between six different combinations of atom pairs are accounted, i.e. the Be-Be pairs, the F-F pairs, the Li-Li pairs, the Be-F pairs, the Be-Li pairs, and the F-Li pairs. The cross-type pairs, i.e. the Be-F pairs, the Be-Li pairs, and the F-Li pairs, are important in compound materials as they account for interactions between different species.  $I_s^{cl}(k, t)$  was also evaluated. The evaluated  $I^{cl}(k, t)$  and  $I_s^{cl}(k, t)$  are then Fourier transformed to  $\omega$  space as  $S^{cl}(k, \omega)$  and  $S_s^{cl}(k, \omega)$ .

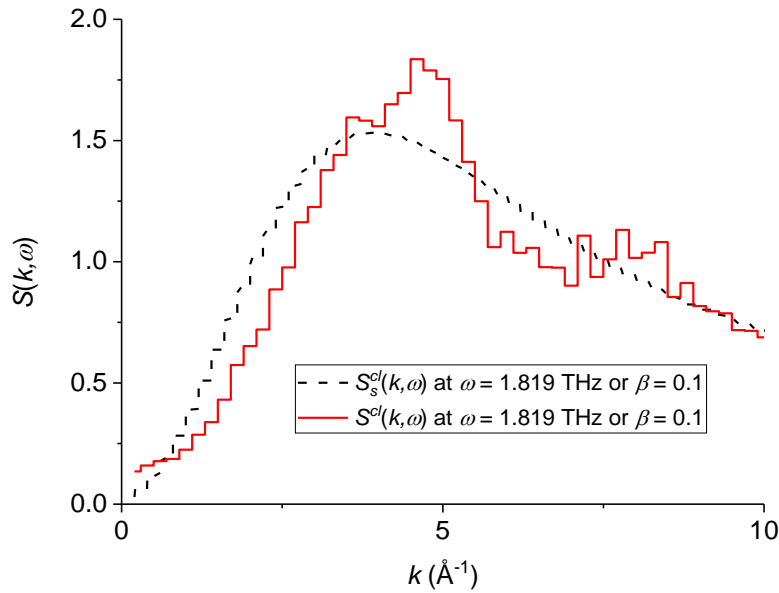


Figure 5-25. The classical thermal scattering law of FLiBe at  $\omega = 1.819 \text{ THz}$ . The red solid line is  $S^{cl}(k, \omega)$  including distinct effects, the black dashed line is  $S_s^{cl}(k, \omega)$  with no distinct effects.

A higher and a lower cutoffs were chosen to evaluate the  $\Gamma(k)$  function. In Figure 5-25, the major divergence between the self and the coherent classical dynamic structure factor is below 9

$\text{\AA}^{-1}$ . Above this reciprocal space distance, distinct effects will be washed out by the random orientation and the averaging effects of the FLiBe liquid. Therefore, it is safe to extrapolate the  $\Gamma(k)$  function as constant one above  $10 \text{\AA}^{-1}$  cutoff. The lower cutoff of the  $\Gamma(k)$  function is set to be  $3 \text{\AA}^{-1}$ . This limit is determined by the MD simulation size. Due to the limited size of simulation box, the resolution of the  $k$  space mesh grid is limited. Therefore, below  $3 \text{\AA}^{-1}$  the sampling of  $I^{cl}(k, t)$  becomes more uncertain. To achieve smaller  $k$  in the evaluation, a larger simulation box must be utilized. However, larger simulation box will exponentially increase the CPU wall time for evaluating the  $I^{cl}(k, t)$ . As an optimized model, a  $21.84 \text{\AA}$  simulation box with 875 atoms was used to evaluate the classical intermediate scattering function with distinct effects, i.e.  $I^{cl}(k, t)$ .

As the second step, the collective structural function  $\Gamma(\alpha)$  can be evaluated from Eq. (2.5.15). The ratio of classical distinct and self thermal scattering law was firstly evaluated at each  $\beta$ . Then the collective structural function  $\Gamma(\alpha)$  was calculated by averaging the ratios at available  $\beta$ . The evaluated  $\Gamma(\alpha)$  function is shown in Figure 5-26. As can be seen, there is enhanced correlation at  $4.5 \text{\AA}^{-1}$  and  $8.5 \text{\AA}^{-1}$ . The correlations at  $k < 4 \text{\AA}^{-1}$  and  $5 \text{\AA}^{-1} < k < 8 \text{\AA}^{-1}$  are diminished. Compared to the incoherent approximation, enhanced or diminished correlation results in a redistribution of scattering angle in a thermal neutron scattering event. This is shown in the differential cross section against scattering angles in the following discussion.

As the third step, the  $\Gamma(\alpha)$  function was applied on the quantum self thermal scattering law  $S_s^{qt}(\alpha, \beta)$ . Following Eq. (2.5.15), the self  $S_s^{qt}(\alpha, \beta)$  was multiplied by  $\Gamma(\alpha)$  to obtain  $S_d^{qt}(\alpha, \beta)$ .  $S_{tot}^{qt}(\alpha, \beta)$  was evaluated by Eq.(2.1.27) from weighting  $S_d^{qt}(\alpha, \beta)$  and  $S_s^{qt}(\alpha, \beta)$ . From Figure 5-27 to Figure 5-29, the total thermal scattering law  $S_{tot}^{qt}(\alpha, \beta)$  and the self thermal scattering law  $S_s^{qt}(\alpha, \beta)$  for each species in FLiBe are demonstrated at  $\beta = 0.1$ .

The Li species displays smaller distinct effects than Be and F in FLiBe. This is because the incoherent bound cross section is as large as the coherent bound cross section of Li. Therefore, the distinct thermal scattering law of Li is contributing only approximately 25% to the total thermal scattering law of Li. In comparison, the total thermal scattering laws,  $S_{tot}^{qt}(\alpha, \beta)$ , of Be and F species in FLiBe consist of almost 50% distinct thermal scattering law,  $S_d^{qt}(\alpha, \beta)$ .

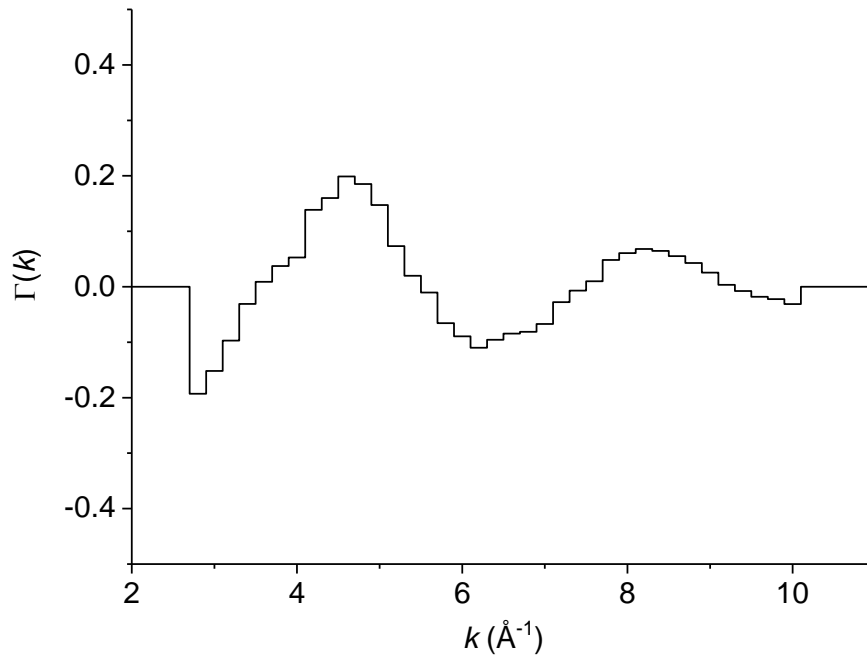


Figure 5-26. The collective structural function of FLiBe.

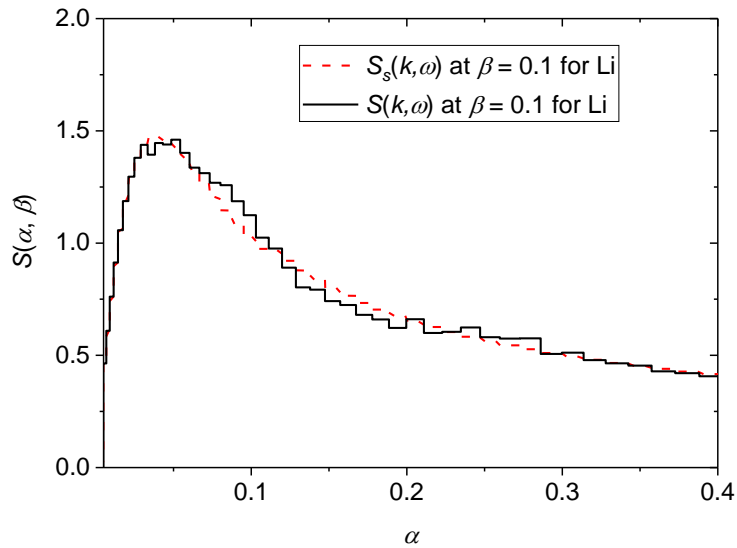


Figure 5-27. The total and the self thermal scattering law for Li in FLiBe at  $\beta = 0.1$ .

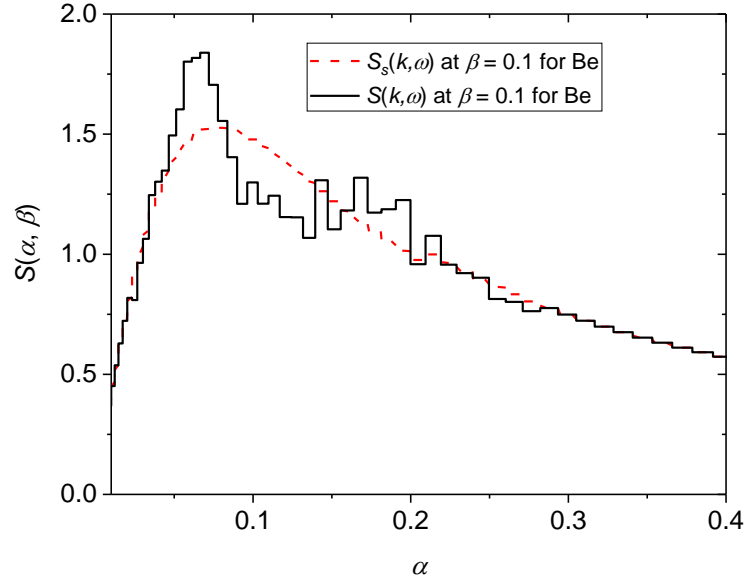


Figure 5-28. The total and the self thermal scattering law for Be in FLiBe at  $\beta = 0.1$ .

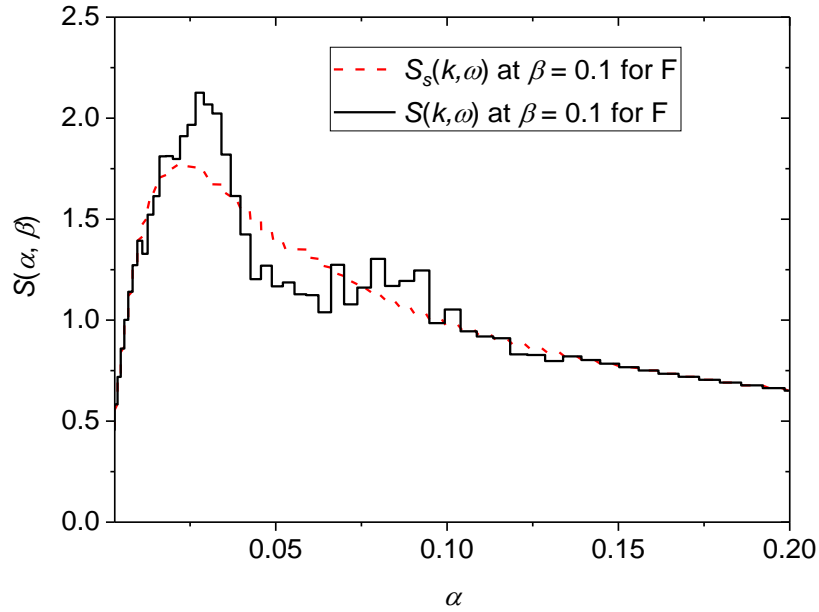


Figure 5-29. The total and the self thermal scattering law for F in FLiBe at  $\beta = 0.1$ .

### 5.3 The Thermal Scattering Cross Section of FLiBe Using the MD TSL

In this section, the thermal neutron scattering cross section of each species in FLiBe will be evaluated and discussed. Firstly, the double differential cross sections for each species in FLiBe are generated based on the total thermal scattering law  $S_{tot}^{qt}(\alpha, \beta)$ , which was evaluated in the

previous section as a weighted sum of the coherent thermal scattering law and the self thermal scattering law. Secondly, the differential cross sections,  $d\sigma/dE'$  and  $d\sigma/d\mu$ , are evaluated by integrating the double differential cross section over the scattering angles  $\mu$  or the secondary energies  $E'$ . Finally, an integral over the secondary energies,  $E'$ , or the scattering angle,  $\mu$ , is executed, and the integrated cross section of FLiBe is obtained.

### 5.3.1 The Double Differential Thermal Scattering Cross Section of FLiBe

The double differential cross section formula, Eq. (2.1.26), can be applied to evaluate the thermal neutron scattering cross section from  $S(\alpha, \beta)$ . In conventional thermal neutron scattering processing codes, such as NJOY and GASKET, the cross section is evaluated under the incoherent approximation. Under this approximation, the distinct thermal scattering law is ignored. Hence the total thermal scattering law can be approximated by the self thermal scattering law,  $S_{tot}(\alpha, \beta) \approx S_s(\alpha, \beta)$ . In this work, the  $S_{tot}(\alpha, \beta)$  was evaluated as a weighted sum in Section 5.1.4. The inclusion of distinct effects removes the incoherent approximation and the Gaussian approximation. The double differential cross section depends on two variables, i.e. the secondary energy and the scattering angle. In Figure 5-30 to Figure 5-32, the cross section is plotted against the secondary neutron energies at six fixed scattering angles, i.e. 30°, 60°, 90°, 120°, 150°, 180°.

As can be seen in all scattering cross sections, when the scattering angle increases, the secondary neutron spectrum broadens to a wider range. This is a result of larger momentum transfer in a larger scattering angle event. The up-scattering phenomenon is also becoming more prominent at larger scattering angles.

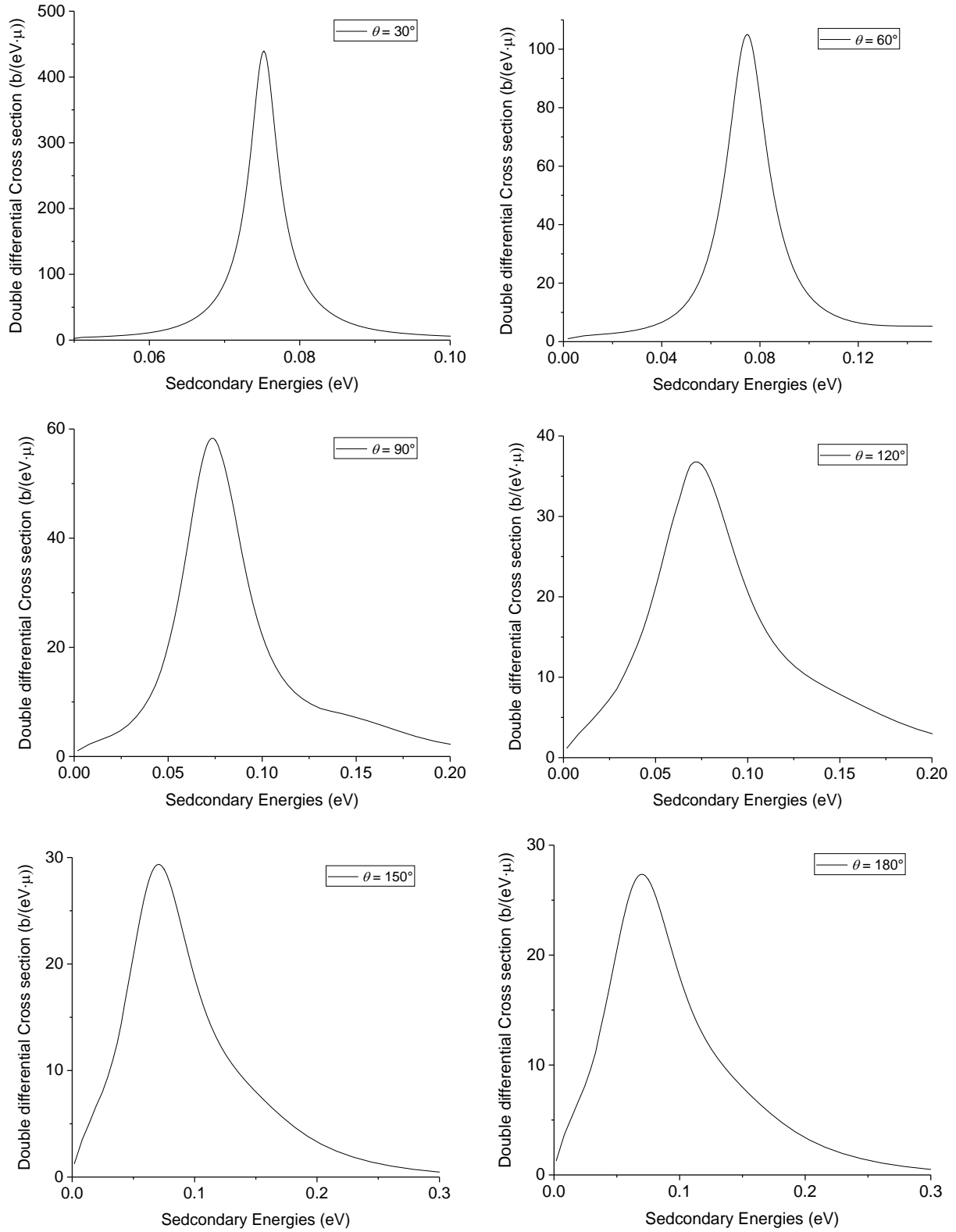


Figure 5-30. Double differential cross section of Be in FLiBe at  $\theta = 30^\circ, 60^\circ, 90^\circ, 120^\circ, 150^\circ, 180^\circ$ . The plot is evaluated at 873 K and  $E_{in} = 0.075$  eV.

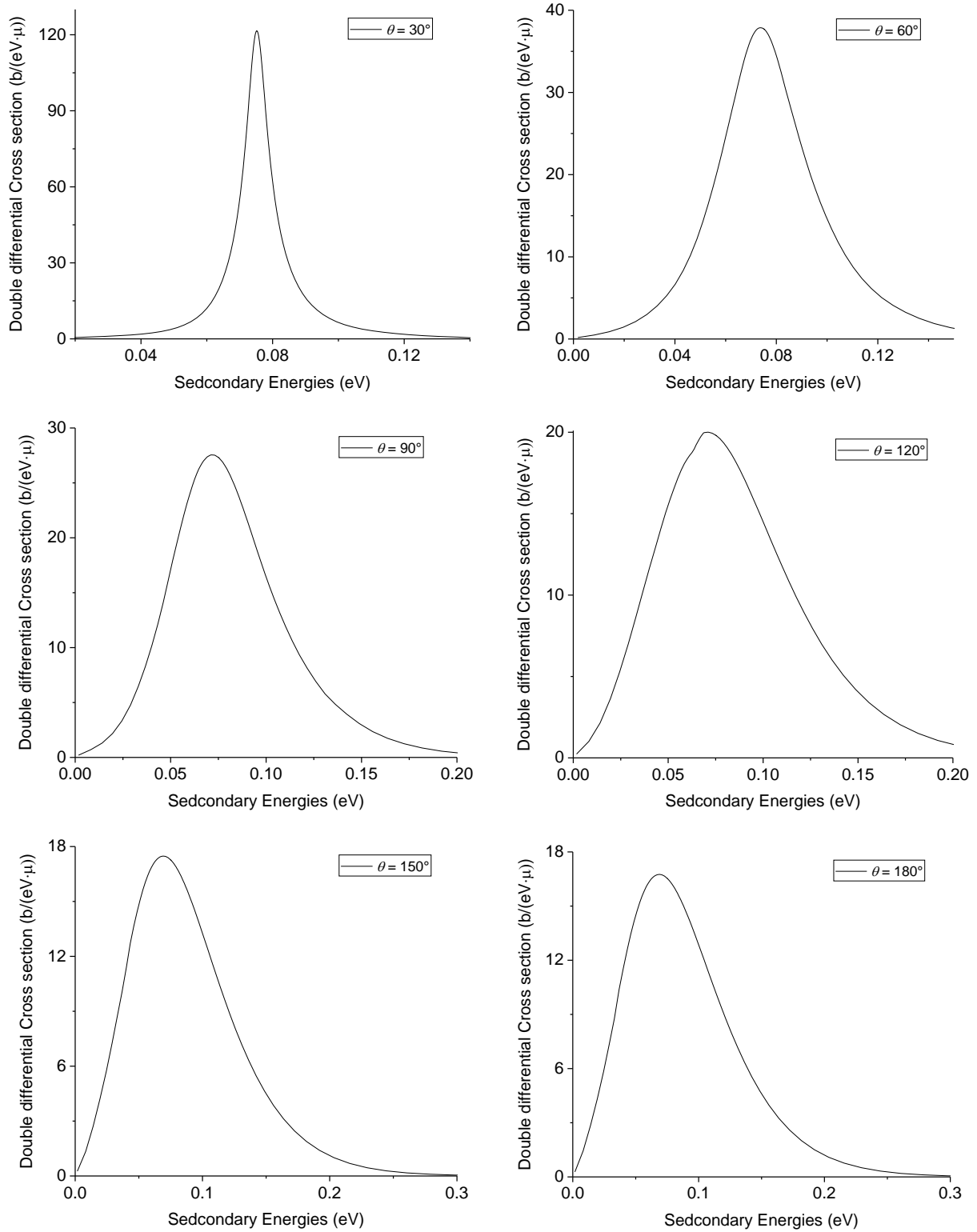


Figure 5-31. Double differential cross section of F in FLiBe at  $\theta = 30^\circ, 60^\circ, 90^\circ, 120^\circ, 150^\circ, 180^\circ$ . The plot is evaluated at 873 K and  $E_{in} = 0.075$  eV.

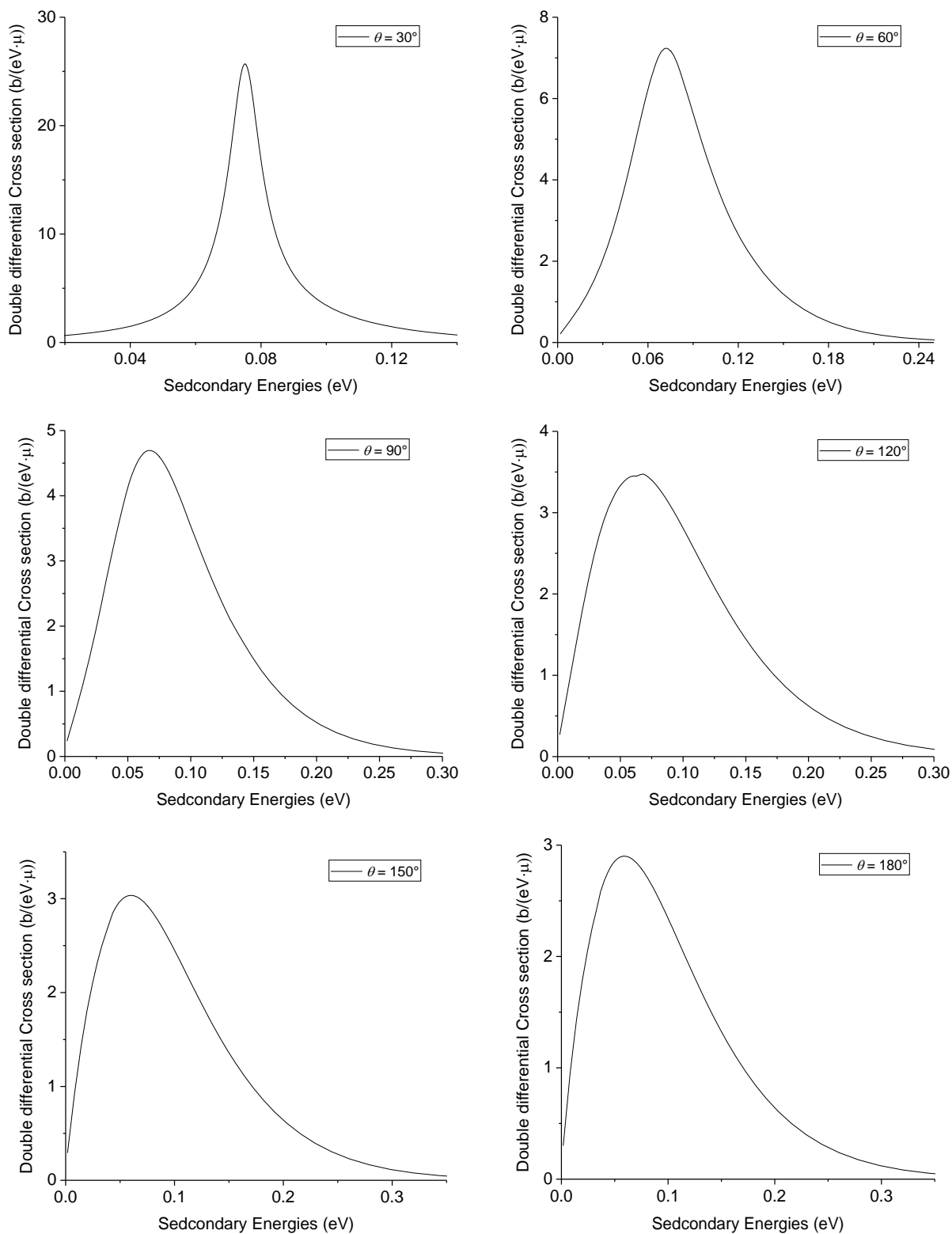


Figure 5-32. Double differential cross section of Li in FLiBe at  $\theta = 30^\circ, 60^\circ, 90^\circ, 120^\circ, 150^\circ, 180^\circ$ . The plot is evaluated at 873 K and  $E_{in} = 0.075$  eV.



The most probable scattering peak is located at the incident energy. As the scattering approaches small angle, the peak becomes sharper and eventually a  $\delta$ -like function. This  $\delta$ -like peak will be further discussed in the next chapter. The quasi-elastic scattering peak in  $d\sigma/dE'$  is characterized by this  $\delta$ -like peak at small scattering angle plus other most probable peaks around the incident energy.

The temperature dependence of double differential cross section is shown in Figure 5-33.

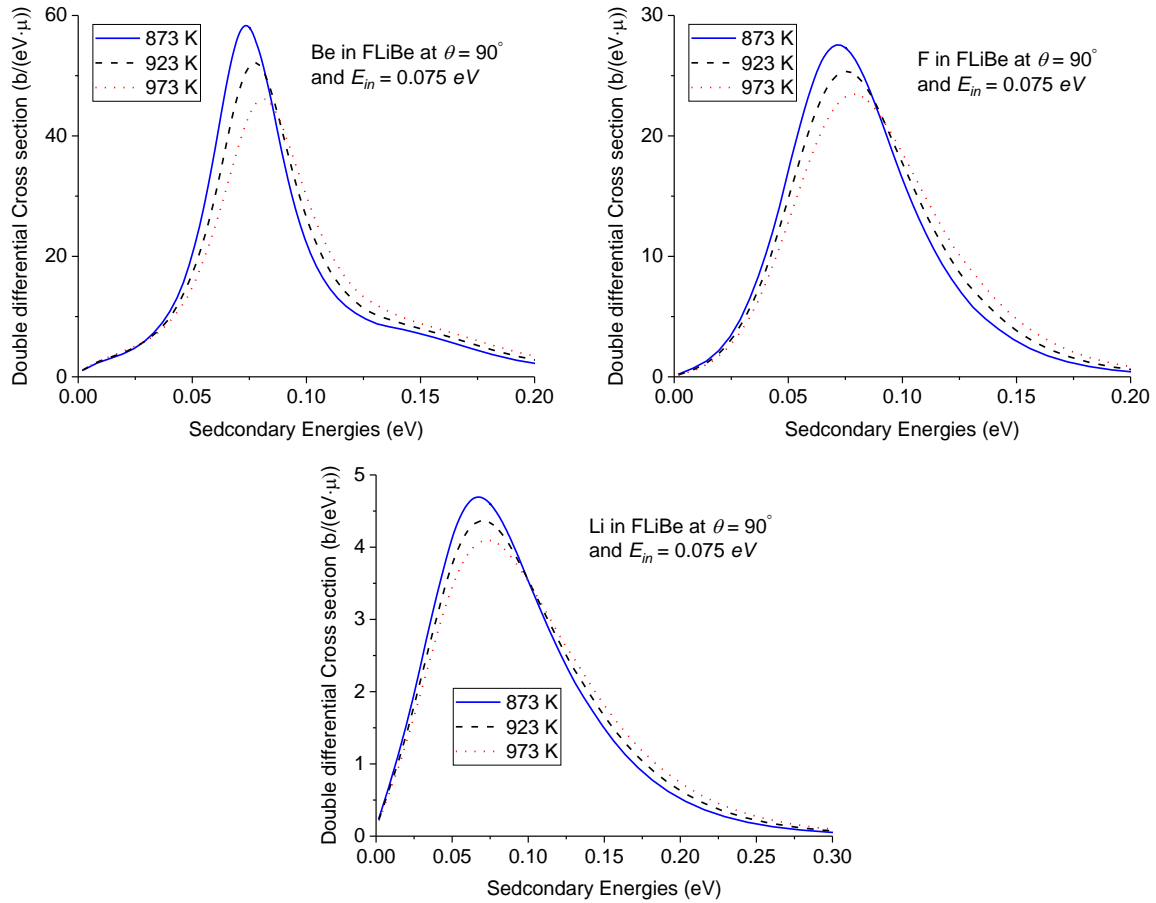


Figure 5-33. Double differential cross section of FLiBe at different representative reactor core temperatures.

The cross sections are evaluated at an incident energy of 0.075 eV and scattering angle 90°. As the temperature increases, the probability of small energy transfer decreases, while the probability of large energy transfer increases. Despite the increase of diffusive behavior with

increasing temperature, the magnitude of the quasi-elastic diffusional peak in  $S(\alpha, \beta)$  decreases. This eventually results in decreased small energy transfer states available in double differential cross section. As temperature increases, the increase in thermal movement in the system of interaction increases the probability of up scattering at large energy transfers.

Overall, larger energy transfer becomes more possible, the height of diffusional peak decreases. As it will be shown later, this phenomenon is consistent with the behavior in the differential cross section.

### 5.3.2 The Differential Thermal Scattering Cross Section of FLiBe

The integral of the double differential cross section  $d^2\sigma/d\mu dE'$  from the previous section over  $\mu$  or  $dE'$  will generate the differential cross section  $d\sigma/dE'$  or  $d\sigma/d\mu$ . The actual integral is executed on the  $S(\alpha, \beta)$  in the  $\alpha, \beta$  space. The integral bounds can be determined by the physically possible energy and momentum transfers.

The scattering angle  $\mu$ , i.e.  $\cos(\theta)$ , ranges from -1 to 1 with the scattering angle  $\theta$  varies between  $180^\circ$  and  $0^\circ$ . Since  $\alpha$  is directly correlated to the scattering angle by Eq. (2.1.10), the lower and upper limits of possible momentum transfer in an scattering event are:

$$\alpha_{\min} = \frac{E' + E_0 - 2\sqrt{E'E_0}}{Ak_B T}$$

$$\alpha_{\max} = \frac{E' + E_0 + 2\sqrt{E'E_0}}{Ak_B T}$$

The double differential cross section could be integrated against  $E'$ , which is equivalent to integrating  $S_{tot}(\alpha, \beta)$  against  $\beta$ , to obtain  $d\sigma/d\mu$ . The evaluated angular differential cross sections at different temperatures are illustrated in Figure 5-34 - Figure 5-36. Distinct effects, diffusional peaks, and temperature dependence can be clearly seen in these cross sections. It should

be noted that the y-axis in Figure 5-34 - Figure 5-36 are broken in the middle to better illustrate details of the angular distribution with the  $\delta$ -like small angle quasi-elastic scattering peak.

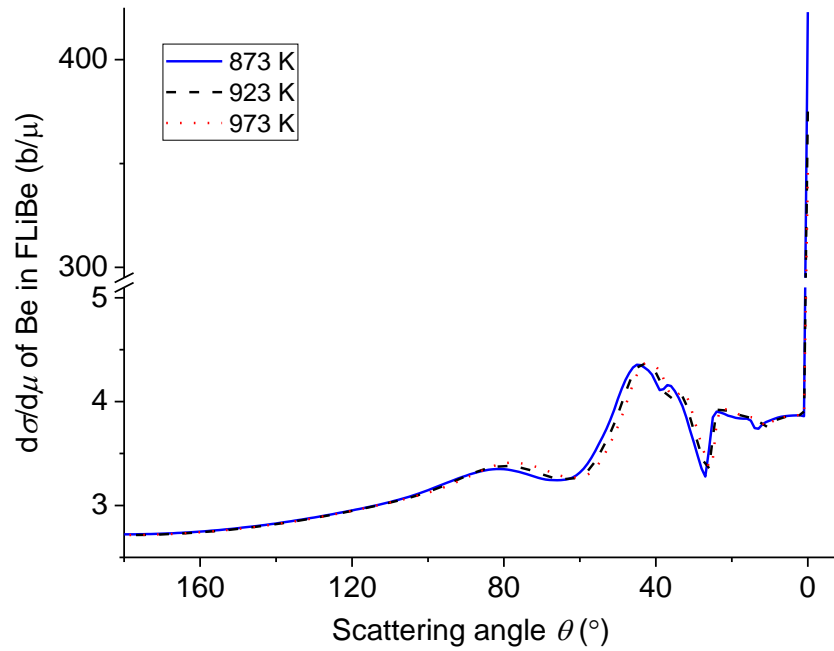


Figure 5-34. The angular differential cross section of Be in FLiBe at representative reactor core temperatures.

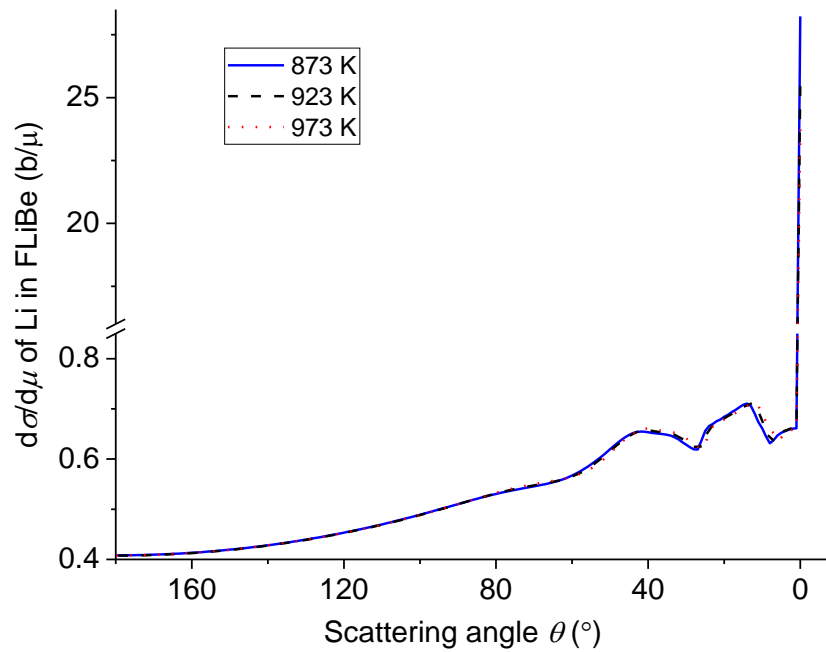


Figure 5-35. The angular differential cross section of Li in FLiBe at representative reactor core temperatures.

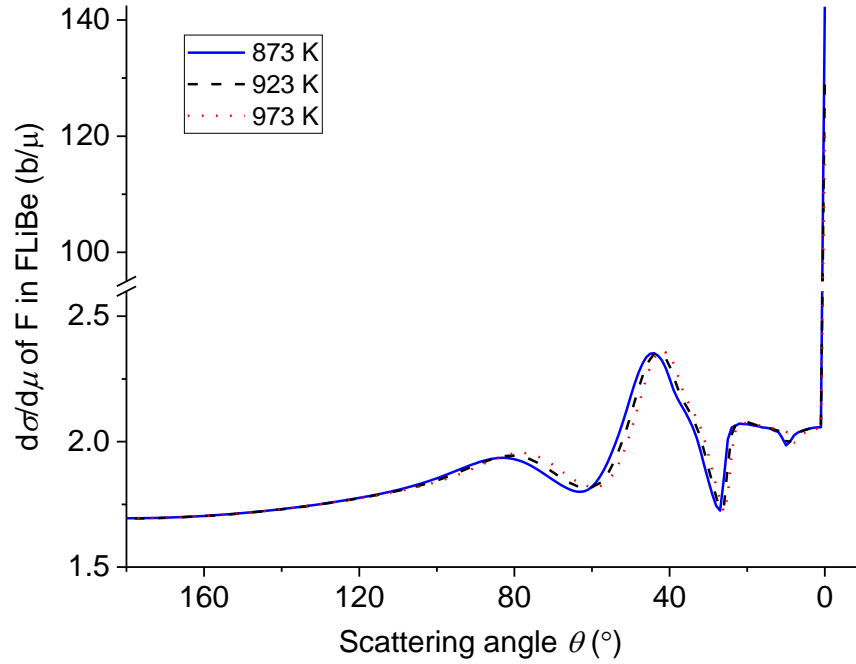


Figure 5-36. The angular differential cross section of F in FLiBe at representative reactor core temperatures.

At small scattering angle close to  $\theta = 0^\circ$ , the cross section rises significantly. This is contributed by the  $\delta$ -like diffusive quasi-elastic peak in the very small  $\alpha$  and very small  $\beta$  region. Therefore, scattering at small angle is highly probable in diffusive materials. With increasing temperature, the height of diffusional peak decreases. This is consistent with the decrease of the height of  $S(\alpha, \beta)$  at  $\alpha \ll 1$  and  $\beta \ll 1$ .

At scattering angle  $\theta < 90^\circ$ , the distinct effects become evident. The distinct effects relaxed the Gaussian approximation and the incoherent approximation. Distinct effects are less prominent in Li than Be and F. This is because the incoherent bound cross sections for Li are significantly larger than that for Be and F. Hence, the distinct effects are not the dominant effects in  $S_{tot}(\alpha, \beta)$  weighting. With increasing temperature, the volume of the interaction medium expands. This creates smaller reciprocal space grids, which is directly proportional to the scattering angle. Therefore, the scattering gradually shifts to smaller scattering angles.

A numerical procedure is written to integrate  $S_{tot}(\alpha, \beta)$  against  $\alpha$  over the appropriate range. The calculated differential cross section against secondary energies for each species in FLiBe are demonstrated in Figure 5-37 to Figure 5-39.

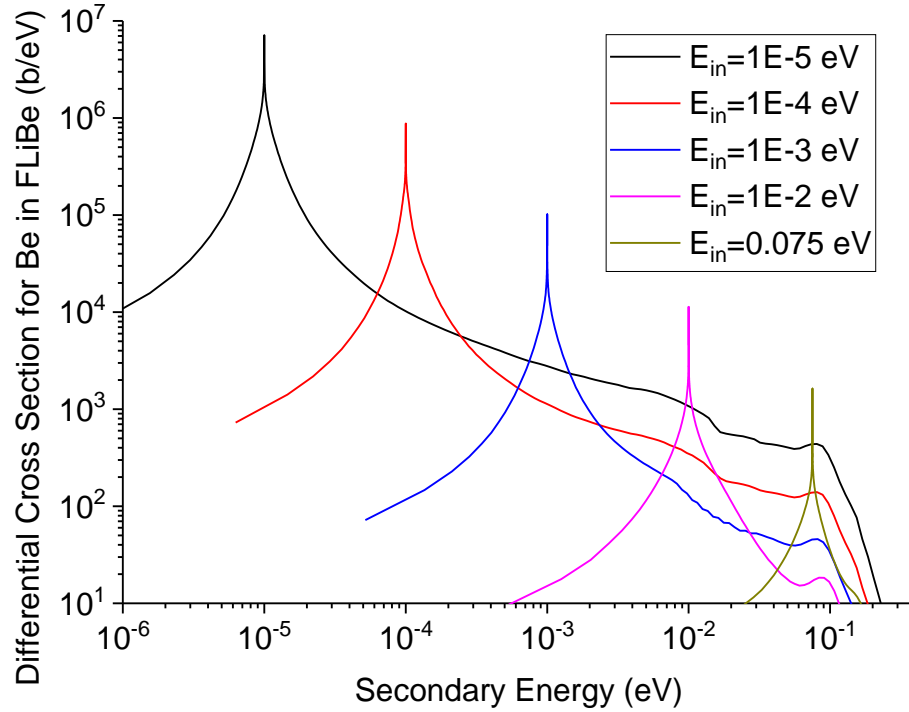


Figure 5-37. The differential cross section of Be in FLiBe at different incident energies at 873K.

Because the Be atoms possess a higher bound cross section than F and  $^7\text{Li}$  atoms ( $7.63\text{ b}$  vs  $4.018\text{ b}$  and  $1.4\text{ b}$ ) [136], the differential cross section of Be is correspondingly higher than that of F and Li in FLiBe. Like liquid lithium, the secondary energy distribution from FLiBe shows a significant quasi-elastic peak from the diffusional motion. As discussed in the previous section, the quasi-elastic peak is a result of the diffusional behavior in liquids. Within this peak, the scattered neutron exchanges energy with low energy diffusional excitation modes. This peak is prominent in liquids because of the presence of significant diffusional modes around zero-energy in its DOS. Details of the diffusional DOS will be discussed in the next chapter.

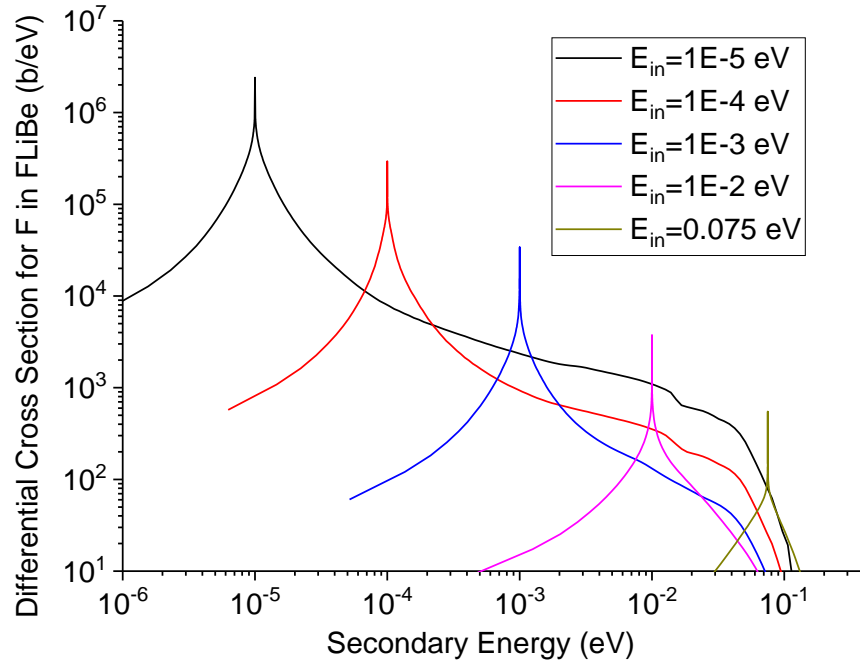


Figure 5-38. The differential cross section of F in FLiBe at different incident energies at 873K.

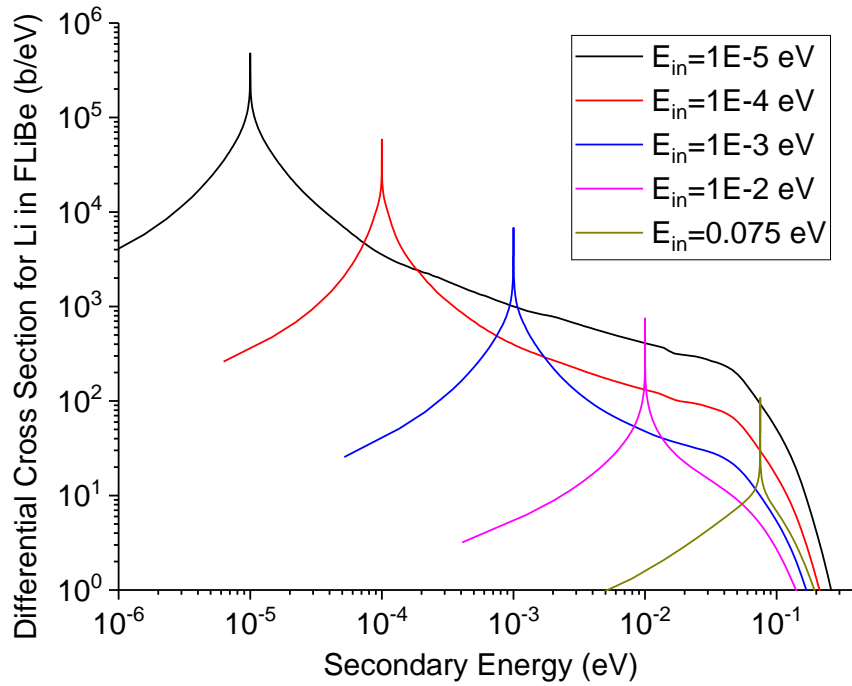


Figure 5-39. The differential cross section of Li in FLiBe at different incident energies at 873K.

The temperature dependence of  $d\sigma/dE'$  is shown in Figure 5-40. The overall trend of  $d\sigma/dE'$  is increasing with temperature as the thermal motion energy increases. One exception is that the

differential cross section around the incident energy is smaller (see bottom right plot in Figure 5-40). This feature is consistent with the discussion with small energy transfers in double differential cross section, which is shown in Figure 5-33.

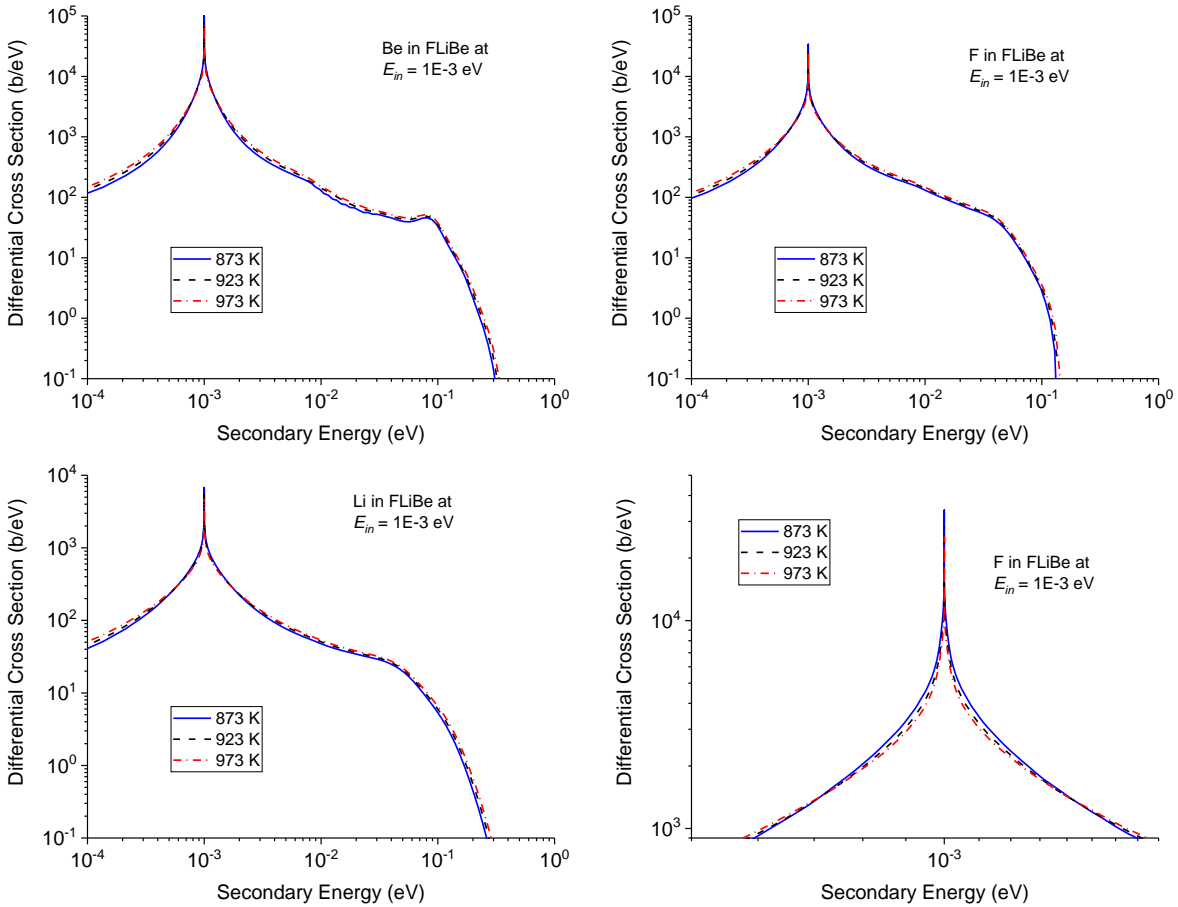


Figure 5-40. The differential cross section of FLiBe at  $E_{in} = 1 \times 10^{-3}$  eV at representative reactor core temperatures of 873 K, 923 K, and 973 K. The bottom right plot is zoomed in around incident energy, showing details at small energy transfer.

To conclude, at higher temperatures, the thermal scattering tends to happen at smaller scattering angle (Figure 5-34 to Figure 5-36) but with larger energy transfer (Figure 5-40). As previously discussed, the expansion of the system volume and increased thermal motion energy are the major respective reasons.

### 5.3.3 The Integrated Thermal Scattering Cross Section of FLiBe

The integrated cross sections  $\sigma(E_{in})$  for FLiBe are shown in Figure 5-41 at three different temperatures. These are obtained by integrating the differential cross section  $d\sigma/dE'$  or  $d\sigma/d\mu$  against secondary energies or scattering angles. As shown in Figure 5-41, the cross section for each species above 1 eV converges to its free atom cross section. The cross section also rises with the temperature. Integrated cross sections for each species of FLiBe show the same decreasing trend with increasing incident energy.

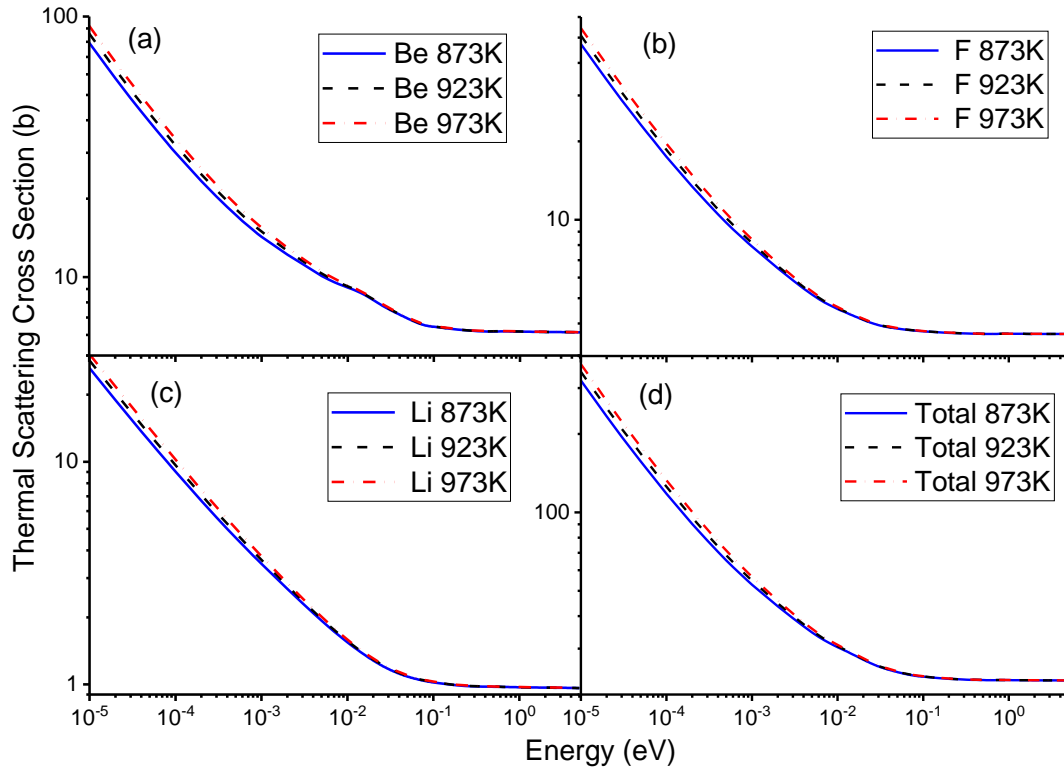


Figure 5-41. The integrated cross section (a) Be, (b) F, (c) Li, (d) total of FLiBe. The blue solid line is 873K. The black dashed line is 923 K. The red dash-dotted line is 973 K.

### 5.4 Comparison to the DOS method

In this section, the thermal scattering law of molten salt FLiBe will be evaluated from the DOS method. Firstly, the VACF for each species of FLiBe is generated from the MD model.



Thereafter, the frequency spectrum of the corresponding VACF is obtained from the Fourier transform. Secondly, by assuming the Egelstaff & Schofield diffusional model, the diffusional DOS is separated from the bound vibrational DOS. Thirdly, the thermal scattering law for both the diffusional part and bound part are evaluated. They are subsequently convolved to obtain the thermal scattering law that contains both vibrational motion and diffusional motion. Lastly, the thermal scattering cross section is calculated and compared to quantum corrected models.

#### **5.4.1 The Density of States of FLiBe**

The density of states (DOS) can be obtained from the Fourier transform of the VACF. Consequently, it consists of the same information as the VACF in frequency domain. The DOS is the probability density of a motion mode sampled at a particular energy. The total DOS for FLiBe (shown as the black line in Figure 5-42 at 873K) is calculated from the VACF which is taken from trajectories of molecular dynamics simulation.

The presence of diffusive mode in liquid systems is a major difference compared to solid systems. In solid systems, the primary motion mode is bound vibration mode. While in liquid systems, the diffusive mode contributes more to the DOS in the low energy region. Diffusional DOS from Eq. 10 is separated from bound vibrational DOS as shown in Figure 5-43. Figure 5-43 (d) demonstrates the Maxwell-Boltzmann distribution for an ideal gas. The most probable energy for an ideal gas at 873K is 0.0376 eV. This same peak can be observed in the DOS of F and Li ions. The bound vibrational DOS of Li ions shows a similar peak position with a compressed tail compared to the ideal gas. This indicates a similar collision/vibration motion to that of the ideal gas. However, the compressed tail at high energy states also indicates hindered motion modes which stem from the applied interatomic potential.

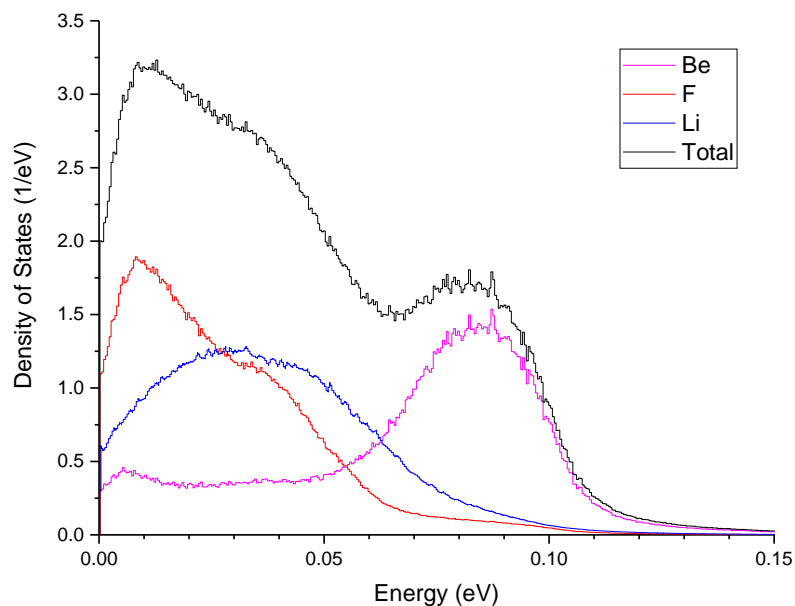


Figure 5-42. The density of states of FLiBe.

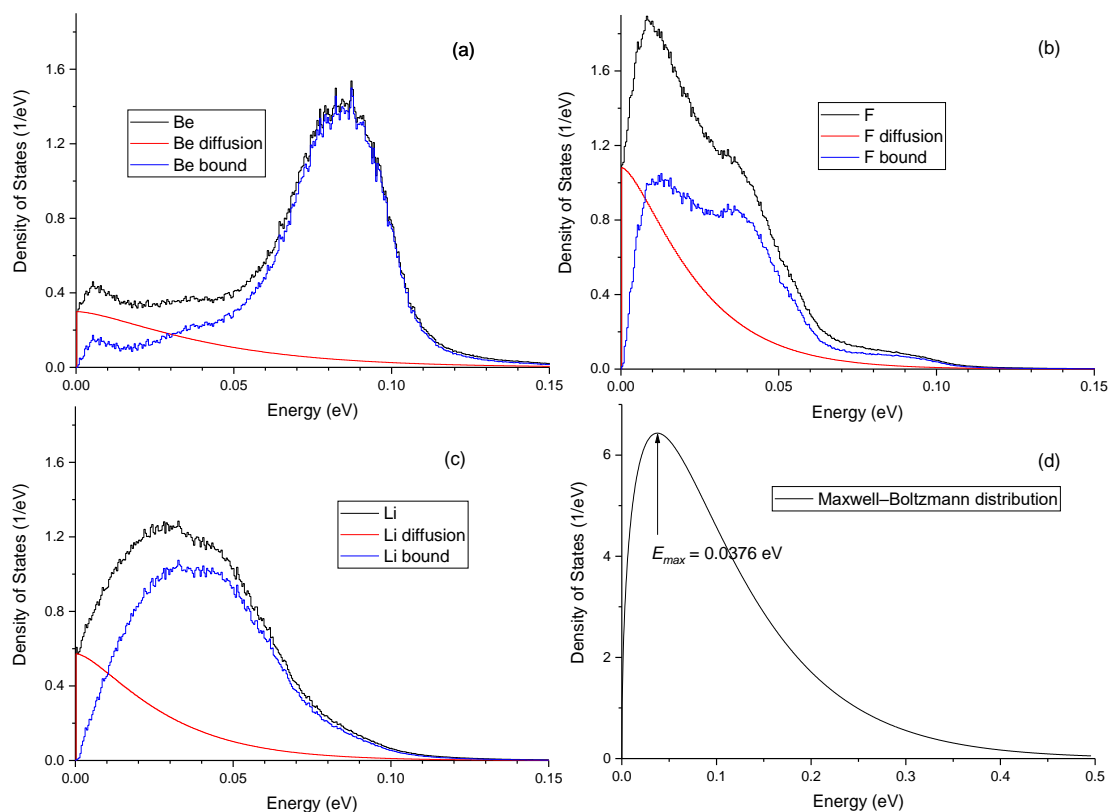


Figure 5-43. The density of states of FLiBe for each species divided into the bound vibrational mode (blue) and the diffusional mode (red). (d) is the density of states of Maxwell-Boltzmann distribution.

The bound DOS of F ions can be decomposed into two peaks, one at 0.012 eV and another one at 0.0376 eV. The later one shows the same behavior as that of Li. The first peak originates from the vibrational mode from  $\text{BeF}_4^{2-}$  binding structure. Corresponding to this vibrational peak for  $\text{F}^-$  are the two vibrational peaks for  $\text{Be}^{2+}$ , i.e. 0.0055 eV and 0.086 eV. The later peak at 0.086 eV with much larger probability corresponds to the vibrational modes in the  $\text{BeF}_4^{2-}$  binding structure as shown in Figure 3-3. The low energy vibration mode at 0.0055 eV is contributed by the second shell structure of Be and F ions. These bound vibrational modes of Be, F and Li ions are used in the phonon model to calculate the  $S_{\text{bound}}(\alpha, \beta)$ .

#### 5.4.2 The Thermal Scattering Law of FLiBe from the DOS method

$S_s(\alpha, \beta)$  is evaluated using the LEAPR module of NJOY code system. The evaluation utilized the Egelstaff & Schofield model. The diffusional  $S_{\text{diff}}(\alpha, \beta)$  is based on the parameters used in diffusional DOSs shown in Table 5-1. The bound  $S_{\text{bound}}(\alpha, \beta)$  is evaluated using the phonon model. The LEAPR module convolves the diffusional  $S_{\text{diff}}(\alpha, \beta)$  with the bound  $S_{\text{bound}}(\alpha, \beta)$  as shown in Eq. (2.3.8).

Table 5-1. Coefficients  $d$ ,  $c$  and DOS weight  $w_t$  used for modeling FLiBe diffusive behavior.

	Temperature (K)	$w_t$	$c$	$d$
<b>Be</b>	873	0.18353	2.5	0.47
	923	0.20701		0.53
	973	0.2344		0.6
<b>F</b>	873	0.37249	4.5	1.7
	923	0.40553		1.85
	973	0.46051		2.1
<b>Li</b>	873	0.23324	3.8	0.9
	923	0.26962		1.04
	973	0.30343		1.17

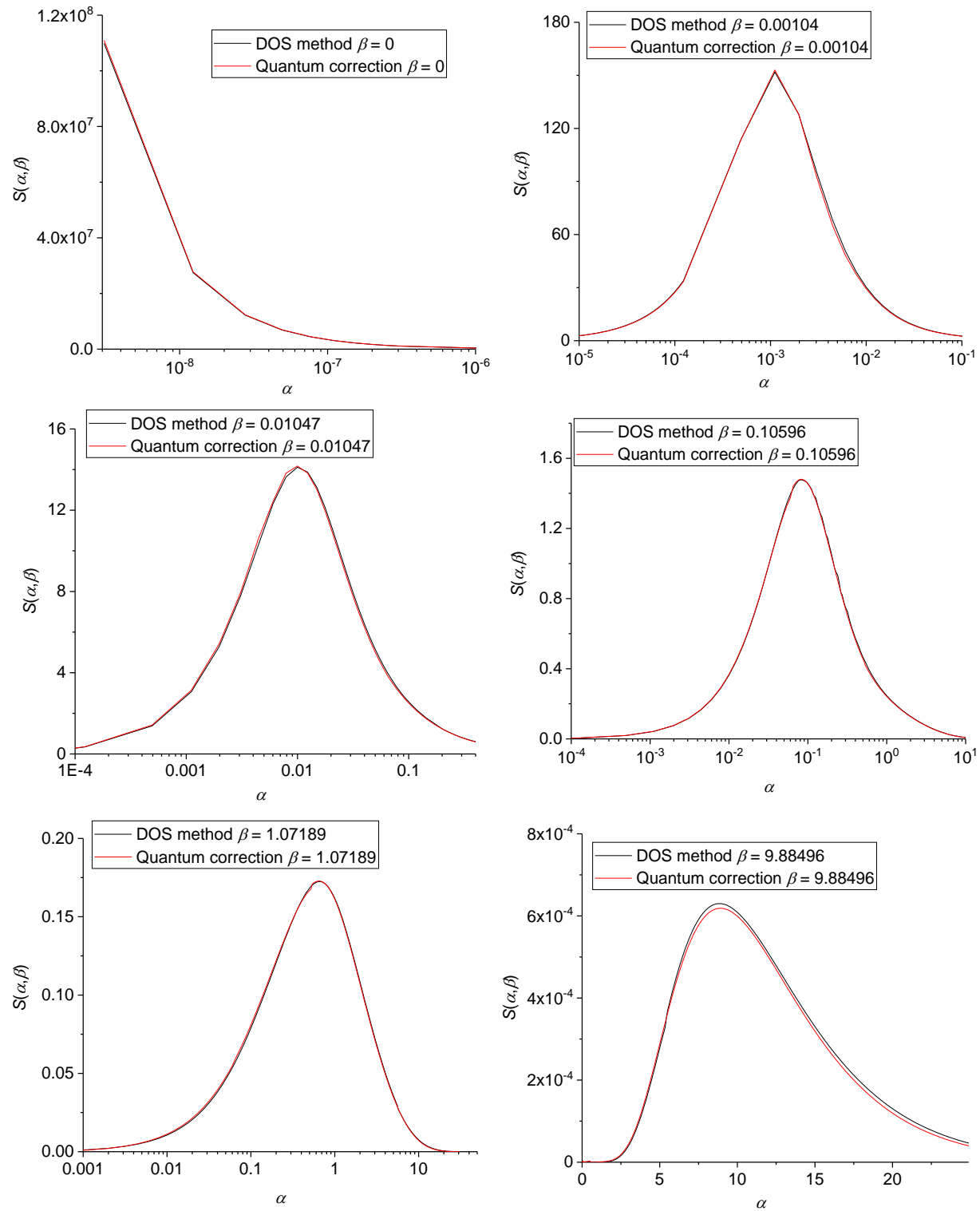


Figure 5-44. The thermal scattering law of Be in FLiBe at 873 K from the DOS method (black) using the Egelstaff & Schofield model and phonon model. The red curve is the corresponding quantum corrected self thermal scattering law in Chapter 5.

It was found that the standard LEAPR module in NJOY code system has utilized the translational weight  $w_t$ , i.e.  $w_{diff}$  in Eq. (2.3.7), as  $d/c$ , whereas the translational weight  $w_t$  is the integral of diffusive DOS. Therefore  $w_t$  is proportional to both  $d$  and  $c$  instead of  $d/c$ . In this work, a modified LEAPR module was created. This modified LEAPR module recognizes explicitly the translational DOS weight  $w_t$  as the integral of the diffusional DOS, and the two coefficients in the diffusional DOS  $c$  and  $d$  separately.

The modified LEAPR module is used with the coefficients in Table 5-1 to evaluate the self thermal scattering law using the DOS method. These results are shown in Figure 5-44 as solid black lines. It is compared to the self thermal scattering law evaluated from the quantum correction method (solid red lines). In Figure 5-44, the symmetric  $S_s(\alpha, \beta)$  is shown. The x-axis is plotted in logarithmic scale. At  $\beta = 0$ ,  $S(\alpha, \beta)$  reaches a  $\delta$ -function like peak as  $\alpha$  approaches zero. This quasi-elastic peak located around  $\beta = 0$  represents small energy transfer in scattering event.

The extremely small energy transfer originates from the diffusive behavior. Diffusion is a low energy motion state that can be easily excited or interrupted in the scattering process. Therefore,  $S(\alpha, \beta)$ , which is directly proportional to the probability of scattering, shows a  $\delta$ -function like peak at this position. The agreement between the peaks from the Egelstaff & Schofield model and the quantum correction method shows that the diffusive behavior can be correctly captured by both models.

In Figure 5-45, the  $S_s(\alpha, \beta)$  diffusional quasi-elastic peaks of the linear diffusion model, the DOS method and the quantum correction method for Li in FLiBe are shown. There are three models in Figure 5-45 that are all derived using different inputs. The linear diffusion model (i.e. Eq. (2.4.4)) only depends on the diffusion coefficient. The input to this model is the MD evaluated diffusion coefficient. The Egelstaff & Schofield model was evaluated from its corresponding

diffusional DOS. The quantum correction utilized the width function. Regardless of the model, the HMHW of the diffusional quasi-elastic peak is directly proportional to the diffusion coefficient.

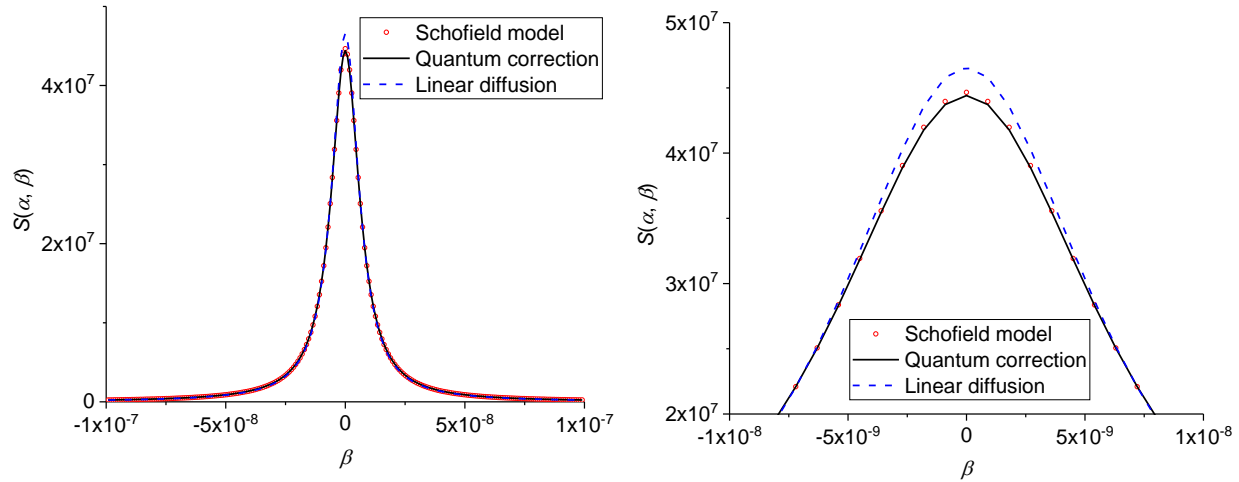


Figure 5-45. The  $S_s(\alpha, \beta)$  diffusional quasi-elastic peak of Li in FLiBe from different models. The linear diffusion model (blue dashed line) uses the diffusion coefficient  $D$  predicted from MD as input. The Egelstaff & Schofield model (red open dots) uses the separated DOS as input. The quantum correction method (black solid line) uses the width function as input.

As can be seen in Figure 5-45, though the three methods used different input, the HMHW of the peak is very close. Therefore, all three models correctly account for the diffusion coefficient. In the small energy transfer (very small  $\beta$ ) region, the linear diffusion model diverges from the quantum correction method and the Egelstaff & Schofield model. This disagreement implies that the linear diffusion model is limited in handling the physics of extremely small energy transfer. In the perspective of the DOS method, the limitation arises from each separated model. In this case for FLiBe, the Schofield diffusion model behaves better compared to the linear diffusion model.

As shown in Figure 5-44 and Figure 5-45,  $S_s(\alpha, \beta)$  from the DOS method is in close agreement with  $S_s(\alpha, \beta)$  from the quantum correction method. The self thermal scattering law from the DOS method using the Egelstaff & Schofield model shows good agreement with that from the quantum correction method. This convergence of the two methods directly demonstrates the trustworthiness of the quantum corrected self thermal scattering law from the validated molten

salt FLiBe MD model. The Schofield diffusional model is known to be capable of modeling monatomic liquids or ionic liquids like FLiBe. In this case, the agreement between the DOS method and the quantum correction method also verifies the model applicability to FLiBe.

As a result, the cross sections not including distinct effects from both methods are not expected to be different. For this reason, the discussion from this point on only compares evaluated results using  $S_s(\alpha, \beta)$  from the DOS method to those using  $S_{tot}(\alpha, \beta)$  from the quantum correction method including distinct effects, which are shown in Figure 5-46.

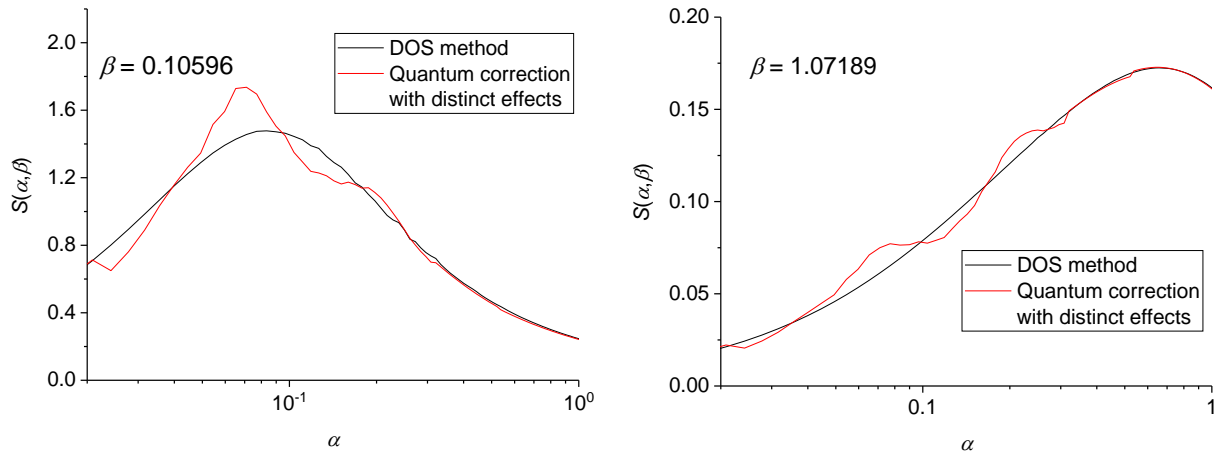


Figure 5-46. The thermal scattering law of Be in FLiBe at 873 K, DOS method (black) compared to the coherent and quantum correction (red). Distinct effects are missing in the DOS method.

As can be seen, the distinct effects are most prominent in small  $\alpha$  and small  $\beta$  region. The distinct effects attenuate with increasing  $\alpha$  and  $\beta$ . As distinct effects are missing in the DOS method, this will result in difference in the double differential cross section against scattering angle. During the evaluation, numerous numerical issues were found in the NJOY code. These issues are documented in Appendix C.

### 5.4.3 The Double Differential Thermal Scattering Cross Section of FLiBe

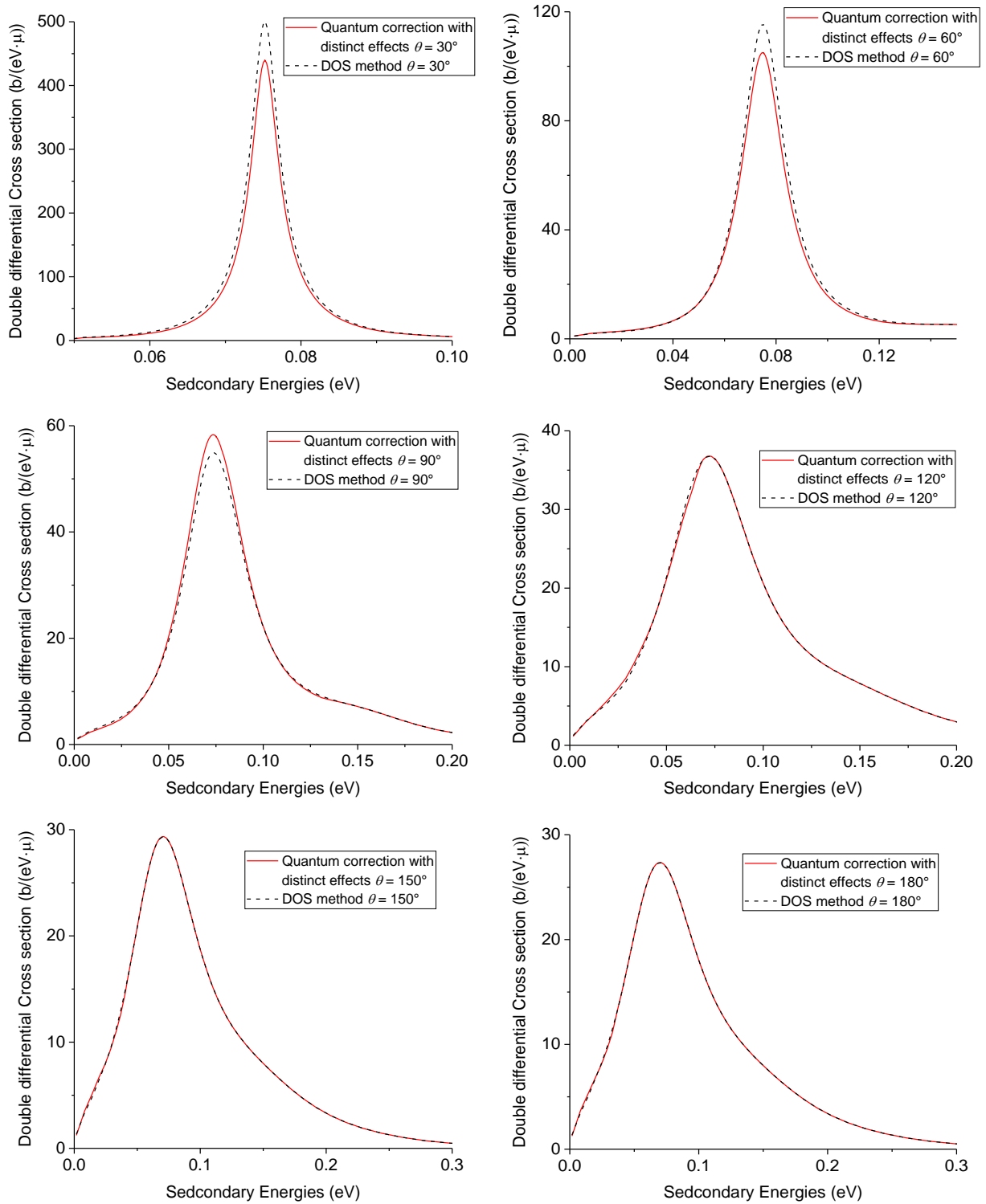


Figure 5-47. Double differential cross sections of Be in FLiBe at 873 K from the DOS method (dashed black) comparing to those from the quantum correction method including distinct effects (solid red). The incident neutron energy is chosen at  $E_{in} = 0.075$  eV.



The double differential cross section can be evaluated from the thermal scattering law. As stated in the previous section, the cross sections using  $S_s(\alpha, \beta)$  from the DOS method and those using  $S_{tot}(\alpha, \beta)$  from the quantum correction method including distinct effects are evaluated and compared.

In Figure 5-47, the double differential cross sections of Be in FLiBe at 6 different scattering angles between  $30^\circ \sim 180^\circ$  are shown as an example for FLiBe. The graphs are plotted at incident energy  $E_{in} = 0.075 \text{ eV}$ .

As can be seen, there are noticeable differences between the DOS evaluation and the quantum correction evaluation including distinct effects. These differences are primarily evident in scatterings below  $90^\circ$ . Increase or decrease of the scattering probability could happen depending on the corresponding  $\alpha$  of the scattering angle.

As shown in Figure 5-46 and Figure 5-47, the increase and decrease tend to compensate each other when integrated against the scattering angle. These effects will show up in the differential and integrated cross sections in later sections. The energy spectrum of scattered neutrons at higher scattering angles tends to be broader than that at smaller scattering angles. This behavior is consistent with the broadened  $S(\alpha, \beta)$  saw at higher momentum transfer in Figure 5-44.

#### 5.4.4 The Differential Thermal Scattering Cross Section of FLiBe

In this section, neutron differential scattering cross sections against scattering angle and secondary energies of each element in FLiBe are evaluated. In Figure 5-48, the differential cross sections against secondary energies for each species in FLiBe are provided at several incident neutron energies. The differential cross section from the DOS method is compared to that from the quantum correction method with distinct effects. As can be seen, the difference between the two

methods of the secondary energy distribution in Figure 5-48 is less prominent than the difference seen in the angular distribution (Figure 5-49). It can be concluded that the impact of distinct effects on the secondary energy distribution is limited compared to the angular distribution. In other words, the distinct effects preferentially affect the angular distribution.

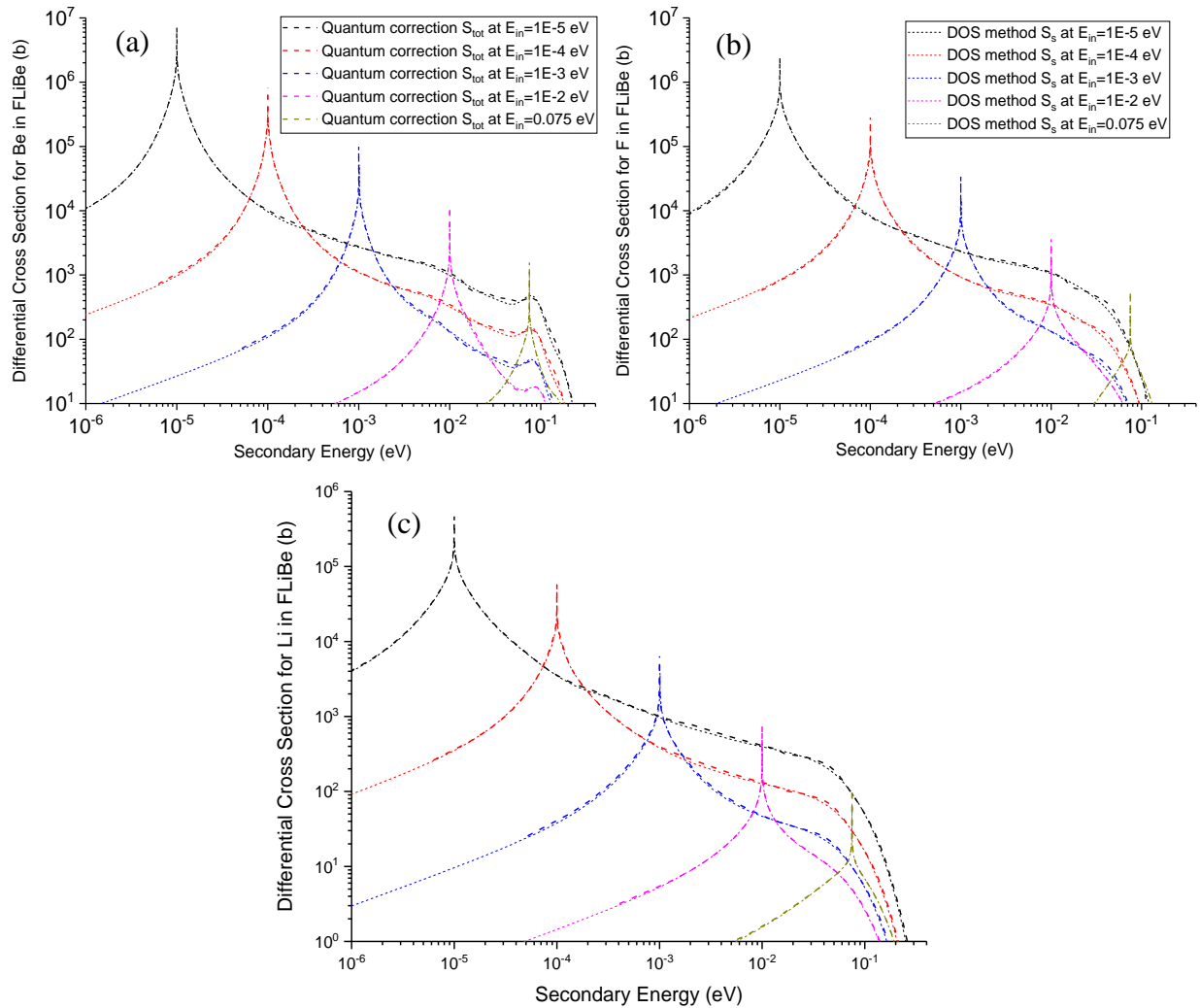


Figure 5-48. Secondary energy differential cross section of (a) Be, (b) F, (c) Li in FLiBe from different incident energies at 873 K. The dashed lines are quantum corrected cross section with distinct effects. The dotted lines are from the DOS method using the Schofield model.

Figure 5-49 to Figure 5-51 are the differential cross section of each species in FLiBe as a function of the scattering angle. A remarkable characteristic of the angular distribution is the significant peak at small scattering angle. This peak is often on to two orders of magnitude higher

than the cross sections at larger scattering angles. The magnitude of the peak is contributed by the integral of the quasi-elastic diffusional peak as shown in Figure 5-45. In other words, the high possibility of exciting the low energy excitation modes of diffusional motion in FLiBe results in the high scattering probability at very small angles.

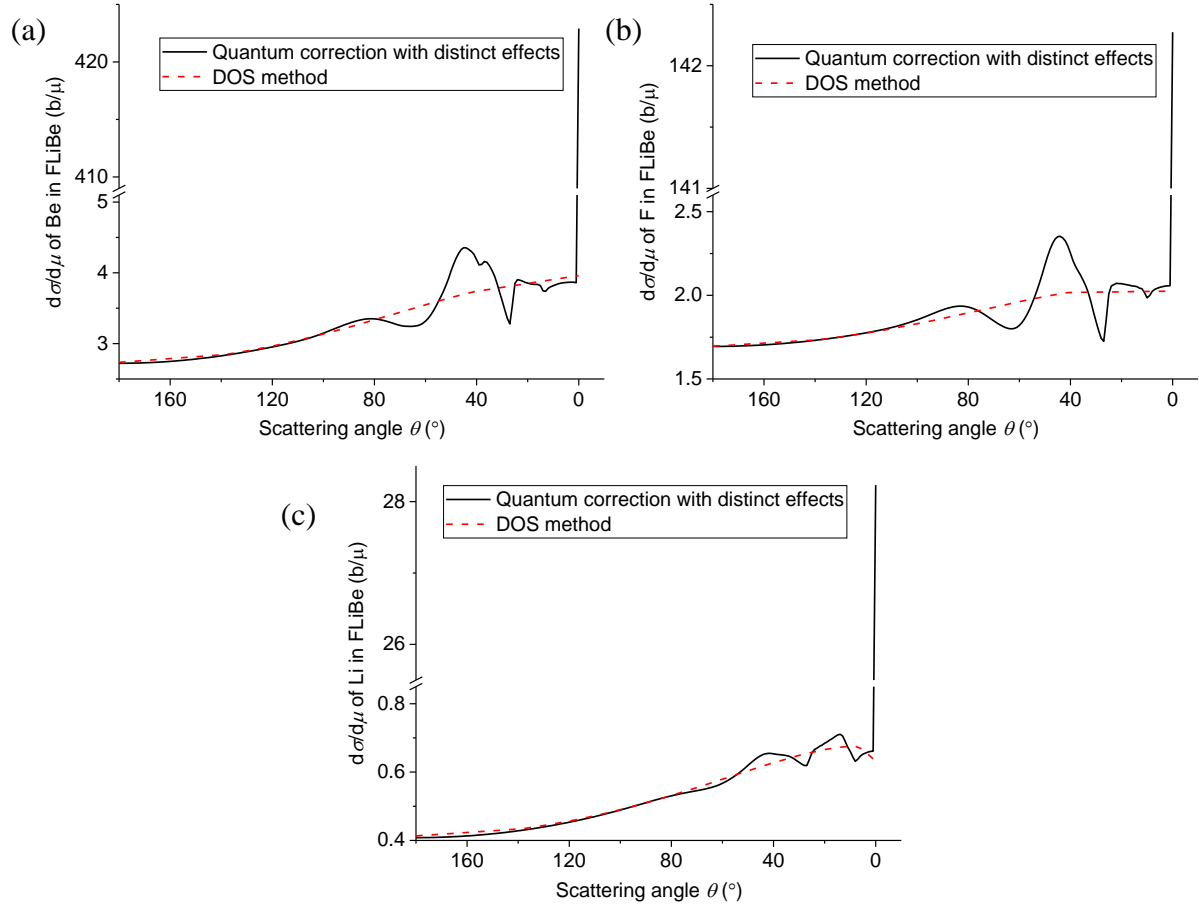


Figure 5-49. Differential cross section against scattering angle of (a) Be, (b) F, (c) Li in FLiBe at 873 K and at  $E_{in} = 0.075$  eV. The solid black line is from the quantum correction method including the distinct effects. The red dashed line is from the DOS method (NJOY). Notice that the y-axis is broken, the peak is  $\delta$ -function like.

$S_s(\alpha, \beta)$  from the DOS method is integrated using the THERMR module of the NJOY system.

In comparison, the quantum corrected  $S_{tot}(\alpha, \beta)$  including distinct effects is integrated by a standalone code. As can be seen by the red dashed lines in Figure 5-49, NJOY completely neglects

the diffusional peak. This is one of the numerical issues found in NJOY relating to the handling of the diffusional behaviors. Other numerical issues found in NJOY are summarized in Appendix C.

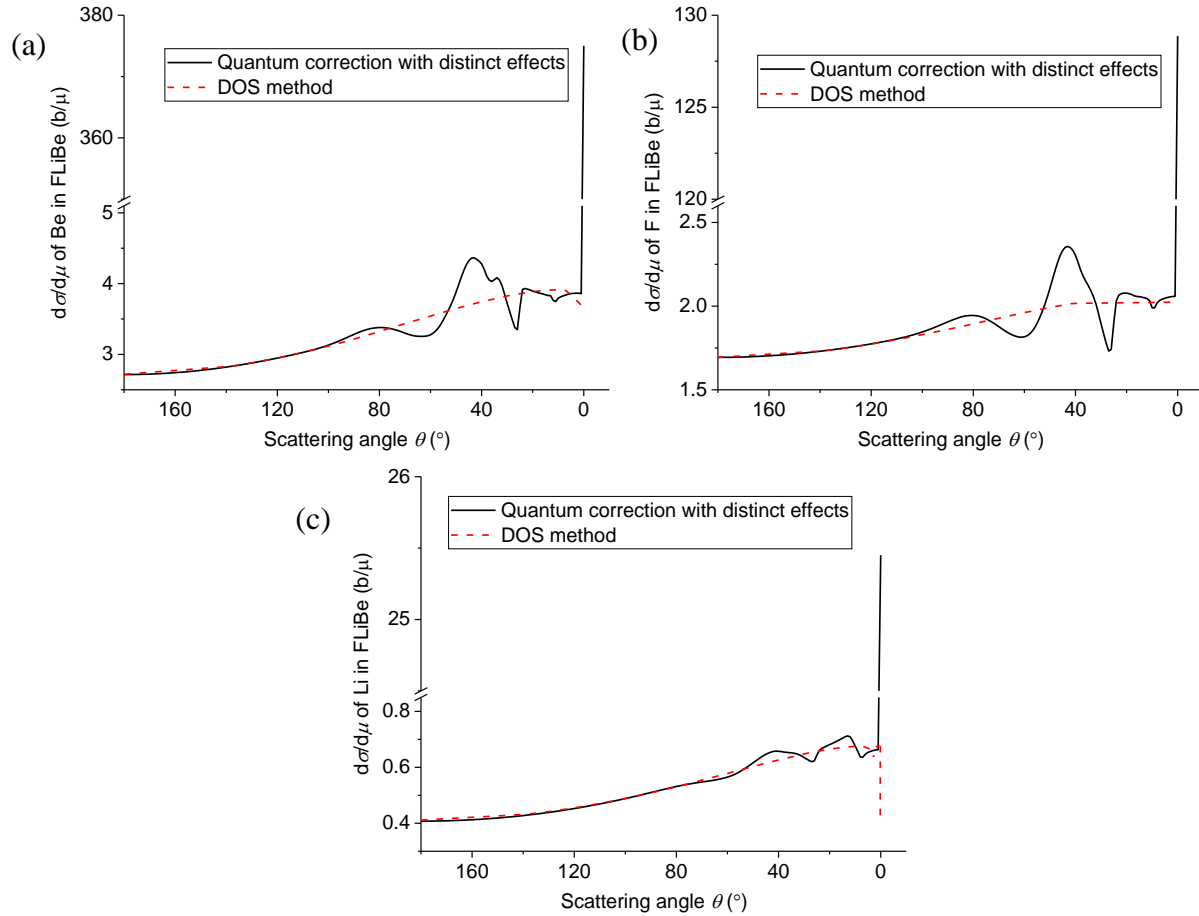


Figure 5-50. Differential cross section against scattering angle of (a) Be, (b) F, (c) Li in FLiBe at 923 K and at  $E_{in} = 0.080$  eV.

Another remarkable feature that is missing in the differential cross section of the DOS method is the angular distribution from distinct effects. As can be seen in Figure 5-49, the angular distribution is remarkably different below  $90^\circ$ . This is caused by the distinct effects, which were discussed in Figure 5-47. The angular scattering cross sections of each species in FLiBe is larger than the cross section using incoherent approximation (DOS method) at  $55^\circ$  and  $80^\circ$ , while smaller at  $25^\circ$  and  $60^\circ$ . Neglecting such distinct effects could have noticeable impact in nuclear analysis where directional aspects become important.

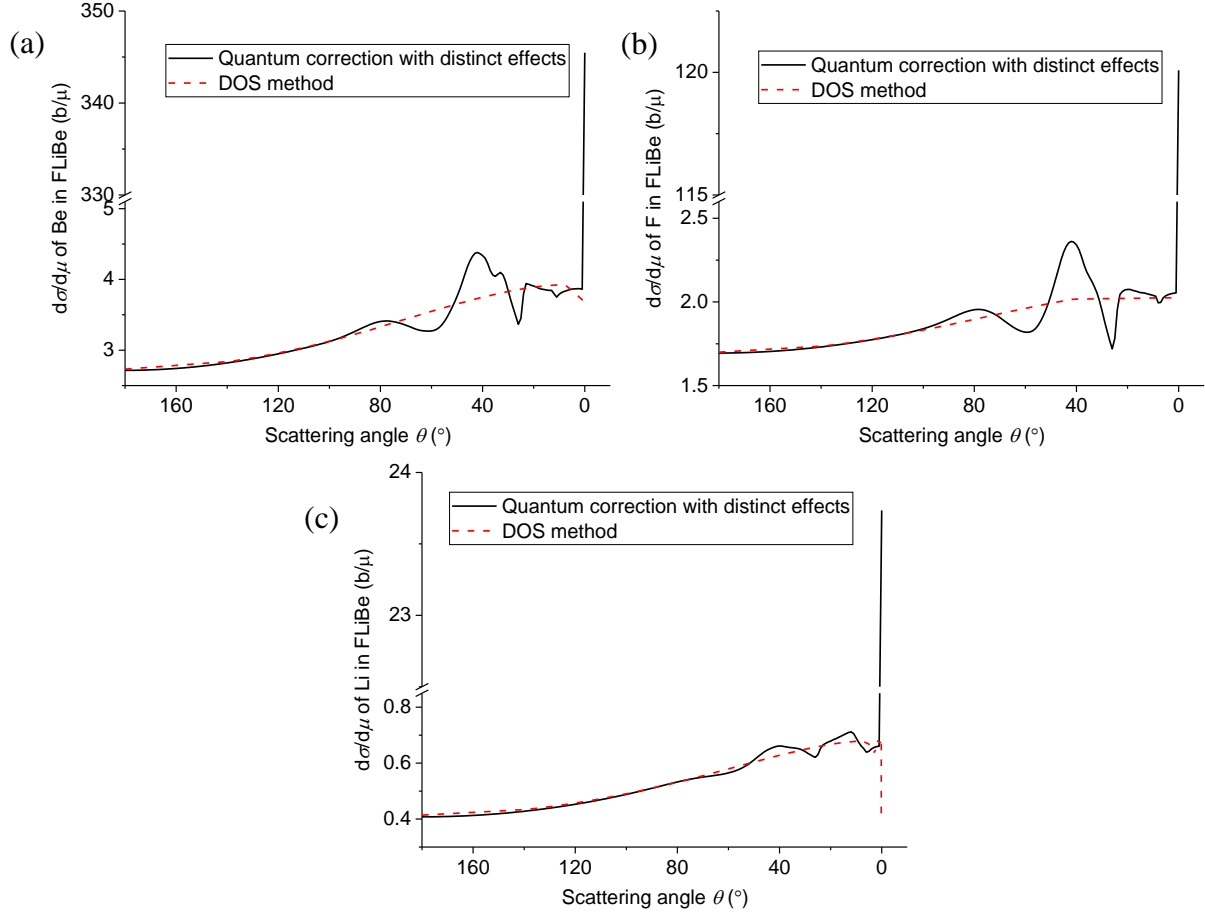


Figure 5-51. Differential cross section against scattering angle of (a) Be, (b) F, (c) Li in FLiBe at 973 K and at  $E_{in} = 0.084$  eV.

#### 5.4.5 The Integrated Thermal Scattering Cross Section of FLiBe

The differential cross section  $d\sigma/dE'$  or  $d\sigma/d\mu$  in the previous section can be further integrated to obtain the integrated scattering cross section as a function of incident energies. The integrated cross sections for each species in FLiBe are shown in Figure 5-52 to Figure 5-54. From the figures, the DOS method using the Schofield model is close to the quantum correction with distinct effects. The distinct effects change the distribution of angular distribution of scattered neutron (see Figure 5-49), but in the angular differential cross section, the increase is compensated by the decrease. Therefore, the integrated cross section is not impacted as much as the angular differential cross section. A slight difference between the methods is observed below the thermal

energy  $0.075 \text{ eV}$ , a large part of which is contributed by the numerical issues in NJOY (see Appendix C).

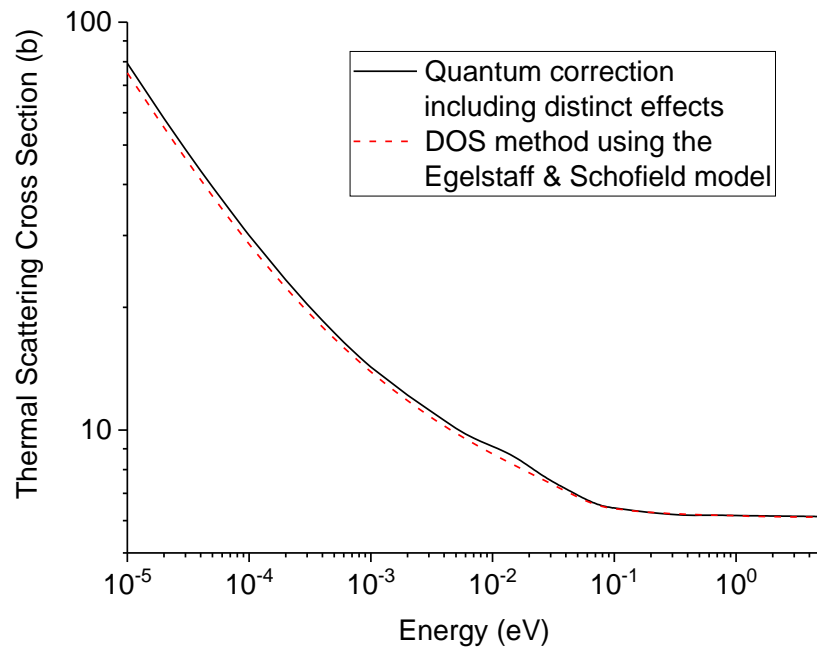


Figure 5-52. Integrated cross section of Be in FLiBe at 873 K at  $E_{in} = 0.075 \text{ eV}$ . Black line is the DOS method using the Schofield model. Red line is the quantum corrected cross section including distinct effects.

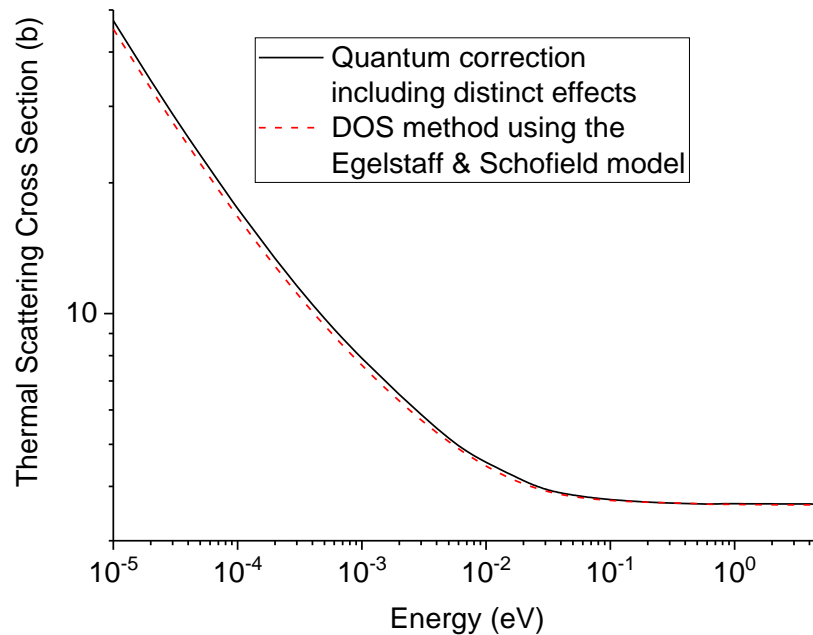


Figure 5-53. Integrated cross section of F in FLiBe at 873 K at  $E_{in} = 0.075 \text{ eV}$ .

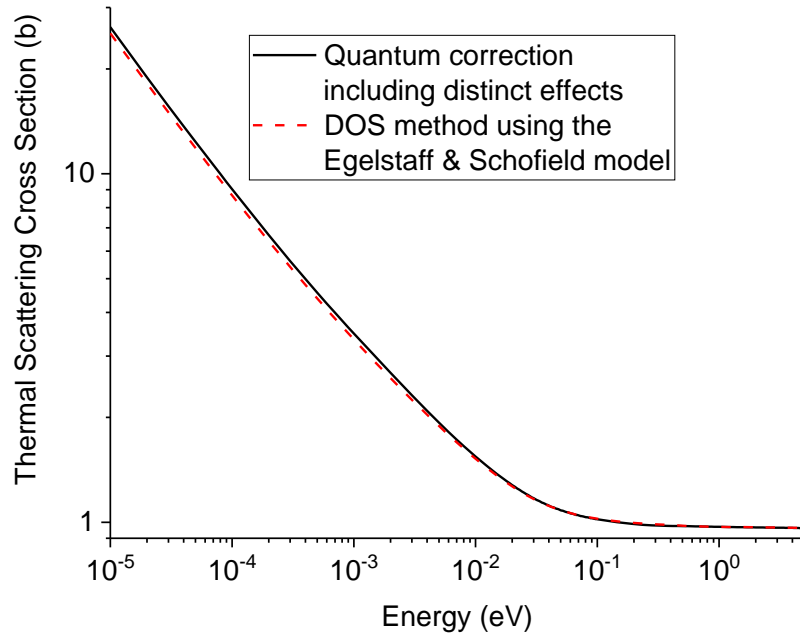


Figure 5-54. Integrated cross section of Li in FLiBe at 873 K at  $E_{in} = 0.075$  eV.

As a conclusion to Section 5.1, the quantum correction method produced a reliable thermal scattering law using MD modeling. It is more general, flexible, and account for complex motion features from MD models, even those not well explained by theoretical models. The quantum correction method, which includes distinct effects, is also more complete compared to the DOS method.

## Chapter 6 Conclusion and Future Work

In this work, molecular dynamics (MD), with quantum corrections, was utilized to evaluate the thermal neutron scattering law (TSL) and subsequently the scattering cross sections for liquid FLiBe. Although FLiBe is the focus of this work, the developed methodology is capable of evaluating the thermal neutron scattering cross section for any liquid system. In addition, a second methods was also implemented to evaluate the FLiBe TSL using the excitation density of states. As discussed previously, this approach uses many assumptions and approximation but is useful for initial cross checks of the MD methodology.

The MD model of liquid FLiBe was established using the Born-Mayer atomistic potential, which is a pair potential for ionic crystals and liquids. The potential was optimized for liquid FLiBe to predict physical properties better than previously reported [40]. The predicted static and dynamic properties, i.e. density, diffusion coefficient, viscosity, thermal capacity, thermal conductivity, were compared to experimental measurements. Good agreements were observed. Subsequently, the MD trajectories were used to generate the intermediate scattering functions for Be, Li, and F in FLiBe, which were Fourier transformed in the time domain to obtain the classical scattering law.

The classical scattering law deviates from physically predicted behavior due to ignoring quantum effects, such as detailed balance. This results in deviations in the first moment of the scattering law, in the width function, and eventually in the calculated thermal scattering cross sections. Furthermore, the system response is linked to the imaginary parts of quantum correlation functions, which originates from the quantum nature of the atomic trajectories. Therefore,



deviations from the quantum behavior are observed. A quantum correction methodology was developed to overcome these deficiencies in classical approximations.

The quantum correction methodology was applied to the classical width function. The input to the quantum correction methodology, i.e. MSD, was obtained from the validated molten salt liquid FLiBe MD trajectories. Evaluation of the scattering functions from MD trajectories applied the fast Fourier transform algorithm, which reduced the complexity from  $O(N^2)$  to  $O(N \log N)$ . Computation of the scattering functions were made more efficient using MPI parallel capability that runs on multi-processors across different compute nodes on a cluster.

To validate the proposed quantum correction methodology, liquid lithium was investigated as a relevant material. The total quantum thermal scattering law and the thermal scattering cross section of liquid lithium were computed. The evaluated scattering law followed quantum behavior such as detailed balance and fulfilled the sum rules. Both the evaluated quantum scattering law and cross sections for liquid lithium were compared to experimental measurements, which showed very good agreement. The distinct scattering law is included in the evaluation by enforcing the same quantum correction ratio as for the self scattering law. Using the liquid lithium example, the distinct effects demonstrated obvious improvement in the total scattering law and the double differential cross section by relaxing the Gaussian and incoherent approximations. The evaluated scattering law and cross sections including distinct effects were proven to be consistent with experimental measurements.

The scattering law of molten salt liquid FLiBe was evaluated using quantum correction and including distinct effects. The scattering law was generated at representative reactor core temperatures of 873K, 923 K, and 973 K. The distinct effects for FLiBe were included in the scattering law as well as the scattering cross section. The evaluated scattering law exhibited

quantum behavior as predicted from the theory. Double differential, differential, and integrated cross sections were generated using the total scattering law including distinct effects. It was found that the distinct effects change the angular distribution of the scattered neutrons, a phenomena that has been verified by liquid lithium experimental measurements.

Alternatively, the density of excitation states (DOS) in FLiBe was calculated by transforming the VACF. The generated DOS was separated into different motion modes, e.g. the bound vibrational mode and the diffusional mode in this work. The corresponding scattering law of the different motion modes was evaluated separately and convolved into the self scattering law. This is in contrast to the previously described MD based method, where the total scattering law including distinct effects can be calculated.

The quantum corrected MD based evaluation was compared to the DOS evaluation for FLiBe. The self scattering law from the DOS method showed very good agreement with the self scattering law from the MD based method. This agreement cross validated the MD based method. However, there are two advantages of the quantum corrected MD based method: first, the processing of the scattering law is independent of theoretical models, e.g. the Egelstaff & Schofield diffusion model etc., and second, it can readily include distinct effects that are not captured in the DOS method.

## **Future work**

### **Implementation into the *FLASSH* Code System**

The cross sections from quantum correction in this work were generated using an in-house program. In recent years, there has been extensive development efforts in this group to develop an advanced nuclear data processing code, i.e. the Full Law Scattering System Hub (*FLASSH*) [137]. Such a code would be a promising platform to implement the quantum correction algorithm. The

inclusion of liquid state physics and quantum correction methodology in *FLASSH* could largely expand the capability of *FLASSH*. However, the *FLASSH* code currently operates in parallel mode under OpenMP bindings. The scattering law evaluation including distinct effects, which is a routine developed in this work, operates on MPI. This difference is demanded by the code structure and computational resources that needs to be accessed. Merging two different parallel programming bindings will need some programming efforts.

### **Producing ENDF TSL Evaluation**

In this work, the evaluation is carried out at three representative reactor core temperatures of 873 K, 923 K, and 973 K. However, under certain scenarios, such as pre-startup core loading, and if considering reactivity excursion transients, the reactor coolant can be near the melting (732 K) or boiling temperature (1703 K) limits. It would be useful to include scattering law evaluations approaching these limits. Therefore, to produce useful TSL ENDF/B libraries for all scenarios, temperatures ranging from 750 K to 1500 K are suggested to be investigated.

### **Experiments in Support of Liquid FLiBe TSL Evaluation**

The evaluation of FLiBe cross sections is established on the validated MD model and quantum correction methodology. However, it is still necessary to validate the evaluation with experimental measurements. The double differential scattering cross section of thermal neutrons is one of the necessary measurements. Such an experiment would require angular detection capability and possibly time of flight (TOF) capability, such as available at the spallation neutron source (SNS). Another recommended experiment would be the diffusion coefficient measurement for Be and F in FLiBe. The diffusion coefficient of Be in FLiBe has not been measured before, it would be

useful to measure this coefficient and compare to the MD prediction. In addition, because it was found that the previously measured diffusion coefficient of F in FLiBe was inconsistent with the Stokes-Einstein relation, a remeasurement of this property is recommended. Finally, measurement of the total cross section of Liquid FLiBe using a neutron transmission type experiment will be highly useful for validation purposes.

## REFERENCES

- [1] Director General, *International Status and Prospects for Nuclear Power 2017*, IAEA (2017).
- [2] *Generation IV International Forum*, [https://www.gen-4.org/gif/jcms/c\\_9260/public](https://www.gen-4.org/gif/jcms/c_9260/public).
- [3] OECD Nuclear Energy Agency, *Technology Roadmap Update for Generation IV Nuclear Energy Systems*, Generation IV International Forum (2014).
- [4] Forsberg, C.W., *Reactors with Molten Salts: Options and Missions*, Frederick Joliot & Otto Hahn Summer School on Nuclear Reactors, Physics and Fuels Systems (2004).
- [5] Peterson, P.F., "Multiple-reheat Brayton cycles for nuclear power conversion with molten coolants", *Nucl. Technol.*, **144**, 279-288 (2003).
- [6] Dulera, I.V., Sinha, R.K., "High temperature reactors", *J. Nucl. Mater.*, **383**, 183-188 (2008).
- [7] Ingersoll, D.T., *Status of Preconceptual Design of the Advanced High-Temperature Reactor (AHTR)*, ORNL/TM-2004/104, Oak Ridge National Lab (2004).
- [8] Ingersoll, D.T., *Status of Physics and Safety Analyses for the Liquid-Salt-Cooled very High-Temperature Reactor (LS-VHTR)*, ORNL/TM-2005/218, Oak Ridge National Lab (2005).
- [9] Williams, D.F., Toth, L.M., Clarno, K.T., *Assessment of Candidate Molten Salt Coolants for the Advanced High Temperature Reactor (AHTR)*, Oak Ridge National Lab., ORNL/TM-2006/12 (2006).
- [10] Clarno, K.T., Forsberg, C.W., Gehin, J.C., Slater, C.O., Carbajo, J.J., Williams, D.F., Taiwo, T.A., Cahalan, J.E., Kim, T.K., Sienicki, J., *Trade Studies for the Liquid-Salt-Cooled very High-Temperature Reactor: Fiscal Year 2006 Progress Report*, ORNL/TM-2006/140, Oak Ridge National Lab (2007).
- [11] Holcomb, D.E., Cetiner, S.M., Flanagan, G.F., Peretz, F.J., Yoder Jr, G.L., *An Analysis of Testing Requirements for Fluoride Salt Cooled High Temperature Reactor Components*, ORNL/TM-2009/297, Oak Ridge National Lab (2009).
- [12] Greene, S.R., Gehin, J.C., Holcomb, D.E., Carbajo, J.J., Ilas, D., Cisneros, A.T., Varma, V.K., Corwin, W.R., Wilson, D.F., Yoder Jr, G.L., *Pre-Conceptual Design of a Fluoride-Salt-Cooled Small Modular Advanced High Temperature Reactor (SmAHTR)*, ORNL/TM-2010/199, Oak Ridge National Lab (2010).
- [13] Holcomb, D.E., Peretz, F.J., Qualls, A.L., *Advanced High Temperature Reactor Systems and Economic Analysis*, ORNL/TM-2011/364, (2011).

- [14] Varma, V.K., Holcomb, D.E., Peretz, F.J., Bradley, E.C., Ilas, D., Qualls, A.L., Zaharia, N.M., *AHTR Mechanical, Structural, and Neutronic Preconceptual Design*, ORNL/TM-2012/320, Oak Ridge National Lab (2012).
- [15] Holcomb, D.E., Flanagan, G.F., Mays, G.T., Pointer, W.D., Robb, K.R., Yoder Jr, G.L., *Fluoride Salt-Cooled High-Temperature Reactor Technology Development and Demonstration Roadmap*, ORNL/TM-2013/401, Oak Ridge National Lab (2013).
- [16] Qualls, A.L., Betzler, B.R., Brown, N.R., Carbajo, J., Greenwood, M.S., Hale, R.E., Harrison, T.J., Powers, J.J., Robb, K.R., Terrell, J.W., *Preliminary Demonstration Reactor Point Design for the Fluoride Salt-Cooled High-Temperature Reactor*, ORNL/TM-2015/700, Oak Ridge National Lab (2015).
- [17] Qualls, A.L., Brown, N.R., Betzler, B.R., Carbajo, J., Hale, R.E., Harrison, T.J., Powers, J.J., Robb, K.R., Terrell, J.W., Wysocki, A.J., *Fluoride Salt-Cooled High-Temperature Demonstration Reactor Point Design*, ORNL/TM-2016/85, (2016).
- [18] Zhang, D., Liu, L., Liu, M., Xu, R., Gong, C., Zhang, J., Wang, C., Qiu, S., Su, G., "Review of conceptual design and fundamental research of molten salt reactors in China", *Int. J. Energy Res.*, **45**, 1834-1848 (2018).
- [19] Kim, T.K., Taiwo, T.A., Yang, W.S., *Preliminary Neutronic Studies for the Liquid-Salt-Cooled very High Temperature Reactor (LS-VHTR)*. no. ANL-GENIV-052, Argonne National Lab (2005).
- [20] Szakaly, F.J., Kim, T.K., Taiwo, T.A., *Neutronics Assessment of Stringer Fuel Assembly Designs for the Liquid-Salt-Cooled very High Temperature Reactor (LS-VHTR)*. ANL-GenIV-074, Oak Ridge National Lab (2007).
- [21] Yoder Jr, G.L., Bopp, A.T., Holcomb, D.E., Pointer, W.D., Wang, D., *Advanced High Temperature Reactor Thermal Hydraulics Analysis and Salt Clean-Up System Description*, ORNL/TM-2014/499, Oak Ridge National Lab (2014).
- [22] Romatoski, R.R., Fluoride-salt-cooled high-temperature test reactor thermal-hydraulic licensing and uncertainty propagation analysis, PhD Thesis, Massachusetts Institute of Technology, (2017).
- [23] Yoder, G.L., Heatherly, D., Williams, D., Caja, J., Caja, M., Elkassabgi, Y., Jordan, J., Salinas, R., *Liquid Fluoride Salt Experiment using a Small Natural Circulation Cell*, Report no. ORNL/TM-2014/56, Oak Ridge National Lab (2014).
- [24] Aaron, A.M., Cunningham, R.B., Fugate, D.L., Holcomb, D.E., Kisner, R.A., Peretz, F.J., Robb, K.R., Wilson, D.F., Yoder Jr, G.L., *High Temperature Fluoride Salt Test Loop*, ORNL/TM-2012/430, ORNL (2015).

- [25] Holcomb, D.E., Ilas, D., Middleton, B., Arrieta, M., *Small, Modular Advanced High Temperature Reactor-Carbonate Thermochemical Cycle*, ORNL/TM-2014/69, Oak Ridge National Lab (2014).
- [26] Weinberg, A.M., "The Status and Technology of Molten Salt Reactors—A Review of Work at the Oak Ridge National Laboratory", *Nucl.Appl.Tech*, **8**, 106 (1970).
- [27] Bettis, E.S., Schroeder, R.W., Cristy, G.A., Savage, H.W., Affel, R.G., Hemphill, L.F., "The Aircraft Reactor Experiment—Design and Construction", *Nucl. Sci. Eng.*, **2**, 804-825 (1957).
- [28] Rosenthal, M.W., Kasten, P.R., Briggs, R.B., "Molten-salt reactors—history, status, and potential", *Nuclear Applications and Technology*, **8**, 107-117 (1970).
- [29] David Samuel, *Working Material for Molten Salt Coolants for High Temperature Reactors*, IAEA (2009).
- [30] Romatoski, R.R., Hu, L.W., "Fluoride salt coolant properties for nuclear reactor applications: a review", *Ann. Nucl. Energy*, **109**, 635-647 (2017).
- [31] Sohal, M.S., Ebner, M.A., Sabharwall, P., Sharpe, P., *Engineering Database of Liquid Salt Thermophysical and Thermochemical Properties*, INL (2010).
- [32] Janz, G.J., *Thermodynamic and Transport Properties for Molten Salts: Correlation Equations for Critically Evaluated Density, Surface Tension, Electrical Conductance, and Viscosity Data*, American Chemical Society and the American Institute of Physics, Troy, New York (1988).
- [33] Delpech, S., Cabet, C., Slim, C., Picard, G.S., "Molten fluorides for nuclear applications", *Materials Today*, **13**, 34-41 (2010).
- [34] Grimes, W.R., *Chemical Research and Development for Molten-Salt Breeder Reactors*, Ornl/Tm-1853, ORNL (1967).
- [35] Auger, T., Barreau, G., Chevalier, J., Doligez, X., Delpech, S., Flocard, H., Haas, B., Heuer, D., Merle-Lucotte, E., *The CNRS Research Program on the Thorium Cycle and the Molten Salt Reactors*, PACEN CNRS, Summary of Activities (2008).
- [36] Forsberg, C.W., Peterson, P.F., Williams, D.F., "Practical aspects of liquid-salt-cooled fast-neutron reactors", Proceedings of the 2005 International Conference on Advances in Nuclear Power Plants: Seoul, Korea., May 15–19 (2005).
- [37] de Zwaan, S.J., Boer, B., Lathouwers, D., Kloosterman, J.L., "Static design of a liquid-salt-cooled pebble bed reactor (LSPBR)", *Ann. Nucl. Energy*, **34**, 83-92 (2007).
- [38] Collins, D.M., Mahar, M.C., Whitehurst, F.W., "Bonding in lithium tetrafluoroberyllate (II)", *Acta Crystallographica Section B: Structural Science*, **39**, 303-306 (1983).

- [39] Seiler, P., "Estimation of ionicity coefficients in  $\text{Li}_2\text{BeF}_4$  crystals by X-ray diffraction", *Acta Crystallographica Section B: Structural Science*, **49**, 223-235 (1993).
- [40] Busing, W.R., "Interpretation of the Crystal Structure of  $\text{Li}_2\text{BeF}_4$  in Terms of the Born-Mayer-Huggins Model", *J. Chem. Phys.*, **57**, 3008 (1972).
- [41] Rosenthal, M.W., Briggs, R.B., Kasten, P.R., *Molten Salt Reactor Program Semiannual Progress Report for Period Ending August 31, 1968*, ORNL-4344, Oak Ridge National Lab (1969).
- [42] Ohmichi, T., Ohno, H., Furukawa, K., "Self-Diffusion of Fluorine in Molten Dilithium Tetrafluoroberyllate", *J. Phys. Chem.*, **80**, 1628-1631 (1976).
- [43] Abe, Y., Kosugiyama, O., Nagashima, A., "Viscosity of  $\text{LiF-BeF}_2$  eutectic mixture ( $\text{XBeF}_2 = 0.328$ ) and  $\text{LiF}$  single salt at elevated temperatures", *J. Nucl. Mater.*, **99**, 173-183 (1981).
- [44] Blanke, B.C., Bousquet, E.N., Curtis, M.L., Murphy, E.L., *Density and Viscosity of Fused Mixtures of Lithium, Beryllium, and Uranium Fluorides*, Mound Lab., MLM-1086 (1956).
- [45] Cantor, S., Cooke, J.W., Dworkin, A.S., Robbins, G.D., Thoma, R.E., Watson, G.M., *Physical Properties of Molten-Salt Reactor Fuel, Coolant, and Flush Salts*, Oak Ridge National Lab., ORNL-TM-2316 (1968).
- [46] Cantor, S., Ward, W.T., Moynthan, C.T., "Viscosity and Density in Molten  $\text{BeF}_2\text{-LiF}$  Solutions", *J. Chem. Phys.*, **50**, 2874 (1969).
- [47] Cohen, S.I., Jones, T.N., *Viscosity Measurements on Molten Fluoride Mixtures*, Oak Ridge National Lab., ORNL-2278 (1957).
- [48] Desyatnik, V.N., Nechaev, A.I., Chervinskii, Y.F., "Viscosity of Fused Mixtures of Beryllium Fluoride with Lithium and Sodium Fluorides", *J. APPL. CHEM-USSR.*, **54**, 2035-2037 (1981).
- [49] Cantor, S., *Density and Viscosity of several Molten Fluoride Mixtures*, Oak Ridge National Lab., ORNL-TM-4308 (1973).
- [50] Janz, G.J., Gardner, G.L., Krebs, U., Tomkins, R., "Molten Salts: Volume 4, Part 1, Fluorides and Mixtures Electrical Conductance, Density, Viscosity, and Surface Tension Data", *Journal of Physical and Chemical Reference Data*, **3**, 1-115 (1974).
- [51] R. B. Briggs, *Molten Salt Reactor Program Semiannual Progress Report for Period Ending August 31, 1965*, Oak Ridge National Laboratory Report (1965).
- [52] Rosenthal, M.W., Briggs, R.B., Kasten, P.R., *Molten Salt Reactor Program Semiannual Progress Report for Period Ending August 31, 1969*, ORNL-TM-4449, ORNL (1970).



- [53] M. W. Rosenthal, R. B. Briggs, P. R. Kasten, *Molten Salt Reactor Program Semiannual Progress Report for Period Ending February 28, 1969*, ORNL-4396, ORNL (1969).
- [54] Bohlmann, E.G., *Heat Transfer Salt for High Temperature Steam Generation*, ORNL-TM-3777, Oak Ridge National Lab (1972).
- [55] Iwamoto, N., Tsunawaki, Y., Umesaki, N., Ohno, H., Furukawa, K., "Self-diffusion of lithium in molten  $\text{LiBeF}_3$  and  $\text{Li}_2\text{BeF}_4$ ", *Journal of the Chemical Society, Faraday Transactions 2: Molecular and Chemical Physics*, **75**, 1277-1283 (1979).
- [56] Thoma, R.E., *Phase Diagrams of Nuclear Reactor Materials*, ORNL-2548, Oak Ridge National Lab (1959).
- [57] Ricci, J.E., *Guide to the Phase Diagrams of the Fluoride Systems*, ORNL-2396, Oak Ridge National Lab (1958).
- [58] Novoselova, A.V., Simanov, Y.P., Yarembash, E.I., "Thermal and X-ray analysis of the lithium-beryllium fluoride system", *Zh. Fiz. Chim.*, **26**, 1244 (1952).
- [59] Roy, D.M., Roy, R., Osborn, E.F., "Fluoride Model Systems: IV, The Systems  $\text{LiF-BeF}_2$  and  $\text{PbF}_2\text{-BeF}_2$ ", *J. Am. Ceram. Soc.*, **37**, 300-305 (1954).
- [60] Grimes, W.R., Blankenship, F.F., Keilholtz, G.W., Poppendiek, H.F., Robinson, M.T., *Chemical Aspects of Molten Fluoride Reactors*, ORNL (1958).
- [61] Douglas, T.B., Payne, W.H., "Measured enthalpy and derived thermodynamic properties of solid and liquid lithium tetrafluoroberyllate,  $\text{Li}_2\text{BeF}_4$ , from 273 to 900 K (Solid and liquid lithium tetrafluoroberyllate enthalpy relative to 273 K measured at temperatures between 323-873 K, deriving thermodynamic properties)", *JOURNAL OF RESEARCH*, **73**, 479-485 (1969).
- [62] Wang, J., Song, H., Hu, Z., Ye, T., Sun, W., "Thermal neutron scattering data for  $^7\text{LiF}$  and  $\text{BeF}_2$ ", Nuclear Data 2016: Bruges, Belgium, Sept 11-16 (2017).
- [63] Mei, L., Cai, X., Jiang, D., Chen, J., Guo, W., Xiong, W., "Investigation of thermal neutron scattering data for  $\text{BeF}_2$  and  $\text{LiF}$  crystals", *J. Nucl. Sci. Technol.*, **50**, 419-424 (2013).
- [64] Hawari, A.I., Al-Qasir, I., Gillette, V.H., Wehring, B.W., Zhou, T., "Ab initio generation of thermal neutron scattering cross sections", PHYSOR 2004: Chicago, IL, United states, April 25 - April 29 (2004).
- [65] Hehr, B., Hawari, A., *Calculation of the Thermal Neutron Scattering Cross Section of Alpha Quartz*, Paul Scherrer Institut - PSI, Switzerland (2008).

- [66] Holmes, J.C., Al-Qasir, I.I., Hawari, A.I., Leal, L.C., "Development of an ENDF Thermal Library for SiO<sub>2</sub> and Testing of Criticality Effects", *Transactions of the American Nuclear Society*, **104**, 438 (2011).
- [67] Hawari, A.I., "Modern Techniques for Inelastic Thermal Neutron Scattering Analysis", *Nuclear Data Sheets*, **118**, 172-175 (2014).
- [68] Wright, A.F., Fitch, A.N., Wright, A.C., "The preparation and structure of the  $\alpha$ - and  $\beta$ -quartz polymorphs of beryllium fluoride", *Journal of Solid State Chemistry*, **73**, 298-304 (1988).
- [69] Ghalsasi, P., Ghalsasi, P.S., "Single crystal X-ray structure of BeF<sub>2</sub>:  $\alpha$ -quartz", *Inorg. Chem.*, **50**, 86-89 (2010).
- [70] Hauback, B.C., Brinks, H.W., Heyn, R.H., Blom, R., Fjellvag, H., "The crystal structure of KAID 4", *J. Alloys Compounds*, **394**, 35-38 (2005).
- [71] Thewlis, J., "Unit-cell dimensions of lithium fluoride made from Li<sup>6</sup> and Li<sup>7</sup>", *Acta Crystallogr.*, **8**, 36-38 (1955).
- [72] Mei, L., Cai, X., Jiang, D., Chen, J., Zhu, Y., Liu, Y., Wang, X., "The investigation of thermal neutron scattering data for molten salt Flibe", *J Nucl Sci Technol*, **50**, 682-688 (2013).
- [73] Li, Z., Cao, L., Wu, H., He, Q., "The impacts of thermal neutron scattering effect and resonance elastic scattering effect on FHRs", *Annals of Nuclear Energy*, **97**, 102-114 (2016).
- [74] Li, Z., Cao, L., Wu, H., He, Q., Shen, W., "On the improvements in neutronics analysis of the unit cell for the pebble-bed fluoride-salt-cooled high-temperature reactor", *Prog. Nuclear Energy*, **93**, 287-296 (2016).
- [75] Li, Z., Cao, L., Wu, H., "The impacts of random effect and scattering effects on the neutronics analysis of the PB-FHR", *Ann. Nucl. Energy*, **108**, 163-171 (2017).
- [76] Jabes, B.S., Agarwal, M., Chakravarty, C., "Structure and transport properties of LiF–BeF<sub>2</sub> mixtures: Comparison of rigid and polarizable ion potentials", *Journal of Chemical Sciences*, **124**, 261-269 (2012).
- [77] Van Hove, L., "Correlations in Space and Time and Born Approximation Scattering in Systems of Interacting Particles", *Physical Review*, **95**, 249-262 (1954).
- [78] Vineyard, G.H., "Scattering of slow neutrons by a liquid", *Physical Review*, **110**, 999 (1958).
- [79] Sjölander, A., "Multi-phonon processes in slow neutron scattering by crystals", *Arkiv Fysik*, **14**, 315-371 (1958).
- [80] Rahman, A., Singwi, K.S., Sjölander, A., "Theory of slow neutron scattering by liquids. I", *Physical Review*, **126**, 986 (1962).

- [81] Egelstaff, P.A., *An Introduction to the Liquid State*, American Association for the Advancement of Science, New York (1968).
- [82] Copley, J., Lovesey, S.W., "The dynamic properties of monatomic liquids", *Reports on Progress in Physics*, **38**, 461 (1975).
- [83] Hess, W., Klein, R., "Generalized hydrodynamics of systems of Brownian particles", *Adv. Phys.*, **32**, 173-283 (1983).
- [84] Egorov, S.A., Everitt, K.F., Skinner, J.L., "Quantum dynamics and vibrational relaxation", *The Journal of Physical Chemistry A*, **103**, 9494-9499 (1999).
- [85] Abe, Y., Tasaki, S., "Molecular dynamics analysis of incoherent neutron scattering from light water via the Van Hove space-time self-correlation function with a new quantum correction", *Ann. Nucl. Energy*, **83**, 302-308 (2015).
- [86] Squires, G.L., *Introduction to the Theory of Thermal Neutron Scattering*, Cambridge University Press, Cambridge CB2 8RU, UK (2012).
- [87] Hawari, A.I., Al-Qasir, I., "Graphite thermal neutron scattering cross section calculations including coherent 1-phonon effects", PHYSOR 2008: Interlaken, Switzerland, Sept. 14 - Sept. 19 (2008).
- [88] Turner, R.E., "The quasi-classical approximation for neutron scattering", *Physica*, **27**, 260-264 (1961).
- [89] Hehr, B.D., Development of the Thermal Neutron Scattering Cross Sections of Graphitic Systems using Classical Molecular Dynamics Simulations. PhD Thesis, North Carolina State University, (2010).
- [90] Balucani, U., Zoppi, M., *Dynamics of the Liquid State*, Oxford: Clarendon Press, New York : Oxford University Press (1994).
- [91] Parks, D.E., Beyster, J.R., Nelkin, M.S., Wikner, N.F., *Slow Neutron Scattering and Thermalization with Reactor Applications*, W. A. Benjamin, Inc, New York, New York 10016 (1970).
- [92] Egelstaff, P.A., Schofield, P., "On the evaluation of the thermal neutron scattering law", *Nucl. Sci. Eng.*, **12**, 260-270 (1962).
- [93] Springer, T., "Quasielastic neutron scattering for the investigation of diffusive motions in solids and liquids", *Springer Tracts in Modern Physics*, **64**, 1-100 (1972).
- [94] Schofield, P., "Space-time correlation function formalism for slow neutron scattering", *Phys. Rev. Lett.*, **4**, 239 (1960).

- [95] Aamodt, R., Case, K.M., Rosenbaum, M., Zweifel, P.F., "Quasi-classical treatment of neutron scattering", *Physical Review*, **126**, 1165 (1962).
- [96] Rosenbaum, M., Zweifel, P.F., "Quasiclassical theory of neutron scattering", *Physical Review*, **137**, B271 (1965).
- [97] Bader, J.S., Berne, B.J., "Quantum and classical relaxation rates from classical simulations", *J. Chem. Phys.*, **100**, 8359-8366 (1994).
- [98] An, S., Montrose, C.J., Litovitz, T.A., "Low-frequency structure in the depolarized spectrum of argon", *J. Chem. Phys.*, **64**, 3717-3719 (1976).
- [99] Berne, B.J., Harp, G.D., "Correlation Functions", *Advances in chemical physics*, **17**, 63 (2009).
- [100] Oxtoby, D.W., "Vibrational population relaxation in liquids", *Advances in Chemical Physics: Photosensitive Chemistry. Part 2*, **47**, 487-519 (1981).
- [101] Haile, J.M., *Molecular Dynamics Simulation*, Wiley, New York (1992).
- [102] Zhu, Y., Hawari, A.I., "Thermal neutron scattering cross section of liquid FLiBe", *Prog. Nuclear Energy*, **101**, 468-475 (2017).
- [103] Daw, M.S., Baskes, M.I., "Embedded-atom method: Derivation and application to impurities, surfaces, and other defects in metals", *Physical Review B*, **29**, 6443 (1984).
- [104] Daw, M.S., Foiles, S.M., Baskes, M.I., "The embedded-atom method: a review of theory and applications", *Materials Science Reports*, **9**, 251-310 (1993).
- [105] Tersoff, J., "New empirical approach for the structure and energy of covalent systems", *Physical Review B*, **37**, 6991 (1988).
- [106] Jorgensen, W.L., Chandrasekhar, J., Madura, J.D., Impey, R.W., Klein, M.L., "Comparison of simple potential functions for simulating liquid water", *J. Chem. Phys.*, **79**, 926-935 (1983).
- [107] Huggins, M.L., Mayer, J.E., "Interatomic distances in crystals of the alkali halides", *J. Chem. Phys.*, **1**, 643-646 (1933).
- [108] Born, M., Mayer, J.E., "Zur Gittertheorie der Ionenkristalle", *Zeitschrift für Physik*, **75**, 1-18 (1932).
- [109] Fumi, F.G., Tosi, M.P., "Ionic sizes and born repulsive parameters in the NaCl-type alkali halides—I: The Huggins-Mayer and Pauling forms", *Journal of Physics and Chemistry of Solids*, **25**, 31-43 (1964).
- [110] Tosi, M.P., Fumi, F.G., "Ionic sizes and born repulsive parameters in the NaCl-type alkali halides—II", *Journal of Physics and Chemistry of Solids*, **25**, 45-52 (1964).

- [111] Abrahamson, A.A., "Born-Mayer-type interatomic potential for neutral ground-state atoms with  $Z=2$  to  $Z=105$ ", *Physical review*, **178**, 76 (1969).
- [112] Gaydaenko, V.I., Nikulin, V.K., "Born-Mayer interatomic potential for atoms with  $Z=2$  to  $Z=36$ ", *Chemical Physics Letters*, **7**, 360-362 (1970).
- [113] Sangster, M., Dixon, M., "Interionic potentials in alkali halides and their use in simulations of the molten salts", *Adv. Phys.*, **25**, 247-342 (1976).
- [114] Plimpton, S., "Fast Parallel Algorithms for Short-Range Molecular Dynamics", *Journal of Computational Physics*, **117**, 1-19 (1995).
- [115] Van der Meer, J P M, Konings, R.J.M., "Thermal and physical properties of molten fluorides for nuclear applications", *J. Nucl. Mater.*, **360**, 16-24 (2007).
- [116] Forsberg, C., Hu, L., Peterson, P., Sridharan, K., *Fluoride-Salt-Cooled High-Temperature Reactor (FHR) for Power and Process Heat*, DOE/NEUP--11-3272; MIT-ANP-TR--157, MIT (2015).
- [117] Forsberg, C., Peterson, P.F., "Basis for Fluoride Salt–Cooled High-Temperature Reactors with Nuclear Air-Brayton Combined Cycles and Firebrick Resistance-Heated Energy Storage", *Nucl. Technol.*, **196**, 13-33 (2016).
- [118] Kubo, R., "Statistical-mechanical theory of irreversible processes. I. General theory and simple applications to magnetic and conduction problems", *Journal of the Physical Society of Japan*, **12**, 570-586 (1957).
- [119] Green, M.S., "Markoff random processes and the statistical mechanics of time-dependent phenomena. II. Irreversible processes in fluids", *J. Chem. Phys.*, **22**, 398-413 (1954).
- [120] Rawlings, J.O., Pantula, S.G., Dickey, D.A., *Applied Regression Analysis: A Research Tool: 4.6 Univariate and Joint Confidence Regions*, Springer Science & Business Media, New York (2001).
- [121] de Jong, Paul Harmen Kenneth, Microscopic dynamics and structure of liquid lithium and liquid lithium-based alloys, PhD Thesis, Delft University of Technology, (1993).
- [122] Azez, K.A., Al-Omari, I.A., "Effect of screening on resistivity of liquid metals", *Acta Physica Polonica-Series A General Physics*, **92**, 563-568 (1997).
- [123] Hoshino, K., Young, W.H., "A simple local pseudopotential for lithium", *Journal of Physics F: Metal Physics*, **16**, 1659 (1986).
- [124] Shaw Jr, R.W., "Application of the optimized model potential to calculation of energy-wave-number characteristics for simple metals", *Journal of Physics C: Solid State Physics*, **2**, 2335 (1969).

- [125] Gonzalez, L.E., Gonzalez, D.J., Silbert, M., "The pair distribution functions of the liquid alkali metals: Comparison between the VMHNC theory and molecular dynamics simulations", *Physica B: Condensed Matter*, **168**, 39-44 (1991).
- [126] Das, S.K., Roy, D., Sengupta, S., "A modified Ashcroft pseudopotential: application to aluminium", *Pramana*, **17**, 419-427 (1981).
- [127] Ashcroft, N.W., "Electron-ion pseudopotentials in metals", *Physics Letters*, **23**, 48-50 (1966).
- [128] Miranda, J.G., Torra, V., "The effect of the Born-Mayer core on the properties of liquid lithium and sodium at their melting points", *Physics Letters A*, **103**, 126-128 (1984).
- [129] Miranda, J.G., "An effective pair potential for liquid lithium at 455 K", *Physics Letters A*, **108**, 35-38 (1985).
- [130] Canales, M., Gonzalez, L.E., Padr, J.n., "Computer simulation study of liquid lithium at 470 and 843 K", *Physical Review E*, **50**, 3656 (1994).
- [131] Gonzalez, L.E., Gonzalez, D.J., Hoshino, K., "The structure and electronic density distribution in the liquid alkali metals", *Journal of Physics: Condensed Matter*, **5**, 9261 (1993).
- [132] Gonzalez, L.E., Gonzalez, D.J., Silbert, M., Alonso, J.A., "A theoretical study of the static structure and thermodynamics of liquid lithium", *Journal of Physics: Condensed Matter*, **5**, 4283 (1993).
- [133] Canales, M., Padr, J.A., Gonzalez, L.E., Gir, A., "Molecular dynamics simulation of liquid lithium", *Journal of Physics: Condensed Matter*, **5**, 3095 (1993).
- [134] Gonzalez, D.J., Gonzalez, L.E., Hoshino, K., "Static and dynamic structure of liquid lithium", *Journal of Physics: Condensed Matter*, **6**, 3849 (1994).
- [135] Salmon, P.S., Petri, I., de Jong, P.H., Verkerk, P., Fischer, H.E., Howells, W.S., "Structure of liquid lithium", *Journal of Physics: Condensed Matter*, **16**, 195 (2004).
- [136] Sears, V.F., "Neutron scattering lengths and cross sections", *Neutron news*, **3**, 26-37 (1992).
- [137] Zhu, Y., Hawari, A.I., "FULL LAW ANALYSIS SCATTERING SYSTEM HUB (FLASSH)", Proc. PHYSOR 2018: Cancun, Mexico, April 22-26 (2018).
- [138] Nelkin, M., "Scattering of slow neutrons by water", *Physical Review*, **119**, 741 (1960).

## **APPENDICES**

## Appendix A. Thermal Neutron Scattering for Solid Materials

### A.1 The Gaussian and Cubic Approximation

In Section 2.2.1, the width function from the Gaussian approximation for liquid materials has been reviewed. Under the Gaussian approximation, the self van Hove correlation function  $G_s(r, t)$  is a Gaussian function of  $r$ ; the self intermediate scattering function  $I_s(k, t)$  is a Gaussian function of  $k$ . In this section, it will be proven that the Gaussian Approximation and the width function model also apply to crystalline materials. The same quantum width function in Eq. (2.2.15) will be deduced for crystalline solid materials through utilizing the phonon model.

In a solid crystalline material, the thermal motions of atoms emerge around its equilibrium position. Thanks to this, the interatomic forces, to a large extent, are harmonic. Therefore, by assuming harmonic forces, the displacement of atom is well described by harmonic oscillator with normal modes given by

$$\mathbf{u}_l = \sqrt{\frac{\hbar}{2MN}} \sum_s \frac{\mathbf{e}_s}{\sqrt{\omega_s}} \left[ a_s e^{iq \cdot l} + a_s^\dagger e^{-iq \cdot l} \right] \quad (\text{A.1})$$

where the  $\mathbf{e}_s$  is the polarization vector, describing the direction of oscillation,  $M$  is the mass of the atom,  $\omega_s$  is the frequency of oscillation,  $a_s$  and  $a_s^\dagger$  are the rising and lowering operator of the harmonic oscillator,  $\mathbf{q}$  is the plane wave vector which indicates the propagation direction of the oscillation wave. The  $\mathbf{u}_l$  is the summed displacement from all the oscillators contributions for the  $l^{\text{th}}$  atom in the unit cell. This assumption of harmonic forces is conventionally named the harmonic approximation.

Substitution of this oscillator displacement as the  $\mathbf{R}_j$  position in Eq. (2.1.8) will give us the Heisenberg quantum displacement operator  $\mathbf{R}_j(t)$ . Further analysis [86] into Eq. (2.1.20) using the quantum operator  $\mathbf{R}_j(t)$  will give



$$I_s(\mathbf{k}, t) = e^{\langle U^2 \rangle + \langle UV_0 \rangle} \quad (\text{A.2})$$

$$\langle U^2 \rangle = -2W = -\frac{\hbar}{2MN} \sum_s \frac{(\mathbf{k} \cdot \mathbf{e}_s)^2}{\omega_s} \coth\left(\frac{\hbar\omega_s}{2k_B T}\right) \quad (\text{A.3})$$

$$\langle UV_0 \rangle = \frac{\hbar}{2MN} \sum_s \frac{(\mathbf{k} \cdot \mathbf{e}_s)^2}{\omega_s} [\langle n_s + 1 \rangle e^{i\omega_s t} + \langle n_s \rangle e^{-i\omega_s t}] \quad (\text{A.4})$$

At this point, we will assume that the displacement of atoms in the unit cell does not favor particular directions so that  $\sum_s (\mathbf{k} \cdot \mathbf{e}_s)^2 = \frac{1}{3} k^2$ . This approximation is commonly recognized as the cubic approximation and is true for cubic crystalline materials. Even for non-cubic crystal, the average of  $(\mathbf{k} \cdot \mathbf{e}_s)^2$  over the same normal mode is often close to  $\frac{1}{3} k^2$ . In most cases, the cubic approximation holds closely to reality. By applying the cubic approximation,  $\langle U^2 \rangle$  and  $\langle UV_0 \rangle$  become

$$\begin{aligned} \langle UV_0 \rangle &= \frac{\hbar k^2}{2M} \frac{1}{3N} \sum_s \frac{1}{\omega_s} [\langle n_s + 1 \rangle e^{i\omega_s t} + \langle n_s \rangle e^{-i\omega_s t}] \\ &= \frac{\hbar k^2}{2M} \frac{1}{3N} \sum_s \frac{1}{\omega_s} \left[ \frac{e^{\hbar\omega_s/k_B T}}{e^{\hbar\omega_s/k_B T} - 1} e^{i\omega_s t} + \frac{1}{e^{\hbar\omega_s/k_B T} - 1} e^{-i\omega_s t} \right] \end{aligned} \quad (\text{A.5})$$

$$\begin{aligned} &= \frac{\hbar k^2}{2M} \frac{1}{3N} \sum_s \frac{1}{\omega_s} \left[ \frac{e^{\hbar\omega_s/k_B T} + 1}{e^{\hbar\omega_s/k_B T} - 1} \cos(\omega_s t) + i \sin(\omega_s t) \right] \\ &= \frac{\hbar k^2}{2M} \int_0^{\omega_m} \frac{Z(\omega)}{\omega} \left[ \coth\left(\frac{\hbar\omega}{2k_B T}\right) \cos(\omega t) + i \sin(\omega t) \right] d\omega \\ \langle U^2 \rangle &= -\frac{\hbar k^2}{2M} \int_0^{\omega_m} \frac{Z(\omega)}{\omega} \coth\left(\frac{\hbar\omega}{2k_B T}\right) d\omega \end{aligned} \quad (\text{A.6})$$

where the  $Z(\omega)$  is the phonon density of states. The phonon generation state  $\langle n_s + 1 \rangle$  and the phonon absorption state  $\langle n_s \rangle$  are

$$\begin{cases} \langle n_s \rangle = \frac{1}{e^{\hbar\omega_s/k_B T} - 1} \\ \langle n_s + 1 \rangle = \frac{e^{\hbar\omega_s/k_B T}}{e^{\hbar\omega_s/k_B T} - 1} \end{cases} \quad (\text{A.7})$$

With Eq. (A.2), (A.6) and (A.5), the  $I_s(k, t)$  can be evaluated by

$$I_s(k, t) = \exp \left\{ -\frac{\hbar k^2}{2M} \int_0^{\omega_m} \frac{Z(\omega)}{\omega} \left[ \coth\left(\frac{\hbar\omega}{2k_B T}\right) (1 - \cos(\omega t)) - i \sin(\omega t) \right] d\omega \right\} \quad (\text{A.8})$$

It is shown in the above equation that the self intermediate scattering function is a Gaussian function of reciprocal space vector  $k$ . The width function of the Gaussian is exactly the same as Eq. (2.2.15) shown for liquid. A full derivation of Eq. (A.8) without applying the cubic approximation in the first place can be found in Alf Sjolander's paper [79].

## A.2 The Phonon Expansion

In the previous section, the width function of crystalline material has been deduced. The underlying assumptions of Eq. (A.8) are the harmonic approximation and the cubic approximation. In this section, a more implementation-friendly form of Eq. (A.8) will be deduced. The methodology is known as the phonon expansion. Based on the derivation, the principle of detailed balance will also be proven.

The interacting forces in a crystalline material can be approximated as harmonic forces. Under the harmonic approximation, the phonon density of states shows a quadratic form in its low frequency region. This behavior is important because it makes the exponential in  $I_{inc}(k, t)$  starts from 0 when  $\omega = 0$ . Therefore, it is possible to Tylor expand  $I_{inc}(k, t)$  to different phonon orders in  $\omega$  domain. This methodology is named phonon expansion.

Before we progress to the phonon expansion, some mathematical manipulation on the width function needs to be done. In the second step in Eq. (A.9), the frequency domain is unfolded from the positive real domain to the full real domain.

$$\begin{aligned}
\langle UV_0 \rangle &= \frac{\hbar k^2}{2M} \frac{1}{3N} \sum_s \frac{1}{\omega_s} \left[ \frac{e^{\hbar\omega_s/2k_B T}}{e^{\hbar\omega_s/2k_B T} - 1} e^{i\omega_s t} \delta(\omega - \omega_s) + \frac{1}{e^{\hbar\omega_s/2k_B T} - 1} e^{-i\omega_s t} \delta(\omega + \omega_s) \right] \\
&= \frac{\hbar k^2}{2M} \frac{1}{3N} \sum_s \frac{1}{\omega_s} \left[ \frac{e^{\hbar\omega_s/2k_B T} + 1}{e^{\hbar\omega_s/2k_B T} - 1} e^{i\omega t} \right], \quad (\omega \in R) \\
&= \frac{\hbar k^2}{2M} \int_0^{\omega_m} \frac{Z(\omega)}{\omega} \left[ \coth\left(\frac{\hbar\omega}{2k_B T}\right) e^{i\omega t} \right] d\omega
\end{aligned} \tag{A.9}$$

So that the width function can be written as

$$\gamma(t) = \frac{\hbar}{2M} \int_{-\infty}^{+\infty} \frac{Z(\omega) e^{\frac{\hbar\omega}{2k_B T}}}{2\omega \sinh\left(\frac{\hbar\omega}{2k_B T}\right)} \left[ 1 - e^{i\omega t} \right] d\omega \tag{A.10}$$

It is worth noting that Eq. (A.10) is the quantum correction for solid materials that Brian Hehr applied in his previous PhD thesis research. With the power of Eq. (A.10), the phonon expansion can be applied. Define function  $K(\omega)$ ,  $G(\omega)$  and Debye-Waller coefficient  $\lambda$  as following

$$K(\omega) = \frac{Z(\omega) e^{\frac{\hbar\omega}{2k_B T}}}{2\omega \sinh\left(\frac{\hbar\omega}{2k_B T}\right)} \tag{A.11}$$

$$\lambda = \int_{-\infty}^{\infty} K(\omega) d\omega \tag{A.12}$$

$$G(\omega) = K(\omega) / \lambda \tag{A.13}$$

Then  $S_s(k, \omega)$  is the Fourier transform of  $I_s(k, t)$ . The Taylor expansion in the last step is conventionally called the phonon expansion

$$\begin{aligned}
S_s(k, \omega) &= \int e^{-i\omega t} I_{inc}(k, t) dt = \int e^{-i\omega t} e^{-k^2 \gamma(t)} dt \\
&= \int e^{-i\omega t} e^{-\frac{\hbar k^2}{2M} \int_{-\infty}^{+\infty} K(\omega') [1 - e^{i\omega' t}] d\omega'} dt \\
&= \int e^{-i\omega t} e^{-\alpha \lambda \int_{-\infty}^{+\infty} G(\omega') [1 - e^{i\omega' t}] d\omega'} dt \\
&= e^{-\alpha \lambda} \sum_{n=0}^{\infty} \frac{(\alpha \lambda)^n}{n!} \int dt e^{-i\omega t} \left[ \int_{-\infty}^{+\infty} G(\omega') e^{i\omega' t} d\omega' \right]^n
\end{aligned} \tag{A.14}$$

Here, a new function  $G_n(\omega)$  can be assigned as

$$G_n(\omega) = \int dt e^{-i\omega t} \left[ \int_{-\infty}^{+\infty} G(\omega') e^{i\omega' t} d\omega' \right]^n \quad (\text{A.15})$$

As the Fourier transform of multiplication can be evaluated by convolution, the above equation can be evaluated by

$$G_n(\omega) = \int_{-\infty}^{\infty} G_1(\omega') G_{n-1}(\omega - \omega') d\omega' \quad (\text{A.16})$$

with

$$\begin{aligned} G_0(\omega) &= \delta(\omega) \\ G_1(\omega) &= \frac{Z(\omega) e^{\frac{\hbar\omega}{2k_B T}}}{2\lambda\omega \sinh\left(\frac{\hbar\omega}{2k_B T}\right)} \end{aligned} \quad (\text{A.17})$$

From Eq. (A.14)-(A.17) are the set of formula deployed in conventional thermal neutron scattering cross section evaluation code, e.g. LEAPR module in NJOY code system. The approximation applied are the harmonic approximation, the cubic approximation, and the incoherent approximation. In conventional TSL code, such as NJOY, the phonon expansion technique is utilized in combination with the classical diffusional models proposed in Section 2.2.2 to capture both vibrational and diffusional motion modes in liquid systems. The theoretical background of this methodology is discussed in Section 2.5.

Mathematical deduction can be applied to prove that all terms in  $G_n(\omega)$  follows the principle of detailed balance. First,  $G_1(\omega)$  obviously follows the principle of detailed balance

$$G_1(-\omega) = G_1(\omega) e^{\frac{\hbar\omega}{k_B T}} \quad (\text{A.18})$$

Second, assume that the  $G_{n-1}(\omega)$  term follows the principle of detailed balance. The following deduction can be made

$$\begin{aligned}
G_n(-\omega) &= \int G_1(\omega') G_{n-1}(-\omega - \omega') d\omega' \\
&= \int G_1(\omega') G_{n-1}(\omega + \omega') e^{\frac{\hbar(\omega + \omega')}{k_B T}} d\omega' \\
&= \int G_1(-\omega') G_{n-1}(\omega + \omega') e^{\frac{\hbar\omega}{k_B T}} d\omega' \\
&= e^{\frac{\hbar\omega}{k_B T}} \int G_1(\omega'') G_{n-1}(\omega - \omega'') d\omega'' \\
&= e^{\frac{\hbar\omega}{k_B T}} G_n(\omega)
\end{aligned} \tag{A.19}$$

Therefore, it is proved that all terms in  $G_n(\omega)$  follows the principle of detailed balance. This is an implicit proof that  $S_s(k, \omega)$  transformed from  $I_s(k, t)$  with quantum width function  $\gamma(t)$  is self-consistent with the principle of detailed balance.

## Appendix B. Derivation of the Width Function of the Self Thermal Scattering Law for Liquid Materials

In this appendix, the derivation of quantum width function from Rahman's work [80] will be reviewed in the first part. In the second part, a derivation from Rahman's formula to the quantum correction algorithm will be shown.

### B.1 The Derivation of the Quantum Width Function

In Rahman's paper, the self intermediate scattering function  $I_s(k, t)$  was assigned with the notation  $A(\mathbf{k}, t)$ . The  $I_s(k, t)$  function is known to be symmetric in  $t$  and can be expanded to the following form [90]

$$I_s(k, t) = \exp \left\{ \sum_{n=1}^{\infty} (-\kappa^2)^n \cdot \gamma_n(t) \right\} \tag{B.1}$$

The first order in Eq. (B.1) is the Gaussian approximation. By applying the Gaussian approximation, it is equivalent to ignore the second and higher order terms in Eq. (B.1)

$$I_s(k, t) = \exp[-\kappa^2 \gamma_1(t)] \quad (\text{B.2})$$

where

$$\gamma_1(t) = -i(\hbar t / 2M) + \int_0^t (t - t_1) \langle \mathbf{v}(0) \cdot \mathbf{v}(t_1) \rangle_T dt_1 \quad (\text{B.3})$$

The imaginary part comes from the existence of  $i$  and Hamiltonian  $H$  in the quantum definition of  $I(k, t)$

$$I(\mathbf{k}, t) = \exp(i\hbar \mathbf{k}^2 t / 2M) \sum_j \left\langle \exp \left\{ -i\mathbf{k} \cdot [\mathbf{r}_0(0) - \mathbf{r}_j(0)] \right\} \right. \\ \left. \cdot \exp(iH'_j t / \hbar) \cdot \exp(-iHt / \hbar) \right\rangle_T \quad (\text{B.4})$$

Due to this definition, the velocity in Eq. (B.3) is defined as the Heisenberg operator

$$\mathbf{v}(t) = \frac{1}{M} \exp\left(\frac{iHt}{\hbar}\right) \cdot \mathbf{p} \cdot \exp\left(\frac{-iHt}{\hbar}\right) \quad (\text{B.5})$$

where  $\mathbf{p}$  is the momentum operator

$$\mathbf{p} = -i\hbar \frac{\partial}{\partial \mathbf{z}} \quad (\text{B.6})$$

By Eq. (B.5), it is clear that the velocity correlation function in Eq. (B.3) is a complex function. Here two frequency spectra,  $g(\omega)$  and  $f(\omega)$ , related to the real and imaginary parts of the velocity correlation function are defined

$$\text{Im} \langle \mathbf{v}(0) \cdot \mathbf{v}(t_1) \rangle_T = \frac{\hbar}{2M} \int_0^\infty \omega f(\omega) \sin(\omega t) d\omega \quad (\text{B.7})$$

$$\text{Re} \langle \mathbf{v}(0) \cdot \mathbf{v}(t_1) \rangle_T = \frac{k_B T}{M} \int_0^\infty g(\omega) \cos(\omega t) d\omega \quad (\text{B.8})$$

where the function  $g(\omega)$  and  $f(\omega)$  are related by the thermal equilibrium of the scattering system.

$$g(\omega) = \frac{\hbar \omega}{2k_B T} \coth\left(\frac{\hbar \omega}{2k_B T}\right) f(\omega) \quad (\text{B.9})$$

This can be proved by the fluctuation-dissipation theorem. By substituting the above three equations in to Eq. (B.3), the quantum width function can be deduced

$$\gamma_1(t) = \frac{\hbar}{2M} \int_0^\infty \frac{f(\omega)}{\omega} \left[ (1 - \cos \omega t) \coth \frac{\hbar \omega}{2k_B T} - i \sin \omega t \right] d\omega \quad (\text{B.10})$$

It should be noted that this quantum width function for liquid system is the same as the one we deduced for solid crystalline system using the phonon model in Eq. (A.8).

## B.2 Application of the Quantum Width Function Algorithm

In the previous section, the quantum width function, i.e. Eq. (B.10), has been deduced. In this section, this equation will be developed into a computational applicable algorithm that can correct the classical width function to its quantum counterpart. To begin with, recall that the classical width function from MD is Eq. (2.2.12) from reference [91]

$$w(t) = \frac{2k_B T}{M} \int_0^\infty \frac{f^{cl}(\omega)}{\omega^2} (1 - \cos \omega t) d\omega \quad (\text{B.11})$$

The classical width function is related to the MSD by Eq. (2.2.9). Therefore, by combining Eq. (B.11) and Eq. (2.2.9), transforming the frequency  $\omega$  to  $\beta$ , we have

$$\frac{f^{cl}(\beta)}{\beta^2} = FFT \left( \frac{Mk_B T}{3\hbar^2} \delta r^2(t') \right) \quad (\text{B.12})$$

The constant 1 together with  $\cos \omega t$  is ignored because it is simply a relocation constant to relocate  $w(t)$  to origin at  $t = 0$ . The 1 in Eq. (B.10) has the same effect. In the computational algorithm, the evaluated real part of the quantum width function will be reset to origin to compensate the ignorance of 1.

Transforming Eq. (B.10) into  $\beta$  notation and expand the range of integral from  $-\infty$  to  $\infty$

$$\begin{aligned}
\gamma_1(t') &= \frac{k_B T}{2M} \int_0^\infty \frac{f(\beta)}{\beta} \left[ (1 - \cos \beta t') \coth \frac{\beta}{2} - i \sin \beta t' \right] d\beta \\
&= \frac{k_B T}{2M} \int_{-\infty}^\infty \frac{f(\beta)}{\beta^2} \left[ (1 - \cos \beta t') \frac{\beta e^{\beta/2}}{2 \sinh \beta/2} - i \frac{\beta}{2} \sin \beta t' \right] d\beta
\end{aligned} \tag{B.13}$$

As mentioned above, by ignoring the 1 associated with the  $\cos \omega t$  function, the quantum width function can be connected to the evaluated  $f^{cl}(\beta)/\beta^2$  function in Eq. (B.12)

$$\gamma_1(t') = \frac{k_B T}{2M} FFT \left\{ \text{Re} \left[ f^{qt}(\beta) \right] + i \text{Im} \left[ f^{qt}(\beta) \right] \right\} \tag{B.14}$$

where

$$\begin{cases} \text{Re} \left[ f^{qt}(\beta) \right] = \frac{\beta e^{\beta/2}}{2 \sinh(\beta/2)} \cdot \frac{f^{cl}(\beta)}{\beta^2} \\ \text{Im} \left[ f^{qt}(\beta) \right] = -\frac{\beta}{2} \cdot \frac{f^{cl}(\beta)}{\beta^2} \end{cases} \tag{B.15}$$

It should be noted again that the real part of the quantum width function evaluated from Eq. (B.14) should be treated with caution. To compensate for the ignorance of 1 in both Eq. (B.11) and (B.13), the real part of the Fourier transformed quantum width function should be reallocated to origin point (zero). The rest of the real part should be shifted by the same amount. This shift is physical because it enforces the value of  $I_s(k, t)$  at  $t = 0$  equals to unity 1. The autocorrelation of the atom with itself at  $t = 0$  equals 1 basically means that the atom is fully correlated with itself at zero correlation time, which is required by the law of physics.

## Appendix C. Numerical Issues in the NJOY Code

The goal of this appendix is not to cover all the numerical issues that exist in the NJOY code. Instead, the issues related to diffusional thermal scattering law will be reviewed. The first of such issue is the lack of diffusional peak in angular differential cross section in Figure 5-49.



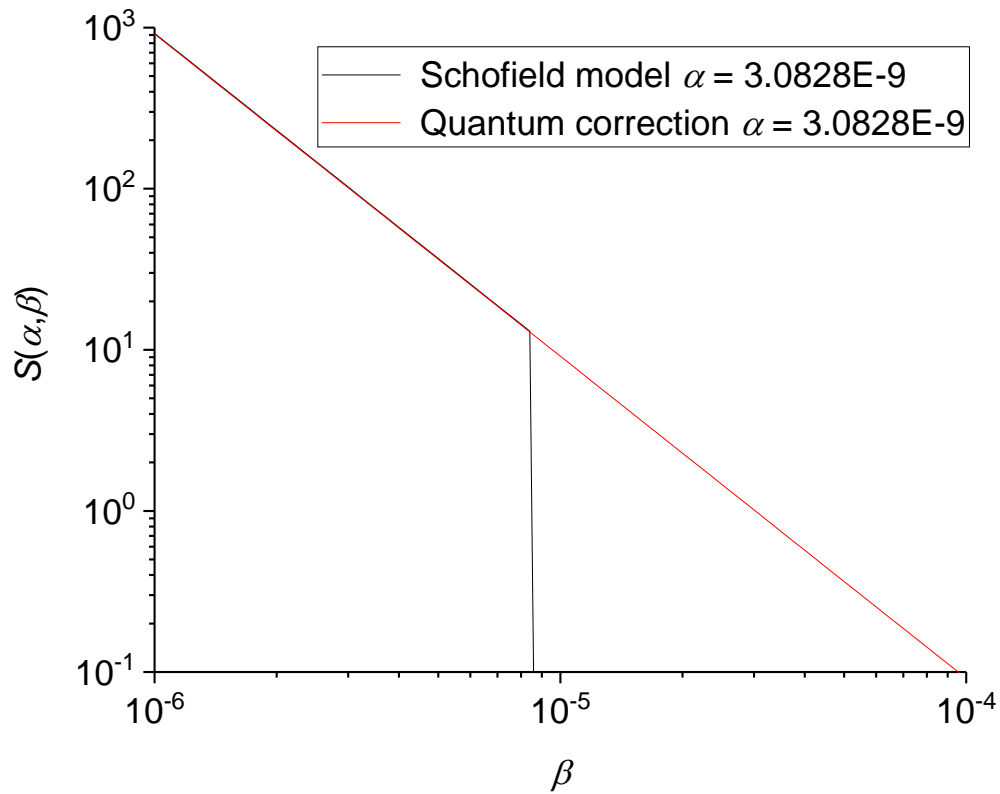


Figure 6-1.  $S(\alpha, \beta)$  showing cut off at  $\alpha = 3.1 \times 10^{-9}$ .

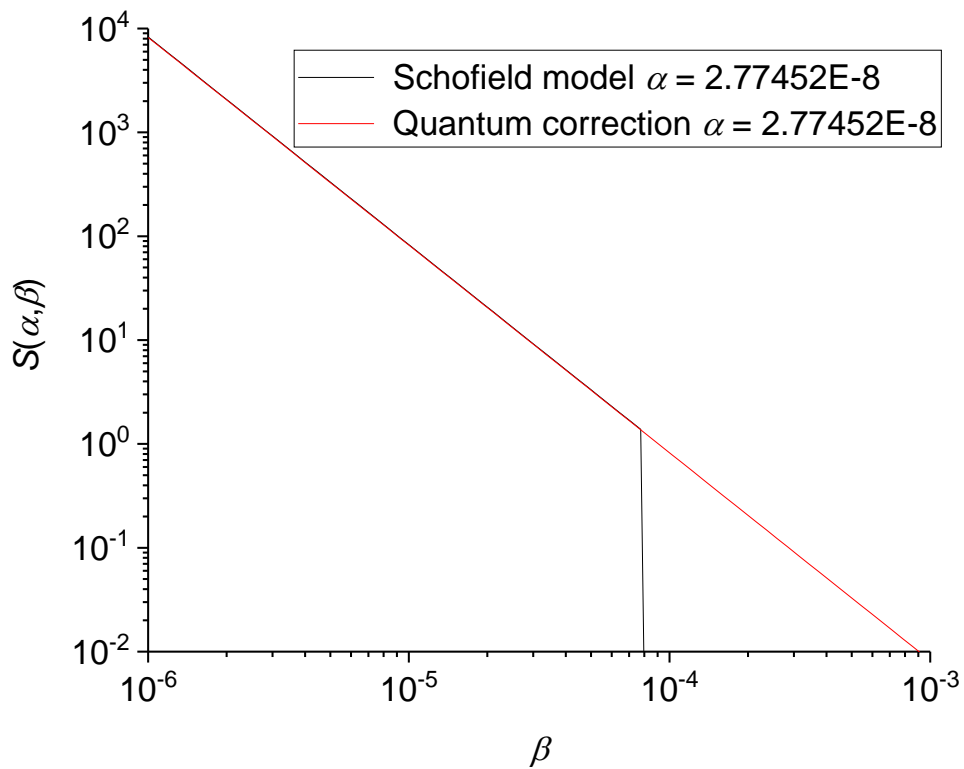


Figure 6-2.  $S(\alpha, \beta)$  showing cut off at  $\alpha = 2.8 \times 10^{-8}$ .

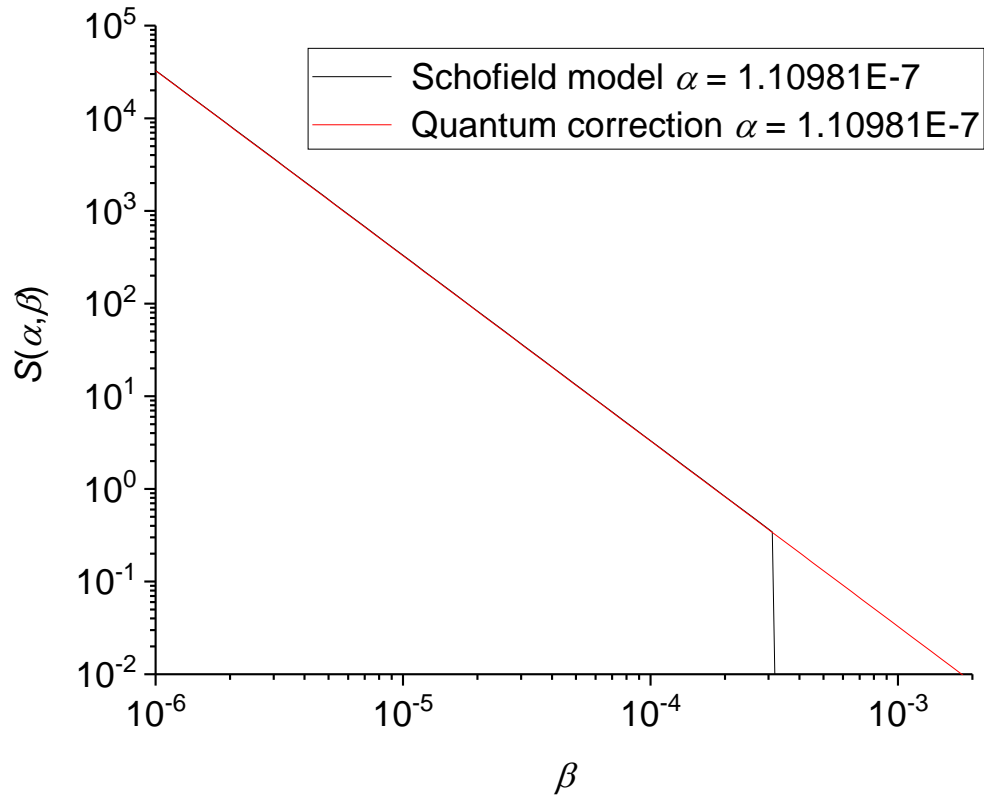


Figure 6-3.  $S(\alpha, \beta)$  showing cut off at  $\alpha = 1.1 \times 10^{-7}$ .

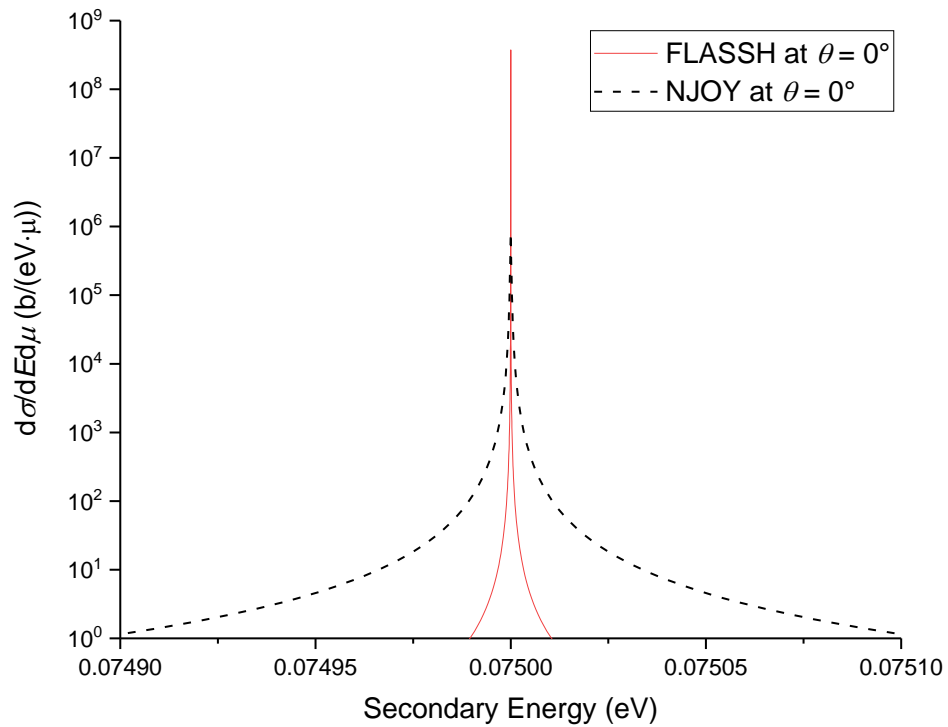


Figure 6-4. Different shape of diffusional peak at very small scattering angle.

The second issue is the quasi-elastic diffusional peak in self thermal scattering law evaluated from LEAPR/NJOY. As can be seen in Figure 6-1 to Figure 6-3, the  $S_s(\alpha, \beta)$  shows a cutoff at early  $\beta$  values. The cutoff is more severe at small  $\alpha$  values.

The third is the shape and magnitude of double differential cross section at small angles, these differences represent a lack of proper integration and interpolation algorithms in NJOY. These differences eventually contribute the integrated cross sections.

#### **Appendix D. Comparison to the Existing FLiBe thermal scattering law analysis**

As discussed in Section 1.4, two recent studies have been performed on the thermal scattering law library of FLiBe. Li et al. [73-75] duplicated the evaluation from Mei et al. [72] and applied it in reactor analysis. Mei et al. [72] applied the DOS method with the Schofield diffusion model in the evaluation of the inelastic scattering cross section. In this section, the evaluation from the DOS method used in this work and Mei et al. [72] will be compared in detail. Table 6-1 summarizes the differences between this work and Mei et al. [72].

The differences of how the DOS method is applied in this work and Mei et al. [72] are explained in detail below:

1. In this work, the diffusional behavior of FLiBe is investigated through a validated MD model.

Physical properties such as diffusion coefficient, viscosity, density etc. are benchmarked against available experimental measurements. In the work by Mei et al. [72], the diffusion coefficients were taken from a cited MD model [76]. The research adapts an MD potential [40] that was developed for solid crystalline FLiBe. Because this potential is not suited for liquid FLiBe, the predicted properties deviate from the experimental measurements. For example, the evaluated diffusion coefficient [76] is an order of magnitude smaller than experimental measurements [42,55].

Table 6-1. Comparison of FLiBe cross section calculation using the Schofield model

	<b>DOS method in this work</b>	<b>Mei et al. [72]</b>
<b>Modeling</b>	An MD FLiBe model as molten salt liquid	DFT model of crystalline LiF and BeF <sub>2</sub> , and MD model of FLiBe
<b>Total DOS</b>	From a validated MD model, FLiBe as a molten salt liquid	From summing the DOS of crystalline LiF and BeF <sub>2</sub> DFT models
<b>Diffusional DOS</b>	Extracted from total DOS	Based on assumed effective mass $M^*$ and $c$
<b>The effective mass <math>M^*</math> and weight of DOS <math>w_d</math></b>	$w_d = \frac{M}{M^*}$	$w_d = \frac{1}{M^*}$
<b>Diffusion coefficient <math>D</math></b>	From the MD model benchmarked against experimental measurements	From an MD model with pair potential prepared for crystal FLiBe
<b>Schofield model</b>	$d$ as diffusion coefficient $D$ $c$ as relaxation time $\tau_0$	$c$ as diffusion coefficient $D$ $w_d$ as reverse $M^*$
<b>LEAPR module in NJOY</b>	Approximation $w_d = d/c$	$w_d$ , and $c$ coefficients are read in separately

2. In this work, the DOS is obtained by Fourier transforming the VACF from the validated liquid FLiBe MD model. The work by Mei et al. [72], by comparison, evaluates the bound vibrational part of density of states from crystalline LiF and crystalline BeF<sub>2</sub> DFT models. As stated in Section 1.4, the crystalline state and liquid state do not share the same bound DOS. The comparison is shown in Figure 6-5. Another discrepancy in the work by Mei et al. is that the DOS from two distinct materials, i.e. crystalline LiF and crystalline BeF<sub>2</sub>, cannot be summed together to represent a mixed material. Instead, proper bonding and energy excitations should be considered for compound FLiBe.

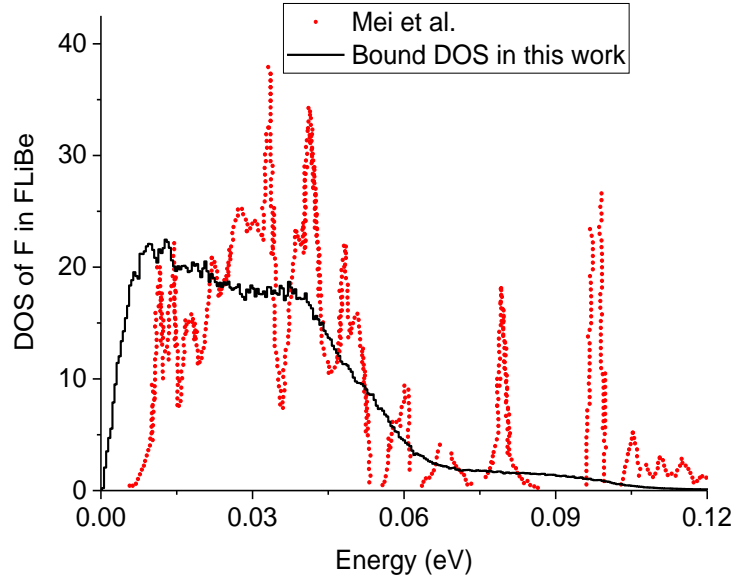


Figure 6-5. The bound DOS of F in FLiBe used in this work compared to Mei et al [72].

3. The diffusional DOS in this work is subtracted from the MD total DOS. Mei et al. implied the diffusional density of states based on assumed constant  $w_d$  and  $c$  in the Schofield model.
4. For the weight of the diffusional DOS, the physical definition should be  $w_d = M/M^*$  [91,138], whereas Mei et al. used  $w_d = 1/M^*$ . As a result, the effective mass proposed by Mei et al. is an order of magnitude larger than the physical definition. Furthermore, Mei et al. also proposed a universal effective mass for all species in FLiBe. In this situation, FLiBe is assumed to have clustered motion like a molecule. However, in this work, species in FLiBe show different diffusion coefficients. In such an ionic liquid, where the movement of ions is more independent compared to that of a molecule, it is not advisable to assume a universal effective mass.
5. In the Egelstaff & Schofield model [92], two constants,  $c$  and  $d$ , are defined;  $d$  is directly proportional to the diffusion coefficient  $D$  and  $c$  is directly proportional to the relaxation time  $\tau_0$ . In the work by Mei et al., the constant  $c$  was misused as the unitless diffusional constant. Additionally,  $d$  was not used and  $w_d$  was evaluated from  $1/M^*$ .

6. In the LEAPR module of the NJOY code system,  $w_d$  is used as an approximation of  $d/c$ . In this work, the LEAPR module is modified so that the treatment of diffusional constant  $d$  and DOS weight  $w_d$  in Schofield model is separated. Compared to this work, Mei et al. used the original approximation.

Due to the above differences, the integrated cross section from Mei et al. [72] shows significant divergence from this work. As shown in Figure 6-6, Mei et al. applied  $w_d = 0.01$  to 0.05. The resulting cross section is two to ten times higher than the cross section evaluated in this work.

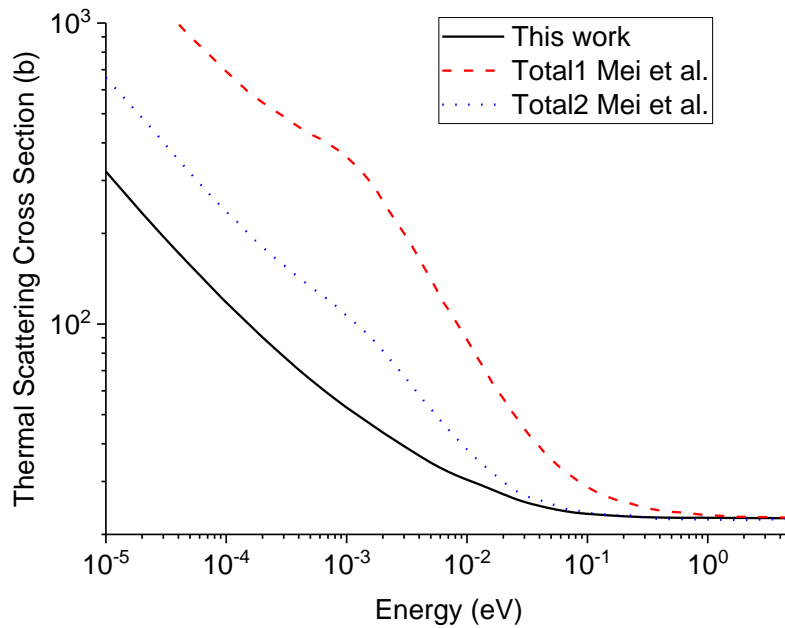


Figure 6-6. The integrated cross section of FLiBe in this work compared to Mei et al. [72]. The dotted blue and dashed red lines adapted different  $w_d$  values.